Politecnico di Torino

Master's degree: Environmental and Land Engineering
A.Y. 2023/2024
Graduation Session: December 2024

Innovative Ground Treatments in Clay Formations

Numerical analysis and quantitative improvement evaluation

Supervisors:

Prof. Daniele Martinelli

Eng. Vincenza Floria

Candidate:

Fabio Romito

ABSTRACT

The excavation of tunnels under water table has always represented a challenge in any geological condition, particularly when dealing with fine-grained soils, or more in general when the presence of fine rules the permeability and consequently affects the consolidation process, strictly connected with the stability of contour and tunnel face over the time.

This thesis focuses on the numerical simulation of an innovative technique for stabilizing the tunnel face and surrounding ground by using a special soil nail consisting of a fiberglass bar element and an external sheath devised to contain the injected grout, which can also be integrated with a coaxial drain.

This kind of reinforcement combines the effects of drain, fiberglass element and adds the compression of the surrounding soil thanks to grout injection in the geotextile sheath. In Italy, the technology is named commercially P.E.R.Ground® (Pressure Earth Reinforcement Ground), but all over the world is identified as 'x-Nail', 'Capsule grouting' or more generally grouted soil nails.

The well-known advantage of this technique is an increase in terms of pull-out strength thanks to a better adhesion between the element and the soil as demonstrated by in-situ test. However, to date the quantification of improvement effects has not been sufficiently thorough, leaving a gap in the technical literature useful for design purposes.

TABLE OF CONTENTS

LIST OF FIGURES

LIST OF TABLES

INTRODUCTION

The excavation of tunnels below water table presents significant challenges across several geological conditions. This is especially true in the presence of fine-grained soils, where permeability is reduced, and the consolidation process is affected, directly influencing the stability of the tunnel excavation over time.

Aim of this thesis is to investigate on the expected improvement effects, by using numerical methods mainly regarding the rate of decrease in terms of pore pressure and consequent increase of short-time resistance (undrained shear strength).

Chapter 1 briefly introduces the main aspects of clayey soils, focusing on the strength aspects in drained and undrained conditions.

Chapter 2 gives an overview of the ground improvement for tunnelling conventional method with attention to the different types of elements used in the practice engineering.

Chapter 3 describes the technical characteristics of each component that once assembled will constitute the innovative technology. In addition, the operational phases to be executed for the installation into the worksite are reported with a possible scheme of intervention in a general underground excavation context. Subsequently, a short overview of the actual diffusion over the world is given, highlighting differences and similarities with the Italian state of art and knowledge regarding the improvement effects.

Chapter 4 shows the results of a parametric Hydro-Mechanical Coupled (HMC) numerical modelling in small-scale. The modelling provides an accurate simulation of the reinforcement, with the final aim of quantifying the improvement effects generated by the use of the technology previously described. A description is given regarding the most important aspects such as geometry, boundary condition, constitutive model and type of computational technique adopted. Then, the different cases analysed are described and compared to quantify the improvement effects for different geometry of the intervention useful to facilitate the design process.

Chapter 5 deals with the geotechnical characterization and the numerical modelling performed for a real case-study in Italy taking into account the results of the parametric numerical modelling in small-scale.

Geotechnical characterization has been carried out according to the ground investigation (laboratory and in situ tests) provided during the design process. This part assumes great relevance because the input parameter for the numerical model came from the interpretation of tests, that unfortunately were not necessary for a complete knowledge of the geomaterial behaviour which was difficult to identify with the common classification adopted in geotechnical engineering.

After the definition of the geotechnical parameters, 3D total-stress numerical analyses have been performed with focus on the FOS (factor of safety) versus the geometry of the ground treatment (spacing between the elements/drains).

Chapter 6 summarizes the most important findings, highlighting the possible future developments and critical aspects of numerical analysis and laboratory implementation.

1 CLAY FORMATIONS

The clay deposits are characterized in the research and practice of geotechnical engineering for their great variety in terms of geological origins and ages but also for the wide range of physical-chemical phenomena linked to their own mineralogy, however, many aspects affect the final mechanical behaviour of clays, that will be highlighted in the following paragraphs.

The first distinction to be made for soils is between cohesive and granular, this differentiation is present in every field of geotechnics and arises from the nature of the solid constituents: the grains of the cohesive soils are made up at least in part of phyllo-silicate minerals, commonly called clays, while for granular soils the solid constituents are made up of grains that interact with each other thanks to frictional actions.

Clays are endowed with special physicochemical properties, which give them the ability to actively interact with each other and with interstitial fluids. In addition, to this differentiation, also the average grain size of clay (d<0,002mm), gives the capacity to retain water for pressure higher than the atmospheric one.

However, a preliminary distinction is important to distinguish between fine-grained soils and coarse, due to the different characterization approaches used in practice. For coarse-grained soil, the expected behaviour is inferred from the grain distribution curve, shape of particles, and degree of packing. Instead, in the case of fine-grained soils (silt and clay), the final behaviour depends on the type of clay minerals and the amount of clay particles that control the interaction with water.

For this reason, the first set of parameters have been defined by Albert Atterberg in the early 1900s, regarding the quantity of water that causes a change in the physical state (*consistency condition*).

The four states are identified and schematically represented in Figure 1.1: solid, semi-solid, plastic and liquid.

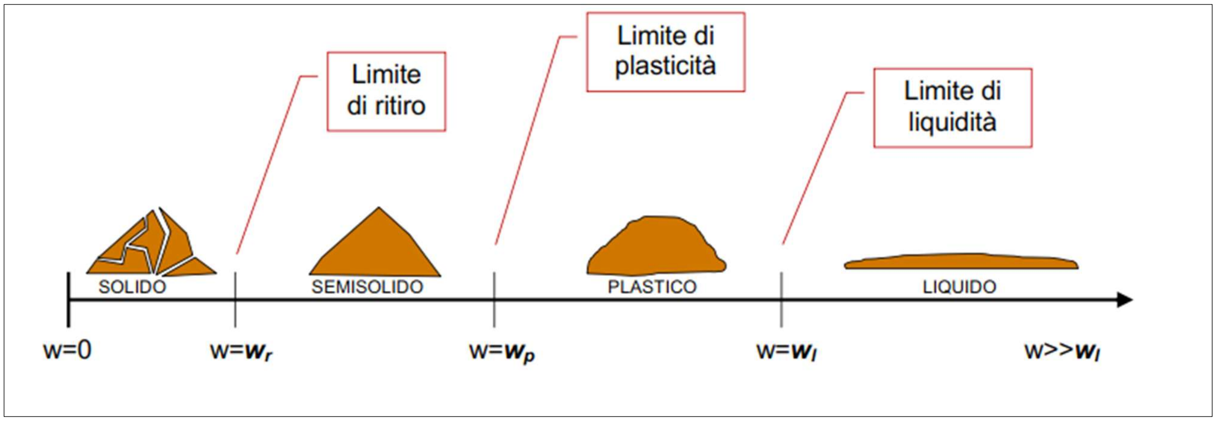

Figure 1.1 - Atterberg limits.

The plastic limit w_p is defined as the water content below which the remoulded soil sample ceases to behave as a plastic material, instead the water limit w_l is recognized as the water content above which the soil sample is not able to maintain its own shape acting as a liquid material.

The plasticity is defined by the **PI (plasticity index),** as the difference between liquid and plastic limit that practically defines a range over which the plastic condition is detectable.

$$PI = w_p - w_l$$

Commonly, the PI ranges from 5 to 15 for low plasticity soil and up to 40 for high plasticity.

The current natural water content is related to Atterberg limits through the **LI (liquid index)**, which expresses the same meaning as the relative density for coarse-grained soils.

$LI = \frac{w - w_p}{PI}$

Usually, **soft clays** have a liquidity index near a unit, whereas **stiff clays** may have values near zero.

In addition to the content of water, the colloidal properties play a key role and depend on: the amount of clay (i.e. the *clay fraction*, *CF*) and the mineralogy. Therefore, it can be expected that, at a given clay fraction, clays with higher *PI* will be more colloidally active than clays with a lower *PI*. Moving from this observation, Skempton (1953) introduced a parameter called **activity**:

$A = \frac{PI}{CF}$

Based on this parameter, clay samples are distinguished as follows: inactive clays, if A < 0.75 normal clays, if 0.75 < A < 1.25 active clays, if A > 1.25.

By using Atterberg limits, fine-grained soils can be classified according to the **plasticity chart (**Figure 1.2), developed by Casagrande (1948). The chart is divided into six regions by three lines, one inclined (Eq.1.1) and two verticals respectively at w_L=30 and w_L=50.

$PI = 0.73(w_L - 20)$ (1.1)

The soils represented in the diagram that lie over line “A” are **inorganic clays** of low $w_L < 30$, medium ($30 < w_L < 50$) and high plasticity ($WL < 50$), while soils under line ‘A’ are classified by inorganic silts, organic silts and organic clays.

Inorganic silts are defined by low, medium or high compressibility, if the liquid limit is lower than 30, between 30 and 50, or higher than 50%.

Inorganic clays have relatively high dry strength; inorganic silts have little or no dry strength and can be easily crumbled. **Organic silts** are represented in the region with a liquid limit between 30 and 50 and **organic clays** correspond to a liquid limit higher than 50%.

Organic soils have a dark brown, dark grey or bluish-grey colour and the presence of H_2S, and CO_2 (deriving from decomposition of organic matter) gives them a distinctive odour.

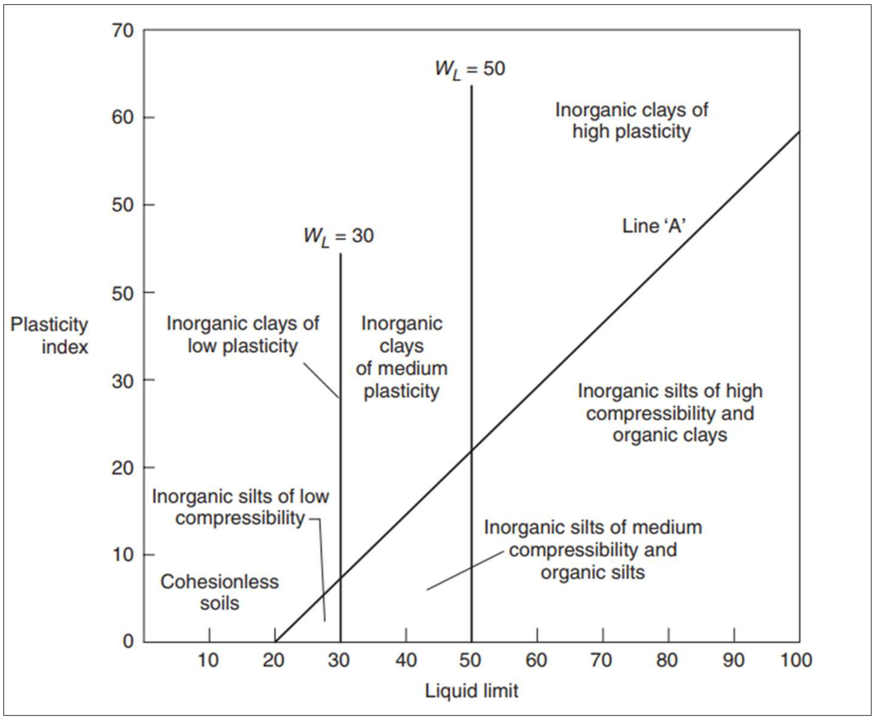

Figure 1.2 – Plasticity chart by Casagrande (1948) from Lancellotta R.,2009 [1].

1.1 Mechanical characteristics

In the geotechnical engineering field, the parameters that identify and characterize the behaviour of soils are linked to deformability and strength. However, especially for the clays (but extendable for all geological formations) the stress history highly affects the mechanical behaviour which must be correctly modelled thanks to the use of the most appropriate constitutive model.

The stress history to which a soil is subjected depends on many geological aspects such as the structure of the earth, its behaviour and the geostatic stress state, especially, every significant change in the state of stress affects the structure of the soil which will change its response to the next perturbation.

In addition, to stresses generated by a mechanical geological process such as deposition, erosion, movements along a fault, and formation of folds; the original stress state is frequently altered by other phenomena (chemical cementation, "aging", dissolution linked to changes in the chemical deposition environment) which are not stresses, but which have a major influence on the behaviour of the soil and must be considered as elements belonging to the stress history of the deposit.

Based on stress history, the cohesive soil deposits are generally classified into normally consolidated (NC) or over consolidated (OC) soils, so to determine and understand the soil behaviour is necessary to quantify the maximum vertical effective stress, which acted over its geological stress history, this quantity is defined as *preconsolidation stress* $\boldsymbol{\sigma'_p}$ and allows to make a first distinction between different classes of consolidation by definition (Eq. 1.2) of a second parameter called **OCR** (Over Consolidation ratio):

$$OCR = \frac{\sigma'_p}{\sigma'_{vo}} \qquad (1.2)$$

Where the actual vertical effective stress $\boldsymbol{\sigma'_{v0}}$ is the stress state at a given depth in natural soil deposits.

The OCR allows the quantitative distinction between **NC** (Normally consolidated) and **OC** (Over consolidated) clay, this is not only an academic definition but highly affects the evaluation of an engineering problem since many parameters (analysed in a second moment) are linked to OCR.

An example of geological history to which an element of soil is subjected is reported in Figure 1.3 where is present the curve describes the densification state (void-ratio) on the vertical axes and effective overburden stress on the horizontal axes.

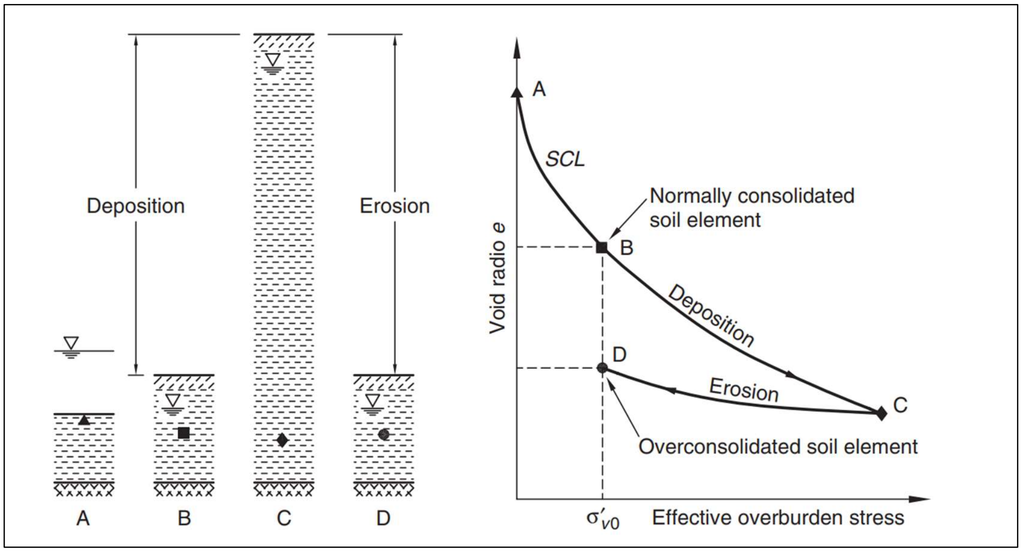

Figure 1.3 - Stress history of a soil element from Lancellotta R.,2009 [1].

1.1.1 Normal consolidated (NC) and Over-consolidated soils (OC)

A clayey soil that has recently been deposited and under the effect of its weight reached a condition of equilibrium, it is termed normal consolidated. During the consolidation phase, under the load of the weight of the overlying layers, a generic soil element undergoes axial compression without lateral deformation, this condition has been defined as eodometric. The results can be transposed in a decrease in the void ratio e due to the compression process, so starting from this consideration by plotting e and the vertical effective stress **σ'_v** on a semi-logarithmic scale a linear relationship is obtained (Figure 1.4a).

A clayey soil, after the sedimentation and consolidation phase under the vertical tension determined by the load of the overburden **σ'_B** (point B in Figure 1.4b), underwent an erosion phase with stress relief up to lower value of vertical stress **σ'_D** lower (points C and D in Figure 1.4b).

In these cases, the maximum tension sustained during the geological history (**σ'_{v0}**) is higher than the present. Thanks to the pre-loading effect, referred to in geotechnical literature as preconsolidation, the clay gained a more stable structure, characterised by higher shear strength and lower compressibility. As shown by the compressibility curve in Figure 1.4b, the soil can sustain additional loads without significant deformation as long as the preconsolidation stress is not reached.

If the preconsolidation stress is reached and exceeded an abrupt change occurs because the clay returns to behaving as a normally consolidated material. Deposits that have been subjected throughout their history to tensions **σ'_v** higher than the current tension **σ'_{v0}** are defined as over-consolidated and the extent of the over-consolidation phenomenon is quantified by the OCR previously mentioned.

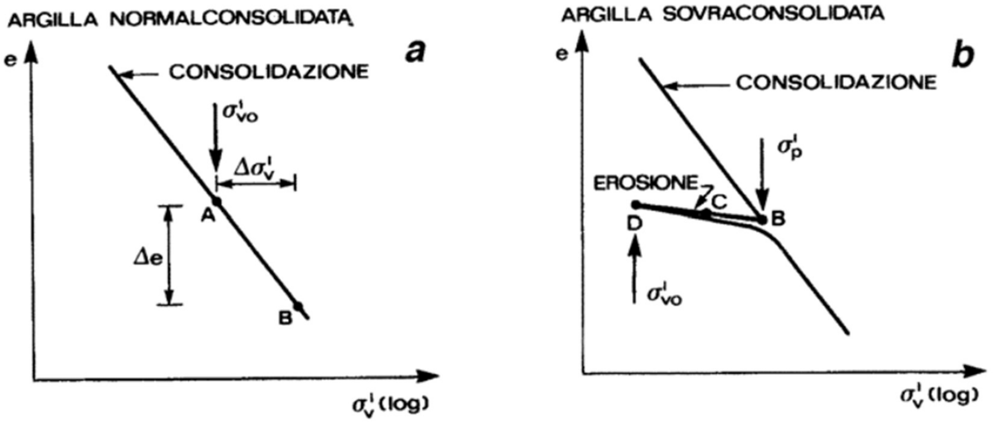

Figure 1.4 – (a) Stress history of NC deposit and of (b) OC deposit (from Lancellotta, 1991)

1.1.2 Shear strength

Continuing the discussion about clays is important to differentiate the strength into two categories, the undrained strengths important for short-term loading conditions, and drained strengths important for long-term conditions. This distinction is made because over time the strength properties of clays are subject to changes through consolidation, swelling, weathering, development of slickensides, and creep.

The shear strength of clays in terms of effective stress can be formulated (Eq.2.3) by the Mohr-Coulomb strength criterion as:

$$\tau = c' + \sigma' \tan(\varphi') \qquad (1.3)$$

Where τ is the shear strength, c′ the effective stress cohesion intercept, and φ′ the effective stress angle of internal friction.

The shear strength of clays in terms of total stress (Eq.1.4) can be expressed as:

$$s_u = c + \sigma \tan(\varphi') \qquad (1.4)$$

Where $\boldsymbol{s_u}$ and φ′ are the total stress cohesion intercept and the total stress friction angle.

For saturated clays, φ′ is equal to zero, and the undrained strength (1.5) can be formulated as:

$$s_u = c \qquad (1.5)$$

The two formulations represented in the planes τ – σ’ and τ – σ have been reported in Figure 1.5.

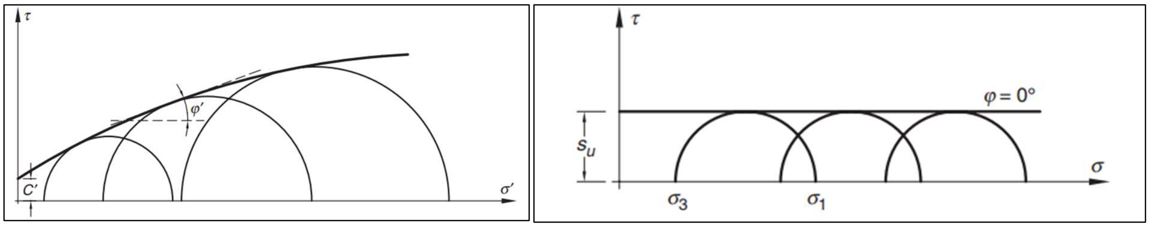

Figure 1.5 - Failure criterion in terms of effective stresses (left) and total stress (right).

However, some further implementations have been made by the Critical State Theory [2], that by analysing the results of different laboratory tests observed that the points at a stationary state (defined as critical state) all lie to a single locus, called **critical state line**, represented by a straight line in the plane (*p′, q*) by the following equation (Eq.1.6) that has the same physical meaning of the Mohr-Coulomb criterion.

$$q = M * p' \qquad (1.6)$$

Where, M corresponding to the slope of CSL (Eq.1.7) is defined as:

$$M = \frac{6\,\mathrm{si}\ \ (\varphi_{cv})}{3-sen(\varphi_{cv})} \qquad (1.7)$$

In soil mechanics, the specific volume **υ** is plotted as a function of the natural logarithm of the mean effective stress **p’**; in this plane, two curves can be drawn representing the curve of normal consolidation (NCL) and the curve of critical state (CSL), linear and parallel each other.

This plane can be used to determine soil strength both in drained loading conditions for which the variation in pore pressure is allowed with a consequent volumetric variation, and the undrained loading conditions in which if the rate of loading is faster respect the hydraulic conductivity so that water cannot flow out from the voids during loading causing no volume variations. All these phenomena described are appreciable in Figure 1.6 where the drained path BC and the undrained have been represented.

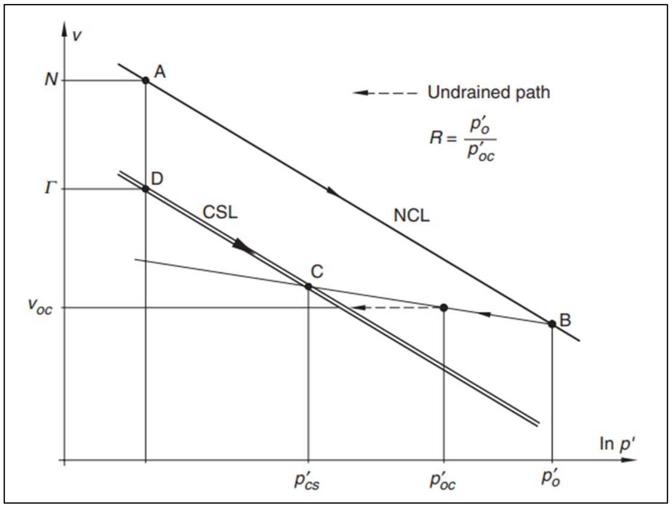

Figure 1.6 – Stress history of an over-consolidated clay (Ref.[1]).

At this point, by considering the Eq. 1.6 and the one characterizing the CS, by combing both:

$$s_u = \frac{1}{2} * q = \frac{1}{2} * Mp'_f = \frac{1}{2} Mexp^{\left(\frac{\Gamma-\nu_0}{\lambda}\right)} \qquad (1.7)$$

Where Γ represents the specific volume at p'_0=1kPa, υ_0 represents the specific volume for a given value of p'_0 and λ is the slope of NCL and CSL obtained from test interpretation.

The Eq.1.7 condensate some key aspects in the evaluation and determination of the undrained shear strength, indeed the relationship between the undrained strength and the specific volume, cannot be considered as a soil property, but it is rather a soil behaviour depending on the stress path applied and previous stress history at which was subjected.

Starting from the previous equation (Eq. 1.7), some consideration can be made regarding the NC clays, which will be of interest in the next paragraphs, so the relationship expressed by (Eq. 1.7) can be improved and normalized by considering the NCL (Eq. 1.8), indeed just by substituting expression into (Eq.1.7) obtaining (Eq.1.9).

$$\nu_0 = \mathrm{N} - \lambda ln p'_0 \qquad (1.8)$$

$$\frac{s_u}{p'_0} = \frac{M}{2} exp\left(\frac{\Gamma-\mathrm{N}}{\lambda}\right) \qquad (1.9)$$

By, assessing in a simplified way the mean consolidation pressure (Eq.1.10) at a certain depth as:

$$p'_0 = \frac{1+2K_0}{3} \sigma'_{v_0} \qquad (1.10)$$

The undrained strength of a NC clay deposits increases linearly with depth.

In addition, to these considerations has been largely documented the anisotropy of the undrained shear strength can be divided into two types: *inherent anisotropy* related to the flat-plate shape of clay particles that tend to assume an orientation perpendicular to the major principal strain direction during consolidation and as a result shows a direction-dependent stiffness and strength. The second type of anisotropy is defined as stress system-induced anisotropy and is related to the magnitudes of the stresses during consolidation which change depending on the orientation planes considered, then by considering also the pore pressures changes induced by undrained loading, they vary with the orientation of the changes in stress.

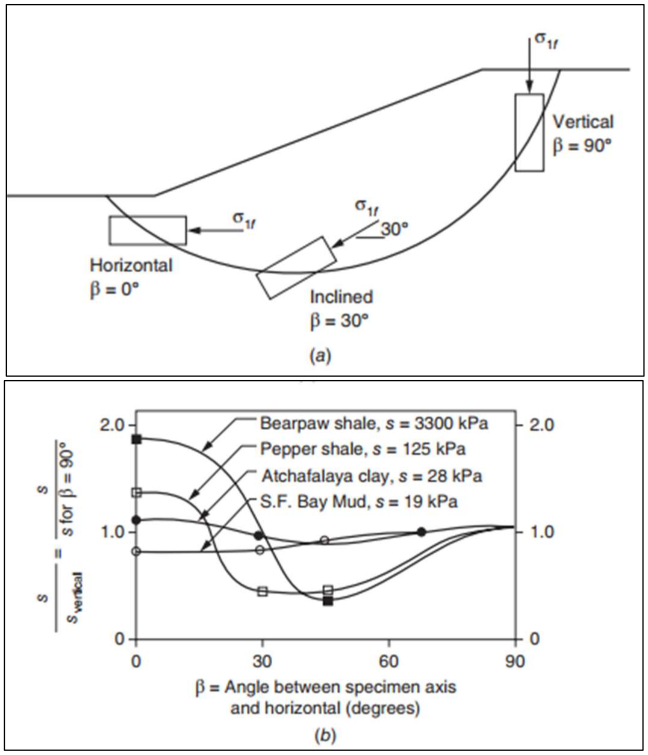

Figure 1.7 - Stress orientation at failure and undrained strength anisotropy of clays and shales: (a) stress orientations at failure and (b) anisotropy of clays and shales—UU triaxial tests.(Ref. [3])

1.1.3 Operative aspects

In case of operative conditions where the critical state does not represent the state of the soil, and the reconstruction of pore pressure evolution is possible, the provision of undrained shear strength can be carried out by considering the state of stress of the soil in terms of effective stress in the Mohr-Coulomb plane.

In Figure 1.8 the difference between the two conditions is drawn in the Mohr-Coulomb plane, particularly, when the shearing phase is conducted in undrained conditions, so in a short time the failure conditions can be expressed as (Eq.1.11):

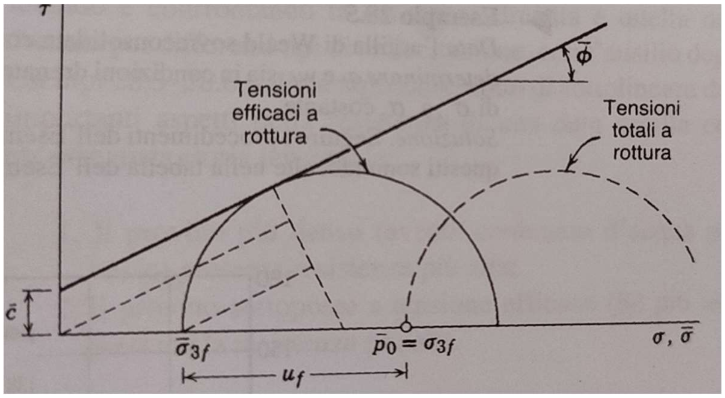

Figure 1.8 – Undrained shear strength in total stresses and effective stresses (Lambe, W. T. et al.,1997 [4]).

$$C_u = \frac{1}{2} * \left(\sigma_{1f} - \sigma_{1f}\right) = C_u = \frac{c' \cos(\varphi) + \sigma_3\left(sen(\varphi)\right)}{1 - sen(\varphi)} \qquad (1.11)$$

But considering the Skempton parameter **A** that describes the variation of pore pressure in case of a deviatoric change of state of stress during a triaxial consolidated undrained test defined as (Eq.1.12).Usually, A is between 0.7 and 1.3 for NC clays (Lambe, W. T. et al.,1997 [4]).

$$A = \frac{\Delta u - \Delta\sigma_3}{\Delta\sigma_1 - \Delta\sigma_3} \quad \text{where for } \Delta\sigma_3 = 0 \quad \Rightarrow A = \frac{\Delta u}{\Delta\sigma_1} \qquad (1.12)$$

By the combination of the previous equations (Eq.1.11 and 1.12), Ladd [5] express the short-term cohesion and the effective strength parameter as (Eq.1.13):

$$c_u = \frac{c'\cos(\varphi) + p_0{'}sen(\varphi)}{(1+(2A-1)*sen(\varphi)} \qquad (11.13)$$

The equation quantifies the undrained shear strength and relates it with the average stress state before the failure p'$_0$, the Skempton parameter **A** which is a function of the stress history and must be determined with CU triaxial test (consolidated undrained) and on soils parameters (cohesion and friction angle)

2 CONVENTIONAL TUNNELING METHOD

The Conventional Tunnelling Method is commonly defined as the cyclic excavation process adopted for the realization of underground structures, divided into the following stages:

1. **Drainage and pre-support:** lowering of the water table (if present) and installation of pre-support elements as fiberglass nailing, forepoling, or ground treatments like permeation grouting and jet grouting, that ensure the stability of the tunnel during the next steps.
2. **Excavation phase**: removal of material at the excavation face by using the drill and blast method (used in rock formation with high UCS values); or by using mechanical excavators used in soils (clayey, silty and sandy formations).
3. **Mucking phase**: collection and loading of the excavated material on dump trucks or conveyor belt system to move it outside and free the working space.
4. **Installation of primary support elements**: placement of reinforcement on the tunnel face and contour to stabilize and control any possible collapse of variable magnitudes, such as detachment of small blocks or detachment of entire wedge (some m^3) in case of rock excavation. In the case of soils, the main problems regard the collapse of the excavation phase causing the extrusion of the material in a short time (seconds).

   This phase is important because will affect the safety of the subsequent working phase, and also the load on the final lining considered for the long-term stability.
5. **Impermeabilization**: installation of an impervious membrane that avoids any entrance of water into the tunnel over the service lifetime, and controls the flow of water towards the collection system to maintain the tunnel drained over the service life,
6. **Secondary support**: installation of final lining in addition to the primary supports, to accommodate all the permanent loads forecasted into the design process.

For each of the above-mentioned phases different techniques have been developed over the years all over the world, in the next paragraphs a brief overview will be given for the sake of exhaustiveness.

2.1 Excavation methods

The excavation methods adopted for Conventional Tunnelling are divided mainly into two groups:

1. Drilling and blasting are usually applied in hard rock ground conditions.
2. Mechanically supported excavation is mainly used in soft ground and weak rock conditions (using roadheaders, excavators with shovels, rippers, hydraulic breakers etc.).

In case of variation of ground conditions, both excavation methods can be adopted in the same project, carrying out step by step in rounds of the fixed advancement chosen in the design stage.

a) b)

Figure 2.1 –(a) Excavation by using drill and blast method, Mechanical excavation by using excavator (b).[6]

Generally, the round length varies from 4 m in good conditions to 1 m or less in soil and poor ground conditions (e.g. squeezing rock), however, this parameter has a key role in the determination of the advance speed and consequently the productivity of the process.

2.2 Excavation sequence

The first phase of the Conventional Tunnelling Method can be carried out in different ways (Figure 2.2), generally, the main distinction is made between the full-face and the partial excavation of the tunnel cross-section. Based on the mechanical characteristics of the excavated medium, working equipment is available and a final cross-section is needed.

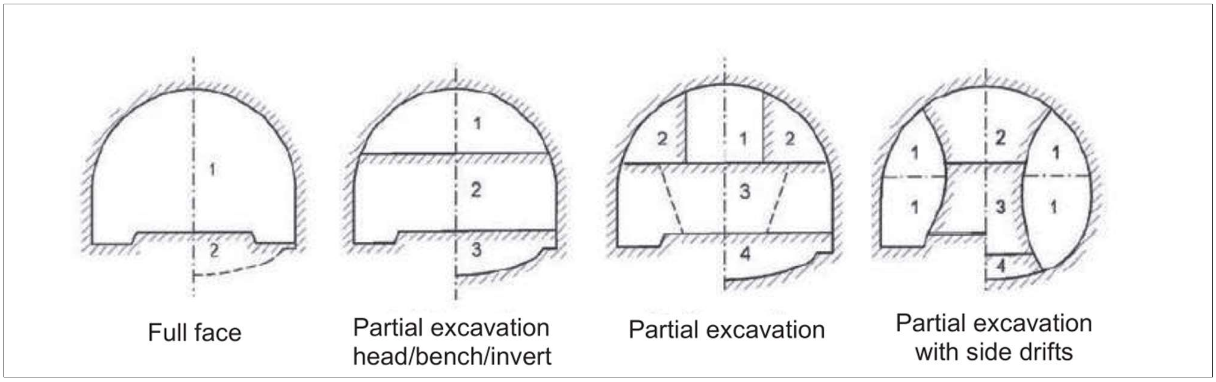

Figure 2.2 - Different solutions for the face excavations, where numbers indicate the order of execution. (Bilotta E. et al. [7])

The choice among different operative solutions is mainly based on the stability of the tunnel face and control of contour convergence, following these aspects Lauffer (1958) [8] proposed the definition of two quantities:

- **Stand-up time**: the amount of time a tunnel will support itself without any added support structures.
- **The unsupported span**: the span of the tunnel or the distance between the face and the nearest support, that can remain stable without any reinforcement.

Over the years, these two parameters have been related to the rock quality using different rock mass classification systems RMR (Bieniawski, 1993), Q-system (Barton et al., 1975), GSI (Hoek & Brown,1997).

However, the two quantities above-mentioned depend also on the excavation method, excavation cycle rock reinforcement method time to install rock support and length of the excavation steps.

In other words, the stand-up time is a function not only of rock mass properties but also of excavation technique, additionally, the concept widely developed for rock mass formations can be extended also in soil formations, with the difference that another approach to the issue was developed over the years, particularly, by focusing the attention on the stability of the excavation face.

2.2.1 Face stability

The stability of the excavation face is essential for the correct development of the underground construction because the safety of workers but also settlements at the ground surface must be avoided and mastered, for all the ground conditions encountered during the project.

The analysis of the face stability in tunnels can be divided between *shallow tunnels* (**z**[*]<2.5**D**[†]) and *deep tunnels* (**z**>5**D**), this peculiar distinction is made since different physical phenomena are involved.

For deep tunnels, stress redistribution (which may or may not require interventions at the face, depending on the quality of the ground), enhances the formation of an arch able to self-support the volume involved by the tunnel excavation.

For shallow tunnels, these arching effects are obtained with greater difficulty and stresses that are not correctly dealt with can give rise to surface settlements or sinkholes, causing damage to neighbouring structures. The considerable deformation of poor ground at great depth can lead to a decompressed zone at the edge of the excavation area and may lead to a chimney caving mechanism with the creation of a sinkhole because the failure surface formed at the excavation reaches the ground surface.

The solution to maintain the face stability is the application of stabilizing action against the tunnel section, in this way any sliding movement is prevented.

In the scientific literature authors developed models that can be grouped into the following categories:

- **Experimental:** The failure of the working face is generally caused by the displacement of a rigid wall or the deflation of a flexible membrane at the working face (
- Figure 2.3), mainly adopted to understand the kinematism to be considered in analytical models.

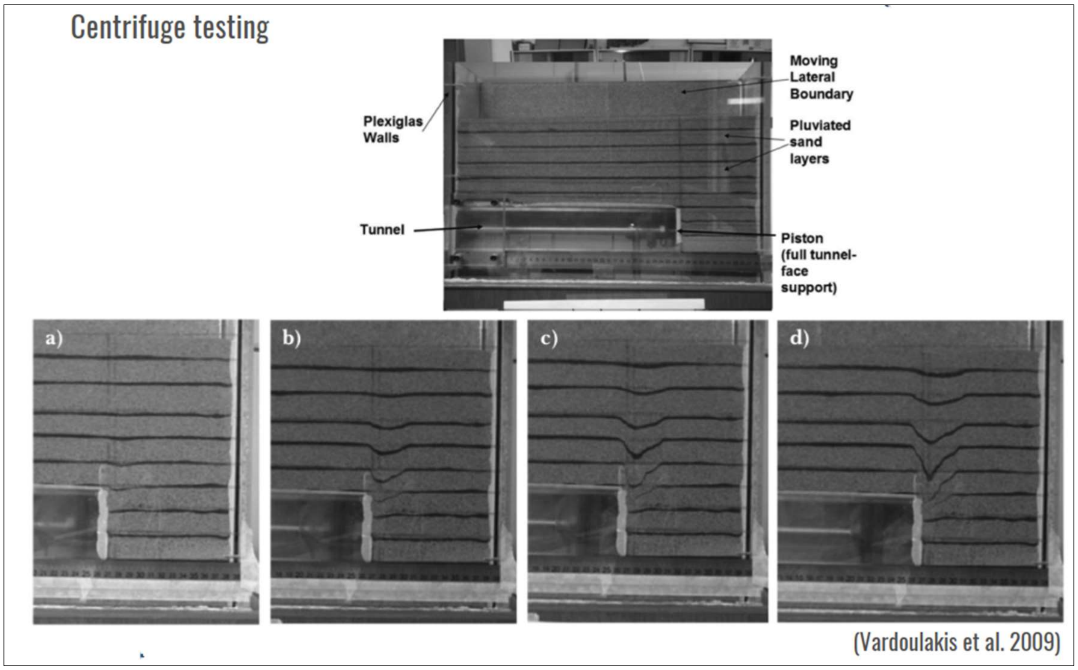
Centrifuge testing

(Vardoulakis et al. 2009)

Figure 2.3 - Simulation of tunnel face collapse in centrifuge test apparatus.

- **LEM (Limit Equilibrium Method**): This approach consists of directly assessing the forces in play (Figure 2.4b). Its implementation in soil masses, or materials that can be considered as continuous at the scale of the structure, requires strong assumptions

---

[*] z - Depth of tunnel axis respect the ground surface [m]

[†] D – Diameter of the tunnel [m]

regarding geometry, stresses acting and strength of the material. An example is given in Figure 2.4 showing the model developed by Anagnostou & Kovari (1996) [9].

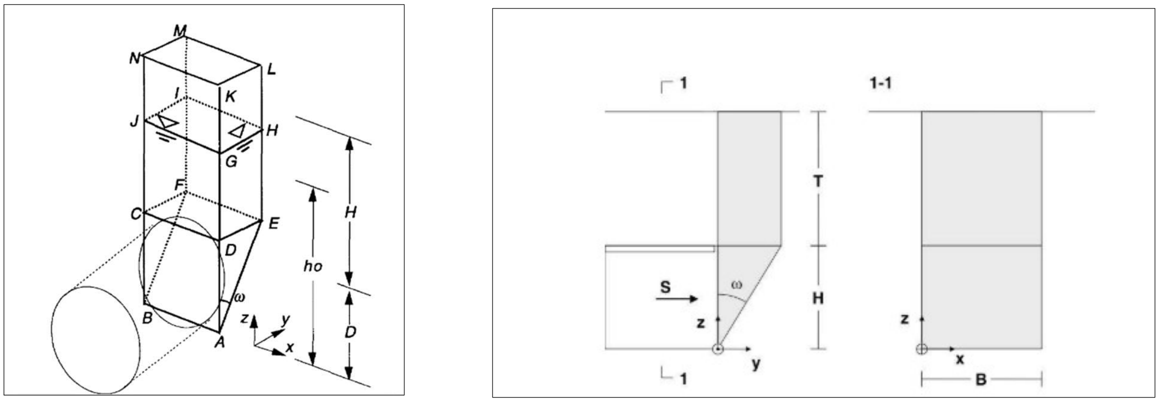

a) Failure mechanism.

b) Geometrical characteristics of failure volumes.

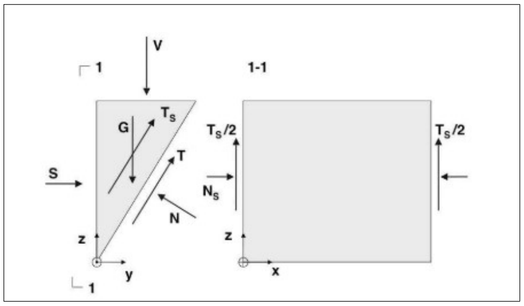

c) Forces acting on the failure volumes.

Figure 2.4 – Geometrical characteristic of the failure volumes, Anagnostou & Kovari (1996)[9]

- **Numerical Models:** The numerical models considered consist of solving the system with partial derivatives resulting from equilibrium equations, the ground's behaviour law, boundary conditions and initial conditions, by rewriting the problem in discrete form (in finite elements or explicit finite differences). An example of the results obtained with a parametric analysis carried out by (Vermeer et al. 2002) [10] is reported in (Figure 2.5).

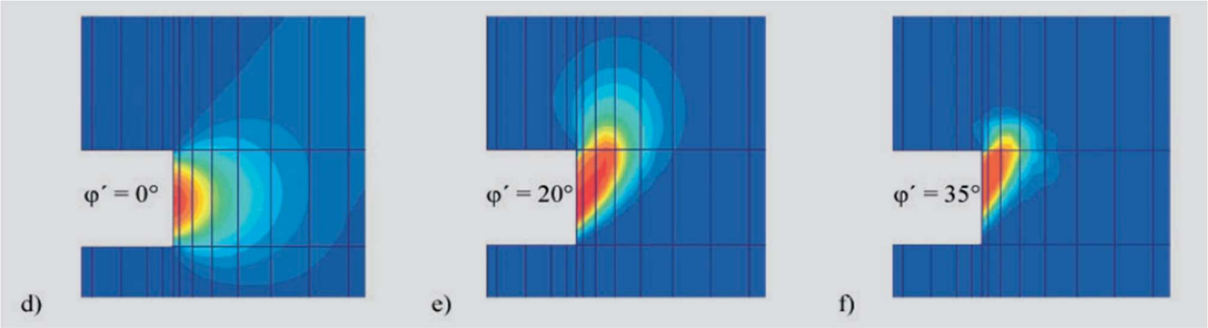

Figure 2.5 – Incremental displacements (d - f) at failure, close-up around the face for a tunnel with H/D = 5 (P. A. Vermeer et al. 2002[10]).

2.3 Primary support

The solution to problems regarding the stability and safety of the tunnel during the excavation and in the short term have been solved by the use of the primary support are structural elements helping the self-sustaining ability of rock masses and soils, improving the confinement degree and damping the decay of material properties.

The systems adopted to furnish the primary support will be described in the next paragraph, particularly the most used in the last decades are sprayed concrete, steel arches, and anchors/bolts.

2.3.1 Bolts

Over the years the bolts have been effectively used in a wide variety of rock conditions, thanks to the development of several bolt types, mainly distinguished by the behaviours and design characteristics.

The main difference is how the force is applied, which can be active if acts once the support is installed, or passive if the force is developed over time, additionally, another distinction in the bolt design and consequent installation regards the durability and so if the support given by the bolts is temporary (duration of construction) or permanent (entire service life of the infrastructure).

The elements that compose a bolting system are generally: the resisting element, a coupling device able to connect the ground and the resisting element and the bearing plate.

Three main types of anchoring systems widely used are:

- **Fully grouted bolt:** this type of reinforcement is composed of a steel rebar acting as a resisting element, the cement grout that fills the gap between the rebar and the drilled holes, and the faceplate that allows the pre-tensioning and/or fixation of the bolts thank to tightening of the nut. This kind of support can be identified as passive due to the application of force once the deformation of the ground begins**.**

  In Figure 2.6 a simplified scheme of fully grouted rebars is shown, while in Figure 2.7 the difference between a temporary and permanent bolt is shown, particularly the use of a coating element (rubber, epoxy rubber or a film of galvanization) that protects against the corrosion as widely discussed by Bruland, A. et al. (2021) [11].

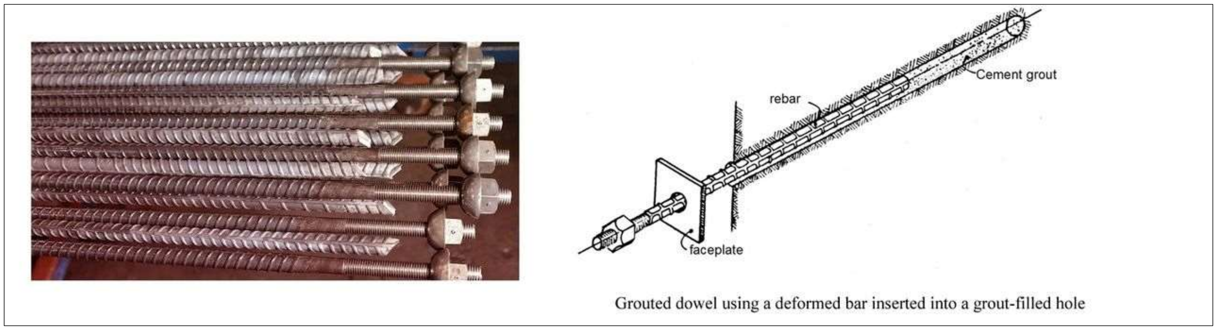

Grouted dowel using a deformed bar inserted into a grout-filled hole

Figure 2.6 - Fully Grouted rebar bolt. (Reference: Geotechnical Designs website)

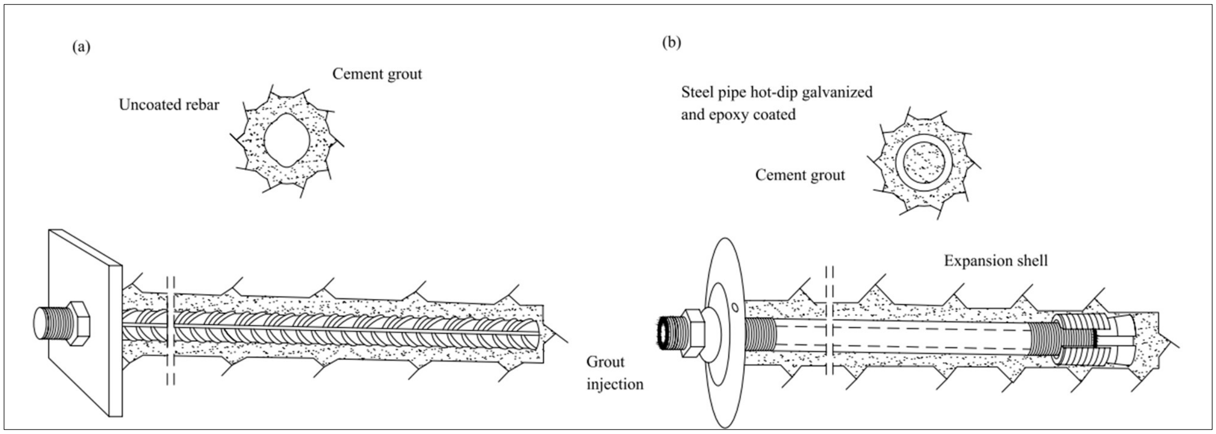

Figure 2.7 – Difference between temporary and permanent fully grouted bolt.(Bruland, A. et al. (2021) [11]).

- **End-point-anchored bolts**: this element is composed of a resisting element that is fixed with the ground by an expansion head, that during the installation enlarges its size until the blockage of the system is guaranteed. The bolt can be pre-tensioned just after installation by fastening the bearing plate, in a second moment is also possible to grout the rebar to avoid a possible relief of the expansion head will cause the loss of reaction capacity of the system.

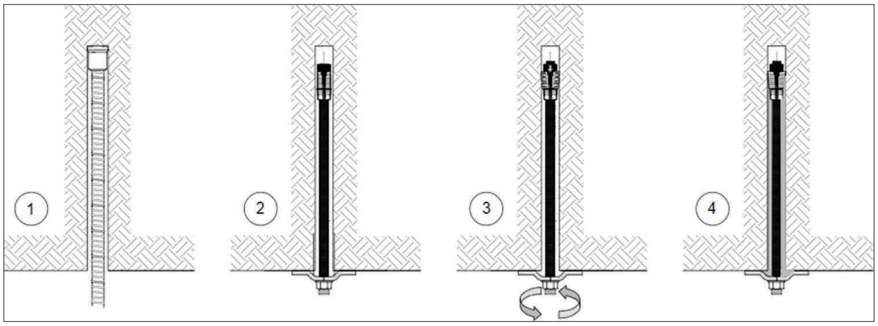

a) drilling (1); bolt insertions (2); anchoring the bolt at the end (3); grouting (4-eventual).

b) Bolts anchored with an expansion sleeve anchor (Reference: Norwegian Rock Bolting (Publication n.21))

Figure 2.8 – a) Installation procedure of end-anchored bolt; b) Example of end-anchored bolt.

- **Frictional Bolts:** these kinds of bolts exploit the friction between the ground and the bolts, mainly two types of technology are available, one is the *Split set* composed by two parts, a steel slotted tube and a matching domed bearing plate. One extremity is tapered for easy insertion into a drill hole, and the other has a welded ring flange to hold the bearing plate.

  The second type of frictional device is the Swellex, which is composed of a folded steel tube inserted into a pre-drilled hole in the rock. Water is pumped at high pressure around 30 MPa, enlarging the fold with consequent expansion of the tube into the hole size, by adhering to the irregularity.

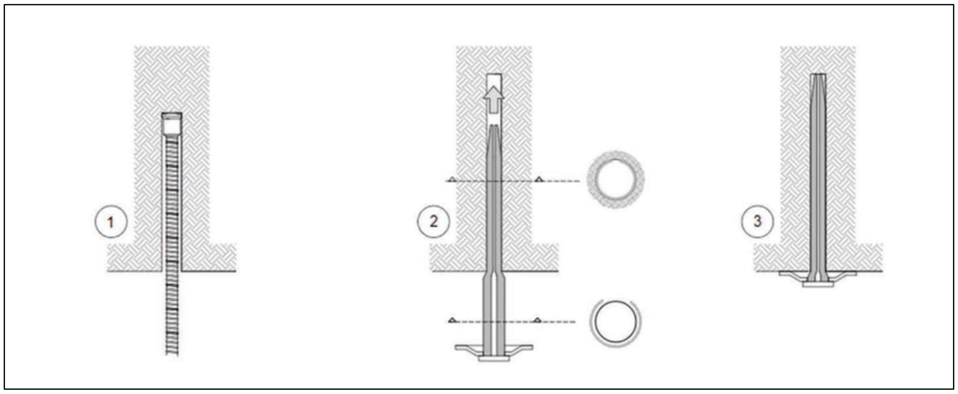

Figure 2.9 - Split Set installation sequence: drilling (1); bolt insertions (2) and final layout (3).

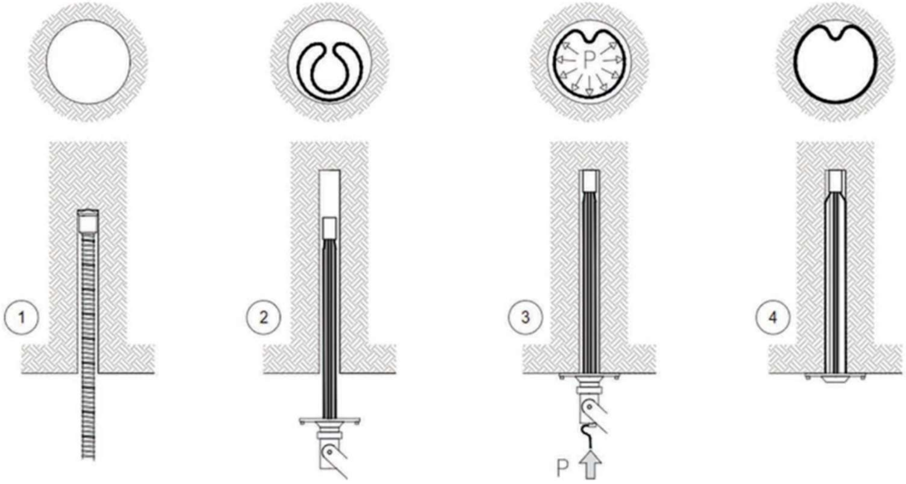

Figure 2.10 - Swellex bolts Installation sequence: drilling (1); bolt insertions (2); pumping of water (3) and final configuration (4).

2.3.2 Fiberglass bolts

A widely adopted technology in tunnelling is the use of fiberglass bolts, thanks to the mechanical characteristics of the material. The first is related to the high tensile strength $\mathbf{f_{yk}}$ [‡] that allows applying a confining force on the zone of application while the soil is showing deformation in the failure zone; the second advantageous characteristics is the easiness to be cut and resistance to corrosion.

[‡] $\mathbf{f_{yk}}$ - 450 MPa for percentage of glass content bigger than 50%; 900MPa for percentage of glass content bigger than 70%

Unfortunately, the fiberglass does not show high performance regarding frictional characteristics, and for this reason different types of bolts profiles are used by the industry, the simplest is made up of a ribbed circular section (Figure 2.11), an advanced system is made of profiles made of a circular cross-section and a system made up of three fiberglass plates assembled with a PVC or polyethylene plastic pipe where a grout injection is performed in the annular region between the bolt and the soils, in this way the continuity of the contact is ensured.

Both types feature had an irregular surface that enhances adhesion to the cement grout, thereby improving pull-out resistance. In tunnel face reinforcement with fiberglass soil nailing, the process involves inserting the fiberglass profile into a pre-drilled borehole. This borehole is then filled with low-pressure injected cement grout, either through holes in the fiberglass pipe or via the PVC/polyethylene pipe in profiles comprising three fiberglass plates.

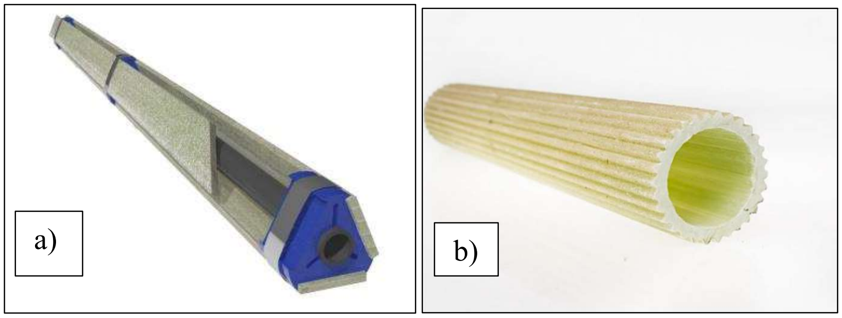

Figure 2.11 – Fiberglass profile types: a)three plates assembly b)ribbed circular section (Courtesy of Sireg S.p.A)

2.3.3 Sprayed concrete

In the last decades, the use of sprayed concrete lining systems has become very common in soft ground because of the flexibility it can offer in terms of the shape of the tunnel and the combination of support measures, indeed after the application of a 10-15 cm of shotcrete is possible to install additional support elements such as bolts and steel arches.

The sprayed concrete called also spritz beton or shotcrete is a cementitious mixture projected to the surface to be supported thanks to a nozzle able to create a high-pressure jet of concrete.

Once the shotcrete touches the ground, adheres to it and is able to maintain the position without any water loss or detachment, thanks to its rapid setting time. In this way is possible to spray different layers of shotcrete, one over the previous, until obtaining the designed thickness.

The spritz beton is mainly composed by:

- **Cement:** Ordinary Portland cement is usually preferred according to the performance in combination with setting accelerators or slow reaction additives. The amount of cement content usually adopted is generally 300–450 kg/m^3.
- **Water:** The characteristics of hardened concrete and its durability over time are influenced by the water content, that must be coupled with the aggregate. The range for $\frac{w}{c}$ ratio for different allowance level is between 0.55 (low specification level) and 0.46 (high specification).
- **Aggregate:** 75% of the shotcrete volume is composed of aggregates with a maximum size of 4mm to reduce the rebound projection, and facilitate the transport, with special attention to the finer fraction (d<0.125mm) has an important role for the transport in dry-mix with the counter-effect of dust production.

  The usual proportion of aggregates for wet mix is 0–4 mm: 60%; 4–8 mm: 40%; and ≤0.125 mm: 4%–9%.

- **Additives**: The main additives used are fly ash, micro silica, stone dust, lag, limestone filler and superplasticizer. The silica fume has the function of filling the microscopic voids with a consequent reduction in permeability and increasing in density and improvement of concrete mechanical performance (thanks to the pozzolanic nature of silica fume).

  Additional drawbacks are an increase in cohesion of the mix and therefore both the resistance to runoff and the lower tendency to rebound.

  The usual amount of silica fume at a rate of 5%–7% of the cement mass (about 20–30 kg/m^3).

- **Accelerators:** guarantee the self-support capability of the shotcrete immediately after the spraying phase due to the reduction of the setting time. Divided into two classes: alkaline and alkali-free accelerators, the second class is the most used nowadays due to lower production of harmful alkali in working environment and better long term-strength.

  The usual amount of accelerators lies between 15% and 20% for the alkali class, and 4-7% for the alkali free.

- **Reinforcement:** steel or polymeric fibers of different shapes (corrugated, double hook, profiled, ecc…) added to the shotcrete to give rise to a diffuse matrix able to improve the mechanical characteristics. The amount usually adopted is 30/40 kg/m^3.

The composition is designed not only on the base of performance (strength, setting times, viscosity) but also on the type of technique adopted, dry or wet mix.

A scheme able to summarize the dry process is reported in Figure 2.12, the sprayed concrete is conveyed by compressed air using rotor machines most frequent method of thin flow conveyance for sprayed concrete. The material passes through a feed hopper into cylinder chambers and is blown out in portions by compressed air and conveyed at high speed through hoses or tubes, where the water with alkali or alkali-free accelerators is added before the ejection from the nozzle.

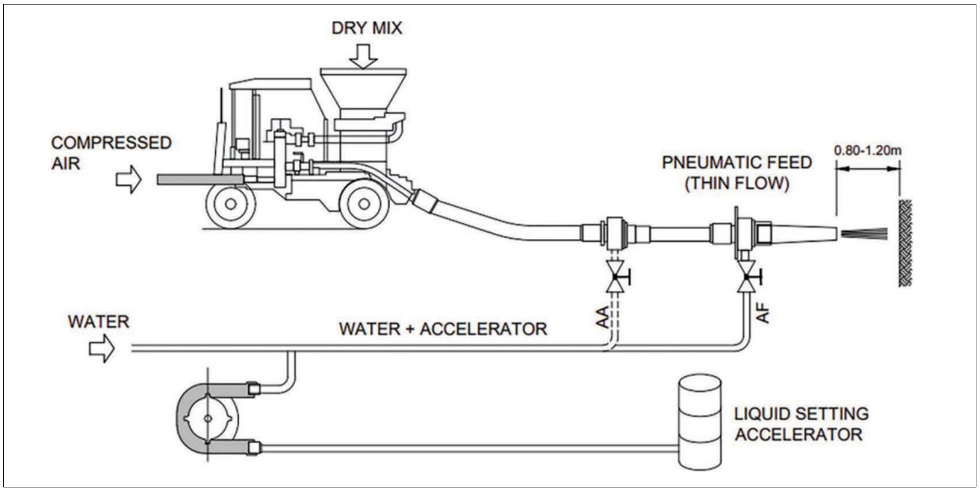

Figure 2.12 - Thin flow process for dry-sprayed shotcrete. AA, alkali accelerator; AF, alkali-free accelerator.(Bilotta, E. et al. [7])

The wet mix method illustrated in Figure 2.13 is organized into two main stages, in the first there is a mixing station where cement, water and aggregates are mixed up and pumped towards the nozzle where the other two lines convey the compressed air and the liquid accelerator. The second stage consists of the addition of an accelerator to reduce setting time and compressed air to increase the speed of the concrete mix flow so that good compaction and adherence to the substrate or surface are achieved.

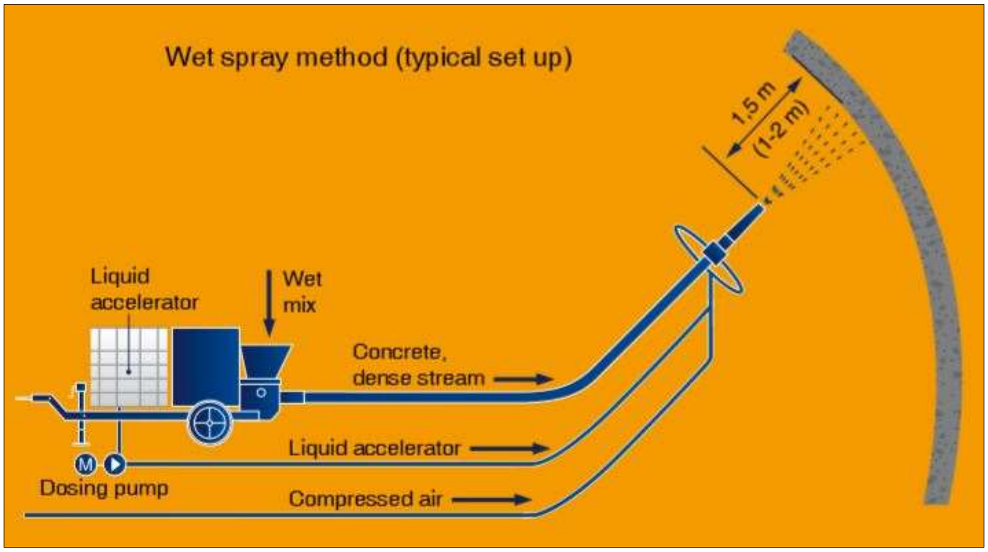

Figure 2.13 - Wet-mix process for sprayed concrete (Courtesy of Sika)

2.3.4 Steel arches

The adoption of support system by use of steel arches become necessary when the inward movement of the soil or rock medium has to be controlled to maintain stable the excavation contour in short and long term.

The use of steel arches was subjected over the years to conceptual evolution, moving from a use of the support as a passive load-bearing components to an active structural elements. This evolution was introduced with the use of shotcrete, that in cooperation with the steel arches forms an active support system for excavation, because the shotcrete embeds inside these supports and increases their resistance and their ductility, with advantages also for the management of safety at work. This cooperation between elements leads as result in a limitation of deformation and facilitates the creation of an arch effect around the excavation, enhancing overall stability.

These types of support are used in poor quality of the rock mass or when the rock strength respects the stress state show an evident need for a robust support.

The most used profiles include HEA, HEB and HEM, which maintain the same profile but are differentiated by thickness of central web connecting the upper and lower flanges (also differentiated in thickness) and consequently by the weight, for a fixed width of the profile (Figure 2.14).

Other types of steel arches profile are IPN or IPE which maintain the same profile but differs in the inclination of the flanges (Figure 2.15). This kind of profile often arranged in pairs to address differences in resistance along the two axes and reduce the risk of instability compared to the first type which are more suitable for axial load.

These high-stiffness elements provide immediate support upon installation and are positioned at intervals defined by the project specifications and are linked together using bars, which ensure consistent spacing between the ribs and streamline the assembly process.

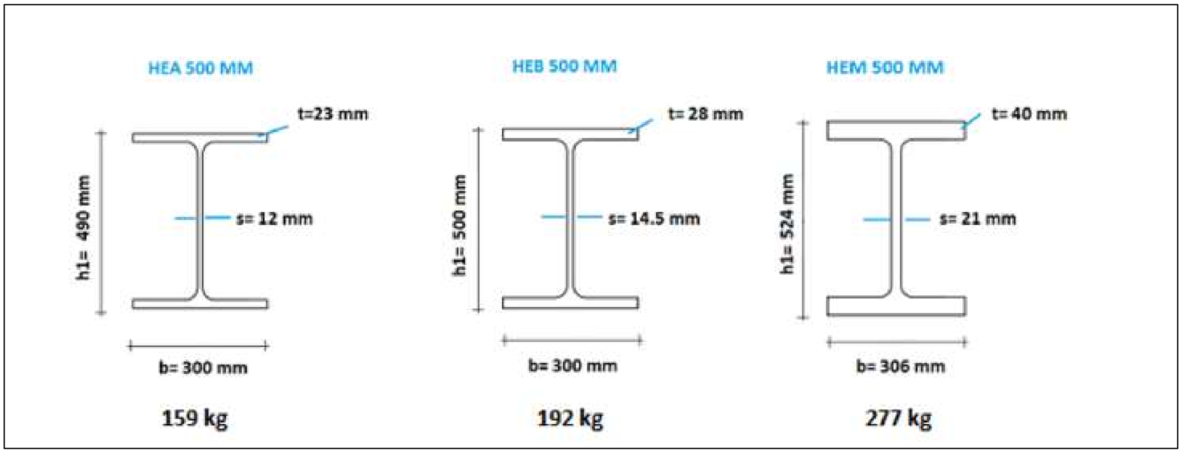

Figure 2.14 - Different steel profile adopted for steel arches HEA, HEB, HEM from left to right.

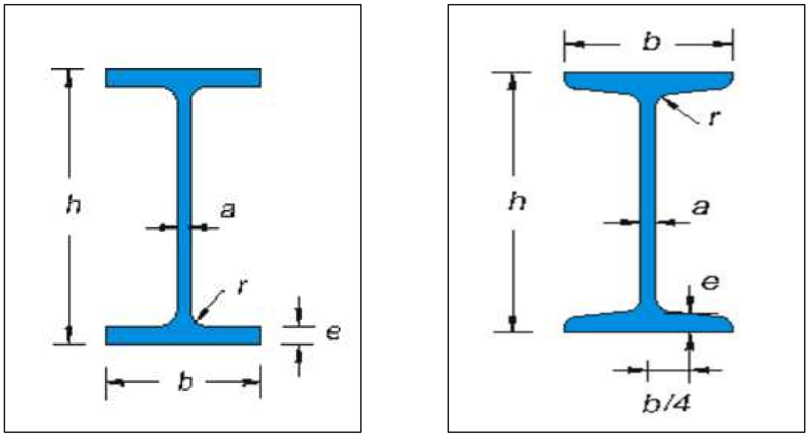

Figure 2.15 -IPE (sx) and IPN (dx) profiles. (Courtesy of OPPO)

At the end of the installation of all the elements that characterize the primary supports such as bolts, steel arches and wire mesh and shotcrete, different configurations can be obtained An example of these results is schematized in Figure 2.16.

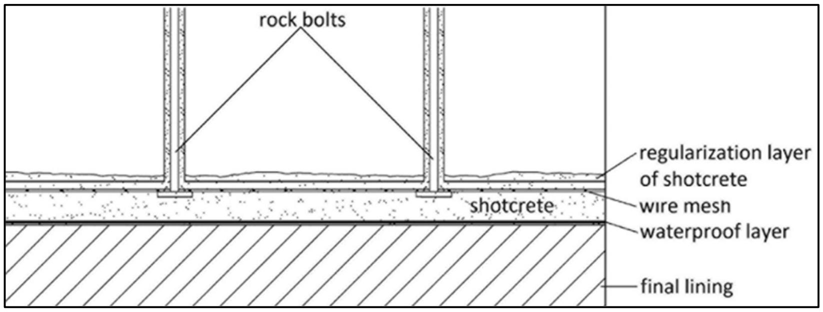

a)

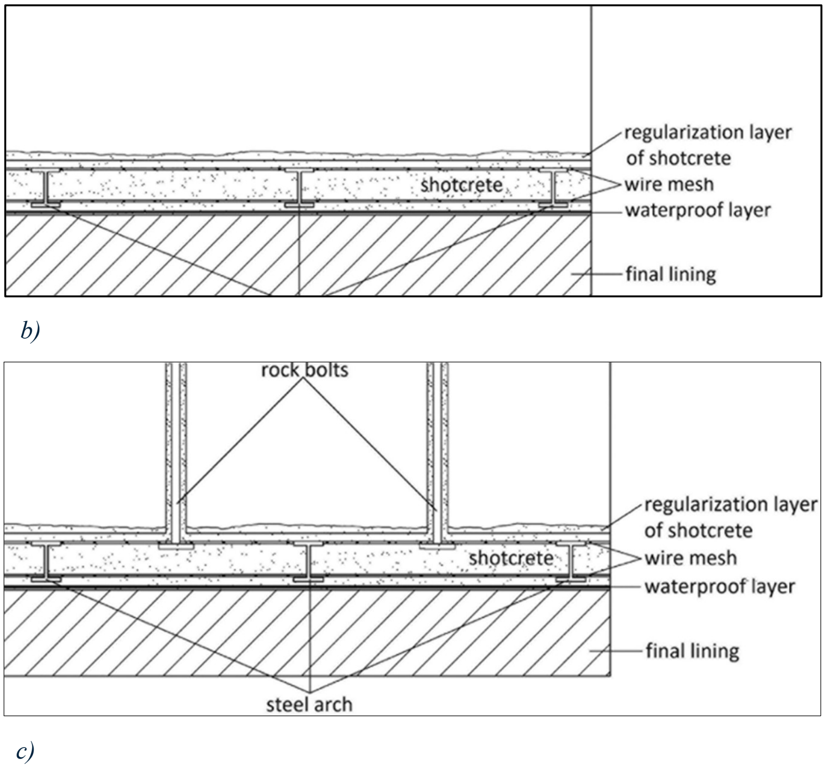

Figure 2.16 - Scheme of the possible combinations of the basic elements of the first-phase lining. (Bilotta, E. et al. [7])

3 SOIL NAILING IMPROVEMENT

The soil nailing technique is one of the most used stabilization systems, to reinforce the soil in place by insertion of solid or hollow steel or fiberglass bars called nails. Usually, the nails are installed in a pre-drilled holes and grouted to ensure the contact between the surrounding soil and the structural element.

The most important function of nails is the reinforcement of soil portion in which is applied by the transmission of the load from the potential unstable mass to a more competent zone that is outlined by a potential failure surface to be identified.

However, the technique was born for the stabilization of slopes, retaining walls and excavations, where the soil-nailed system is required to fulfil requirements of stability, serviceability and durability during construction and throughout its design life following all the possible potential modes of failure (Figure 3.1).

Soil nailing system can be used on different soil, from cohesive to non-cohesive soil depending upon local geotechnical conditions and project need. The performance of the system relies on well-designed and executed construction, which should be in accordance with the requirements defined on technical specifications, standards and guidelines. Soil nailing remains a versatile and proven solution for the stability and safety of civil infrastructure, with the advancements in technologies and materials.

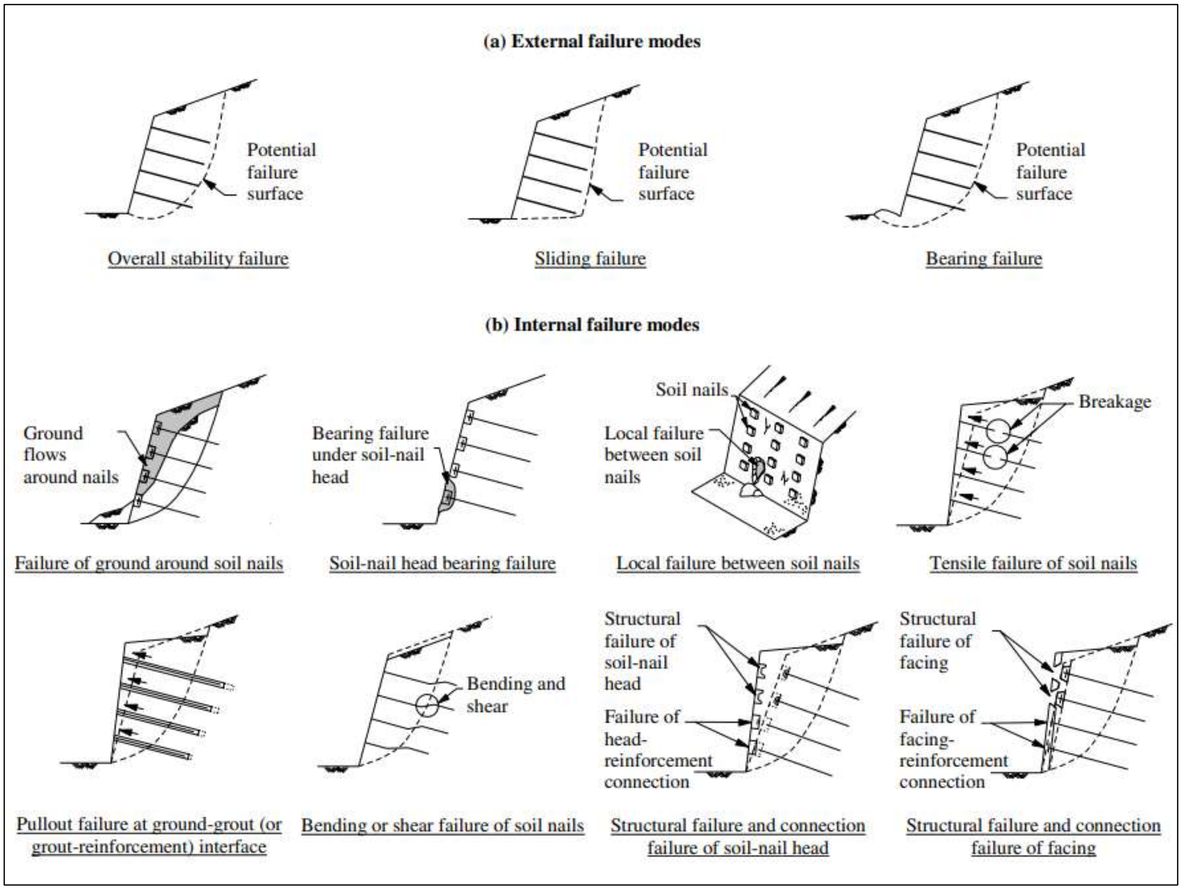

Figure 3.1 - Classes of possible failure modes for a nailed system.

The basic elements that constitute a soil-nailed system are reported in Figure 3.2 which shows the cross-section of a typical soil-nailed cut slope, constituted by the following elements:

- **Soil-nail reinforcement** is the main element of a soil-nailed system. Its primary function is to provide tensile resistance. The reinforcement is typically a solid high yield deformed steel bar. Other types of materials, such as fibre reinforced polymer, can also be used as a soil-nail reinforcement.
- **Reinforcement Connector** (Coupler): Couplers are used for joining sections of soil-nail reinforcing bars.
- **Cement Grout Sleeve**: Cement grout, made of Portland cement and water, is placed in a pre-drilled hole after the insertion of a soil-nail reinforcement. The cement grout sleeve serves the primary function of transferring stresses between the ground and the soil-nail reinforcement. It also provides a nominal level of corrosion protection to the reinforcement.
- **Corrosion Protection Measures**: Different types of corrosion protection measures are required depending on the design life and soil aggressivity. Common types of corrosion protection measures are hot-dip galvanising and corrugated plastic sheathing. Heat-shrinkable sleeves made of polyethylene and anti-corrosion mastic sealant material are commonly used to protect couplers.
- **Soil-nail Head**: A soil-nail head typically comprises a reinforced concrete pad, a steel bearing plate and nuts. Its primary function is to provide a reaction for individual soil nails to mobilise tensile force. It also promotes local stability of the ground near the slope surface and between soil nails.
- **Slope Facing**: A slope facing generally serves to provide the slope with surface protection, and to minimise erosion and other adverse effects of surface water on the slope. It may be soft, flexible, hard, or a combination of the three. A soft slope facing is non-structural, whereas a flexible or hard slope facing can be either structural or 18 non-structural. A structural slope facing can enhance the stability of a soil-nailed system by the transfer of loads from the free surface in between the soil-nail heads to the soil nails and redistribution of forces between soil nails. The most common type of soft facing is vegetation cover, often in association with an erosion control mat and a steel wire mesh. Some proprietary products of flexible facing are available. Hard facing includes sprayed concrete, reinforced concrete and stone pitching. Structural beams and grillages can also be constructed on the slope surface to connect the soil-nail heads together to promote the integral action of the soil-nailed system.

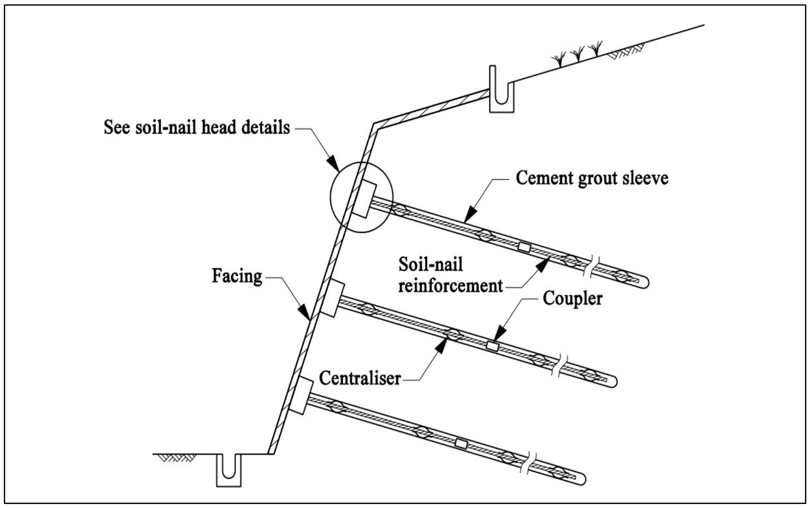

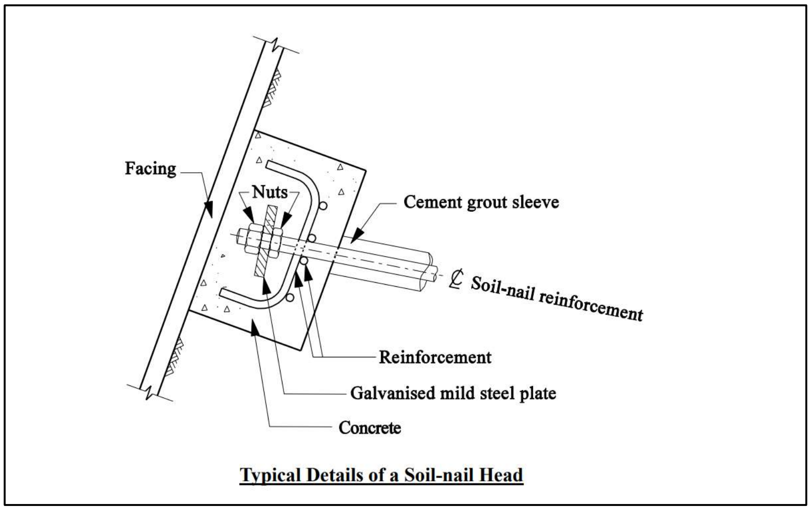

Figure 3.2 -Schematic Diagram of a Soil-nailed Cut Slope. ([12])

Moving towards the tunnelling practice the adoption of the soil nailing technique maintains the same goal of soil reinforcement, but some conceptual variations are present.

Improvement techniques are usually adopted to ensure tunnel stability and an acceptable level of risk before the new excavation profile planned by the advancement is achieved.

For this reason, the durability of the intervention is discarded in tunnelling, leading to the use of fiberglass as soil-nail reinforcement element. In fact, the fiberglass characteristics respect the needs required thanks to the mechanical characteristics, such as the high tensile strength, the resistance to corrosion and the ease to be cut. These characteristics helps to fulfil the needs of the conventional tunnelling, mainly regarding the removal of the already nailing stabilized ground mass during tunnel face excavation.

Particularly, the improvement performed by the use of soil nailing aim to control the extent of displacements due to three main phenomena (Lunardi, 2000 [13]): displacements at the tunnel face (Face extrusion), radial displacement ahead excavation face (Pre-convergence) and behind it (Convergence), not to be neglected will also be the control of water flows in the tunnel and its surroundings.

3.1 Design aspects

The stability of excavation face is the main goal to be ensured thanks to the proper design of the using fiberglass dowels that has been shown to be effective, unfortunately a standardized and reliable design method for routine application has yet to be developed.

The bolting design should specify some key parameters including: the number, length, and cross-section of the elements required to stabilize the face with an adequate safety margin. Additionally, it is crucial to determine the minimum residual length that the elements should have at the end of the advancement stage before new reinforcements are installed in the subsequent zone.

A graphical example of the typical cross section of the reinforced tunnel face with all key parameters involved in the design in sketched in Figure 3.3 (a), while Figure 3.3 (b) shows the overlapping length and installation interval in excavation sequence.

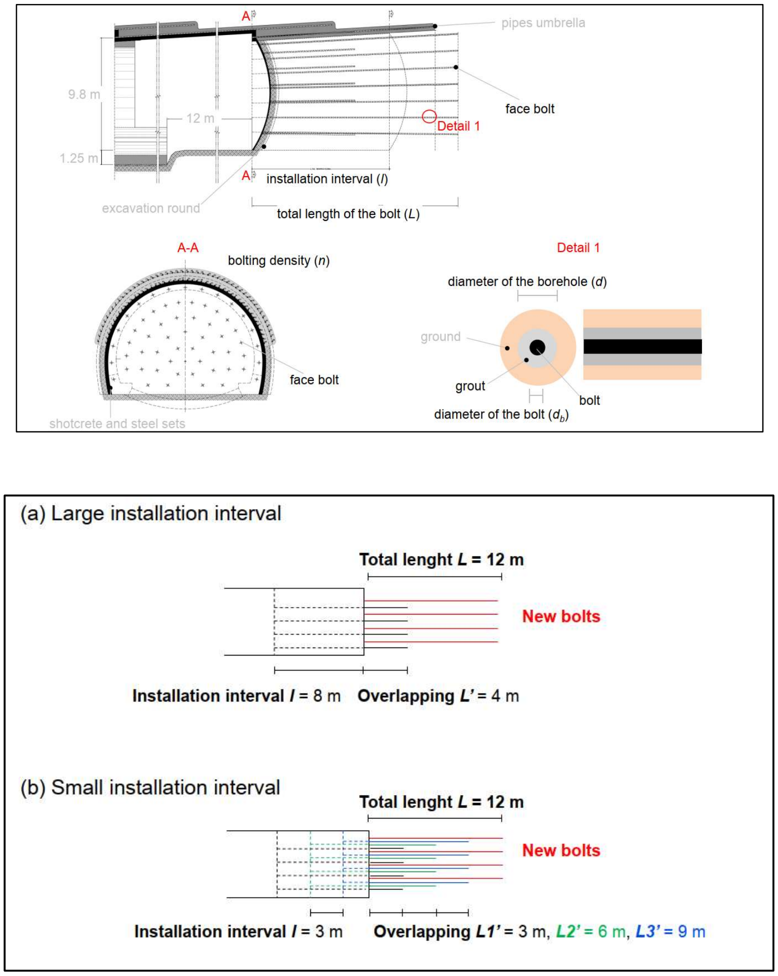

a)

b)

Figure 3.3 –(a)General installation scheme for soil nailing in tunnelling;(b)Sequence of installation during tunnel advancement ([14]).

3.1.1 Simplified Analysis Methods

The simplified methods of analysis are based on LEM (Limit Equilibrium Method), where the portion of soil ahead of the face is dived into two volumes by a failure surface, that separates the unstable soil mass by the stable one.

The determination of these volumes represents a key factor because determines the pressure ***S*** to be applied (see [13]) by the soil nailing intervention, which is consequently translated in a number and a pattern of elements.

Once the force ***S*** is known through empirical laws or using the LEM, the reinforcement elements can be simply dimensioned assuming that they perform their static function only by developing an axial force and considering negligible flexural stiffness for the reinforcement system.

This hypothesis permits the verification of the behaviour of the reinforcement elements to be limited to the following three equations that considers the types of failure mechanism that cause the interruption in the force application performed by the element

The first regards the breakage of the nail by tensile failure, in this case the maximum tensile strength is exceed with the consequent internal failure, it is quantified by the following equation (Eq.3.1):

$$\frac{S}{n} < F_t = \frac{Af_{yk}}{FS_1} \qquad (3.1)$$

The second is the pull-out mechanism which occurs when the force exerted on a soil nail exceed the friction exerted by the contact between soils, in unstable and stable zone and is quantified by the following equations (3.2 and 3.3):

$$\frac{S}{n} < F_{out} = \frac{\tau_a \pi D k L_{act}}{FS_2} \qquad (3.2)$$

$$\frac{S}{n} < F_{out} = \frac{\tau_a \pi D k L_{pass}}{FS_2} \qquad (3.3)$$

Where S=support force to be applied n= number of elements adopted τ_a = shear strength between the injected grout and the surrounding ground; D = borehole diameter; L_{act} = minimum length of bar inside the active zone(unstable); L_{pass} = minimum length of bar inside the stable zone; ; k = 1.5, increased diameter factor; A = element section area; fyk = element yield strength; and $FS1$; $FS2$ = safety factors (equal to 2).

From the previous equations (Eq. 3.1 and 3.2) it is possible to define various soil nailing interventions depending on the engineering choices.

An alternative approach to assess the impact of reinforcement on face stability involves treating the reinforced zone (or the portion where the reinforcement actively contributes) as a material with enhanced mechanical properties, following the concept of equivalent homogenized material. Typically, the cohesion and elastic modulus of the soil after full activation of the reinforcement are determined.

Grasso et al. (1989) [15] proposed a simplified method for this purpose. The process begins by calculating the average longitudinal confining stress ($\Delta\sigma_3$) provided by the reinforcement elements, followed by the determination of an 'improved' cohesion (c^*).

The resulting expressions are expressed as follows (Eq.3.4 and 3.5):

$$c^* = c + \left(\frac{1+sen(\varphi)}{2*\cos(\varphi)}\right) * \Delta\sigma_3 \qquad (3.4)$$

$$\Delta\sigma_{3_r} = \frac{nF_{min}}{2Af} \qquad (3.5)$$

Where F_{max} is the minimum force that can be developed inside each fibreglass element, which is determined with the equations previously mentioned (Eq. 3.1 and 3.2).

Dias et al. (1997[16], 1998[17][16]) developed three-dimensional models using finite-difference calculations to simulate the stress and strain behaviour of a tunnel excavated in Toulon, France. These models incorporated various reinforcement schemes and examined the applicability of the equivalent homogenized material concept (Dias and Kastner 2005([18]);Dias et al. 2002 ([19]).The findings revealed that this approach is more suitable for deep tunnels than shallow ones, provided that the maximum force (F_{max}) in the reinforcement bars is accurately estimated.

For shallow tunnels, when applying the equivalent homogenized material concept to reinforced rock, it becomes necessary to perform three-dimensional numerical analyses. This method simplifies the numerical model by eliminating the need to simulate each reinforcement element individually, allowing the use of larger dimension elements in the calculations.

However, when employing the equivalent homogenized material approach, the behaviour of the dowels is not explicitly considered; only their maximum load-bearing capacity is considered, which may not always be fully mobilized. Consequently, this method does not allow for precise design of the reinforcement system, as accurate calculations for individual elements are not feasible.

3.2 Innovative Technology

The need to reduce pore water pressure in a short time and avoid the formation of overpressure during the entire cycle (§2) has led to the patenting of a new consolidation system called P.E.R. Ground (Pressure Earth Reinforcement).

The first company that patented the technology (described in the following pages) was the Italian society *Elas Geotecnica* of Segrate (Milano), which specialized in the ground improvement technique and was acquired by *Maccaferri* which is one of the main producers.

3.2.1 Technical description

The **P.E.R. Ground ®** is a multipurpose system because acts as ground reinforcement and drainage, by the adoption of the configuration shown in Figure 3.4.

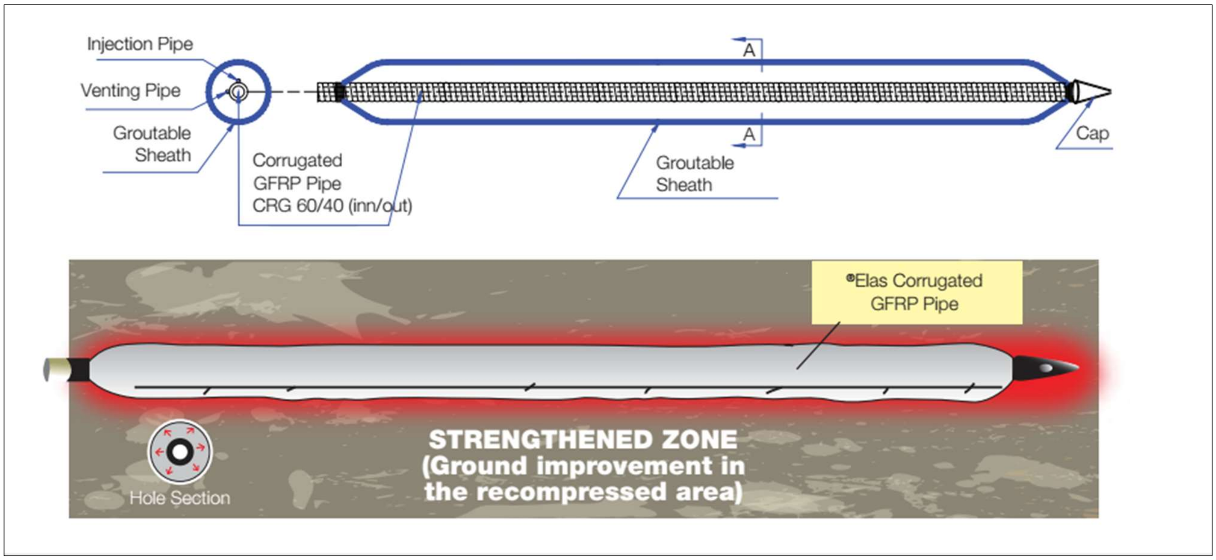

Figure 3.4 – P.E.R ground system F2 type (Courtesy of Maccaferri)

The system (called ***F2 type***) includes the following components:

- **Fully threaded GFRP pipe:** fiberglass reinforced pipe for reinforcement and stiffening (technical characteristics reported in the following paragraph)
- **External groutable sheath:** geotextile layer able to contain and seal the injected grout.
- **Injection and venting pipe:** small tubes that allow respectively the injection and the blow out of air during the filling operation.

Another version (called ***F1 type***) of the technology includes also the possibility of integrating a coaxial drain (Figure 3.5) with the addition of two elements listed below.

- **Metal clump: a** metallic connection between the drain and the P.E.R. ground.

  The system allows the recompression of the surrounding ground if any possible
- **PVC slotted pipe** allows the drawdown of the underground water, which is evacuated via the GFRP pipe (coaxial drain)

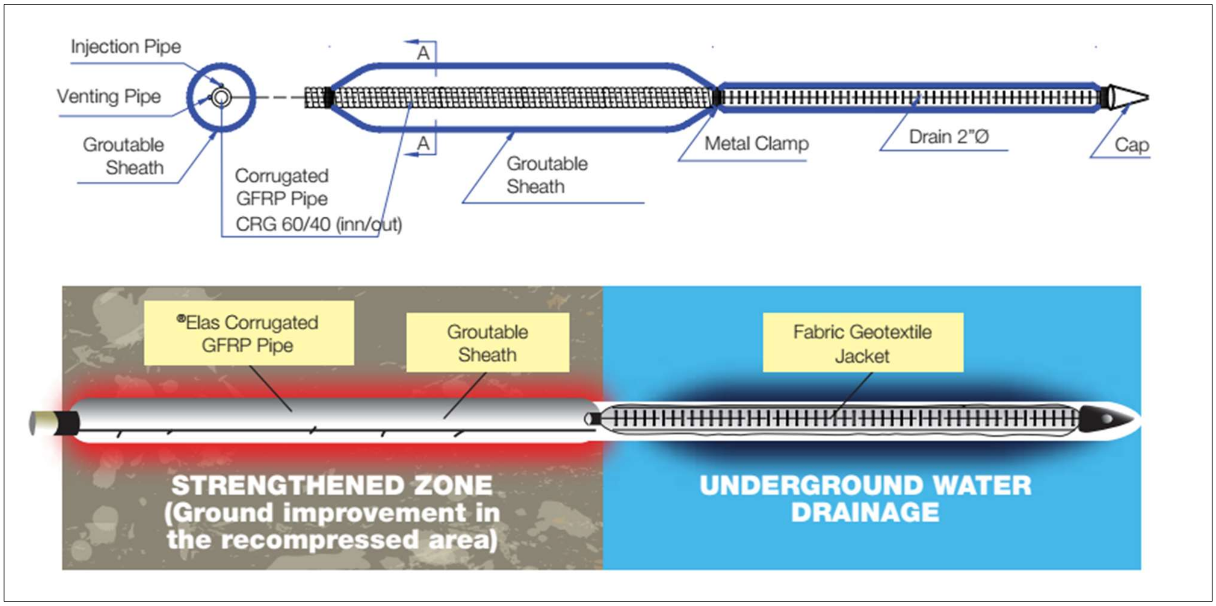

Figure 3.5 – P.E.R. Ground with coaxial drain F1 type (Courtesy of Maccaferri).

3.2.2 Technical characteristics of components

The materials that compose the elements of the technology play a key role in the final assembly, indeed the possibility to use different classes of the basic components (GRFP, PVC pipe, Geotextile) permits to obtaining of different combinations which will be adaptable to several ground and operational conditions.

For the sake of completeness, in the tables below the technical characteristics of the commonly adopted material have been summarized (Table 3.1, *Table 3.2*, Table 5.3).

Table 3.1 -Technical characteristics of fiberglass pipe (GRFP)

Characteristic	**Test Method**		**Value**(2)	**U.M.**
Density	ISO 1183	≥	1,90	kg/dm^3
Glass content	ISO 3451-1	≥	50	%
Tensile failure load	UNI EN 61 mod.	≥	450	N/mm^2
Tangent modulus of elasticity	UNI EN 61 mod.	≥	20.000	N/mm^2
Bending failure load	UNI EN 63	≥	600	N/mm^2
Shear failure load	ASTM D 732	≥	140	N/mm^2
Φext [mm]	**Φint [mm]**	**Area [mm^2]** (1)	**t adherence pipe/concrete 48h [kN/m^2]** (2,3)	
60	50(4)/40	1570	≥ 1750	

Table 3.2 – PVC pipe (Courtesy Maccaferri)

Characteristic	Test Method (1)		Value (2)	U.M.
Density	ISO 1183/87	≥	1,5	kg/dm³
Toughness	ISO 868/85	≥	81	SHORE D
Tensile failure load	ISO R 527/66.	≥	38	N/mm²
VICAT	ISO 306/74_met B	≥	83	C°
Elongation	ISO 306/74	≥	110	%
Resilience IZOD	ISO 180/82	≥	40	j/m
Melt flow Index	MP 01/94	≥	28	gr/10 min

Table 3.3 - Geotextile characteristics (courtesy of Sikaplan)

Characteristic	Test Method	Value	U.M.
Effective thickness	ISO 9863-1	5.4(±0.5)	mm
Static puncture	ISO 12236	9.5(±1)	kN
Dynamic puncture	ISO 13433	3(±1)	mm
Tensile failure load	ISO 10319	Longitudinal -55 (± 7.2)	kN/m
		Transversal - 80(+20%)	
Elongation	ISO 10319	Longitudinal - 70(+16%)	%
		Transversal - 80(+20%)	
Fire Classification	ISO 13501-1	CLASS E	-
Specific weight	ISO 9864	800	g/m^2
Protective efficiency	ISO 14574	1100(±220)	N
Permeability to water	ISO 11058	24 (±8)	l/m^2/s
Aperture size	ISO 12956	60 (±18)	µm

Note: 1. Area due to adhesion preformed 478 mm²; 2. 0,157 m2 surface for linear meter pipe; 3. 48h mortar compression resistance> 19 N/mm2 (TECNOPIEMONTE cert. n°: 10906/CA/63/08); 4. Liner

3.2.3 Construction procedure

The conventional tunnelling method as described in the previous paragraph (§2) is a cyclic process in which each phase can affect the entire work.

The construction sequence that usually is implemented when P.E.R Ground adoption is chosen is chronologically listed below:

1. **Preparation works** installation of the mixing station, grouting pumps and injection facilities, including the grout mix checking tools.
2. **P.E.R. Ground** system assembling
3. **Drilling works**, immediate installation of the PER Ground System

4. **P.E.R. Ground** grouting (first stage grout, '*sheath grouting*'), e.g. TAM injection or use of a small injection and venting pipe.

3.2.4 Drilling

The drilling operation is frequently carried out by a proper Jumbo drilling machine, with a longer boom and with suitable power (torque), since the final length of the P.E.R Ground with drains reaches about 20m.

To adjust the boom alignment laser may be temporarily installed on the boom whilst the inclination may be measured by a sprit level.

The drilling shall be done using coring or downhole hammer technique, and the drilling dimension is around 130mm which will be able to contain 70mm of P.E.R. Ground.

Compressed air (8-24 atm) shall be used as drilling waste removal and soothing agent, however, also a limited amount of water may be added in order to reduce dust formation.

The casing may be required wherever poor ground conditions encroached, to sustain the drilling wall. If the casing is required, drilling shall have reached the designed length, and the pilot bit and drill rod will be

3.2.5 Geometry and pattern of ground treatment

The geometrical characteristics of P.E.R ground and the pattern contribute to and highly affect the efficiency of the consolidation process.

The main geometrical parameters that can be easily controlled in the working phases for the radial installation (Figure 3.6) of the elements are:

1) **Spacing (S) -** Distance between two adjacent P.E.R Ground.
2) **Length (L) –** Total length of the system inside the medium to be consolidated.
3) **Angle of installation (α) –** Angle respects the centre of the tunnel.

In addition to the geometrical pattern, different kinds of combination can be adopted in terms of the P.E.R Ground model (***F1*** [Figure 3.5] or ***F2*** [Figure 3.4]), and combination with drains.

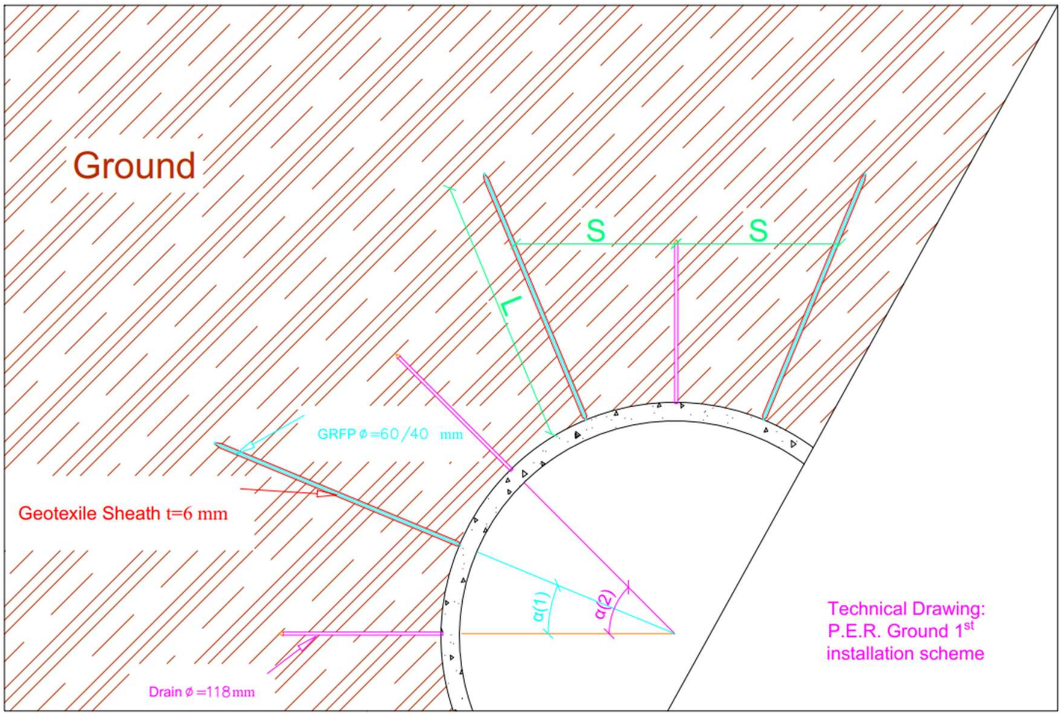

Figure 3.6 - Schematic representation of Installation scheme at the tunnel contour.

However, the installation of PER Ground elements can be carried out at the excavation face following a geometrical pattern that differs between the central zone and the contour one parameters that can be easily controlled in the working phases by adjusting the following parameters:

1) **Vertical distance (D_v)** - Distance between P.E.R Ground and drain.
2) **Horizontal distance (D_h)**– Total length of the system inside the medium to be consolidated.
3) **Distance at the contour (d') –** Distance at the perimeter between P.E.R Ground and drain
4) **Spacing (S) –** Spacing between two P.E.R Ground element.

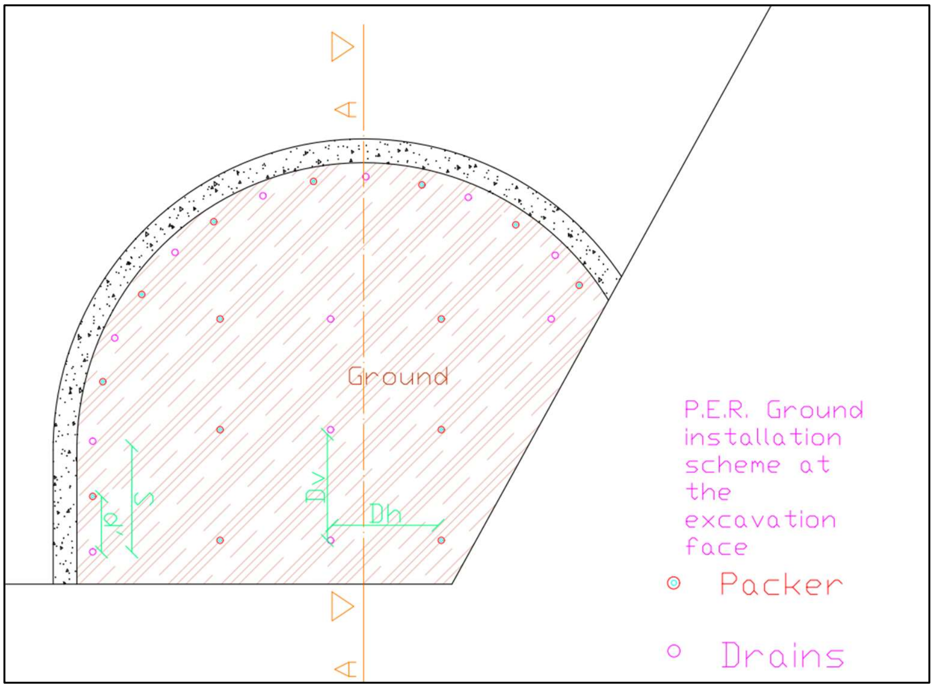

Figure 3.7 -Schematic representation of Installation scheme at the excavation face.

In the numerical analysis, a proper study of the hydromechanical properties that affect the pattern will be done, particularly on the following one:

- **Zone influence:** area/volume affected by the improvement scheme and technique chosen.
- **Mechanical properties:** improvement in terms of cohesion, Young's modulus and consequently strength.
- **Sequence of installation/activation:** order of installation between drains and P.E.R Ground, and consequent activation (grouting of GRFP), such as simultaneous, coupled or single.

3.2.6 Grouting and injection characteristics

Injections mix design, injection pressure and volume, and cut-off criteria shall be revised according to the design requirement, the soil conditions and available equipment at the worksite.

Sheath grout injection shall be done immediately after the PER Ground System installation, by means of OPC grout, by using the allocated grouting kit, i.e. injection and vent line (bottom-up grouting).

The injection line is connected to the grout pump. The second line acts as a vent line to ensure the free flow of grout, till the grout flows back to the head of the system.

Sheath injection shall be done at low pressure (≤ 1 MPa), and with a controlled grout volume up to the theoretic drilling volume. However, such theoretic volume shall be slightly increased to consider the effect given by the release of water due to the press-filtration effect within the sheath, which is strictly related to the aperture of the geotextile (Table 3.3).

Grouting pressure can be increased up to 4-6 bars to induce a 're-compression' effect around the drilling walls, in this way a compaction of ground is obtained with the additional increase in the velocity of water flow.

The mix design usually adopted for injection is quite simple adopting the following components:

- **Cementitious mixture**: mid-fine Portland cement (Blaine >240 m^2/kg)
- **Hyperplasticiser agent**: availability on the market
- **Water**
- **Bentonite**: chosen based on mix-design parameters.

The suggested mix design by Maccaferri for the sheath injection grout is performed by using a water cement $\frac{w}{c}$ = 0.5.

For example, the mix design will use the following quantities of materials (suggestion of Maccaferri):

- Water 100 kg
- Portland cement (type 325) 200 kg
- Hyperplasticizer agent 0,7 kg

However, a more comprehensive approach should consider, the mechanical characteristics of the grout (**UCS**) according to the working phase adopted in the conventional tunnelling method, and starting from this is necessary to couple the acquired strength over time with the needed one for the improvement of the ground conditions.

So, the mix design of the grout is linked to the improved mechanical properties that are needed after the use of the P.E.R Ground technology.

Additionally, to the geotechnical consideration, it is necessary to pay attention to the rheological characteristics of the grout and the so-linked parameters that must be checked for each round of injections following the worksite organization

The most important elements to take into account are:

- Viscosity
- Setting time
- Bleeding/Stability
- Specific weight

A complete overview of the parameters above-mentioned and their relationship to the $\frac{w}{c}$ have been reported in Figure 3.8.

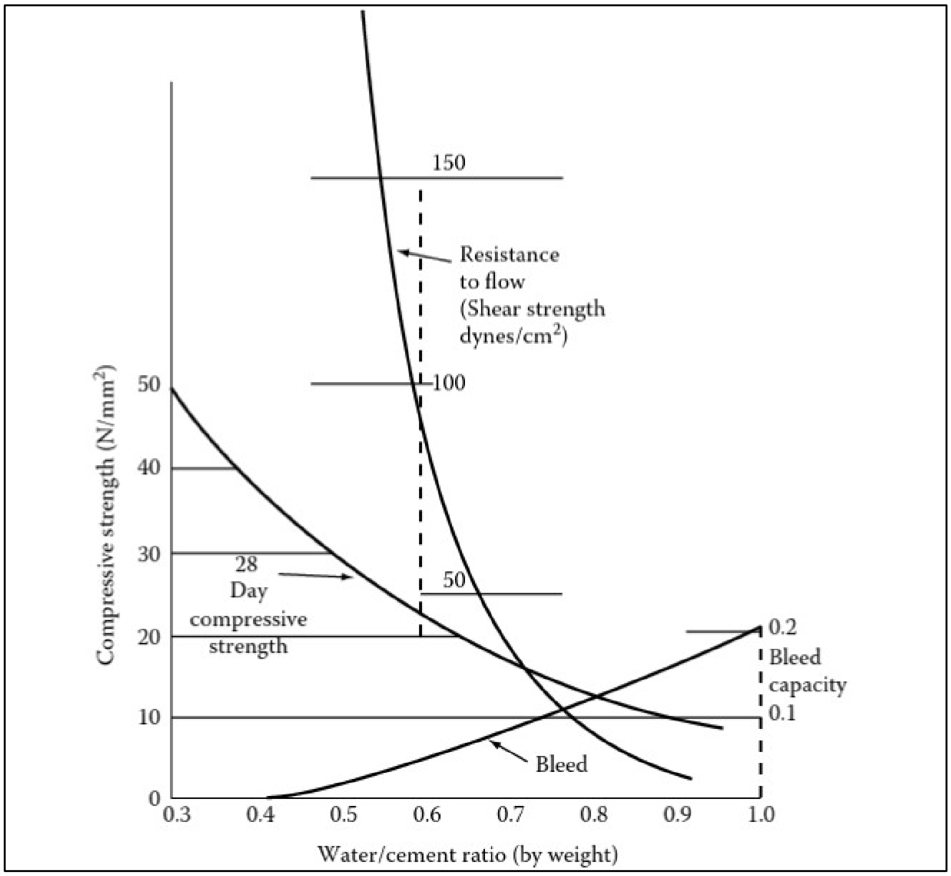

Figure 3.8 - Viscosity, shear strength, and bleeding of OPC suspensions. (Ref.[20]).

3.2.7 Technical Know-How Abroad

Starting from the state of the art in the Italian technological context, in this paragraph an extension looking at a global scale is exposed briefly, in a way to retrieve more insights and bring some innovation in the actual technical know-how.

The most relevant cases of application and testing around the world of technology similar to the one described above are documented in the following countries:

- **China** where the expansive nail is named Capsule grouting technology (CGT) was developed in order to control the deformation caused by underground construction and excavation process adjacent to pre-existing structures (i.e., piles, tunnels, pipes.) [21].

  CGT is used to control the deformation of adjacent structures by injecting slurry into high-strength capsules, causing the capsules to expand in the soil layer and inducing soil stress, as illustrated in Figure 3.9.

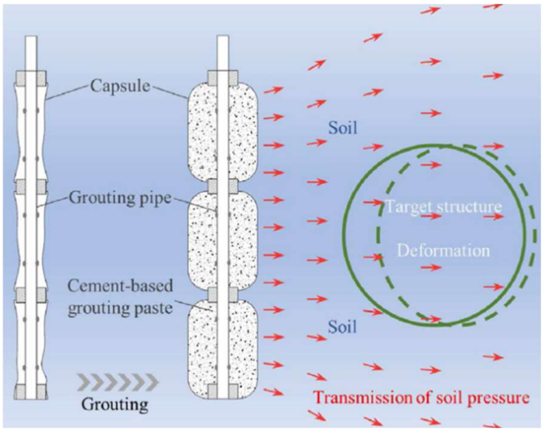

Figure 3.9 - Sketch of CGT.

An extension of this technology was developed by implementing in the anchor system a geotextile that once grouted increases the pull-out force due to both recompression and filling of the surrounding soil voids but also to a better adherence among geotextile and soil, an example is reported in Figure 3.10 and takes the name of 'capsule-anchor'.

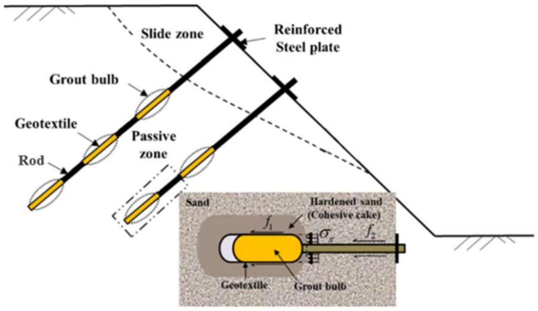

(a) Function mechanism of the capsule-type anchor

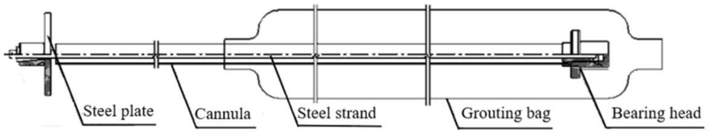

(b) Structure of the capsule-type anchor [26]

Figure 3.10 – Schematic diagram of the capsule-type anchor

- **Australia** where the expansive nail is called 'x-Nail' ([22]) and combines the capabilities of a purely frictional-driven nail and a compaction-grouted nail. The innovative design adopted by X-Nail is in the external coating made with a latex balloon attached that is subsequently used for compaction grouting. The grout bulb is localized at the end of the nail and is used to improve its pull-out resistance. An example of the results obtained after the grouting operation has been reported in Figure 5.8.

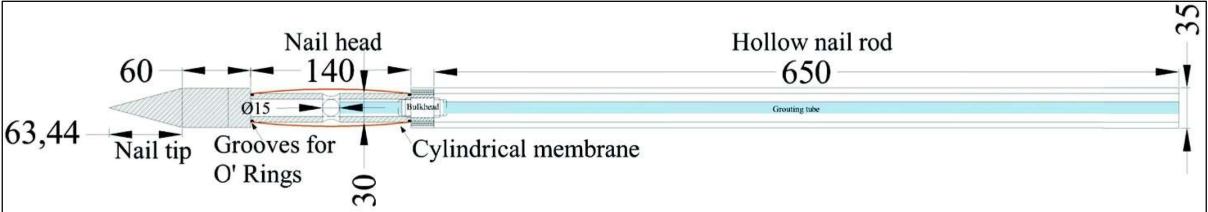

Figure 3.11 – Details of x-Nail (dimensions in millimetres).

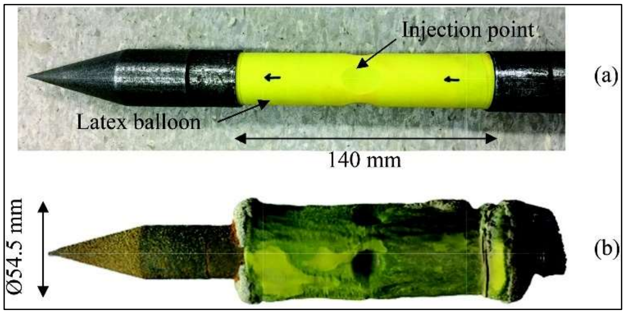

Figure 3.12 - Photograph of (a) x-Nail with grouting facility and (b) grouted nail showing three-dimensional grout bulb [22].

The comparison among the research of the state of the art regarding grouted/expanding nails has led to several results, highlighting some key differences in the developments, established applications, and improvement prospects.

3.2.8 Quantified improvements effects

The improvement effects obtained following the application of recompression and drainage interventions have not yet been determined explicitly and quantitatively, but several studies deriving from pull-out tests (Sterpi et al., 2013 [23]) and laboratory tests (Bhuiyan et al., 2022; [22]) have noted over the years a clear improvement in the characteristics of the reinforcement, that will enhance the variables involved in the design process concerning the pull-out load (Eq.3.1).

$$t_{max} = \frac{F_{pull-out}}{\pi * D * l} \qquad (3.1)$$

Where $F_{\text{pull-out}}$ is the pull-out load at failure; D is the pipe diameter; and l is the embedment length of the sample within the cement grout block.

In Figure 3.13, the results from a set-up for a pull-out test performed have been reported and the comparison of results between a traditional fiberglass and a reinforced one with a groutable sheath shows a difference of 1 order of magnitude.

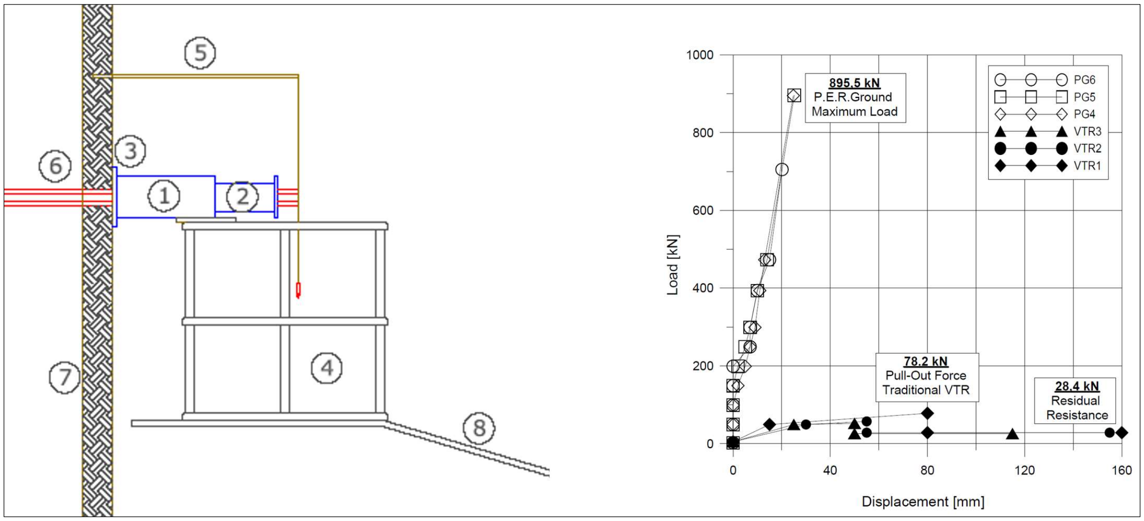

Figure 3.13 - (left) Pull-out test set-up and devices: 1) jack, 2) gripper, 3) stiff steel plate, 4) platform for operator, 5) plumbline, 6) reinforcement system, 7) excavation face, 8) mechanical device for platform positioning. (right) Results from pull-out tests on conventional VTR bars and PERGround© (Renda et al., 2011).

In Figure 3.14 is reported the application of the P.E.R ground system for a case study in Italy ([23]), where difficult ground conditions, induced by poor mechanical properties of the soil and rock mixture and relevant pore water pressures, were faced adopting innovative soil nailing techniques, which allows to successfully complete the tunnelling project.

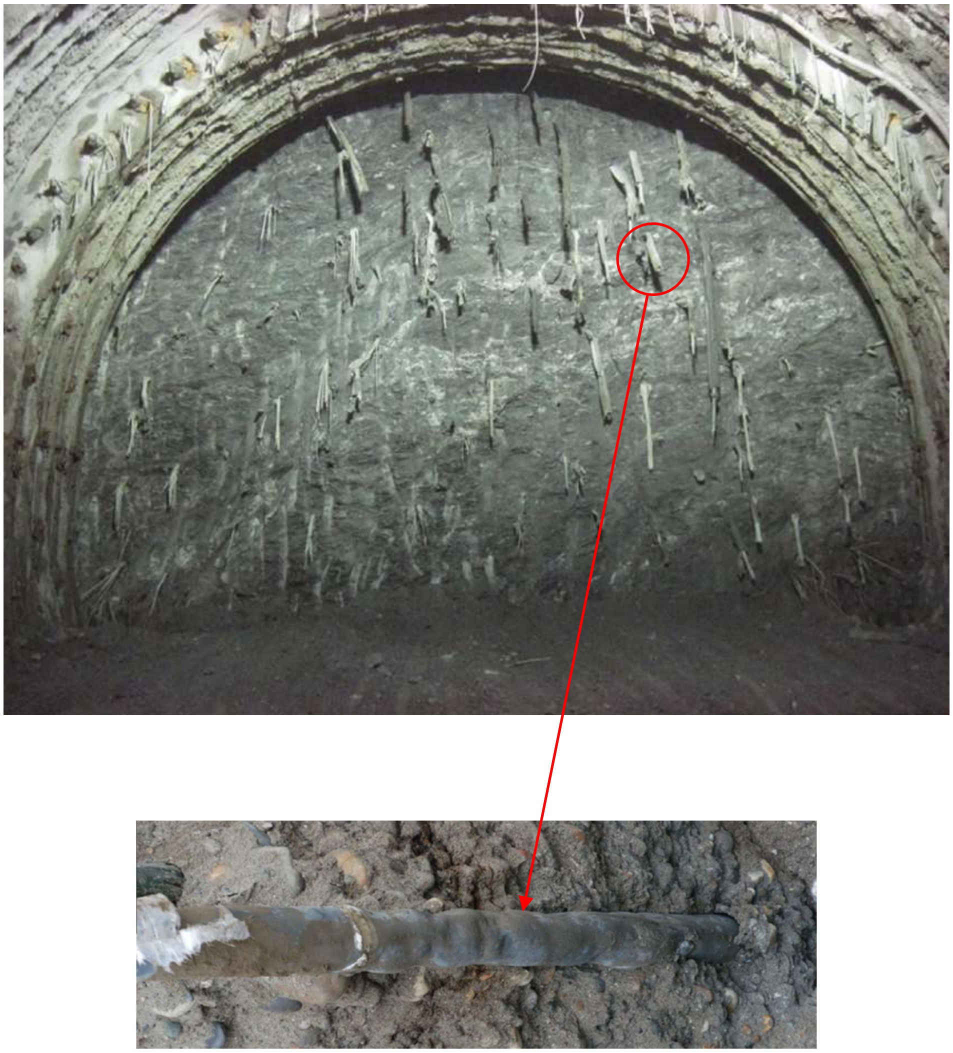

Figure 3.14 –(a) Timpa delle Vigne tunnel face improved by soil nailing;(b) Soil nail bar removed after injection.

4 NUMERICAL SIMULATIONS

The quantification of the improvement effect applied by the consolidation technology discussed in the previous paragraph has been carried out using a numerical method able to simulate the complexity of the phenomenon related to the hydro-mechanical interaction, the work phases and the complexity of the material behaviour. For these reasons, numerical simulations have been performed using FLAC3D (Fast Lagrangian Analysis of Continua in 3 Dimensions).

FLAC3D is based on explicit FDM (finite difference method), allowing the numerical study of the hydro-mechanical behaviour of materials thanks to the use of constitutive models able to simulate the response of materials at a different type of load conditions generated by the main working operations such as excavations, constructions but also flow-variations.

4.1 Model setup

The procedure adopted for the development of the model is summarized in the flow-chart in Figure 4.1 subdivided into 7 main preliminary steps which are followed by the analysis of the results and the application of perturbation coherently with the phases defined during the project definition.

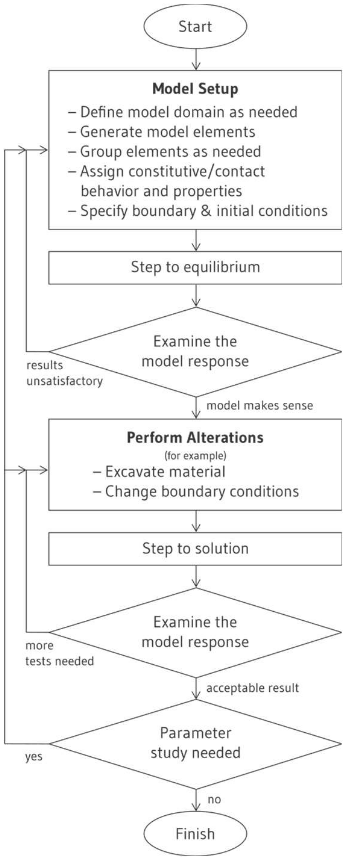

Figure 4.1 - Modelling methodology adopted for the model setup. Itasca Software 2024)

Especially, in the case under study, the HM (Hydro-Mechanical) scheme has been adopted with a coupled computation scheme, in *FLAC3D* the computation scheme occurs in two ways: pore-pressure changes cause volumetric strains that influence the stresses; in turn, the pore pressure is affected by the straining that takes place.

The use of a fluid-mechanical scheme introduces the need to define a constitutive model and boundary conditions for the fluid calculation in addition to the classical mechanical one, used for the usual numerical computation implementation.

4.1.1 Model geometry and mesh

The size of the model was chosen to investigate the action of the *pressurized reinforcement* in the surrounding area, and at the same time to minimize the effects of the boundary conditions applied. Following this logic, the dimension of the model was scaled on the base of the largest spacing between reinforcing elements.

The width (x-axis) of the model was fixed equal to 6 times the distance between the extremes of the reinforcing elements, corresponding to 12m, while the height (z-axis) and depth (y-axis) correspond to 6m due to the geometrical and physical conditions modelled which involves mainly the horizontal direction.

The mesh dimension was fixed according to the zone of interest, one with a finer mesh close to the reinforcement elements to maintain high accuracy of the results, and another external to the interest area with a decreasing mesh by moving away from the reinforcement area until the model boundary.

The final model setup with different groups is shown in Figure 4.2, with a detail of the zone at fine mesh dimension in Figure 4.3.

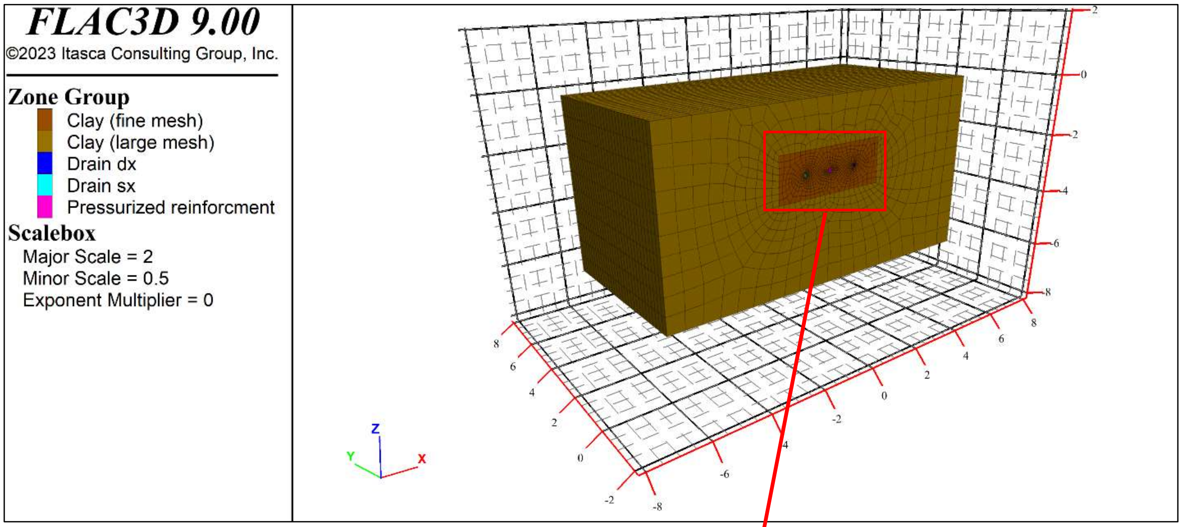

Figure 4.2 – Model size and relative group defined

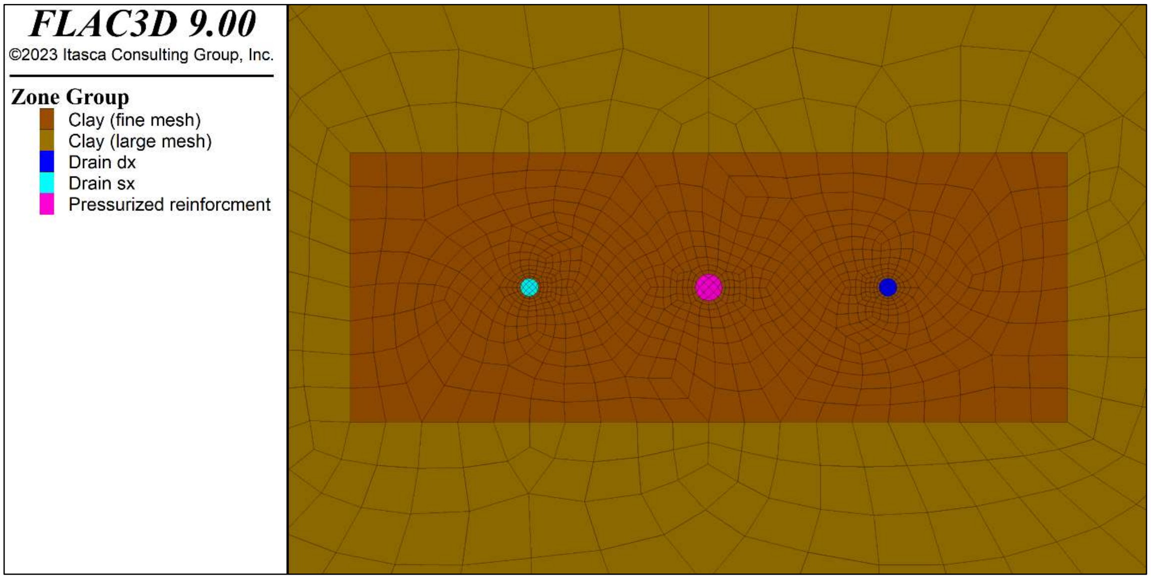

Figure 4.3 – Detail of the mesh in the reinforcement region

4.1.2 Boundary conditions

The boundary conditions applied to the model contour need to be differentiated into mechanical and hydraulic boundary conditions due to the computation scheme adopted.

The mechanical boundary conditions are applied to:

- **Velocity components:** following the explicit-solution scheme adopted by FLAC3D [24] by fixing the velocity components the displacement is modified consequently.
- **Applied stress:** used to simulate a load applied by a structure, a reinforcement or in general a known loading condition.

Especially, on the lateral boundaries the normal velocity with respect to the ‘zone face’ was fixed equal to zero, the reason for the choice is related to the fact that the boundary is far enough from the perturbed regions.

In the lower boundary corresponding to the ‘Bottom’ of the model, the velocity was fixed equal to zero for all the components, coherently with the reasons already explained.

At the upper boundary representing the ‘Top’ of the model, a distributed load was applied, in a way to simulate the state of stress at a given depth and at the same time to reduce the size of the model. Indeed, if the effects of the reinforcement act in superficial conditions (§ 2.2.1) the model dimension needs to consider the ground surface increasing the size of the model respects at the one needed, with a consequent computational time that increase proportionally to the dimension of the model.

Maintaing the size of the model small allows the control the computational time, and gives the possibility to perform some physical model at laboratory scale (as made by [22]) in order to validate and calibrate the model. The mechanical and geometrical model setup used is reported in Figure 4.4, which corresponds in sections to the schematic representation in Figure 4.5.

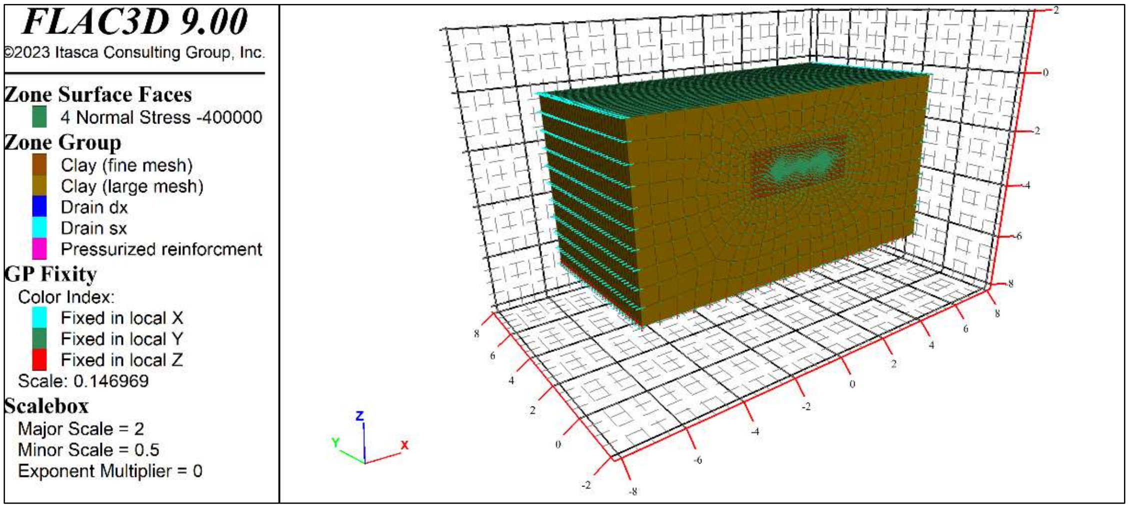

Figure 4.4 – Mechanical Boundary conditions and model geometry.

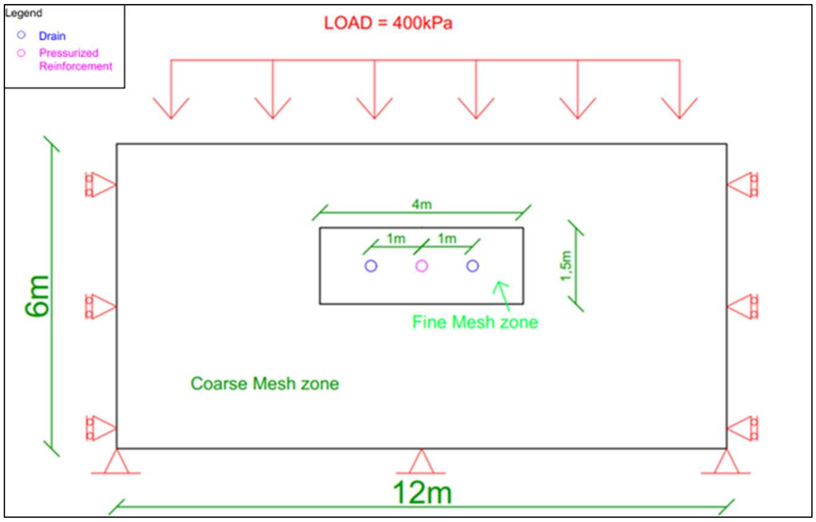

Figure 4.5 – Schematic 2D section of the geometrical features and boundary conditions.

The hydraulic boundary conditions are applied to the following variables:

- **Height of water:** used to simulate a known initial height of water from which the pore pressure distribution is computed
- **Pore pressure:** used to fix the pore pressure along the contour or in specific zones, an example of application in the model built was the simulation of drains with an element with null pore pressure.
- **Hydraulic flux:** used to define if a boundary is permeable or not, and consequently the direction of the flux of recharge from other portions of the model.

Especially, on the lateral boundary the pore pressure is free to vary, this options in FLAC3D induce the generation of an impermeable boundary.

The lower boundary corresponding to the ‘Bottom’ of the model was fixed as impermeable; at the upper boundary representing the ‘Top’ of the model, a height of the water was applied, in a way to simulate the initial hydrostatic conditions corresponding to the moment in which the reinforcement is applied.

The model boundary conditions adopted are summarized in Figure 4.6.

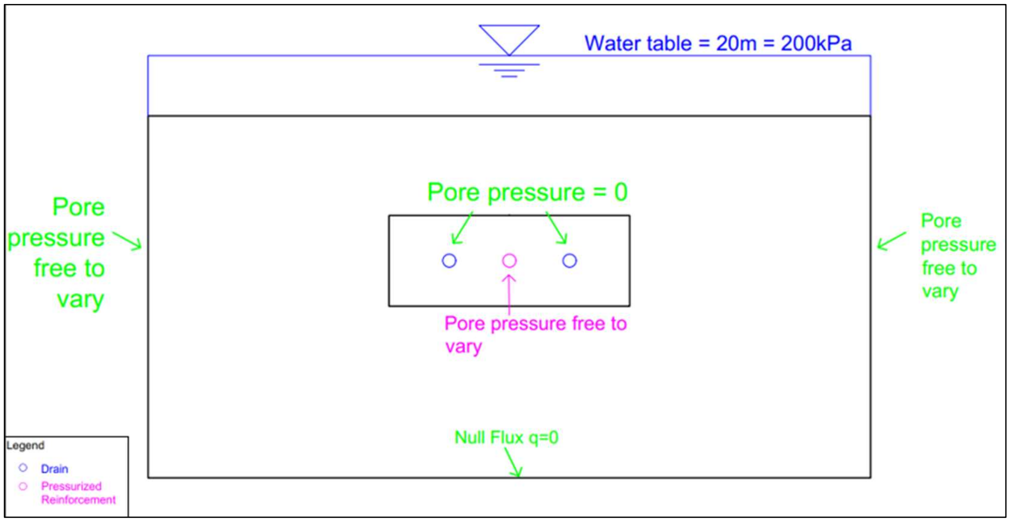

Figure 4.6 - Hydraulic boundary conditions adopted in the model. (Not in scale)

4.1.3 Mechanical constitutive model

The choice of an appropriate constitutive model able to simulate the mechanical and deformational behaviour observed in the laboratory testing phase becomes of fundamental importance during the implementation of a robust numerical model that must be more possibly adherent with the real physical behaviour.

Especially, for the case under study, the constitutive model chosen is the PH (Plastic-Hardening) model formulated for the first time by Schanz and Veermer in 2000 [25].

The main features of the **PH** (Plastic-Hardening) model have been summarized in the theoretical documentation of FLAC3D (Itasca Software © 2024, Itasca) and reported below to give a first overview of the model advantages, then the details of interest for the case under consideration will be discussed.

The PH model is characterized by:

1. hyperbolic stress-strain relationship during axial drained compression.
2. plastic strain in mobilizing friction (shear hardening).
3. plastic strain in primary compression (volumetric hardening).
4. stress-dependent elastic stiffness according to a power law.
5. elastic unloading/reloading compared to virgin loading.
6. memory of pre-consolidation stress.
7. Mohr-Coulomb failure criterion.

The PH model is particularly useful for excavation and soil-structure interaction problems and has been demonstrated (Cheng & Lucarelli, 2016) that it provides a more realistic description of the problem than the Mohr-Coulomb model [26], additionally for the calibration phase the conventional lab tests or in-situ tests are sufficient.

The main difference with the usual elastic perfectly plastic model is that the yield surface is not fixed in principal stress space, but it evolves according to the plastic strains.

Additionally, the model includes two hardening mechanisms that are activated during the shearing and compression phases from which they are named. The main reason for use of two hardening model regards the possibility of a differentiated response of the soil depending on its stress path.

Indeed, shear hardening is adopted for the simulation of irreversible strains caused by a primary deviatoric loading, while compression hardening is used in modelling irreversible plastic strains caused by a first compression in the oedometer loading condition and a consequent isotropic loading.

The model also uses nonlinear elastic behaviour that links the elastic modulus to the stress level, this feature plays a major role in the tunnelling process, indeed the stiffening that can be induced by a loading process contributes to the reduction of displacement and consequent loading on the final lining.

The Plastic-Hardening model was designed by [25] to reproduce basic macroscopic phenomena exhibited by soils such as:

- **Densification** - decrease of void volume due to plastic deformations.
- **Stress-dependent stiffness**: observed phenomena of increasing stiffness modules with increasing confining stress.
- **Stress-history**: accounting for preconsolidation effects.
- **Plastic yielding**: development of irreversible strains with reaching a yield criterion.
- **Dilatancy**: an occurrence of negative volumetric strains during shearing.

The parameters describing the deformational behaviour are deeply described in the documentation of Itasca Software in the section on constitutive models related to the plastic model group [24].

However, the key aspects regarding the stiffness and strength of the soil model are reported, especially the three different conditions:

1. Unloading-reloading stiffness modulus $\boldsymbol{E_{ur}}$ that considers the amount of elastic strains recovered during and unloading process, and so the plasticity induced. It depends on maximum principal stress $\boldsymbol{\sigma_3}$[§], cohesion **c**, and the ultimate friction angle $\boldsymbol{\varphi}$, as well as the power **m**, which assumes values between 0.9 and 1 for clays. The stress-dependency of the stiffness modulus is related to **Z** thanks to Eq. 4.1:

   $$E_{ur} = {E_{ur}}^{ref} * Z^m \tag{4.1}$$

   Where the parameter Z is expressed as (Eq.4.2):

   $$Z = \frac{c' cot(\varphi) - \sigma_3}{c' cot(\varphi) + p_{ref}} \tag{4.2}$$

   Where p_{ref} represents the reference pressure at which the stiffness modulus was determined.

2. Secant stiffness $\mathbf{E_{50}}$, which defines the initial slope of the hyperbolic stress-strain curve (Eq.4.3). Also, in this case the parameter E50 obeys to the power law as $\mathbf{E_{ur}}$:

   $$E_{50} = {E_{50}}^{ref} * Z^m \tag{4.3}$$

   Additionally, the ratio between the $\mathbf{E_{ur}}$ to $\mathbf{E_{50}}$ must be bigger than two at least and is usual assumed equal to 3 with a range of variation between 3 and 6.

   $$\frac{E_u^{ref}}{E_{50}^{ref}} > 2 \; ; 6 < \frac{E_u^{ref}}{E_{50}^{ref}} < 3$$

[§] σ_3 = Maximum (minimum compressive) principal stress according to the FLAC convention: negative stresses = compression stresses

3. The failure criterion is consistent with Mohr-Coulomb Model (Eq.4.4) limiting states of stress are by means of the effective shear parameters: cohesion c´, friction angle φ´ and the angle of dilatancy, ψ

$$q_f = \frac{2*sen(\varphi)*(c*\cot(\varphi)-\sigma_3)}{1-sen(\varphi)} \tag{4.4}$$

4. For a standard drained triaxial test, the connection between the axial (vertical compressional) strain, ε1, and deviatoric stress, q, can be described by a hyperbolic relation (Eq.4.5):

$$\varepsilon_1 = \frac{q_a q}{E_i(q_a-q)} \tag{4.5}$$

Equation 4.4 is graphically represented in Figure 4.7 with the cut-off at q_f.

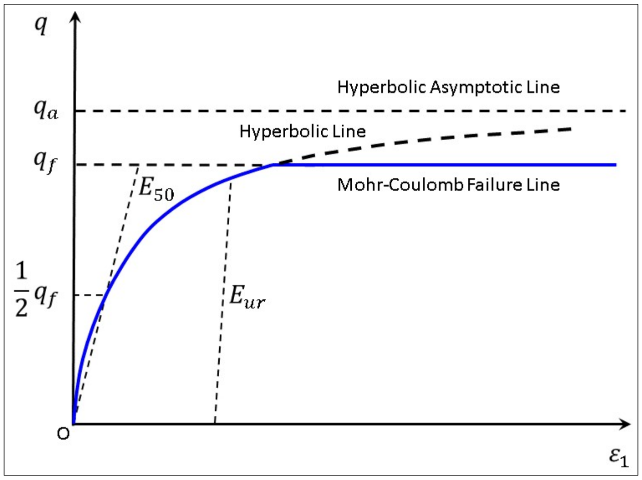

Figure 4.7 - Hyperbolic stress-strain relation in primary shear loading. (Ref.)

The **K** and **G** are the elastic bulk and shear moduli, which can be derived from the elastic unloading-reloading Young's modulus $\mathbf{E_{ur}}$, and the unloading-reloading Poisson's ratio **v**, are obtained using the relations (Eq.4.6 and 4.7):

$$K = \frac{E_{ur}}{3(1-2v)} \tag{4.6}$$

$$G = \frac{E_{ur}}{2*(1+v)} \tag{4.7}$$

The Hardening mechanism is calibrated starting from the initial value of the hardening parameter, which denotes the pre-consolidation pressure determined using the initial stress state and over-consolidation ratio.

4.1.4 Hydraulic Constitutive Model

The simulation of an HM phenomena requires the adoption of a hydraulic constitutive model among the available in FLAC3D, which are: the *isotropic* characterized by equal hydraulic properties along the different directions, the *anisotropic* with the possibility to assign different hydraulic properties for different directions and the null one corresponding to an impermeable object.

The hydraulic properties that characterized the hydraulic model in *FLAC3D* are the permeability coefficient **K**, the fluid mass density **ρ_f**, the Biot coefficient **α**, and Biot modulus **M**, linked with the fluid bulk modulus **K_f**, and porosity, **n**.

The porosity is defined as the ratio between the volume of voids and the total volume of a given sample:

$$n = \frac{V_v}{V} \qquad (4.8)$$

The permeability coefficient **K_h** (m^2/(Pa*sec) used in FLAC3D is also referred to in the literature as the mobility coefficient. It is the coefficient of the pressure term in Darcy's law and is related to the hydraulic conductivity **k_h** (m/s), by the expression 4.9:

$$K_h = \frac{k_h}{\rho_f * g} \qquad (4.9)$$

Where g is the gravitational acceleration, and dynamic viscosity μ (N*sec/m2).

The hydraulic conductivity however depends on the intrinsic permeability **κ** (e.g., in m^2), which is related to **k_h** (hydraulic conductivity) as (Eq.4.10):

$$k_h = \frac{\kappa}{\mu} \qquad (4.10)$$

The mass densities needed as input in FLAC3D are different based on saturation conditions encountered, especially the dry density of the solid matrix **ρ_d**, the saturated density of the solid matrix **ρ_s**, and the density of the fluid **ρ_f**.

The saturated density of each element in the model is computes using the equation 4.11 that relates the fluid density **ρ_f**, the porosity **n**, and the saturation degree **S**:

$$\rho_s = \rho_d + n * S * \rho_f \qquad (4.11)$$

The Biot coefficient **α** is defined as the ratio of the fluid volume variation (gained or lost) in a material element to the volume change of that element when the pore pressure is changed. The range of values assumed by **α** is between 3n/(2+n) and 1.

In the case of an incompressible solid constituent, $\alpha = 1$, however the determination offor an ideal porous material, the Biot coefficient is related to the bulk modulus of the solid component Ks:

$$\alpha = 1 - \frac{K}{K_s} \qquad (4.12)$$

The *Biot modulus*, M, is defined as

$$M = \frac{K_u - K}{\alpha} \qquad (4.13)$$

Where Ku is the undrained bulk modulus of the material.

For an ideal porous material, the Biot modulus is related to the fluid bulk modulus **K_f**.

$$M = \frac{K_f}{n + (\alpha - n)(1 - \alpha)\left(\frac{K_f}{K}\right)} \qquad (4.14)$$

Thus, for an incompressible solid constituent ($\alpha = 1$),

(6)

$$M = \frac{K_f}{n} \qquad (4.15)$$

4.2 Input parameters adopted

The mechanical parameters chosen as input of the numerical model in which the PH constitutive model was adopted are summarized in Table 4.1.

The cohesion c' and the friction angle φ chosen are the results of the procedure explained in the next paragraph (§5.1.6) where the geotechinical characterization for a real case study was carried out.Particurarly, looking at the profile along the depth outlined, the value of cohesion was chosen as the average of the values that present a significant reduction concerning the entire data set. For the friction angle, the value assumed corresponds to the mean among all the data sets, justified by the fact that the variation between the maximum and the minimum value is quite limited and most of the φ values are around 24°.

The soil dry density and the porosity chosen are the results of the laboratory test summarized in Table 5.1.

The deformability parameters, especially the E_{50}^{ref} was determined starting from the interpretation of the oedometer test, assuming the relationship with E_{oed} for an assumed value of Poisson ratio corresponding to 0.25, as an average value, however, the incidence of this ***υ*** highly affects Young's modulus as depicted in Figure 5.25

Defined, the E_{50}^{ref} is possible to compute the E_{ur}^{ref} considering a ratio among the two variables of 3, as described in §4.1.3, then starting from the E_{ur}^{ref} the volumetric K and the shear deformation moduli G are computed.

The value of the earth pressure coefficient K_0 is fixed equal to 1 to simulate a simplified stress state easier to understand during the result analysis process.

The reference pressure $\mathbf{p_{ref}}$ was fixed coherently with the effective state of stress present at the depth analysed, specifically the depth of interest at which the pressurized reinforcement will be applied in a tunnel project at 22 m below the ground surface and a water table 5m below the ground surface, corresponding to vertical effective stress of 250 kPa.

Table 4.1 – Input parameters adopted for the mechanical constitutive model.

Mechanical model	**Cohesion (kPa)**	**Friction Angle (°)**	**Soil dry density (kg/m^3)**	**Soil Saturated Density (kg/m^3)**	**n (-)**	**v (-)**	**OCR (-)**	**m (-)**
PH - Plastic Hardening	15	22	1800	2100	0.3	0.25	1	0.9
	E_{50}^{ref} (MPa)	**E_{ur}^{ref} (MPa)**	**E_{oed} (MPa)**	**K (MPa)**		**G (MPa)**	**K_0 (-)**	**p_{ref} (kPa)**
	150	450	180	300		180	1	250

The hydraulic parameters chosen as input of the numerical model in which the isotropic constitutive model was adopted are summarized in Table 4.2.

The hydraulic conductivity was fixed equal to $1*10^{-9}$ m/s, corresponding to an average value found in clay formations.

The fluid density was fixed to the common water density of 1000kg/m^3, while the fluid bulk modulus was fixed to the value assumed for saturated conditions (S=100%) K_f = 2 GPa, then the Biot modulus is computed accordingly to Eq.4.8

However, this assumption is equivalent to considering that no air bubble intrusion will highly affect the stiffness of the entire fluid mixture, reducing it to a value lower than 1 to 10 orders of magnitude.

Table 4.2 – Input parameters adopted for the hydraulic constitutive model

Hydraulic Model	Hydraulic conductivity (m/s)	Fluid density (kg/m^3)	Fluid Bulk Modulus (MPa)	Biot Coefficient	Biot Modulus (MPa)
Isotropic	1E-09	1000	2000	1	6670

4.3 Numerical cases analysed

The numerical cases developed for the study of the reinforcement interaction with the soil were implemented following the standardized configuration suggested by the manufacturing company (Maccaferri) and reported in the previous paragraph §3.2.1.

Especially, the series of simulations carried out are reported in Table 4.3, where the first case was simulated to understand the simplest case with a unique central pressurized reinforcement surrounded by two reinforcements.

Progressively, the second case analyses a more complex situation, where the central pressurized reinforcement is not anymore equal along the length of the model but alternates the pressurized zone with the drainage elements, that define two types of sections: the first called DE (drain-expansion), and the second DD (Drain-Drain).

In Figure 4.8 the difference between the two schemes is reported by representation of the group subdivision operated in FLAC3D.

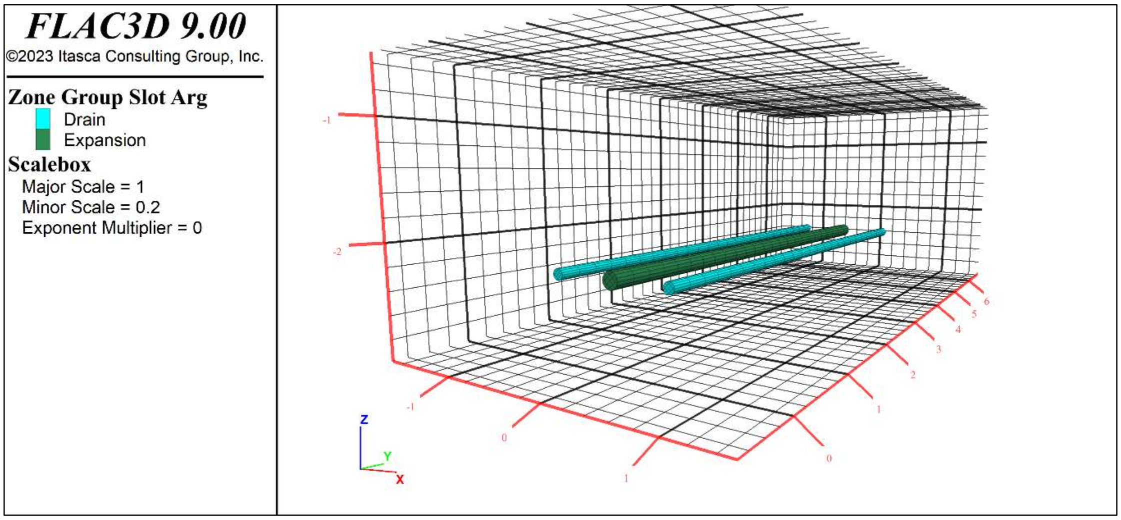

a)

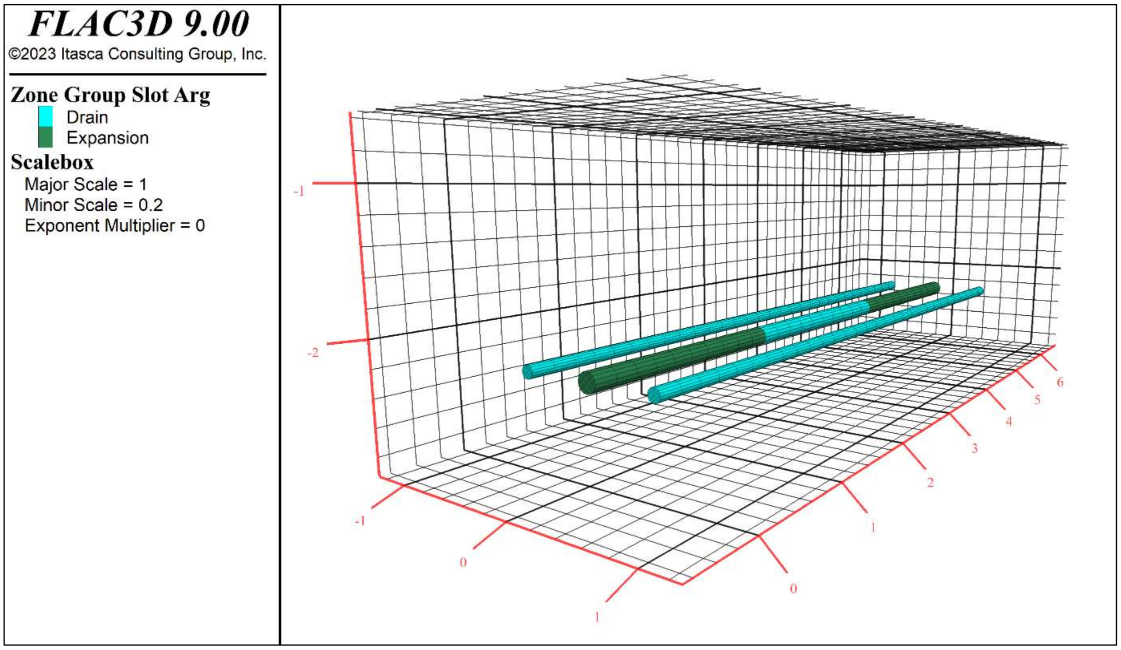

b)

Figure 4.8 – Scheme adopted for the simulations of reinforcement element. a) Simplified scheme with central expansion zone and lateral drains. b) Alternate scheme with various expansion and drainage zone at the centre and lateral drains.

After the comparison of the two different configurations at a fixed spacing, the analysis performed had the goal of quantifying the effects of various spacing on the configuration in Figure 4.8 (b), to give suggestions during the design of the consolidation intervention.

Table 4.3 – Cases analysed with different configurations and spacing

ID	**H** Only drainage	**HM** Only drainage	**HM** Drain. +Expansion	**Spacing**	**Description**
1	1A	1B	1C	0.5m	Pressurized reinforcement (central zone) + Lateral Drainage
2	2A	2B	2C	0.5m	Alternated pressurized reinforcement (central zone) + Lateral drainage
3	3A	3B	3C	1m	(same as previous)
4	4A	4B	4C	0,7m	(same as previous)

Note	H- Only Hydraulic analysis
	HM - Hydro-Mechanical analysis

The investigation of the physical process was assessed initially with a *fluid simulation* without taking into account the mechanical process, in this way the software starts to calculate the variation of pore pressure without performing any calculation in terms of effective stresses.
Consequently, the calculation time needed decreases considerably allowing a first assessment relative to the zone of influence of the drains, however, with this kind of approach, the entire physical behaviour of the system is missing the effects of the soil stiffness.

Once, the results coming from the *hydraulic simulations* were analysed a second simulation was carried out, this time with the activation of the mechanical process (*hydro-mechanical simulation*) and a consequent calculation of the effective stress variation according to time caused by the action of the drain.
The third kind of analysis performed to study the activation of the *pressurized reinforcement* was simulated by removing the drilling zone and assigning a null[**] zone with a consequent application of a radial pressure normal to the annulus considered for the simulation of the consolidation intervention (in this case the *hydro-mechanical* simulation is performed).

The value of radial pressure was fixed equal to 1MPa, considered the effective state of stress §4.2 simulated and the injection pressure suggested, generally for a higher state of stress the pressure of grout injection increases, with a value 3-4 times the state of stress.
The configuration of query locations adopted for the case of 0,5m spacing has been reported in Figure 4.9, while for the configuration with 1m spacing, the same setup was adopted and scaled on the base of the axis between elements.

In all the cases, the queries were repeated for two different sections of the model, one regarding the section that includes the pressurized reinforcement between the two drains, and a second that includes the alignment of three drainage portions (Figure 4.8).

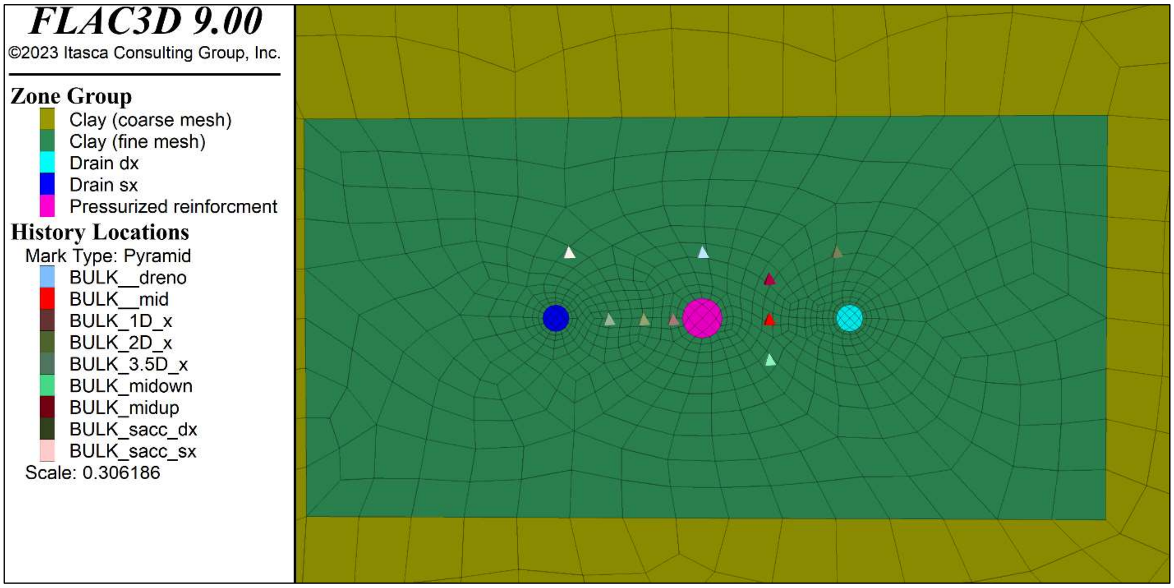

Figure 4.9 - Query configuration for analysis of variables variation spacing 0,5m.

[**] FLAC3D nomenclature for definition of excavated material

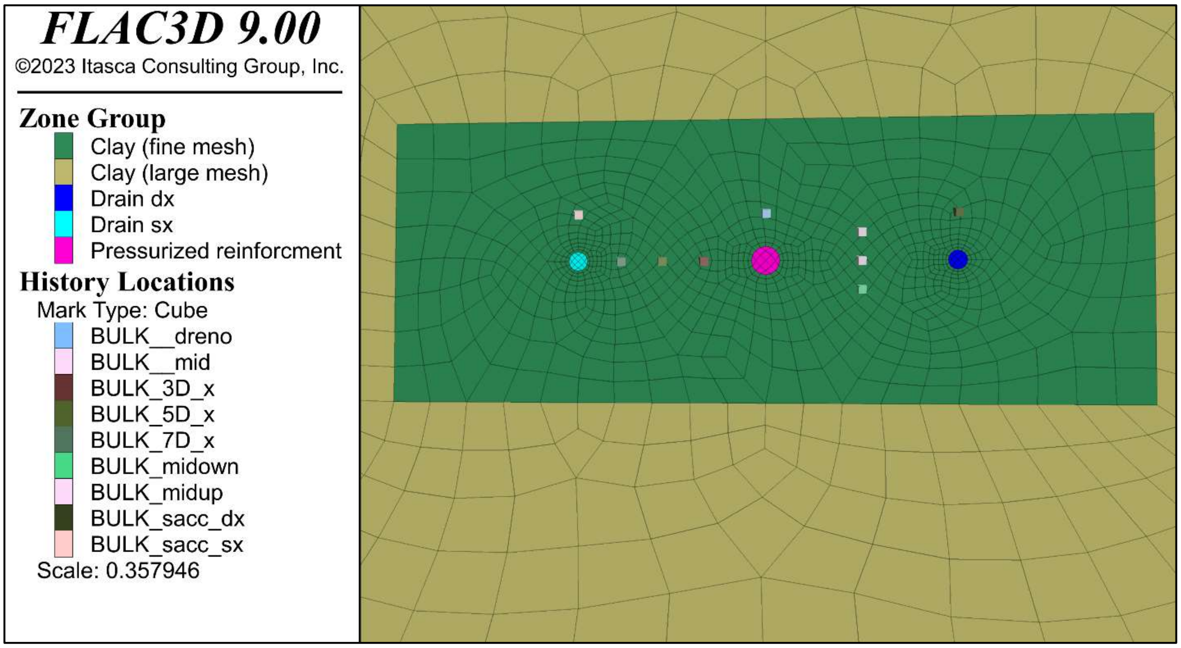

Figure 4.10 - Query configuration for analysis of variables variation spacing 1m.

Each of the models in the set of cases exposed above was checked by ensuring that the initialisation phase was carried out correctly. To this end, the initial stress state was analysed in terms of total stresses (Figure 4.11), pore pressures and effective stresses, verifying that the trend of the three diagrams corresponded to a hydrostatic state for the interstitial pressures, to a linear geostatic trend proportional to the soil's weight (), and finally that the effective stresses corresponded to the differences of the total stress and water pressure according to the Terzaghi's principle of effective stresses.

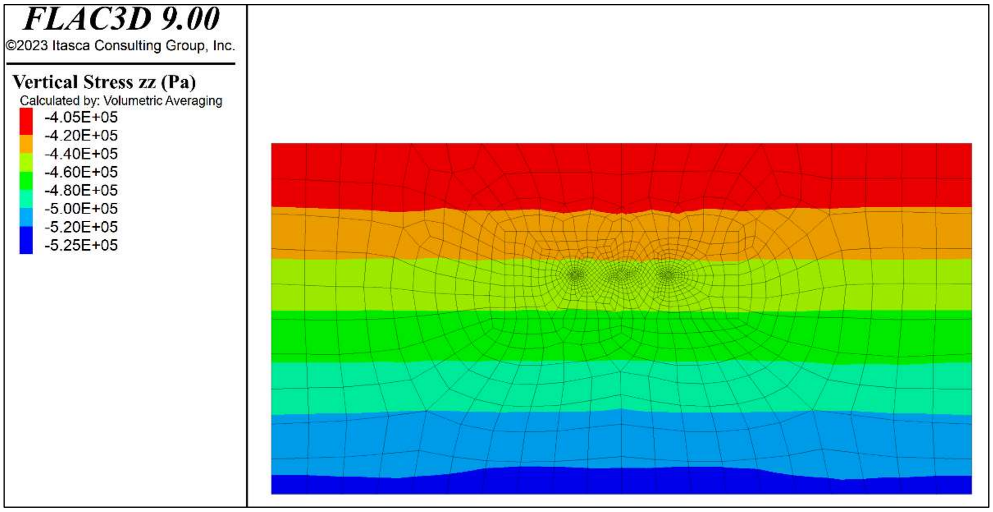

a)

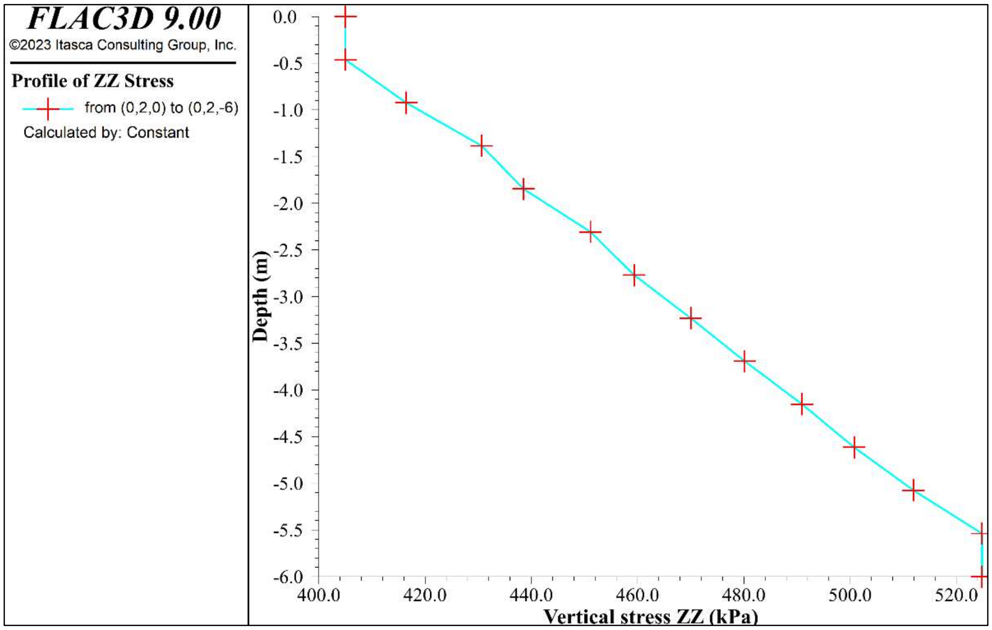

Figure 4.11 – a) Total vertical stress after initialization process, b) Vertical profile of total vertical stress

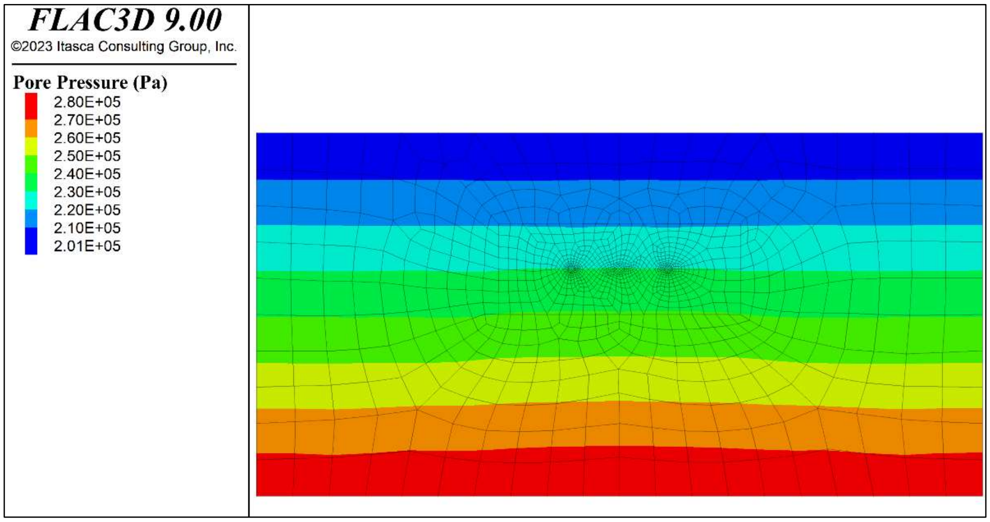

a)

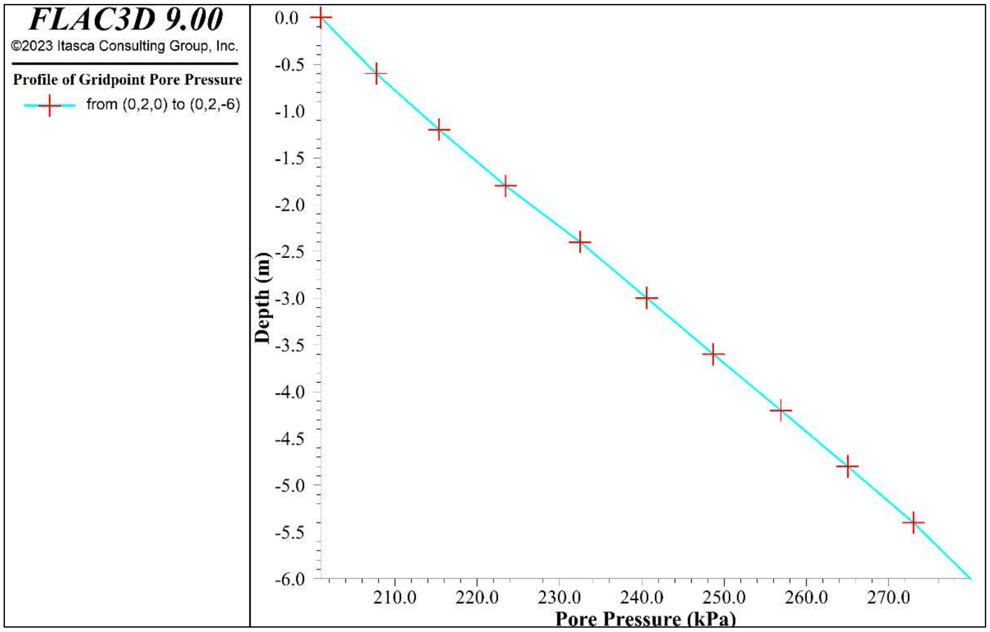

b)

Figure 4.12 - a) Pore pressure after initialization process, b) Vertical profile of pore pressure

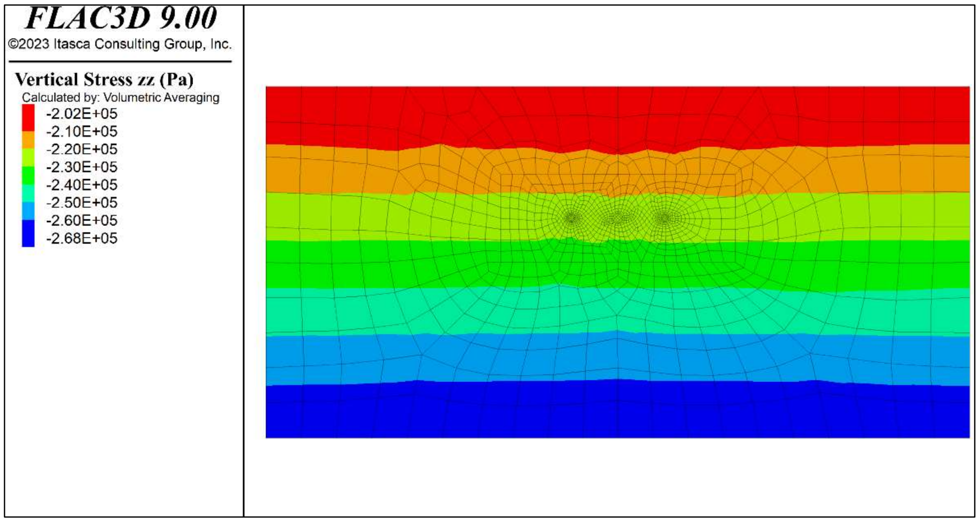

a)

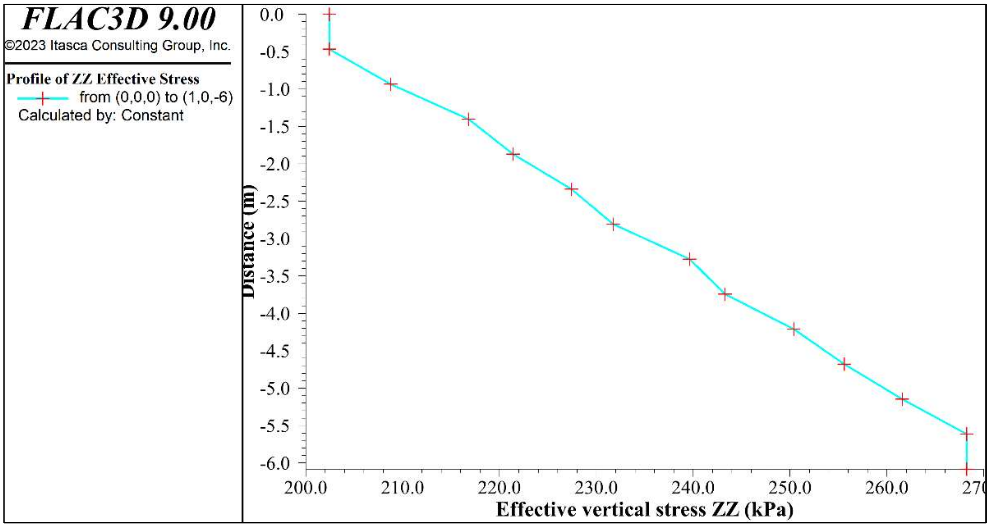

b)

Figure 4.13 - a) Effective vertical stress after initialization process, b) Effective vertical stress profile

4.4 Simplified treatment

The first case analysed in the numerical simulations is the one identified in Table 4.3 with the ID=1 and represented in Figure 4.8 (a) with a simplified intervention configuration to allow a gradual increase in the complexity of model, and better initial understanding of the results.

The initial state of stress imposed was isotropic following the mechanical boundary conditions showed in Figure 4.5 and the hydraulic in Figure 4.6.

4.4.1 Drainage (flow-only simulation)

In the case of fluid simulation, three aspects were investigated for the understanding and comparison of the phenomena, firstly the degree of pore pressure reduction for different distances moving away from the drain, secondly the time needed to complete the process of drainage and thirdly the area of influence at a fixed time.

In Figure 4.14, the pore pressure variation was potted at the end of the simulated process, when the pore reduction reach 50kPa, with a small zone of interaction in the central region.

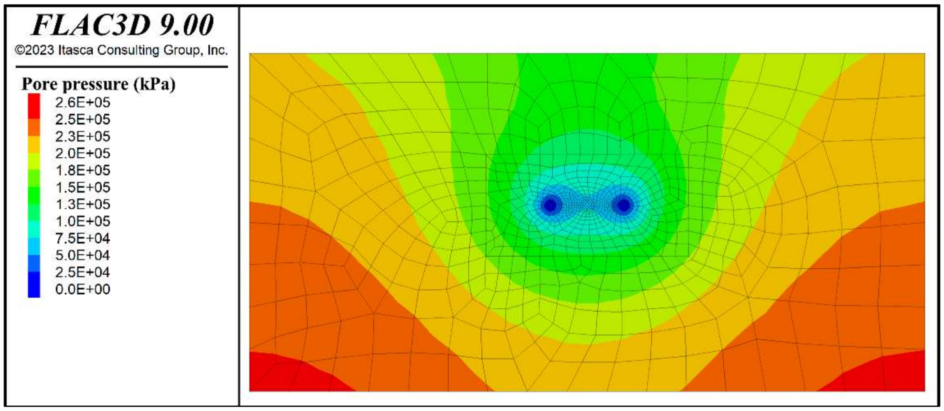

a)

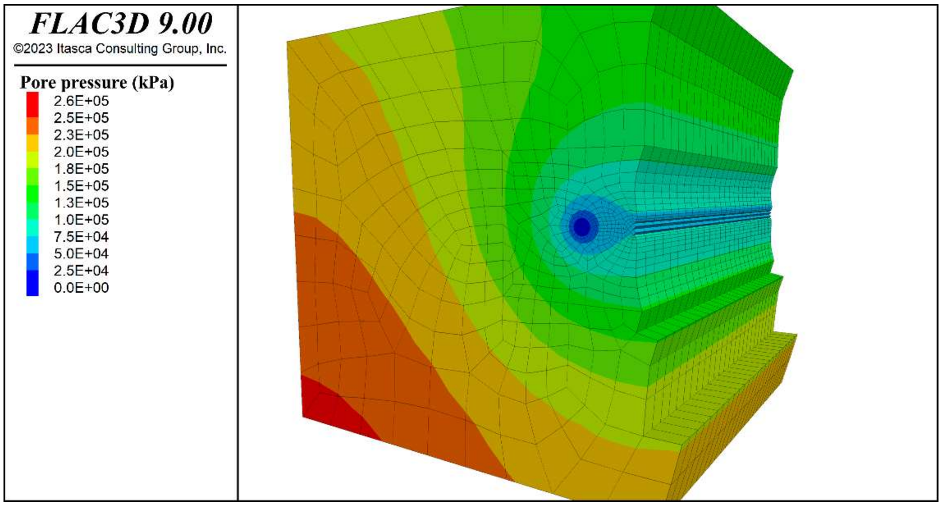

b)

Figure 4.14 –(a) Pore pressure contour frontal view (b) Pore pressure contour longitudinal section.

The first comparison was made by performing a query for three different distances moving from the border of the central pressurized element with steps proportional to the pipe diameter obtaining in this way a normalized distance. The evolution for the pore pressure follows the hyperbolic decline sketched in Figure 4.15.

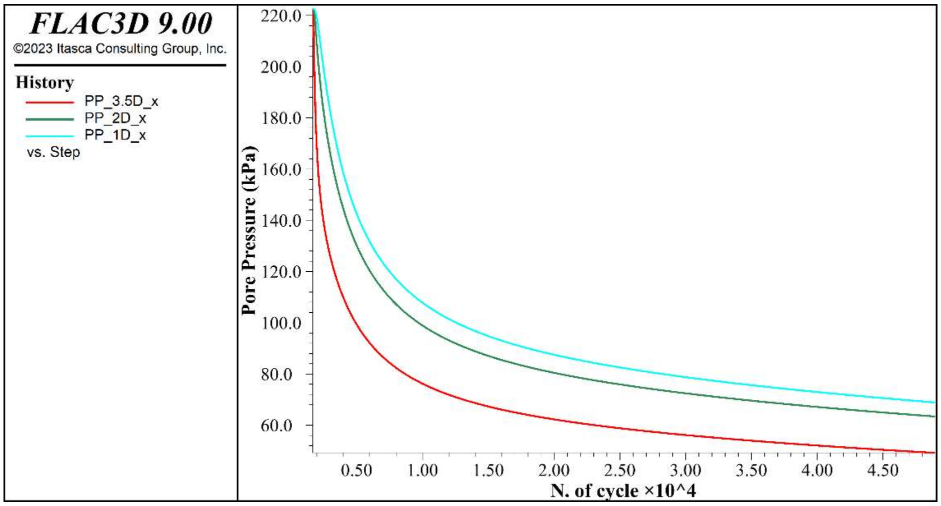

Figure 4.15 -Pore pressure variation for different distances over time.

4.4.2 Drainage (HM fully coupled simulation)

In this section, the case of HM simulation was explored, particularly it enlarges the range of variables to investigate, adding to the analysis of pore pressure variation, the effective stress and consequently the bulk modulus.

In Figure 4.16 , the pore pressure contour is represented in frontal and in longitudinal view, showing a zone of pore pressure reduction in the surrounding of the two lateral drains, which create an annulus region of influence. The evolution of pore pressure at different distances is plotted in Figure 4.17.

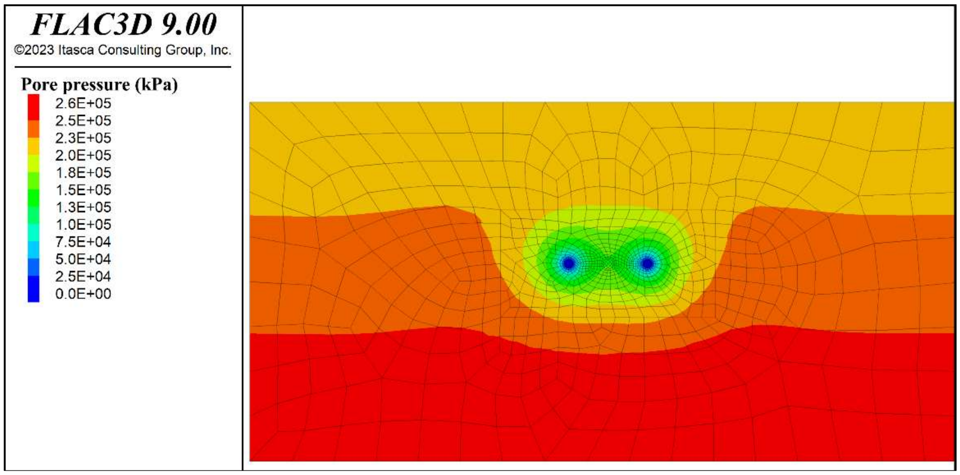

a)

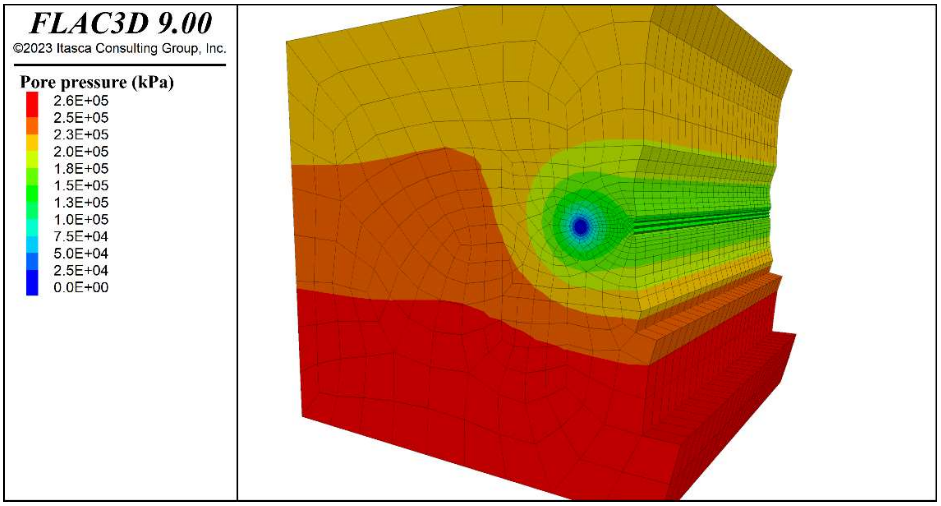

b)

Figure 4.16 - (a)Pore pressure contour (frontal view); (b)Pore pressure contour (longitudinal section). (Hydro-Mechanical simulation)

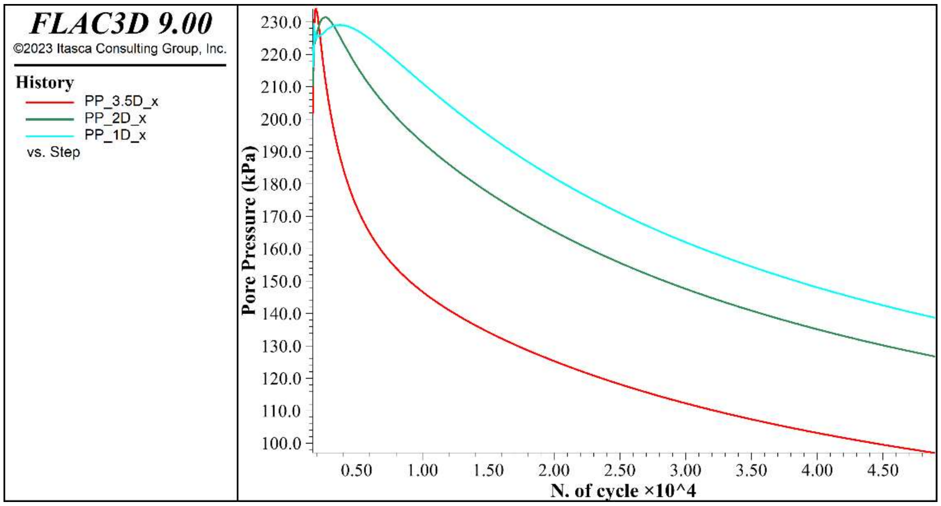

Figure 4.17 - Pore pressure variation for different distances over time (Hydro-mechanical simulation).

As for the pore pressure, also the mean effective stresses contour was sketched to appreciate the action of drains in the regions around them (Figure 4.18).

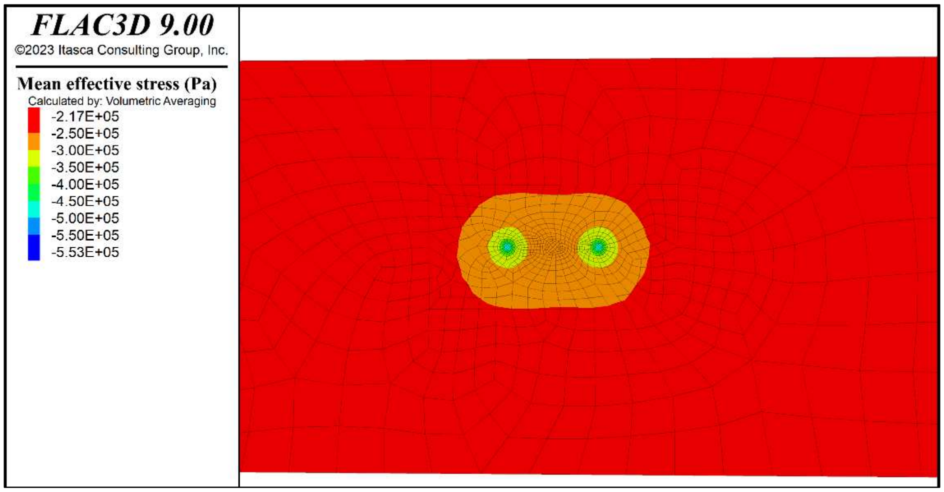

a)

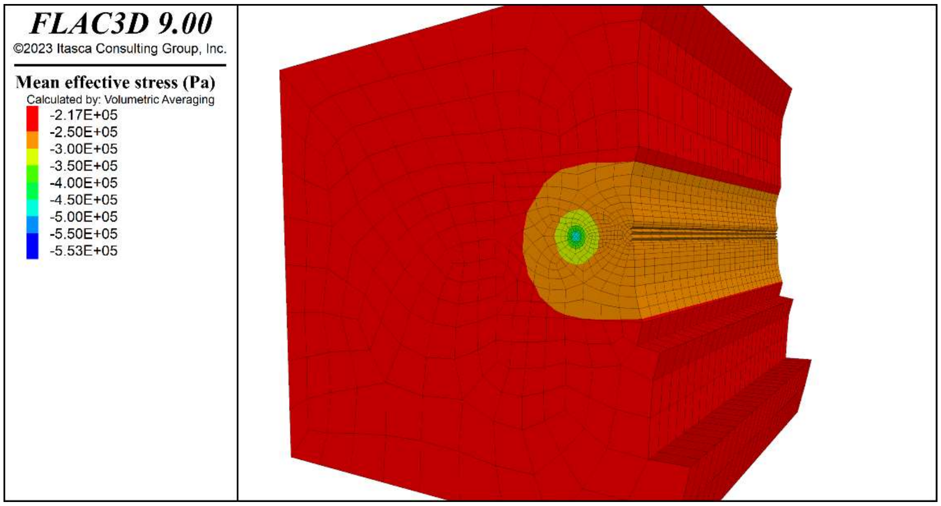

b)

Figure 4.18 -(a)Mean effective stress contour (frontal view); (b)Mean effective stress contour (longitudinal section). (Hydro-Mechanical simulation)

The second variable analysed in this section was the effective stress, with an attention to minimum, maximum and mean stress reported in Figure 4.19, remembering that the convention of signs operated by FLAC3D, considers negative the compressive stresses, and so the minimum value correspond to the maximum compressive.

By observing Figure 4.19, it is evident that all the component maintains the same trend and the difference between the final value of stress is negligible, in fact: σ_{min}=335kPa, σ_{max}=325kPa and σ_{mean}=310kPa , which allows to say that the isotropic stress state is maintained.

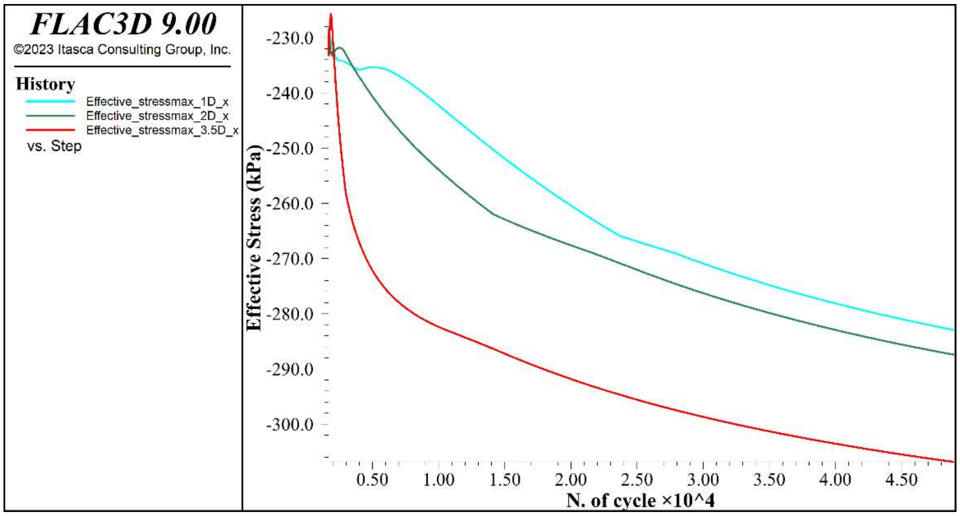

a)

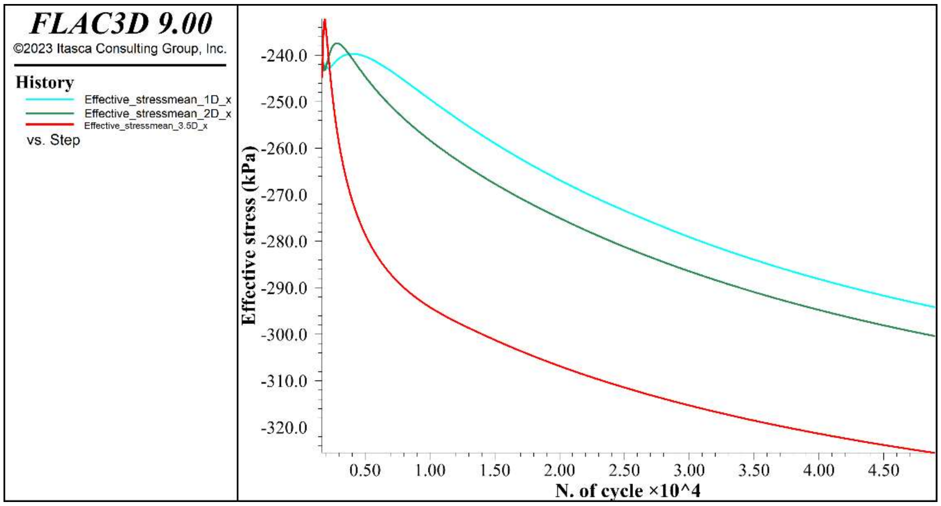

b)

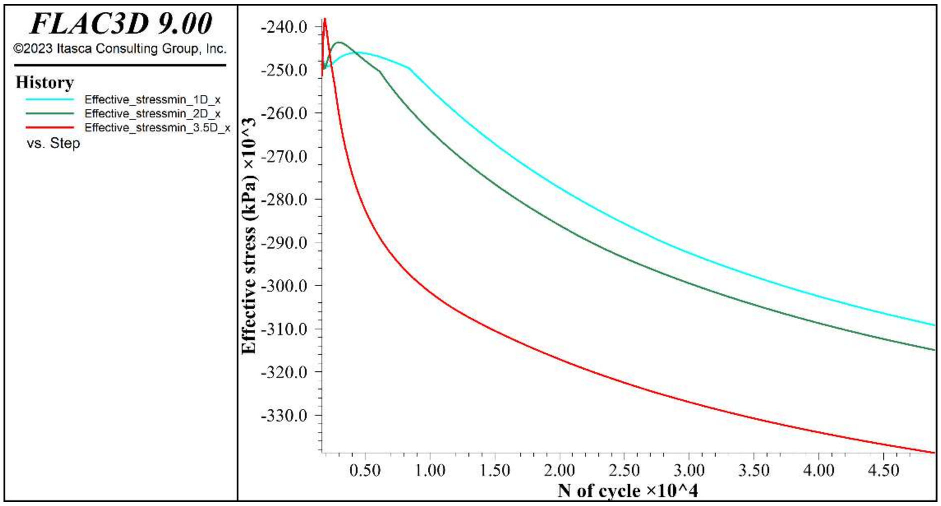

c)

Figure 4.19 – Evolution of: (a)Maximum Effective stress, (b)Mean Effective stress, (c)Min. Effective stress.

As observed for pore pressure and for mean effective stress, the contour (Figure 4.20) of bulk modulus develops an increase in zone around the drains thanks to the stiffening effects simulated by the constitutive model adopted.

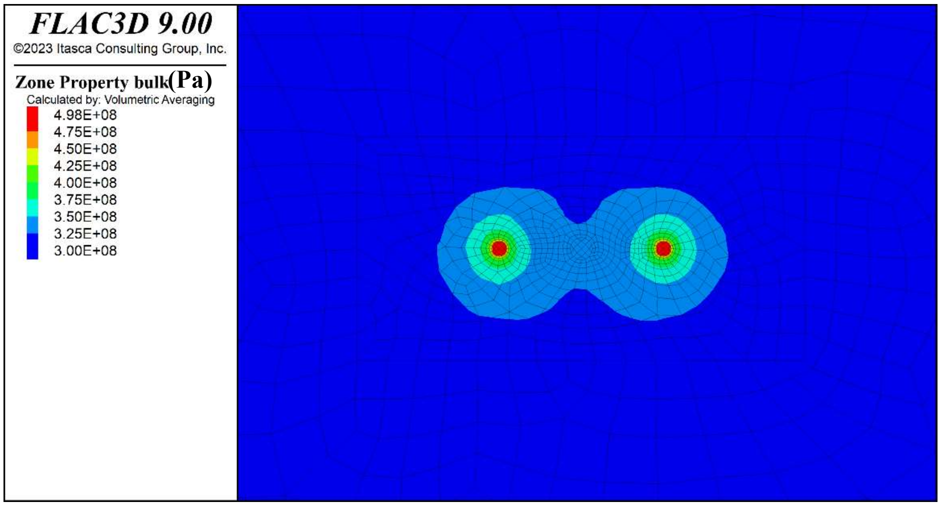

a)

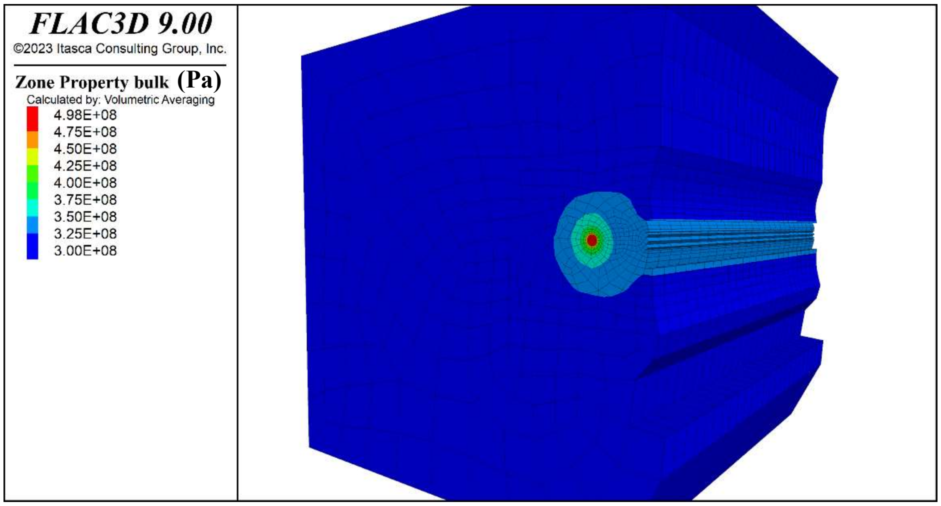

b)

Figure 4.20 - (a) Bulk modulus contour (frontal view) ;(b) Bulk modulus contour longitudinal section (HM simulations)

The evolution over the number of cycles for different distances was reported in Figure 4.21 where it is appreciable the higher increment of bulk modulus moving from the central zone (1D) towards the drains (3.5D) in accordance to the position of histories exposed in the previous paragraph (§4.3)

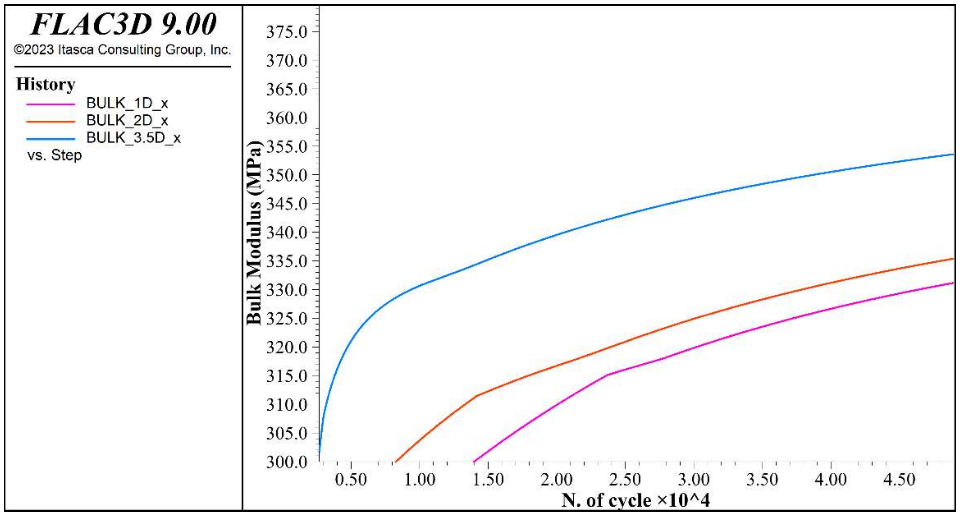

Figure 4.21 – Bulk modulus evolution for HM simulations.

4.4.3 Drainage and Expansion (HM fully coupled simulation)

The last case explored was the combined action of drainage and expansion. First of all, the pore pressure contour did not show significant difference with the previous case were only the drainage actions was activated. However, by plotting the pore pressure variation in Figure 4.22, the initial phase presents a fluctuation of the values that starts to decrease with similar trend of Figure 4.17.

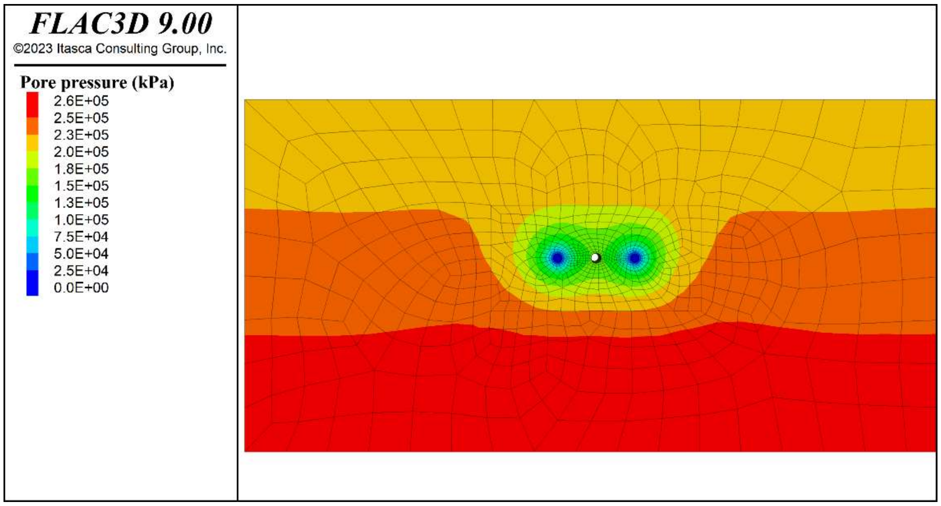

a)

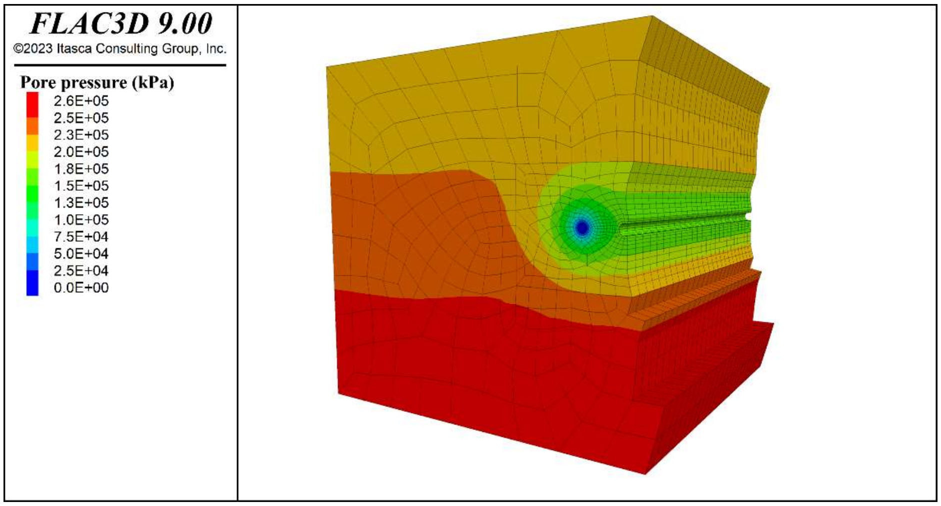

b)

Figure 4.22 -Pore pressure contour (frontal view) ;(b) Pore pressure contour longitudinal section (Drainage + Expansion)

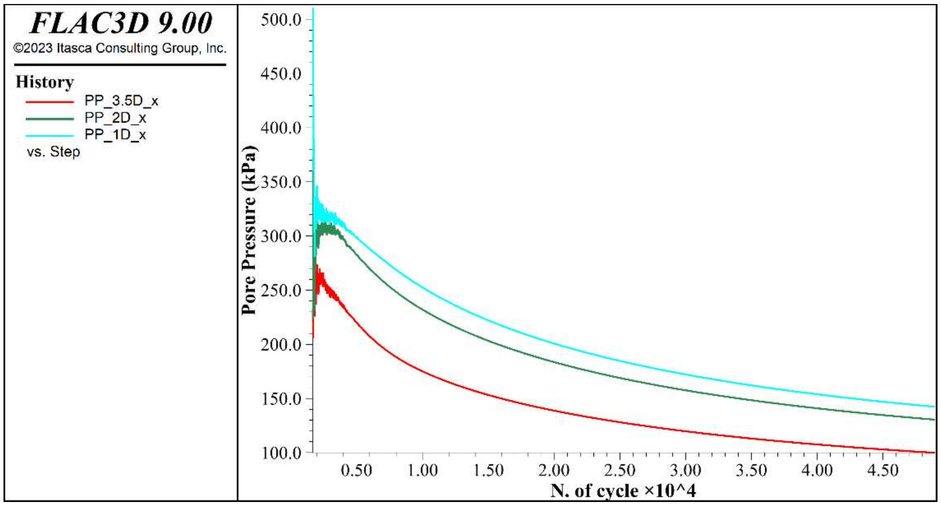

Figure 4.23 - Pore pressure evolution for different spacing (Drainage + Expansion).

The second variable studied was the mean effective stress, which showed a substantial difference respect the previous case, in fact looking at the longitudinal sections of mean effective stress contour (Figure 4.24), is possible to observe a zone with higher mean effective stress which correspond to the expansion zone.

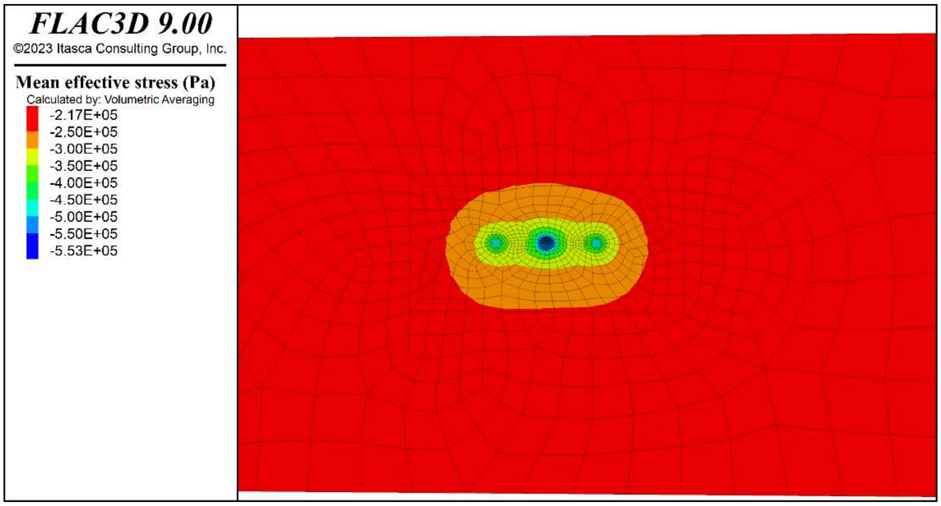

a)

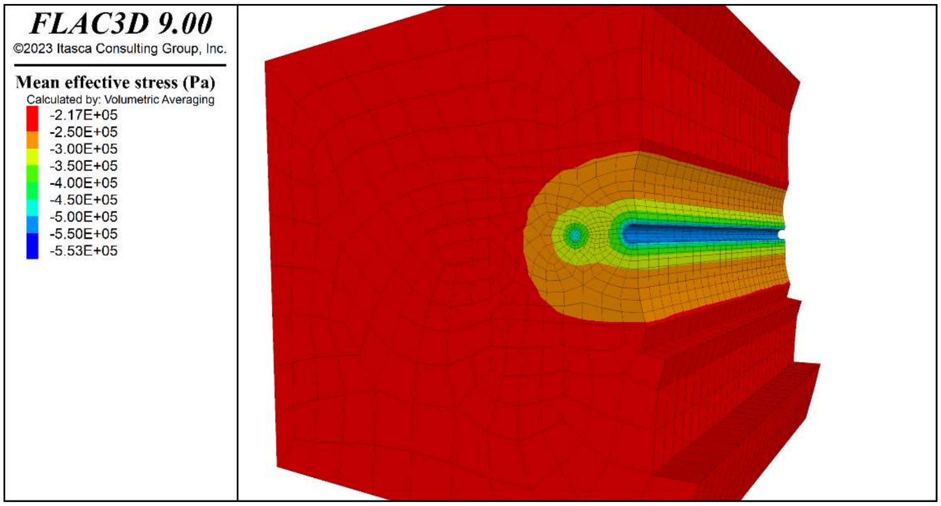

b)

Figure 4.24 – (a) Mean effective stress contour (frontal view) ;(b) Mean effective stress contour (longitudinal section) (Drainage + Expansion)

As done before, the minimum, maximum and mean effective stress were checked in Figure 4.25. Particularly, the increase in effective stress was different for the three components, in fact by analysing the final value of stress: σ_{min}=650kPa, σ_{max}=420kPa and σ_{mean}=315kPa, the surrounding of the expansion zone was subjected to a variation of the stress state that leads to an anisotropic condition, with a relevant increase for the minimum component.

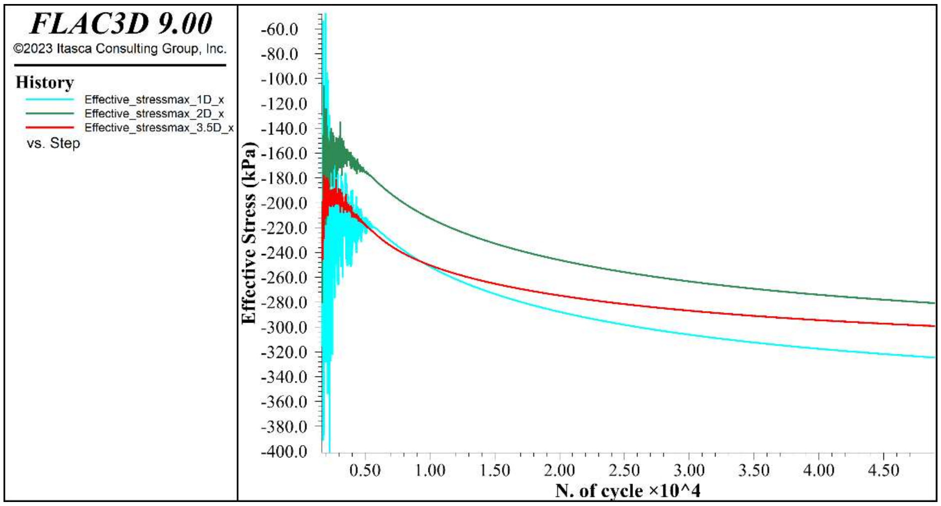

a)

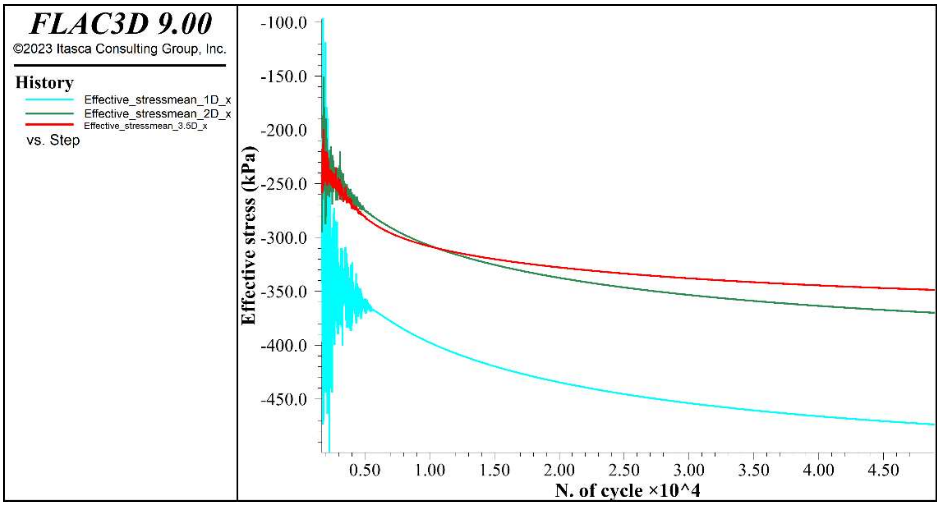

b)

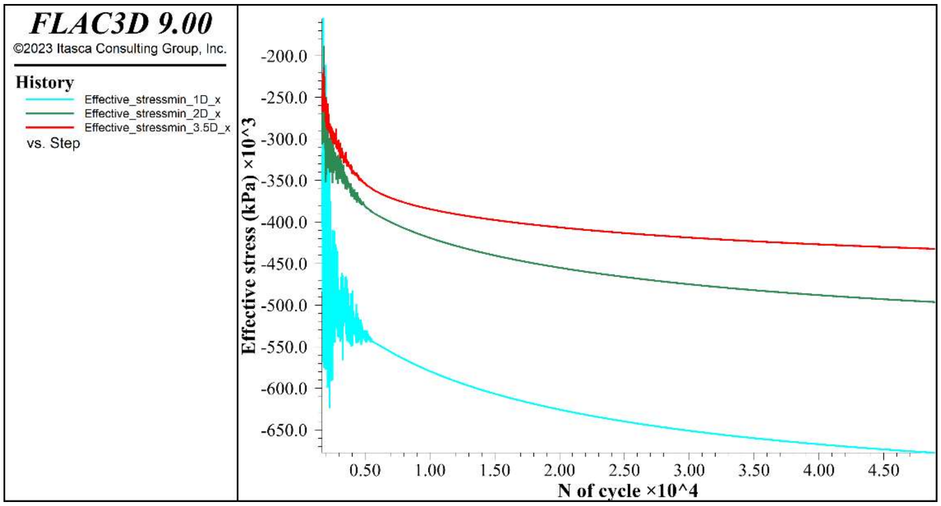

c)

Figure 4.25 -Evolution of: (a)Maximum Effective stress, (b)Mean Effective stress, (c)Min. Effective stress. (Drainage + Expansion)

Finally, the bulk modulus contour was reported in Figure 4.26, where the increase of Bulk modulus involved a smaller region surrounding the drains, but a higher rise was evident close to the expansion zone. This aspect was confirmed by the bulk modulus evolution plotted in Figure 4.27.

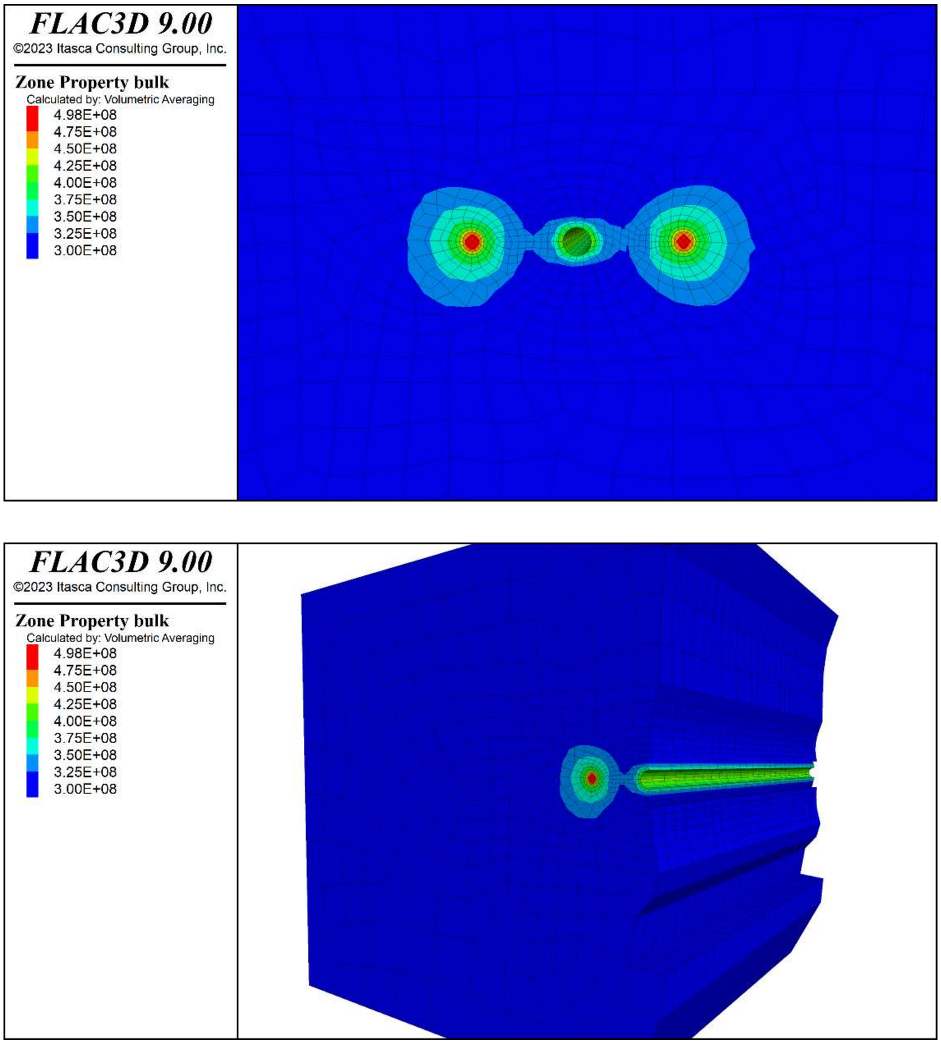

a)

b)

Figure 4.26 -(a) Bulk modulus contour (frontal view) ;(b) Bulk modulus contour longitudinal section (Drainage + Expansion)

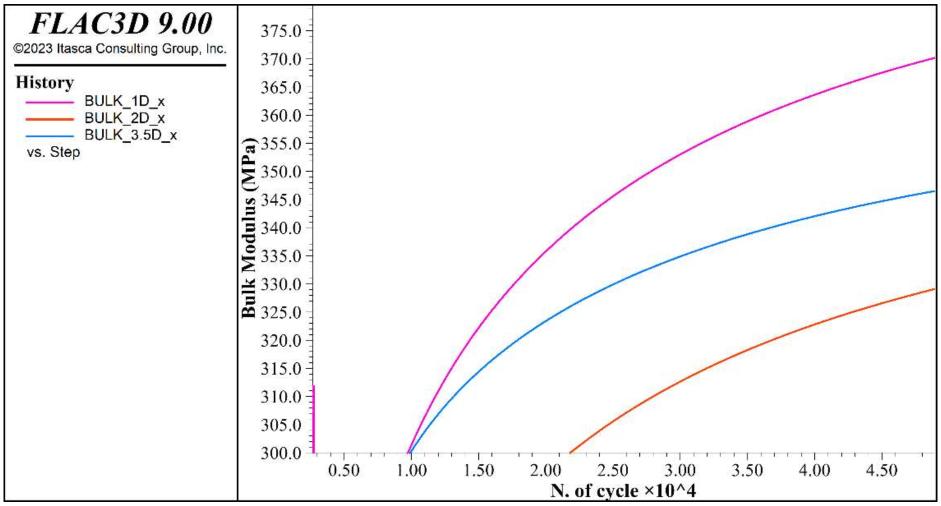

Figure 4.27 – Bulk modulus evolution for Drainage + Expansion case.

4.5 Combined treatment

The second case analysed in the numerical simulations is the one identified in Table 4.3 with the ID=2 and represented in Figure 4.8 (b) with an combined intervention configuration that alternates the drainage and the expansion for the central element. Three different spacing conditions were simulated to study the effects generated on the variables of interest.

The main difference between this configuration and the previous one (simplified), is related to the fact that two different kinds of sections are present and so in the directions y (out of the plane) all the quantities are not anymore constant but vary.

4.5.1 Drainage (Flow-only simulation)

The procedure of comparison adopted for the simplified configuration was repeated for this second case, where the two different sections (DE and DD) were analysed.

Particularly, section DE is considered an inactive zone (no expansion) during the simulations that calculate only hydraulic quantities, so as can be observed in Figure 4.28, the region between the drain is practically a region of the soils, where the two lateral drains can reduce the pore pressure until 50kPa, and interact each other creating zones at equal pore pressures.

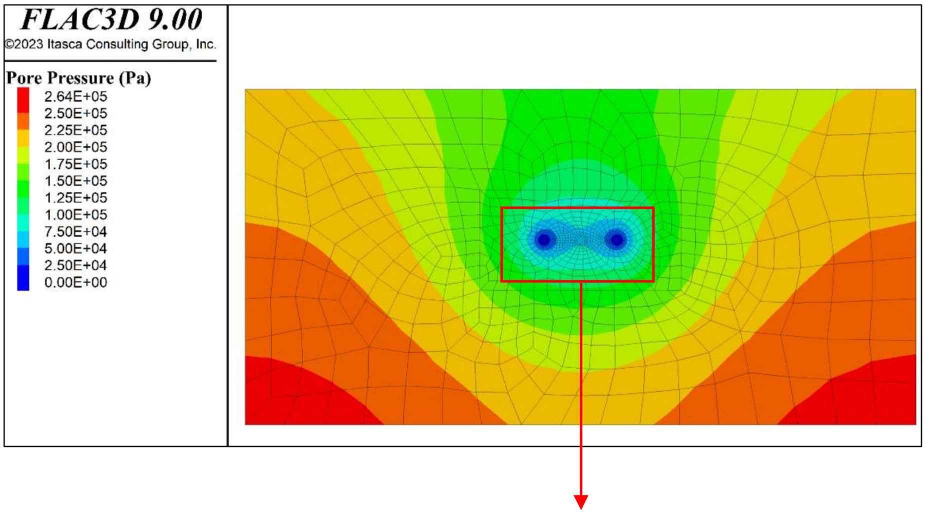

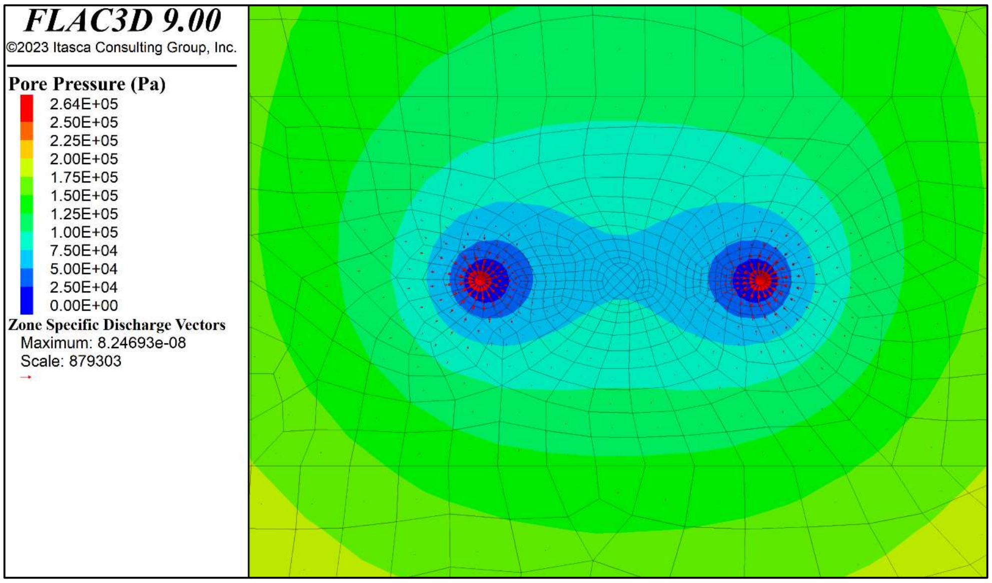

Figure 4.28 - Pore pressure contour at the end of the calculation process in sections DE.

The pore pressure contour for the sections DD, shows a bigger reduction between the central elements and the lateral one, as expected. This is related to the interaction zone between drainage elements that are able to create a contour with low pressure (around 25kPa) for a region of 3-4 times the diameter (Figure 4.29).

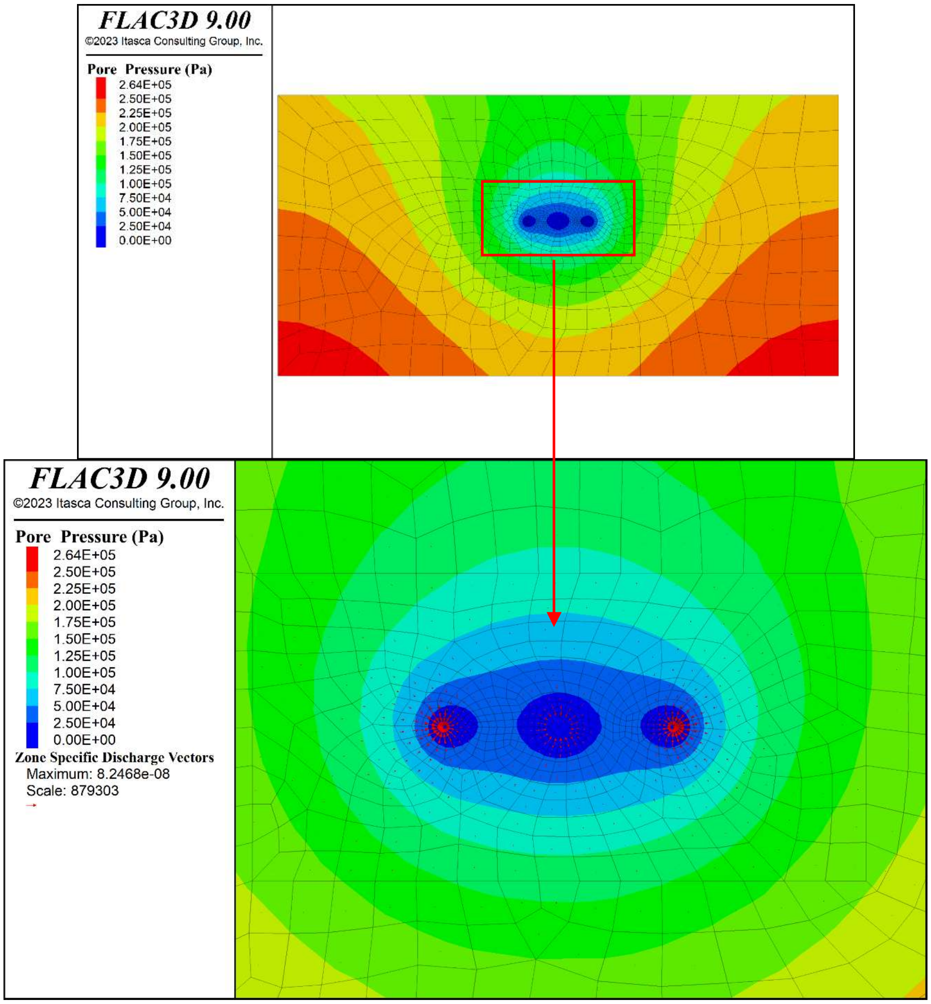

Figure 4.29 – Pore pressure contour at the end of the calculation process in sections DE.

The quantitative evaluation of pore pressure reduction is plotted in Figure 4.30, where for the two sections can be seen that the variation for different distances is less emphasised in the first part of the process, while in the second portion it starts to stabilize.

The amount of pore pressure reduction in sections DE is Δu[††]=160kPa, while for sections DD it reaches Δu=200kPa.

[††] Δu = Absolute difference between final and initial pore pressure.

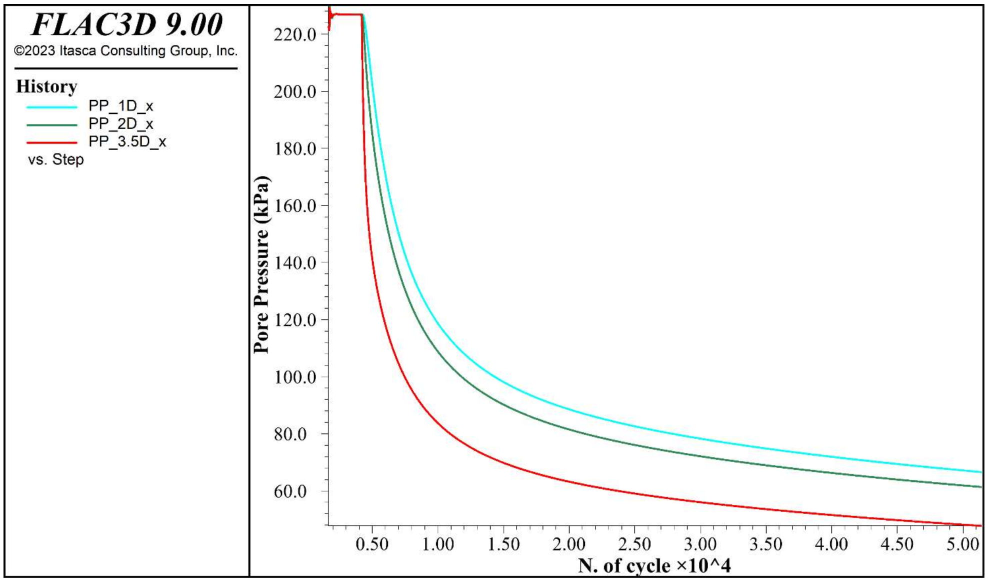

a)

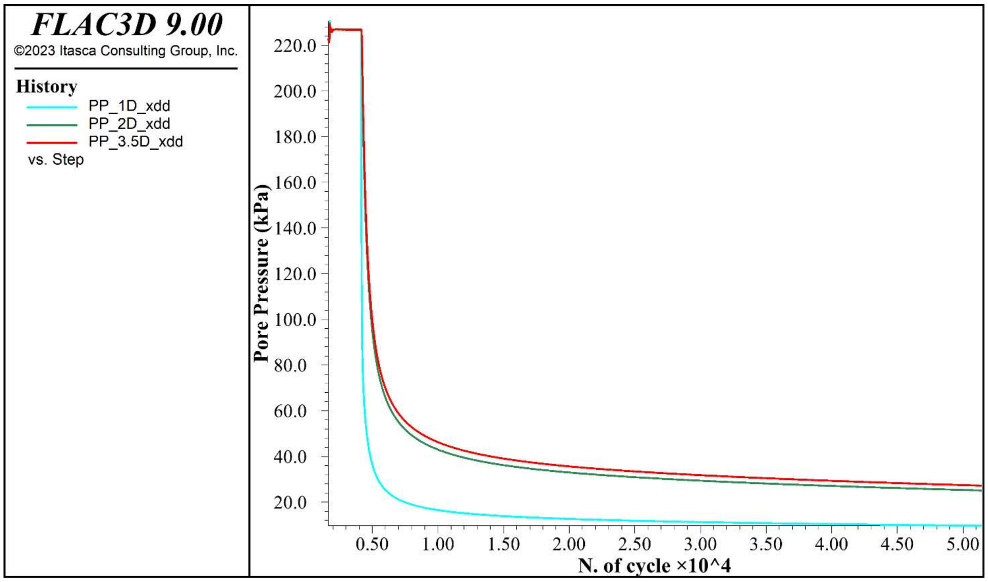

b)

Figure 4.30 – Pore pressure variation for different profiles over time. a) DE section, b) DD section.

4.5.2 Comparison of various spacing

This paragraph focuses attention on the effects of the spacing between elements for the case of fluid-only simulations, showing the comparison between three different spacing: 0.5m, 0.7m and 1m Figure 4.31.

In order to simplify the comparison procedure process, the variation of quantities was analysed at the midpoint between drains and pressurized reinforcement, allowing to consider the influence of each element in the surrounding region.

The pore-pressure reduction was bigger for the lower spacing (0,5m) leading to a final value of water pressure of 60 kPa (**Δu=165**kPa), while for spacing of 0.7m the value reached was about 75kPa(**Δu=150**kPa), for the larger spacing the final value of pore pressure was of85 kPa (**Δu=140**kPa).

Considering the percentage of reduction which helps to normalize the results and transpose it with other interventions or cases, the reduction of pore pressure was 74% for the spacing of 0,5m, 67% for spacing of 0,7m and 62% for the larger spacing of 1m.

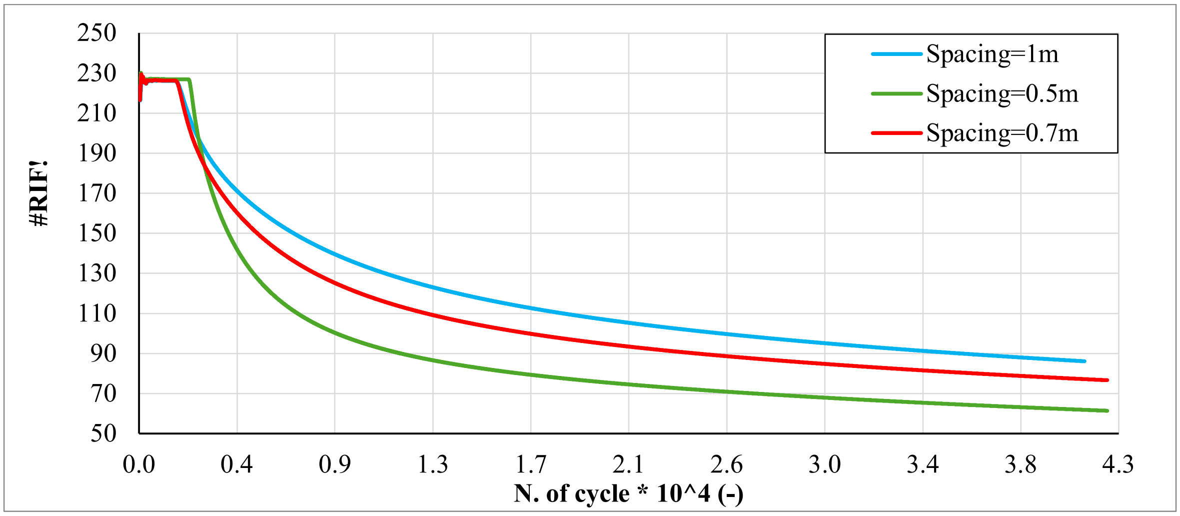

Figure 4.31 – Pore pressure variation after the activation of the drains-flow-only simulation.

4.5.3 Drainage HM coupled simulation

The case of HM simulation, enlarges the range of variables to investigate, adding to the analysis of pore pressure variation, the effective stress and consequently the bulk modulus. Especially from the evolution of effective stress is possible to compute the undrained shear strength thanks to Equation 1.13 (§1.1.3) for short-time stability aspects, which characterize the safety of the advancement.

In addition, the aspects considered in the previous paragraph can be compared with the HM simulation, allowing to appreciate the difference between the two types of simulation.

As for the previous paragraph (§4.5.1), the two types of sections (DD and DE) were compared for the most important variables such as pore pressure, mean effective stress and bulk modulus, at different distances to investigate the effects on the space. Then in the next sections (§4.5.3.1) the effects of the spacing were studied quantitatively.

Particularly, section DE reported in Figure 4.32, shows the interaction between the central portion of the region and the lateral element, with a reduction of pore pressure pore pressure around 140kPa(Figure 4.33), and an interaction between the two drains that creates a zone at equal pore pressures.

Then, section DD was analysed and represented in Figure 4.34, where a higher reduction of pore pressure was recorded thanks to the central portion where the reinforcement system presents a drainage portion as previously described in the technical section(§3.2.1).In this case, the interaction is stronger thanks to the reduced spacing allowing faster decrease of pore pressure appreciable in Figure 4.35.

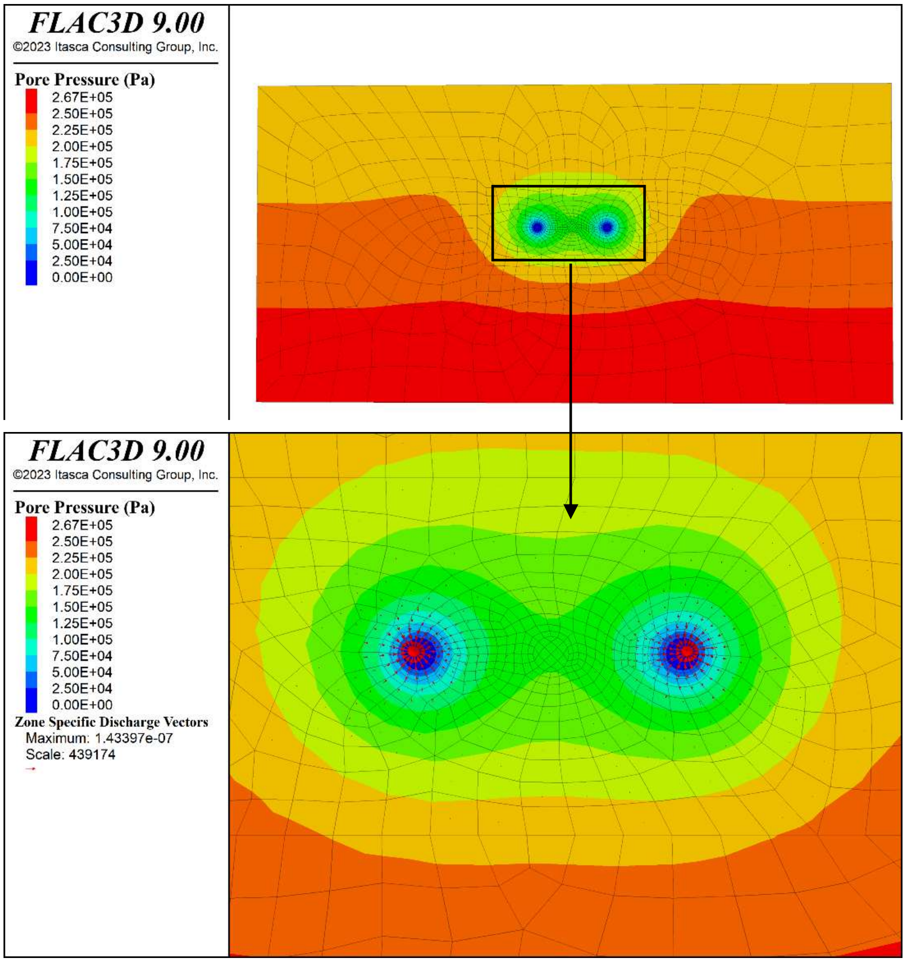

Figure 4.32 - Pore pressure contour at the end of calculation process in sections DD for HM coupled simulation.

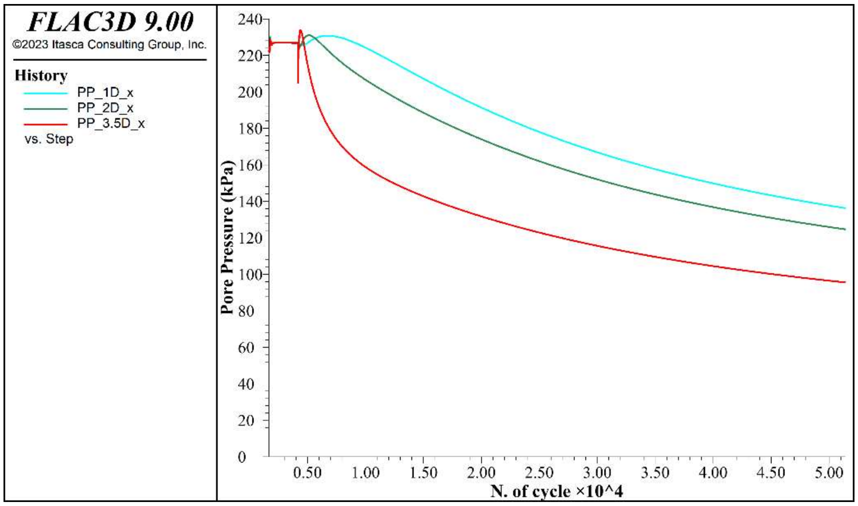

Figure 4.33 - Pore pressure variation at different distances from the centre for section DD.

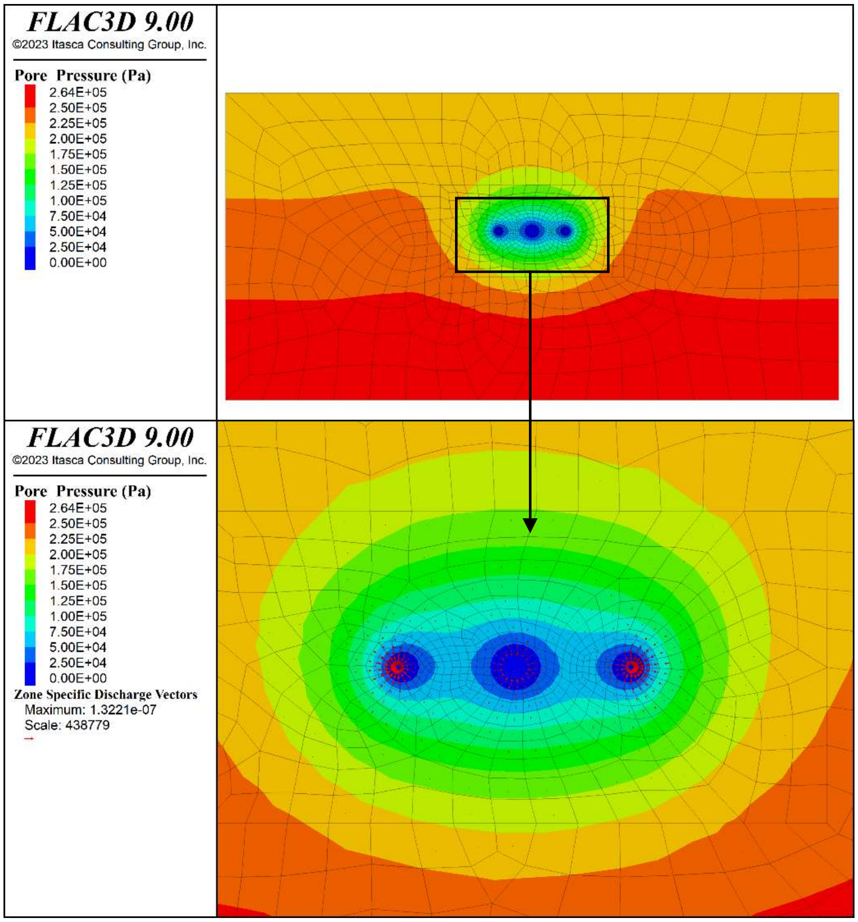

Figure 4.34 - Pore pressure contour at the end of calculation process in sections DE for HM coupled simulation.

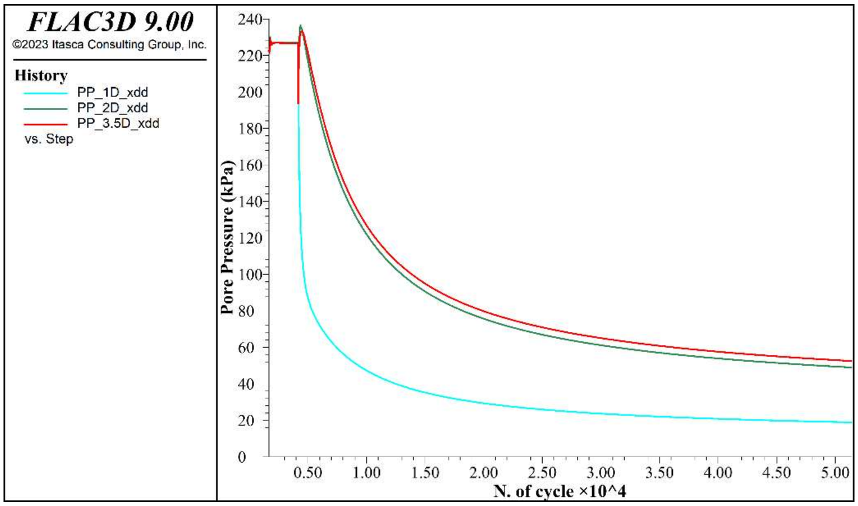

Figure 4.35- Pore pressure variation at different distances from the centre for section DE.

The mean effective stress increment and the associated area of influence for sections DD are represented in Figure 4.36, where is possible to note that in the area around the drain higher values of mean effective stress are present, but remain limited. The quantitative variation for different distances is reported in Figure 4.37.

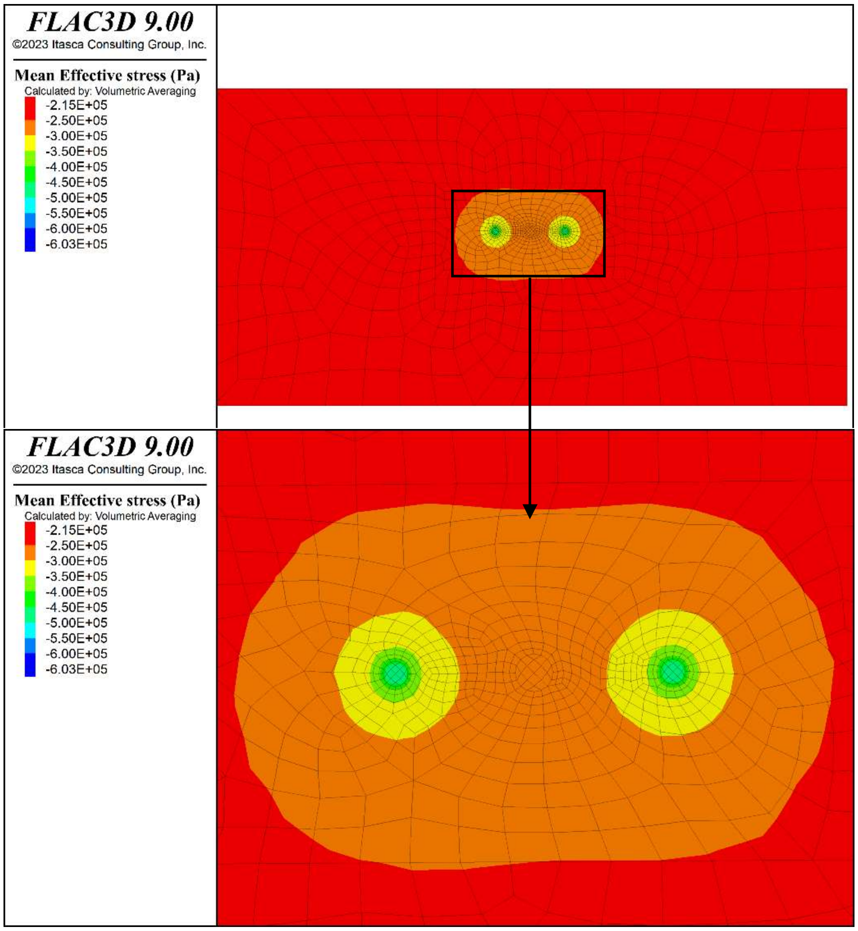

Figure 4.36 – Mean effective stress contour at the end of calculation process in sections DD for HM coupled simulation.

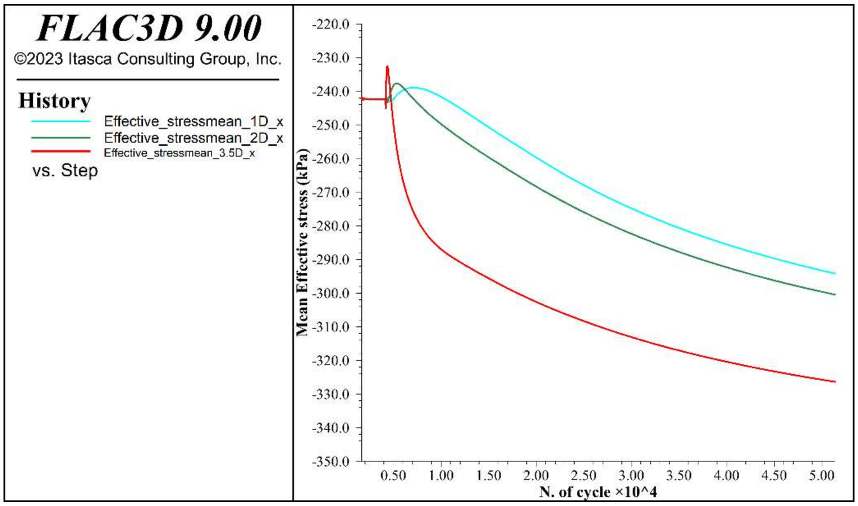

Figure 4.37 – Mean effective stress variation at different distances from the centre for section DD.

The mean effective stress increment and the associated area of influence for sections DE is represented in Figure 4.36, where the area of stress rise is not only around the drain but a diffuse zone is created thanks to the interaction between drains, which allows the creation of spread consolidated zone. The quantitative variation for different distances is reported in Figure 4.39.

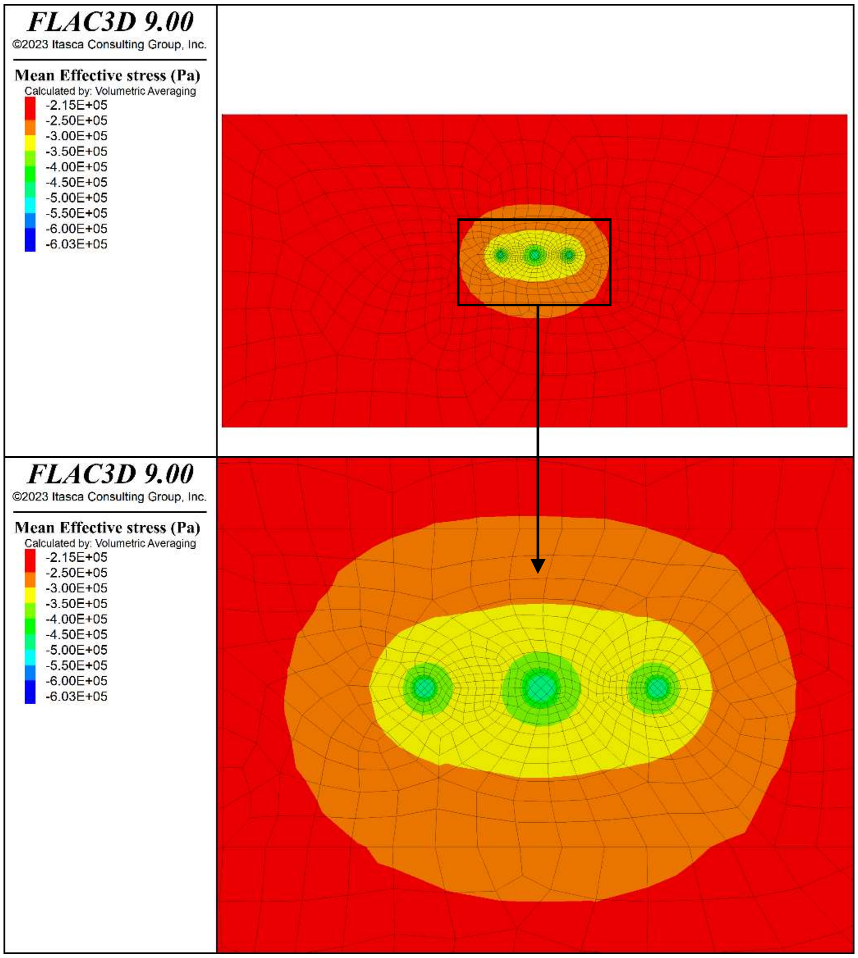

Figure 4.38 - Mean effective stress contour at the end of calculation process in sections DE for HM coupled simulation.

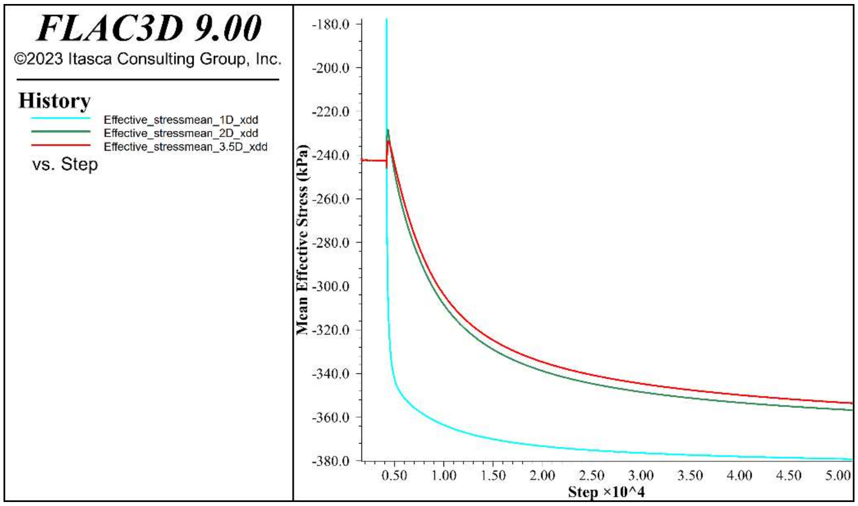

Figure 4.39 - Mean effective stress variation at different distances from the centre for section DE.

The bulk modulus growth and the associated area of influence for sections DE are represented in Figure 4.40, where the area of bulk modulus rise presents a reduced spreading in the central zonebut and a higher diffusion in the regions close to the drains. The quantitative variation for different distances is reported in Figure 4.41.

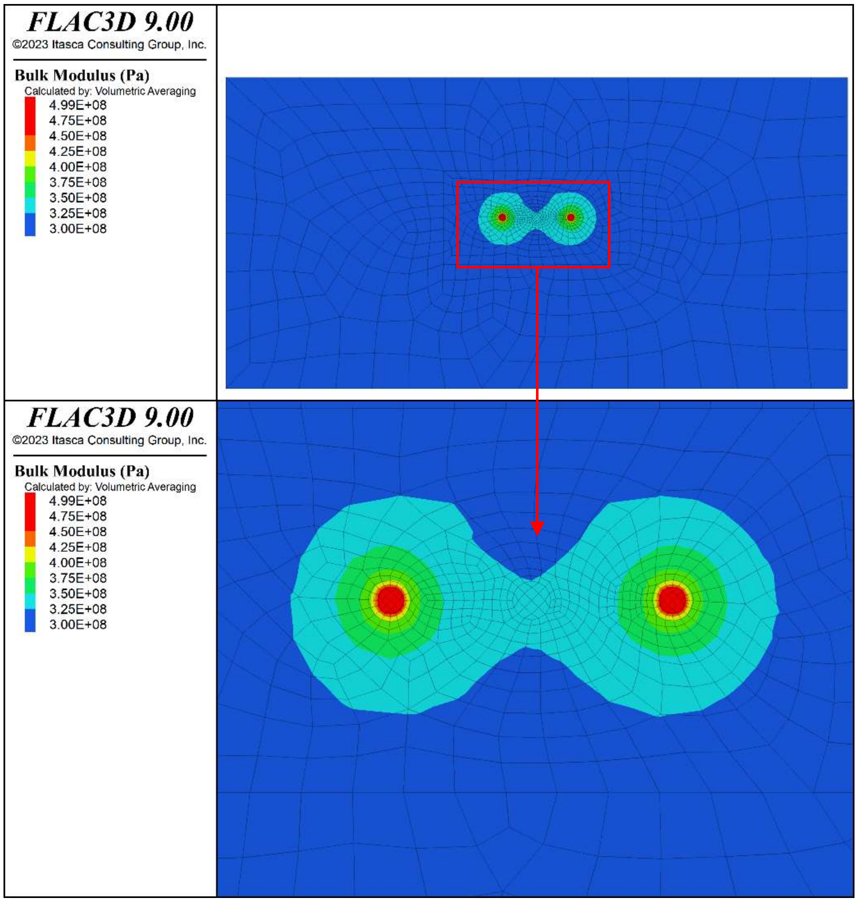

Figure 4.40 – Bulk Modulus contour at the end of calculation process in sections DD for HM coupled simulation.

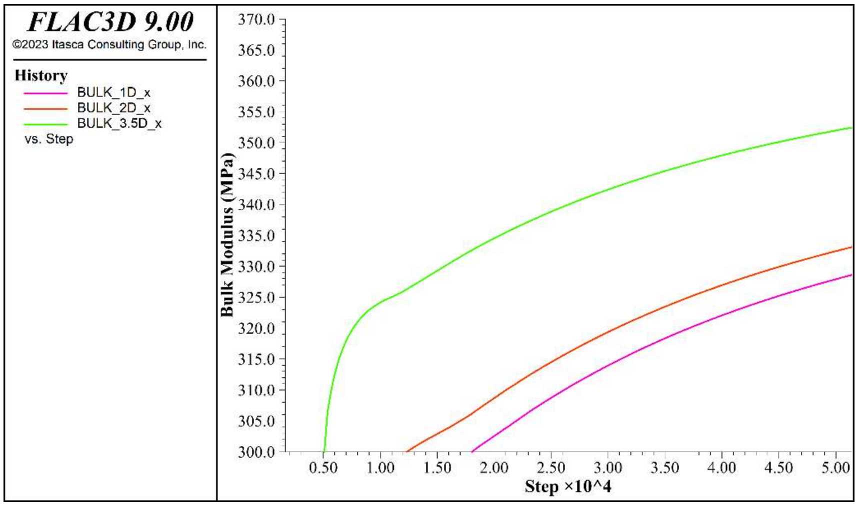

Figure 4.41 – Bulk modulus variation at different distances from the centre for section DE.

The bulk modulus growth and the associated area of influence for sections DD are plotted in Figure 4.42, where the area of bulk modulus rise is spread creating an enlarged consolidated strip. The quantitative variation for different distances is reported in Figure 4.43.

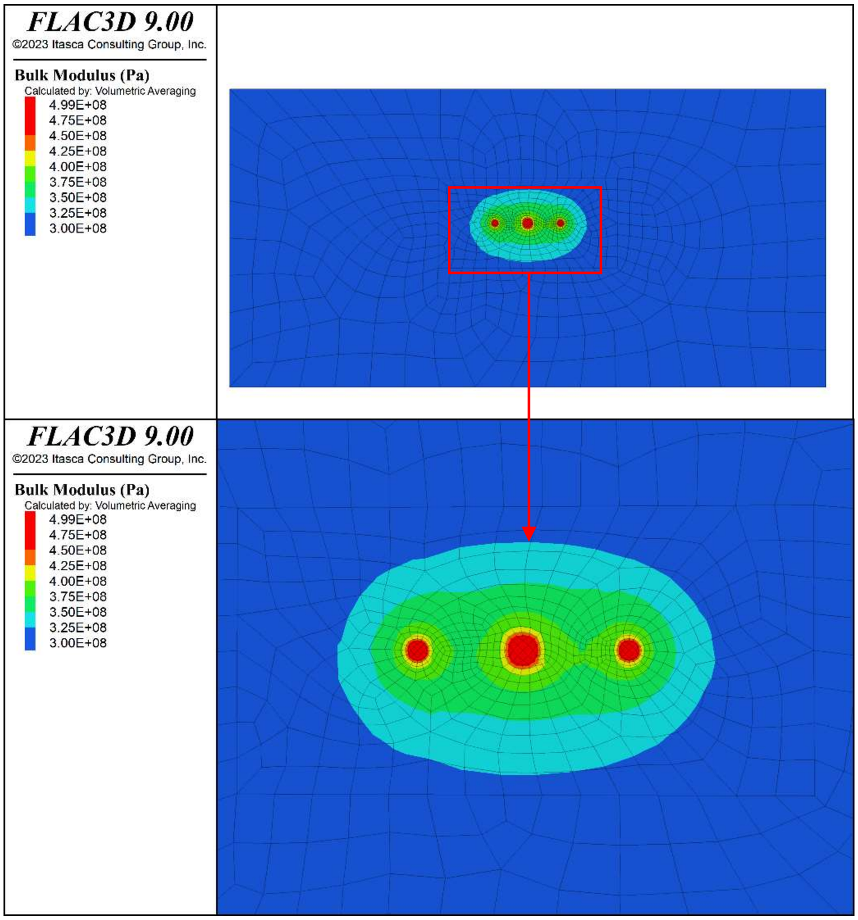

Figure 4.42 - Bulk Modulus contour at the end of calculation process in sections DD for HM coupled simulation

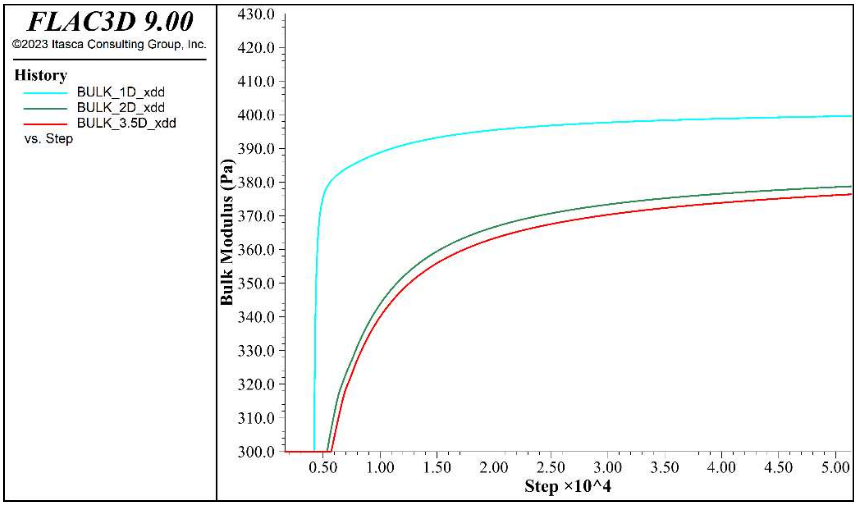

Figure 4.43 - Bulk modulus variation at different distances from the centre for section DE.

4.5.3.1 Effects of spacing

In order to streamline the studying process for different variables, the following section will compare the variations of pore pressure, mean effective stress, bulk modulus and undrained shear strength in the midpoint between the elements for different spacing values. In order to maintain the same reference position and observe what happens over time.

The analysis regarding the pore pressure evolution was carried out again for the case of HM coupled analysis for all the spacing cases and was plotted in Figure 4.44.

The pore-pressure reduction was bigger for the lower spacing (0,5m), confirming the previous result of the hydraulic simulation, however, the rate of reduction shows lower values suggesting a slower process, indeed for the same number of cycles performed by the software the final value of pore pressure was higher respect the hydraulic simulation. The reason for this result is related to the stiffness of the two matrices, the fluid and the soil.

The final value of water pressure was 125 kPa (**Δu=100kPa**), while for spacing of 0.7m the value reached was around 155kPa (**Δu=70kPa**), for the larger spacing the reduction reached 170 kPa(**Δu=55kPa**).

Considering the percentage of reduction which helps to normalize the results and transpose it with other interventions or cases, the reduction of pore pressure was 45% for the spacing of 0,5m, 32% for spacing of 0,7m and 26% for the larger spacing of 1m.

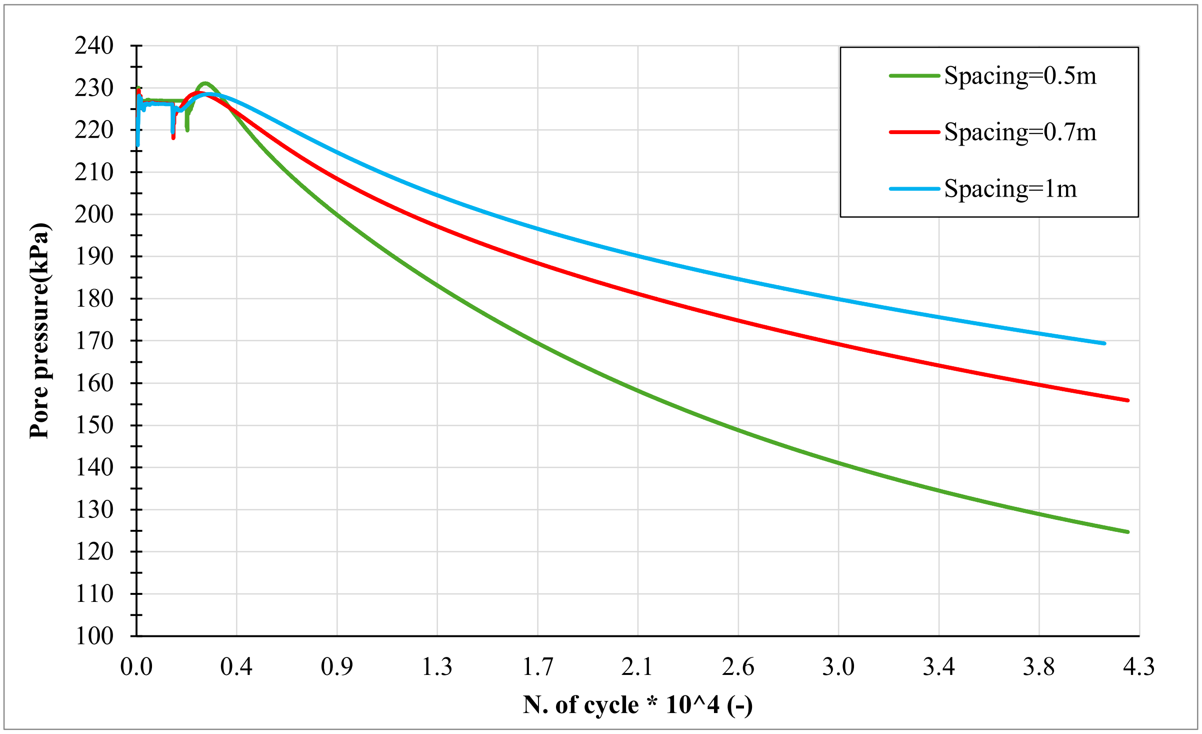

Figure 4.44 - Pore pressure variation after the activation of the drains HM simulation.

The analysis regarding the mean effective stress variation was carried out for all the spacing cases and was plotted in Figure 4.45.

The rate of mean effective stress rise was bigger for the lower spacing (0,5m), in accordance with the pore-pressure variation, while for the other two spacing cases, the mean effective stress variation showed a lower raise, coherently with what has been analysed until now.

The final value of mean effective stresses was 300 kPa (**$\Delta\sigma'_{mean}$[‡‡]= 55kPa**), for spacing=0.5m, while for spacing of 0.7m the value reached was about 281 kPa (**$\Delta\sigma'_{mean}$= 36kPa**), for the larger spacing showed reduction until 275 kPa (**$\Delta\sigma'_{mean}$= 30 kPa**).

Considering the percentage of reduction which helps to normalize the results and transpose it with other interventions or cases, the increase of mean effective stress was 22% for the spacing of 0,5m, 15% for spacing of 0,7m and 12% for the larger spacing of 1m.

[‡‡] $\Delta\sigma'_{mean}$ = Absolute difference between final and initial mean effective stress.

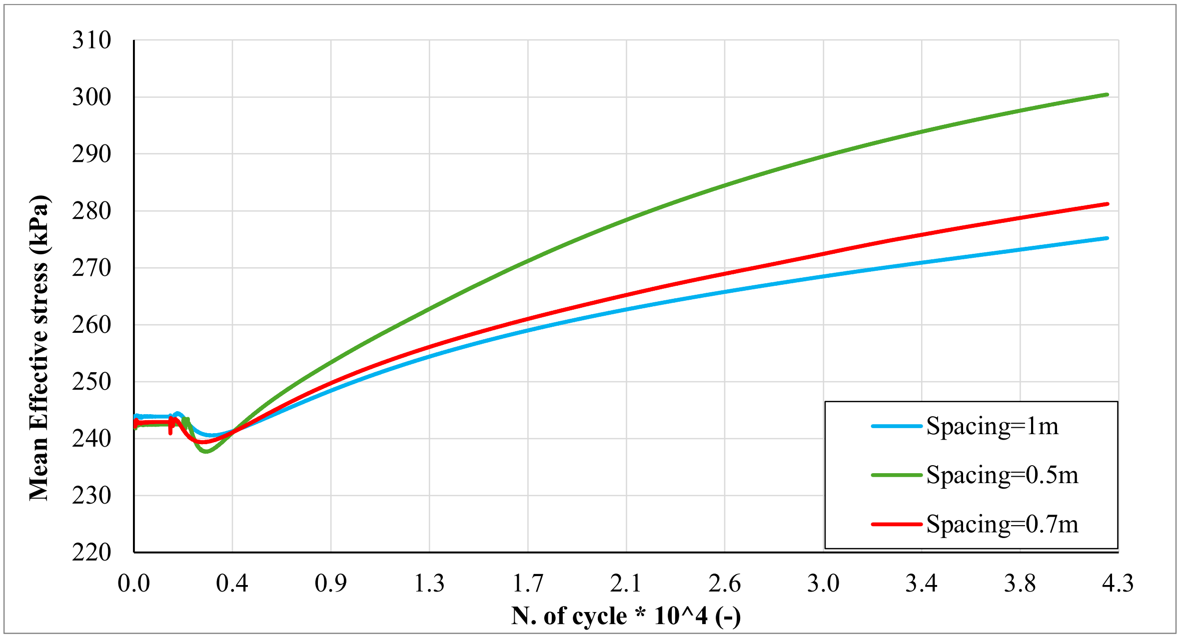

Figure 4.45 - Mean Effective stress variation after the activation of drains.

4.5.3.2 Coupled variation of pore-pressure and effective stress

In the previous paragraph (§4.5.3), the variation of pore pressure and effective stresses was analysed singularly considering the evolution of the two variables independently, however, the analysis performed illustrated that the variation for the pore pressure evolves more faster respect the mean effective stresses, indeed if the variation between initial and final state is considered for the smaller spacing, the $\Delta\sigma'_{mean}$= 55kPa while Δu=100kPa.

This difference highlights the distinction in rates of change of the two quantities over the process evolution, specifically, the mean effective stress variation is delayed concerning the water pressure.

The evidence of what has been discussed can be observed in Figure 4.46 where the coupled variation of ***u*** and $\boldsymbol{\sigma'_{mean}}$ for the three spacing cases was shown.

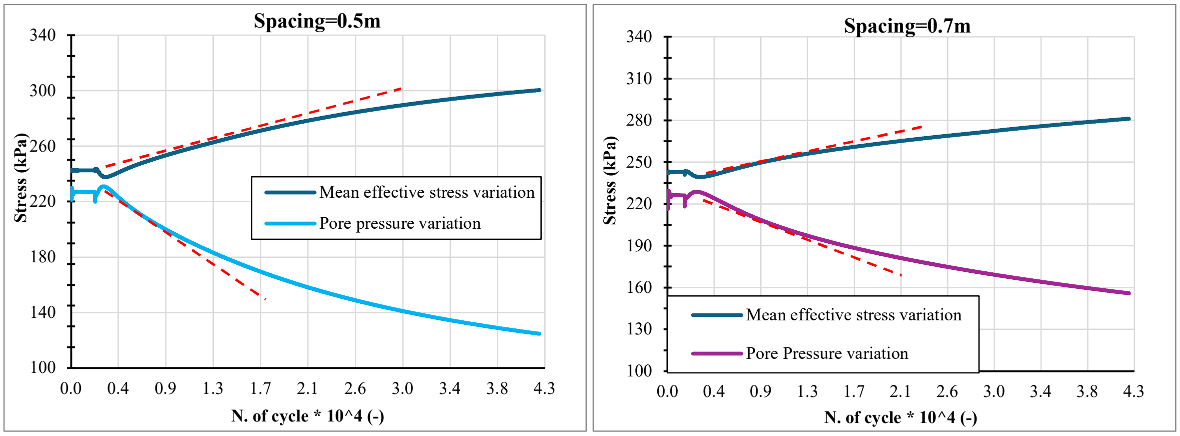

a) *b)*

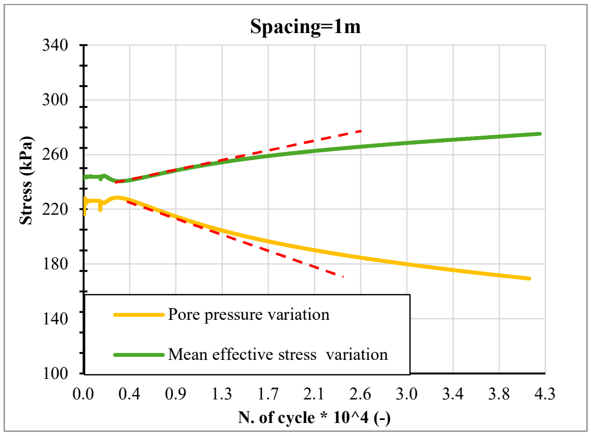

c)

Figure 4.46 – A coupled variation of Pore pressure and effective mean stress during the drain activation for the three spacing cases: a) Spacing=0.5m; b)Spacing=0.7m; c) Spacing=1m. (dashed red line = tangent of the first portion)

An interesting aspect regarding the three cases is that for lower spacing the correspondence between Δu - $\Delta\sigma'_{mean}$ is lower, while for increasing spacing the correspondence is higher with a less delayed process. This can be noted in the first portion of the curves in Figure 4.46, where the initial curvature of pore pressure curve (light blue) and mean effective stress (dark blue) presents a pronounced difference for spacing=0.5m, while almost the same curvature for the spacing=1m.

4.5.3.3 Variation of Undrained Shear Strength

The quantification of the undrained shear strength was carried out by using Ladd's equation (Eq. 1.13 (§1.1.3)), which is related to three parameters **c'**, **φ** and **p'_0**, particularly the parameter over which the intervention acts is the isotropic mean stress (**p'_0**) that in the case analysed correspond to the mean effective stress due to the isotropic state of stress related to K_0=1.

The initial undrained shear strength C_u before starting any intervention is estimated equal to 80kPa, and consequent evolution was plotted in Figure 4.47.

The comparison between the three different spacing conditions shows the bigger effects on the small spacing (0.5m) with a final value of C_u = **99** kPa, the intermediate conditions (0.7m) with a final value of C_u = **93** kPa and the largest setting (1m) with C_u = **91** kPa.

Considering the percentage of increment which helps to normalize the results and transpose it with other interventions or cases, the C_u raise was 25% for the spacing of 0,5m, 16% for spacing of 0,7m and 13% for the larger spacing of 1m.

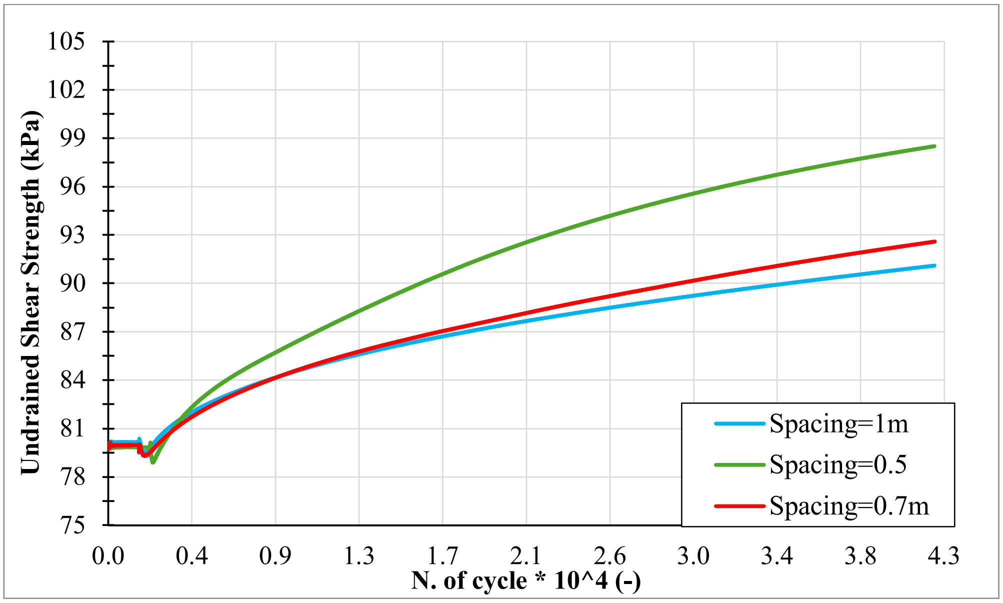

Figure 4.47- Undrained shear strength after drains' activation

4.5.3.4 Variation of Bulk Modulus

The volumetric stiffness of the soil at the initial stage, before the application of any intervention is computed automatically by the software from input parameters reported in Table 4.1 by use of Eq. 4.7 and correspond to a K=300MPa.

The comparison between the three different spacing conditions was plotted in Figure 4.48, where for the small spacing (0.5m) the final value was ***K* = 380** MPa, the intermediate conditions (0.7m) shows a **K = 360** kPa and the largest setting (1m) with ***K* = 344** kPa.

Considering the percentage of increment which helps to normalize the results and transpose it with other interventions or cases, the **K** growth was 27% for the spacing of 0,5m, 20% for spacing of 0,7m and 15% for the larger spacing of 1m.

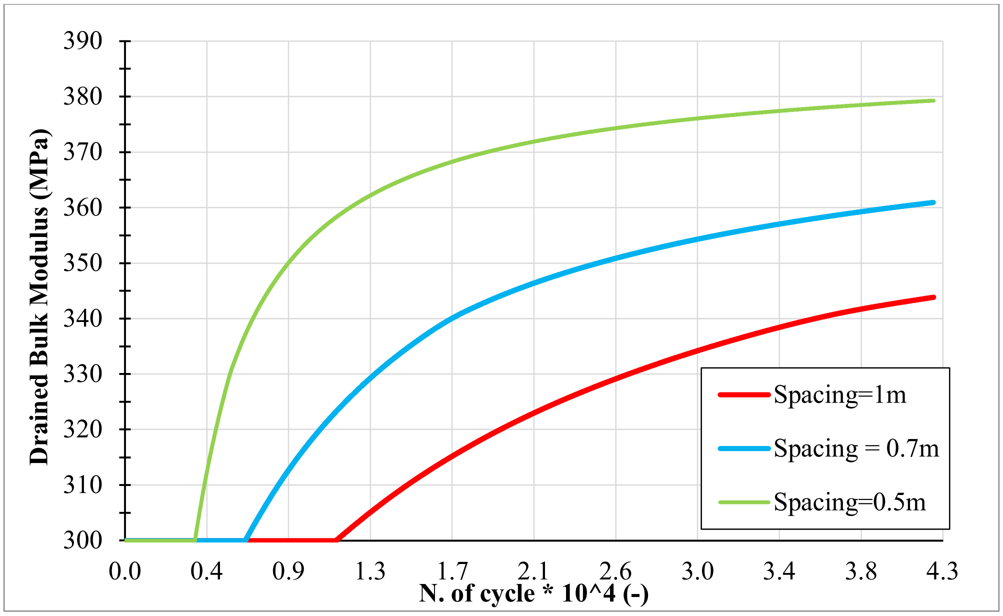

Figure 4.48 – Bulk modulus variation after application of drains

4.5.4 Simulation of the combined system

The final aspect analysed was the effects of the compression performed by the pressurized reinforcement. This allows to make the comparison between the improvement with only drainage (discussed in §4.5.3) and the one with drainage + compression.

An important aspect to be highlighted concerning the study performed in the previous paragraph (§4.5.3) was the fact that section DD was discarded in the study of the following pages due to the similarity in the results with the one already discussed, and so to avoid a repetition only the section DE is exposed.

The first aspect investigated was the pore pressure evolution and as a preliminary step its variation was plotted in Figure 4.49, where the contour with the same value of pressure is quite similar to the one in Figure 4.32. As done before, the evolution of pore pressure at different distances over time is reported in Figure 4.50.

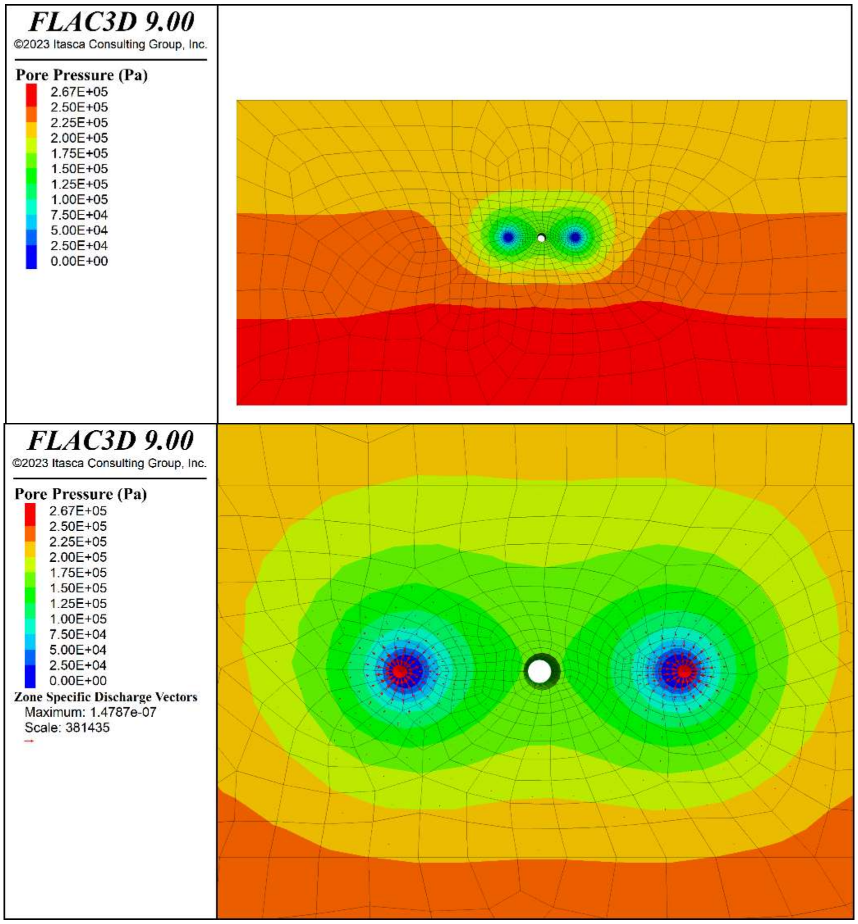

Figure 4.49 - Pore pressure contour at the end of calculation process in sections DD in case of expansion.

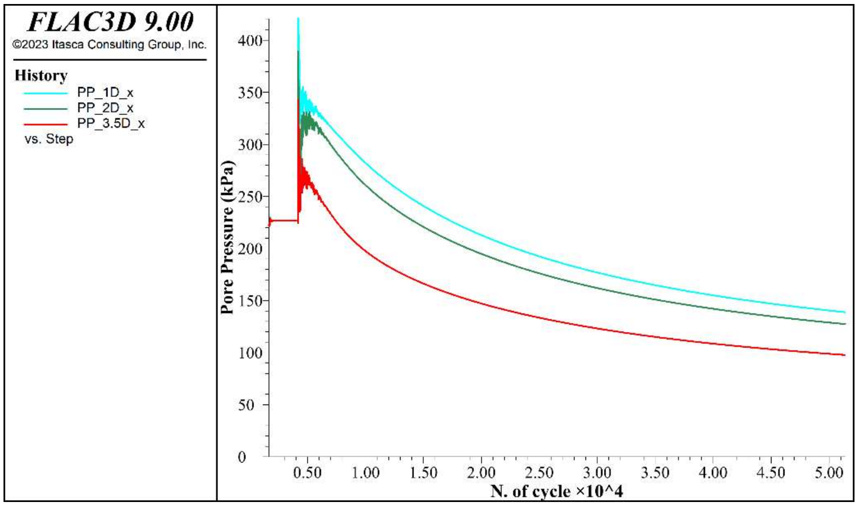

Figure 4.50 - Pore pressure variation at different distances from the centre for section DD.

The second variable addressed was the mean effective stress and the associated area of influence in Figure 4.51, where is possible to note that a diffuse strip with higher mean effective stress(yellow zone) is present, and in the surrounding of the central zone (pressurized portions) the value of mean effective stress is higher respects the one in Figure 4.36. The quantitative variation for different distances from the centre is reported in Figure 4.37, where the initial portion of the curves presents an instability connected to the instantaneous application of the pressure that creates a perturbation in the system for a limited number of cycles.

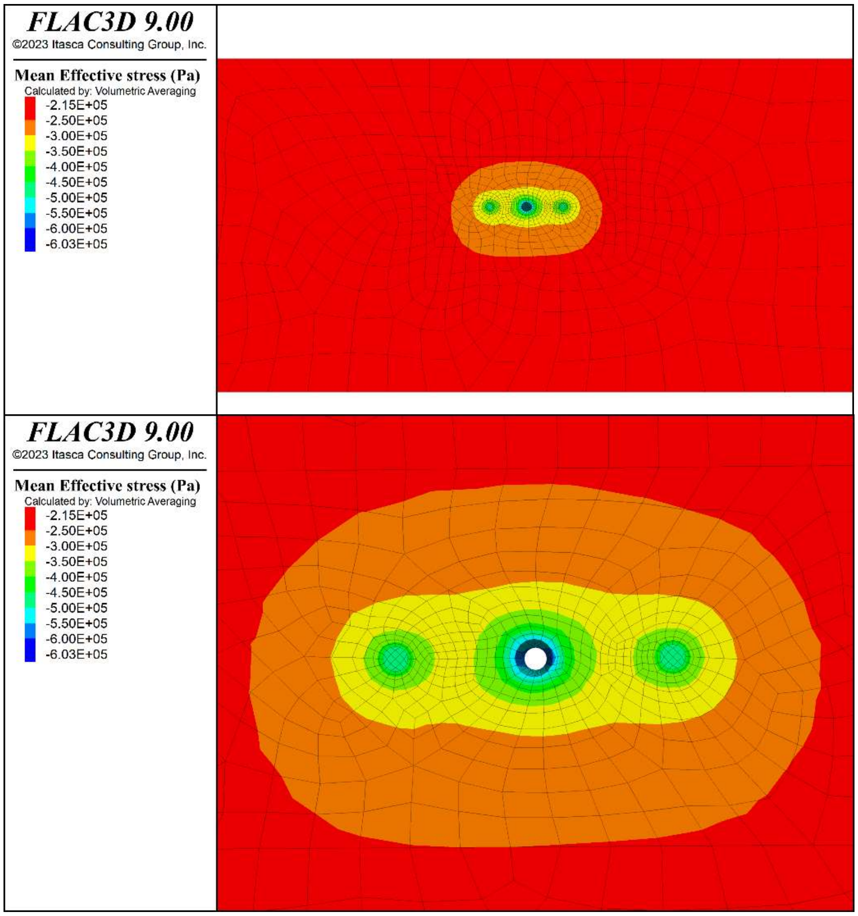

Figure 4.51 - Mean effective stress contour for section DD in case of expansion.

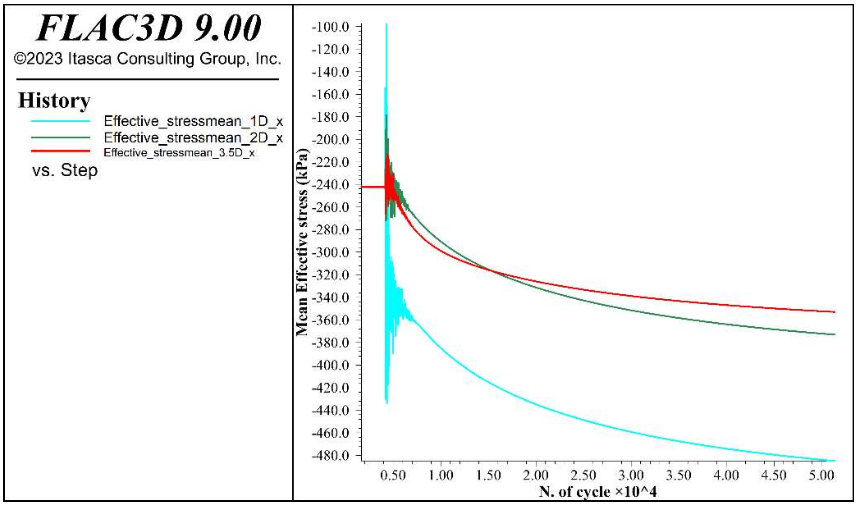

Figure 4.52 - Mean effective stress variation at different distances from the centre for section DD in case of expansion.

The bulk modulus growth and the associated area of influence for sections DD is represented in Figure 4.53, where in addition to the case in Figure 4.40, the surrounding of the central pressurized circular zone presents a restricted portion with further increase of bulk modulus. The quantitative variation for different distances is reported in Figure 4.41.

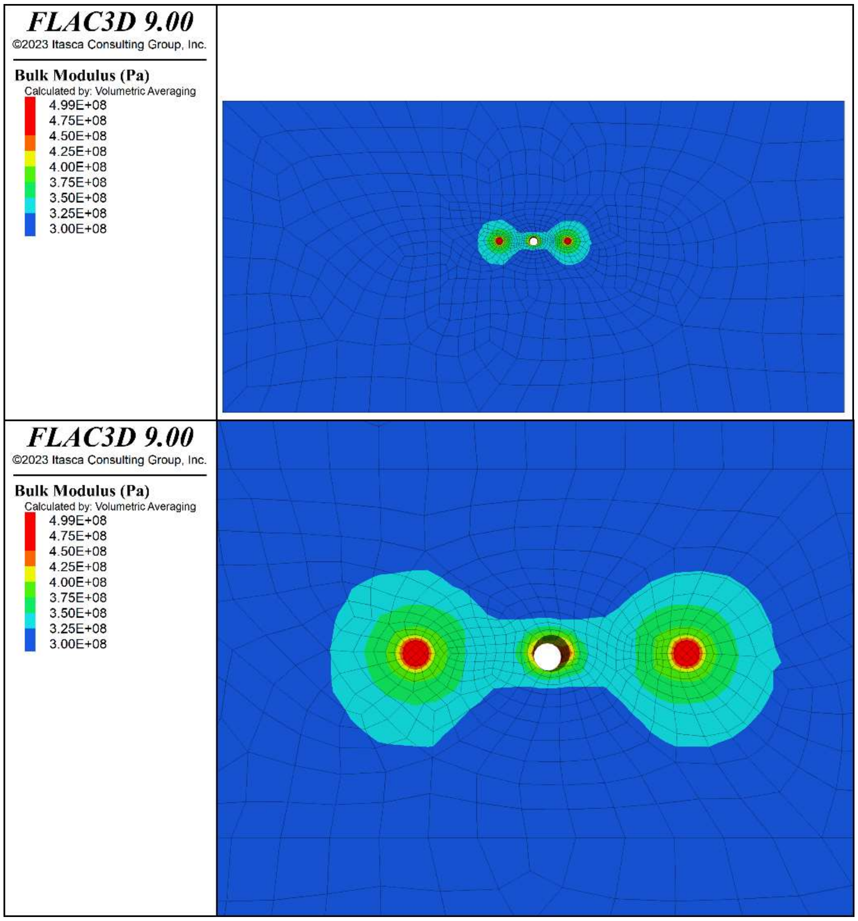

Figure 4.53 - Bulk Modulus contour at the end of calculation process in sections DD in case of expansion.

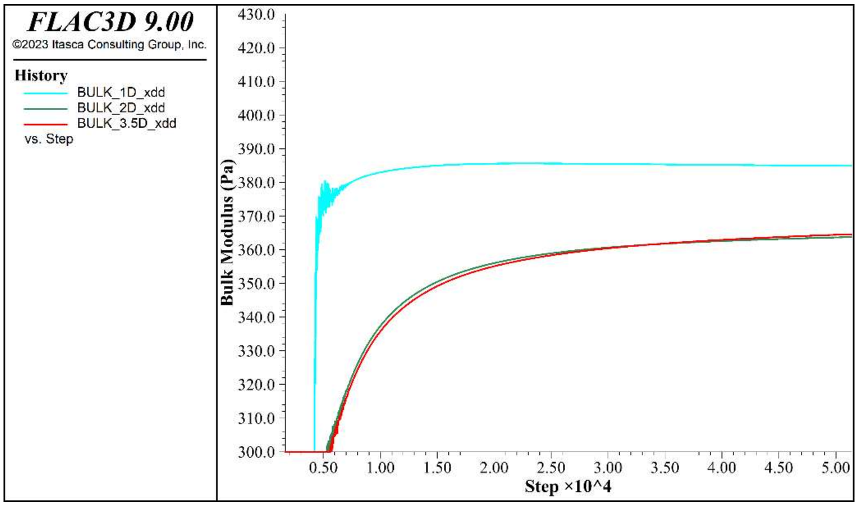

Figure 4.54 - Bulk modulus variation at different distances from the centre for section DE in case of expansion.

4.5.5 Effects of spacing

In order to facilitate the process of analysis and comparison of the different variables under study such as pore pressure, mean effective stress, bulk modulus and undrained shear strength. All of them were investigated in the midpoint between the elements for different spacing values, in order to create a sort of standardized analysis.

This paragraph focuses attention on the comparison of pore-pressure variation for the case where the expansion was simulated and three different spacing: 0.5m, 0.7m and 1m (Figure 4.55).

In this case, from the results of the software, a sudden rise is visible in the initial phase of the model corresponding to the application of the pressure in the central cavity. Then after the initial sudden rise, the pore pressure started to decrease reaching 176 kPa (**Δu=50kPa**) for spacing of 1m, 162 kPa (**Δu=63kPa**) for spacing of 0.7m and 126kPa(**Δu=100kPa**) for 0.5m.

Turning the results in terms of percentage, the reduction of water pressure was 43% for the spacing of 0,5m, 28% for spacing of 0,7m and 22% for the larger spacing of 1m.

An important aspect affecting the initial increase due to the pressurized reinforcement is the effect of the spacing, indeed by using larger spacing the first portion of abrupt rise is reduced until a few tens of kPa for the larger spacing of 1m.

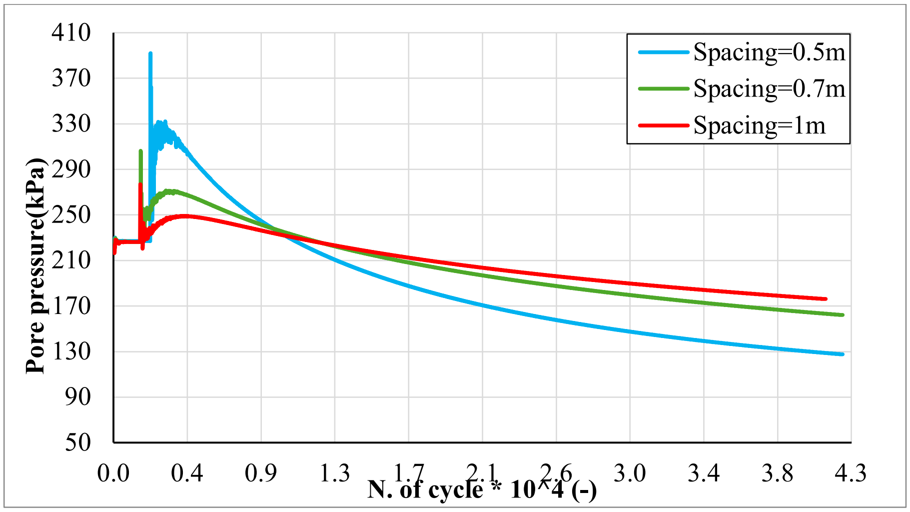

Figure 4.55 – Pore pressure variation after the activation of the drains and expansion zone.

The analysis regarding the mean effective stress variation was carried out for all the spacing cases and was plotted in Figure 4.56.

The final value of mean effective stresses was 373 kPa (**$\Delta\sigma'_{mean}$= 128kPa**), for spacing=0.5m, while for spacing of 0.7m the value reached was about 316 kPa (**$\Delta\sigma'_{mean}$= 71kPa**), for the larger spacing showed a reduction until 275 kPa (**$\Delta\sigma'_{mean}$= 50 kPa**).

Considering the percentage of reduction which helps to normalize the results and transpose it with other interventions or cases, the increase of mean effective stress was 52% for the spacing of 0,5m, 29% for spacing of 0,7m and 20% for the larger spacing of 1m.

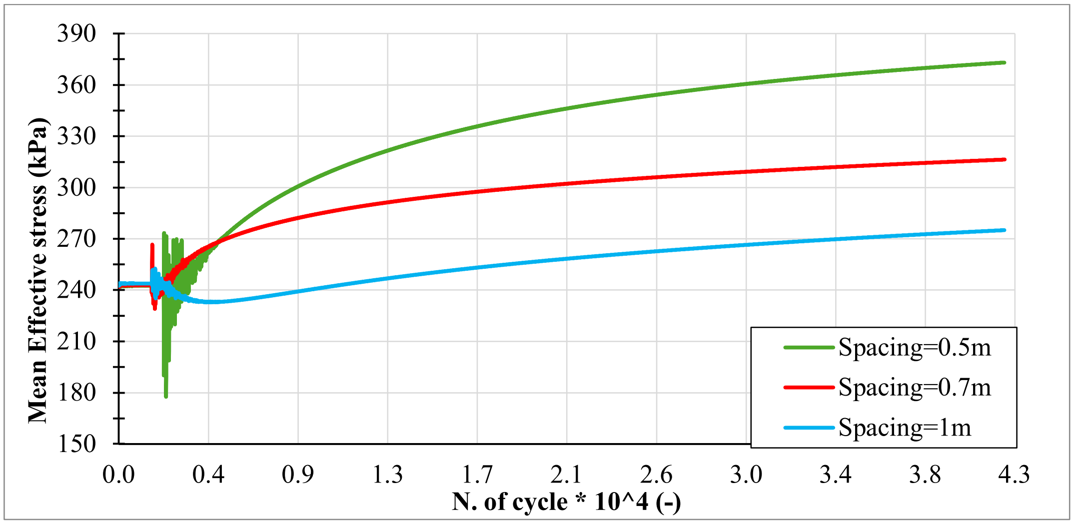

Figure 4.56 – Mean Effective stress variation after the activation of drains and expansion zone

4.5.5.1 Coupled variation of pore-pressure and effective stress

As done in the previous paragraph (§4.5.3.2), the variation of pore pressure and effective stresses was analysed jointly considering the coupled evolution of the two variables. In this case the variation of pore pressure evolves in the same way as the case without the pressurized reinforcement, but the increment of the mean effective stresses is higher bacuase the pressurized reinforcement induce an additional increment of mean effective stress with a variation $\Delta\sigma'_{mean}$ that exceeds the pore pressure decrease, practically $\Delta\sigma'_{mean} > \Delta u$ and numerically the two variation assume the values of $\Delta\sigma'_{mean}$= 128kPa and Δu=100kPa.

The consequence of these results is: firstly, that the pore pressure dissipation takes the same time and is not slowed, and secondly that the value of effective mean stress is higher with a strengthening of the soil.

In Figure 4.57 the coupled variation of pore pressure and mean effective stress is reported.

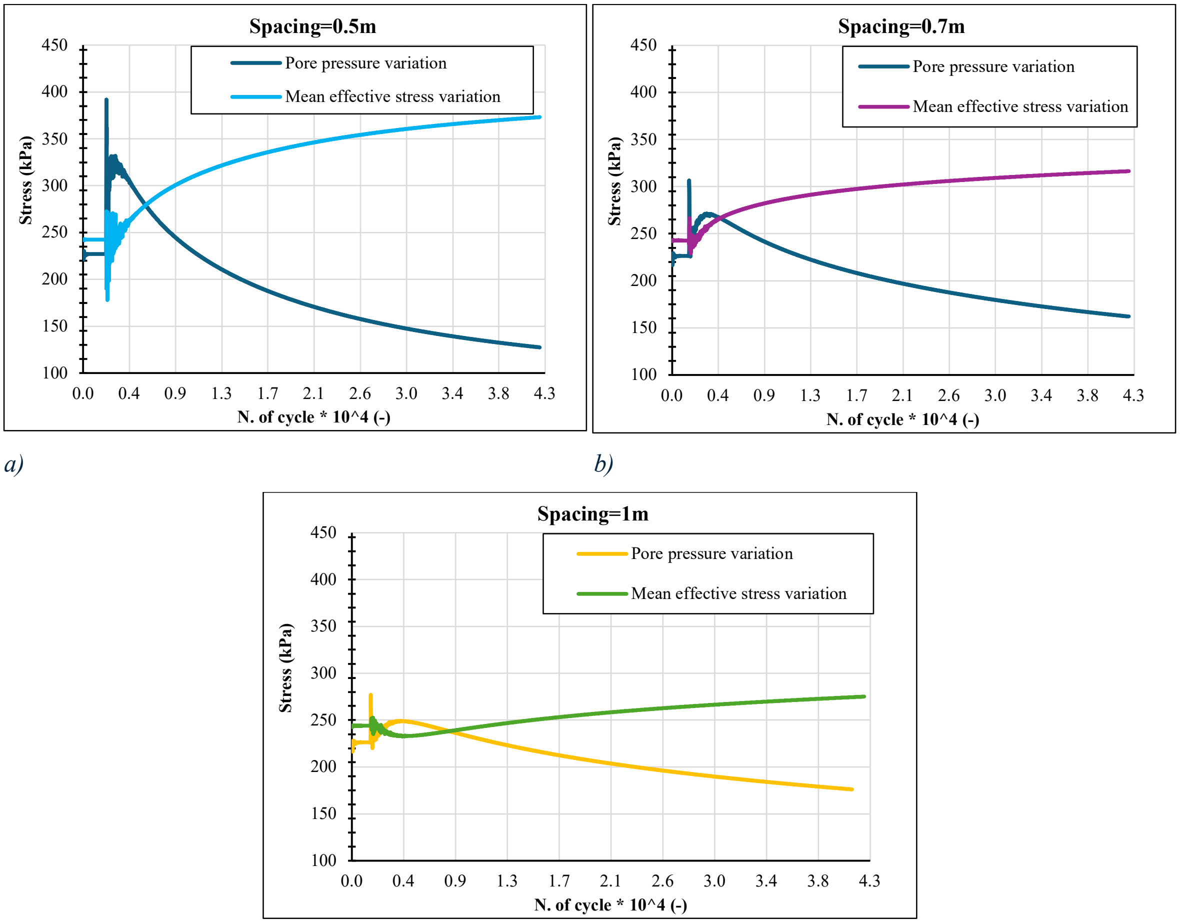

a)

b)

c)

Figure 4.57 - A coupled variation of Pore pressure and effective mean stress during the drain activation for the three spacing cases: a) Spacing=0.5m; b)Spacing=0.7m; c) Spacing=1m.

4.5.5.2 Variation of Undrained Shear Strength

The initial undrained shear strength C_u assumes the same value determined in the previous paragraph (§4.5.3.3) of 80kPa, while the consequent evolution after the intervention was plotted in Figure 4.58. The comparison between the three different spacing conditions shows the bigger effects on the small spacing (0.5m) with a final value of C_u = **126** kPa, the intermediate conditions (0.7m) with a final value of C_u = **100** kPa and the largest setting (1m) with C_u = **91** kPa.

Considering the percentage of increment which helps to normalize the results and transpose it with other interventions or cases, the C_u raise was 56% for the spacing of 0,5m, 25% for spacing of 0,7m and 13% for the larger spacing of 1m.

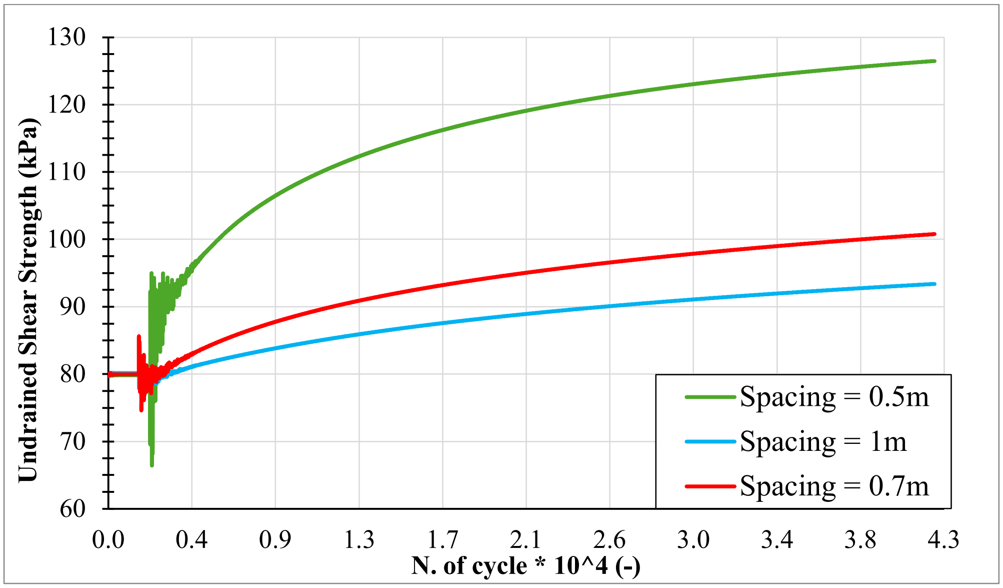

Figure 4.58 - Undrained shear strength after drains and pressurized reinforcement activation.

4.5.5.3 Variation of Bulk Modulus

The drained bulk modulus **K** assumes the same value determined in the previous paragraph (§4.5.3.4) of 300 MPa and the evolution for the three different spacing conditions was plotted in Figure 4.59, where for the small spacing (0.5m) the final value of was ***K* = 365** MPa, the intermediate conditions (0.7m) shows a **K = 350** kPa and the largest setting (1m) with ***K* = 336** kPa.

Considering the percentage of increment which helps to normalize the results and transpose it with other interventions or cases, the **K** growth was 21% for the spacing of 0,5m, 17% for spacing of 0,7m and 12% for the larger spacing of 1m.

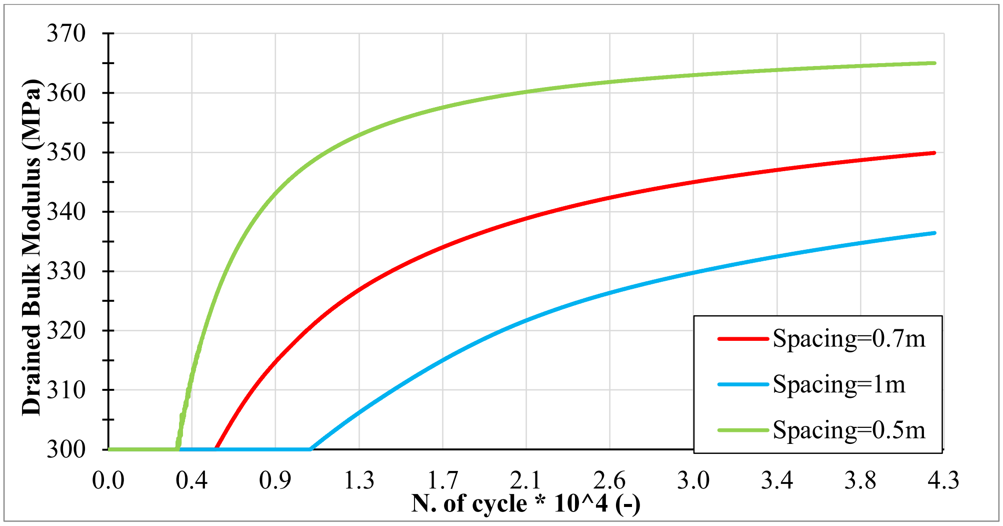

Figure 4.59 - Bulk modulus variation after application of drains and pressurized reinforcement.

4.6 Main results from consolidation type and spacing

This section summarizes the main findings derived in the previous paragraphs from the analysis of different spacing and consolidation methodologies (essentially with or without the pressurized reinforcement), trying to normalize the results obtained as a percentage of increase or decrease of the different variables of interest.

The first synthesis gives all the key features regarding the different effects of the improvement for the consolidation adopted considering a fixed intermediate spacing condition (0.7m).

In Figure 4.60 the comparison between pore pressure variation is reported for three cases, the first linked to the simulation of only hydraulic simulation, where the decrease is the fastest due to the computational process that ignores the mechanical features, while the variation for the “Drainage” and “Expansion + Drainage” after the same number of cycle presents comparable value, which practically means that the process takes the same time.

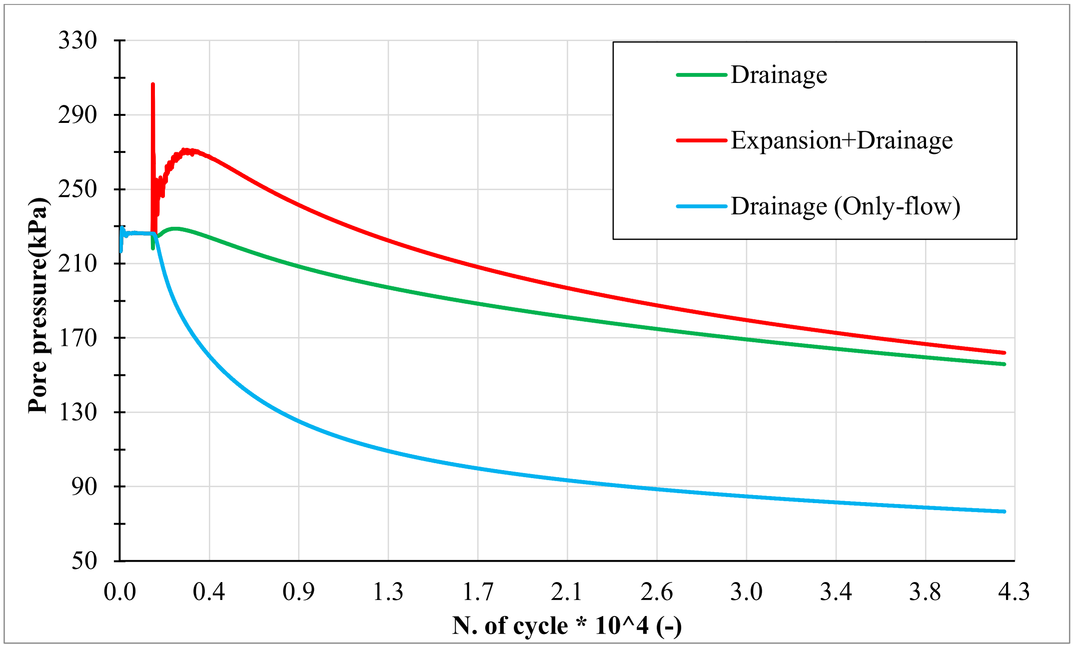

Figure 4.60 – Comparison of pore pressure variation between three different cases.

In Figure 4.61 the comparison shows that the final value of mean effective stresses is much higher leading to a higher stress state, transposed in Figure 4.62 with a higher undrained shear strength.

Taking into account the bulk modulus variation shown in Figure 4.63, the drainage shows better effects with respect to the drainage + expansion, leading to higher final values.

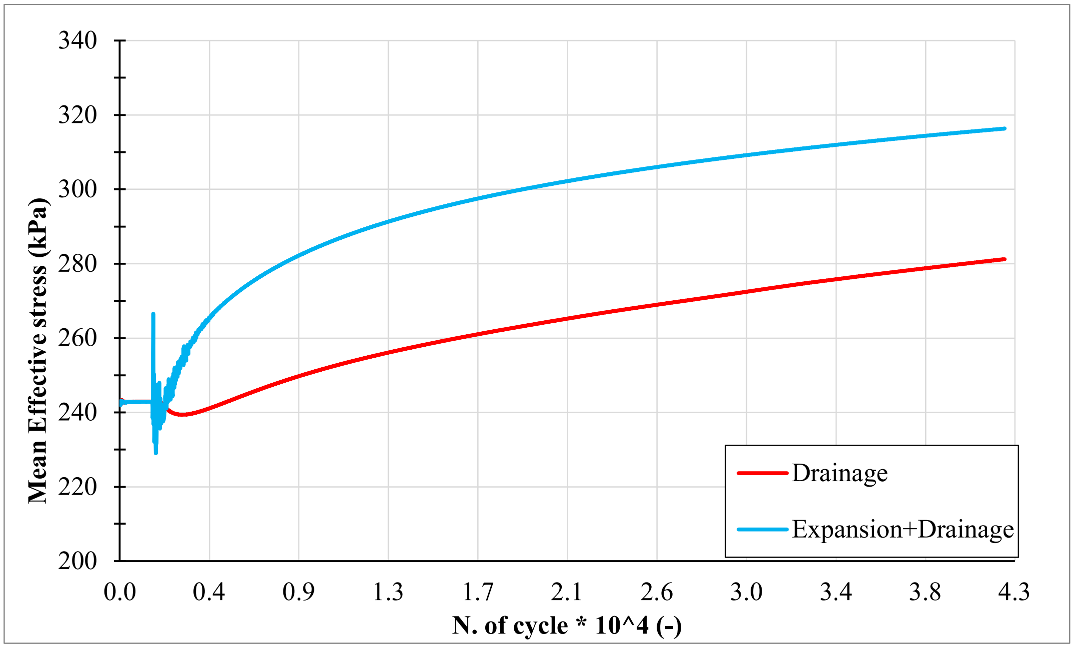

Figure 4.61 - Comparison of mean effective stress variation for two different conditions.

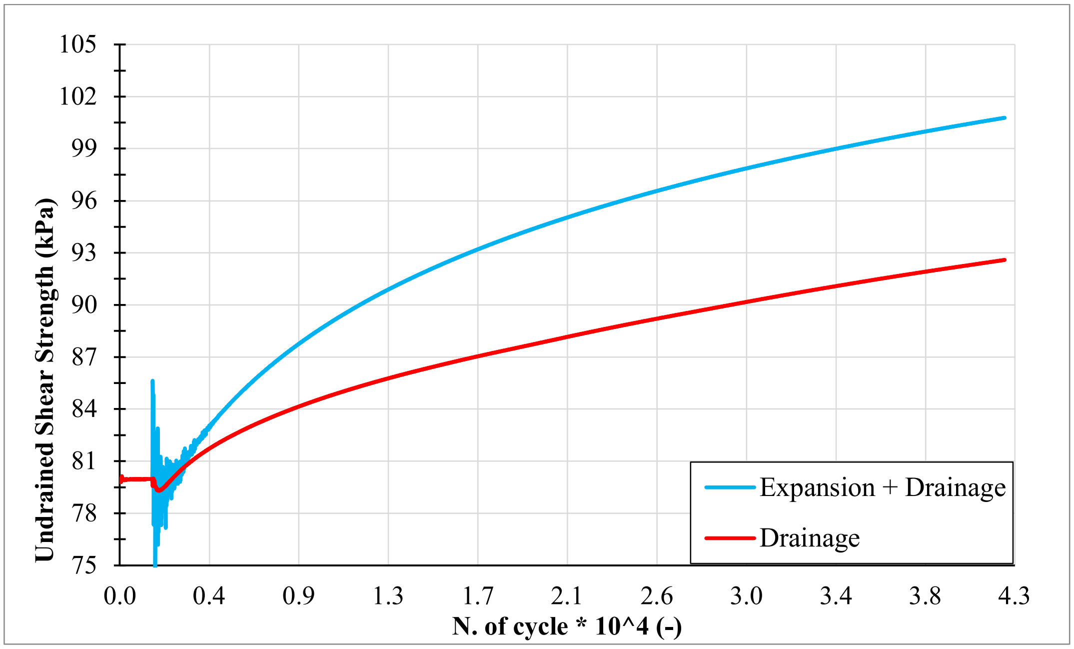

Figure 4.62 - Comparison of undrained shear strength variation for two different conditions.

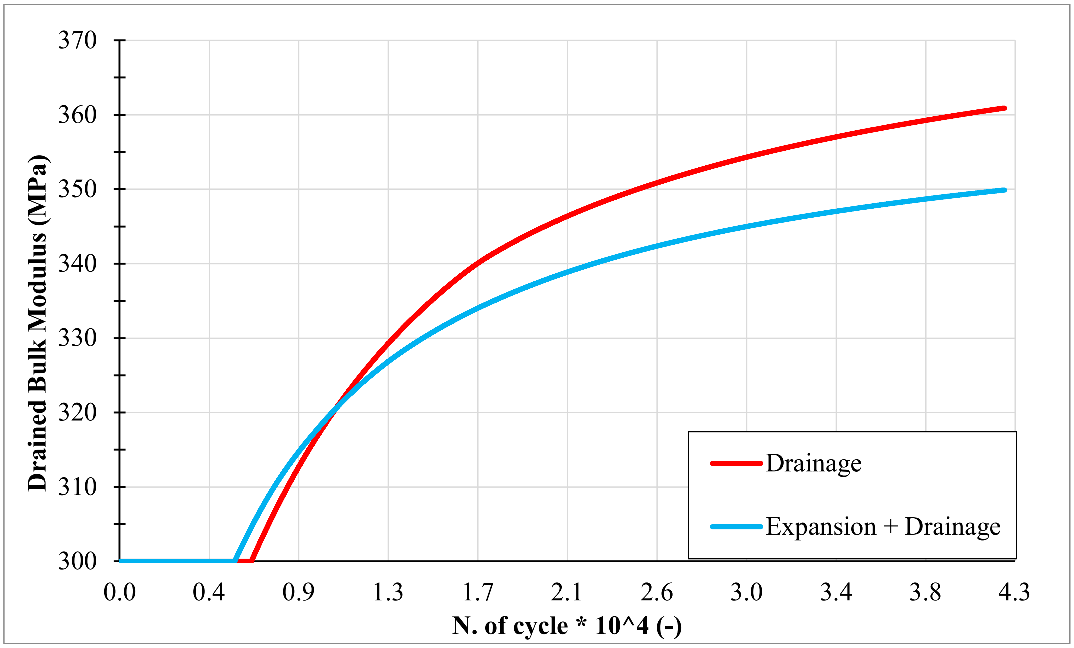

Figure 4.63 – Bulk Modulus variation for two different conditions.

After this initial comparison of different configurations, the effects of spacing are described and synthesized in the following graphs where the percentage of variables' variation is plotted for different spacing.

The decrease in terms of pore pressure lies around 20% for 1 m spacing but reaches about 45% for both cases if the spacing is 0,5m (Figure 4.64), with no significant difference between the two cases.

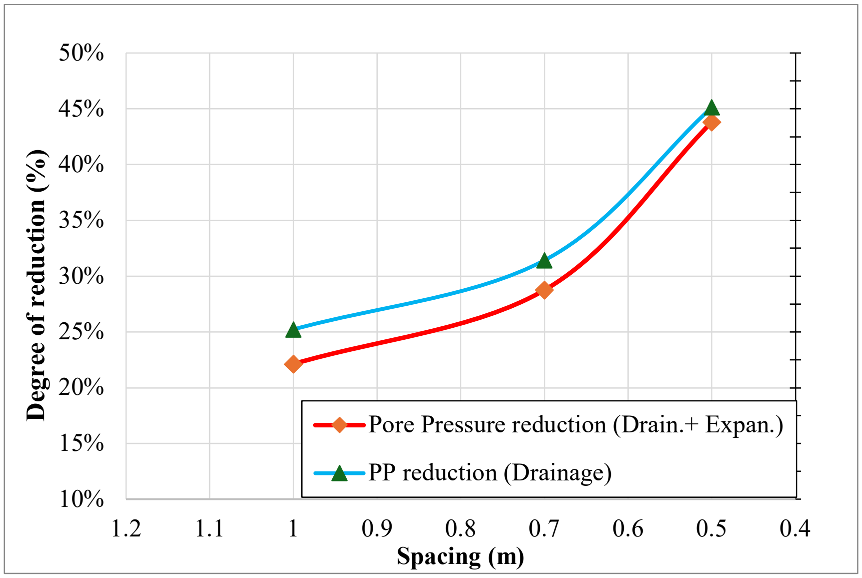

Figure 4.64 – Percentage of pore pressure decrease for two cases.

Looking at the increment of mean effective stress (Figure 4.65), the increment is much higher for "Drainage + Expansion" with about 60% for 0,5m spacing while for the drainage case, the increase stops at 25%.

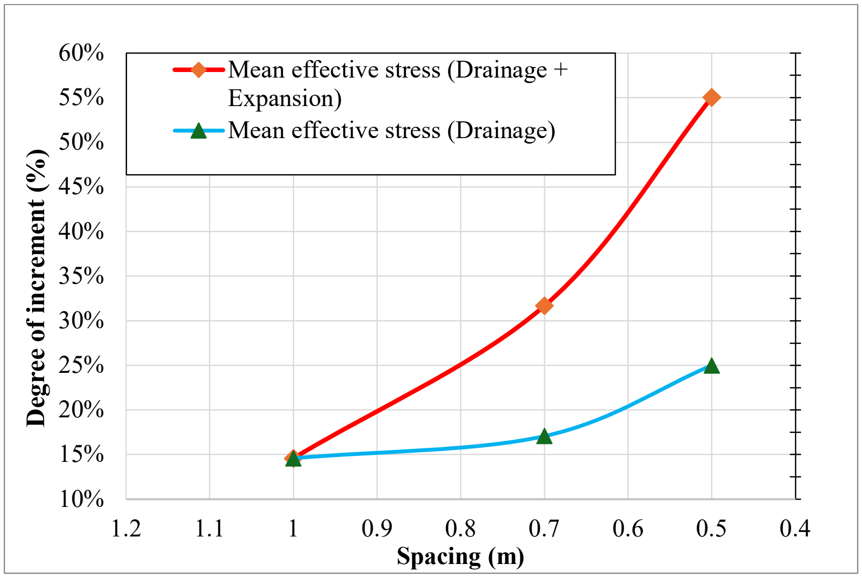

Figure 4.65 - Percentage of mean effective stress growth for two cases.

The rise in terms of **C_u** (Figure 4.66), lies around 15% for 1 m spacing but reaches about 59% for the case of "Drainage + Expansion" with a spacing of 0,5m (Figure 4.64), while by using only the drainage the maximum increase is no more than 25%.

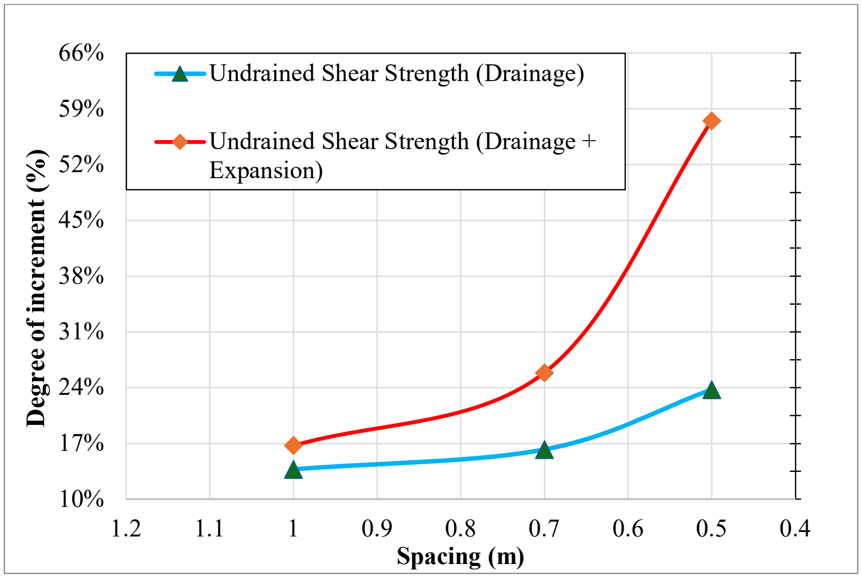

Figure 4.66 - Percentage of undrained shear strength growth for two cases.

Looking at the bulk modulus (Figure 4.65), the mean effective stress increment is higher for the "Drainage" case with about 25% for 0,5m spacing while for the "Drainage + Expansion" case the increase stops at less than 25%.

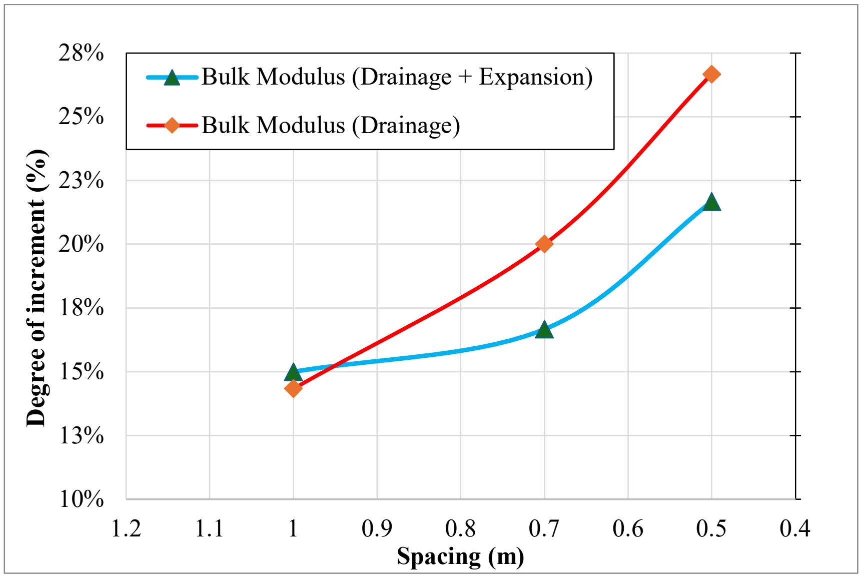

Figure 4.67 - Percentage of bulk modulus growth for two cases.

5 CASE HISTORY

In this chapter the results coming from the quantification of improvement effects performed on the small-scale model (chapter 4) are applied to a real case study regarding an Italian tunnelling project that will be excuted in complex clay formation that has been characterized thanks to the analysis of laboratory and in-situ tests. Then, after the characterization phase the main features of the tunneling projects are exposed in order to set the characteristics of a complete 3D model that simulates the main sequence of works.

Finally, for a given section, the stability of the excavation face will be evaluated using the shear reduction technique to quantify the effects of ground improvement achieved through application of the pressurized reinforcement.

5.1 Geotechnical characterization

The geotechnical characterization has been developed based on several sampling cores performed along the outlined path of the tunnel.

Particularly, two geological units have been identified in the preliminary phase (coring operations) thanks to the visible difference in the collected sample, which was subsequently confirmed in the characterization process and will be treated in the following chapters.

The tests performed on the different materials have been conducted both on-site and, in the laboratory, to obtain complete knowledge about soil properties.

5.1.1 Tested Materials

The first geological unit defined as ***GU1*** discovered during the coring phase is formed by levels and horizons consisting of clasts of strongly heterogeneous size with a diameter of mm to a maximum of 10-20cm, in a sparse silt-clay to sandy/silty matrix generally very compacted and sometimes with even appreciable degrees of cementation (breccias).

The clast's origin is polygenic with a prevalent presence of calcarenites and subordinate sandstones and marls. Despite, the coarse component, it is essential to highlight the presence of silty-sandy clay layers that chaotically interrupt the continuity of the stratigraphy succession.

Figure 5.1 – Box sample of ***GU1*** from 45 to 50m depth.

The second geological unit defined as ***GU2*** is a greyish mudstone containing frequent polygenic blocks and clasts that were intercepted, mainly calcarenites and calcareous-marn, angular to rounded, with sizes varying generally between 5 and 40 cm in diameter.

It is a brecciated facies in which lithoid inclusions appear as angular clasts immersed in the argillitic fraction, however, sometimes the lithoid inclusions do not appear immersed in a chaotic argillitic matrix but localized in some portions as a result of a detrital deposition.


[redacted]

Figure 5.2 - Box sample of **GU2** from *80 to 85m depth.*

5.1.2 Index properties

The starting parameters commonly determined in the geotechnical characterization of soils are the index properties that are a consequence of the coexistence among different phases such as solid, liquid and aeriform.

Usually, the determination of index properties as porosity (***n***), unit weight of solids (γ_s), water Content (**w**), and saturation degree (S_r), determines the starting point for an optimal geotechnical analysis in terms of mechanical characteristics and consequently on the computational and operative aspects.

The values obtained by the laboratory campaign conducted on samples from a depth of 19m to 48m are summarized below, considering that the parameters given by the laboratory were: the water content, the porosity and dry unit weight γ_d, some calculations were necessary to obtain the unit weight of the saturated soil γ_{sat} calculated by the equation:

$$\gamma_s = \frac{\gamma}{1-n}$$

$$\gamma_{sat} = (1-n)\gamma_s + n\gamma_w$$

The values obtained for the available laboratory tests are summarized in

Table 5.1 - Index properties for the given samples

Depth (m)	**Water content w**	**Porosity n**	**γ_d (kN/m3)**	**γ_s (kN/m3)**	**γ_{sat} (kN/m3)**	**Clay Fraction**
19-19.5	0.12	0.34	17.6	26.8	21.0	20%
	0.13	0.34	17.6	26.8	21.0	20%
22.322.8	0.11	0.33	18.0	26.8	21.3	20%
	0.09	0.32	18.3	26.9	21.5	20%
27-27.5	0.10	0.35	18.1	28.0	21.6	20%
	0.10	0.32	18.3	26.9	21.5	20%
47.5-48	0.14	0.33	18.0	27.1	21.3	40%
	0.13	0.33	18.2	27.2	21.5	40%

5.1.3 Granulometric analysis

The dimension and shape of grains that constitute the soil highly affect the mechanical characteristics and behaviour, however, the ***GU1*** shows a level of heterogeneity that does not allow the classification of soil as usual intended since the additional presence of clasts is present at different depth levels without any peculiar concentration.

The collection of the granulometric curves that have been associated with the **GU1** is shown in Figure 5.3, where is possible to appreciate different classes of soils inside the same units.

The first appreciable group was highlighted by the red dashed line, where the coarser group of the formation is composed of coarse gravel (about 50-60%) with an appreciable content of sand (around 30%).

The second group (violet dashed lines) has been grouped by soil samples with a high variability of granulometric composition where about 60-50% have a grain size bigger than 0.06 mm, and the remaining percentage is distributed between silts and clays (about 20-30%).

The third group present shows the highest fine content among the three classes identified, indeed the % of sand is not bigger than 50% and in certain cases (three curves indicated by red arrows) does not exceed 20%.

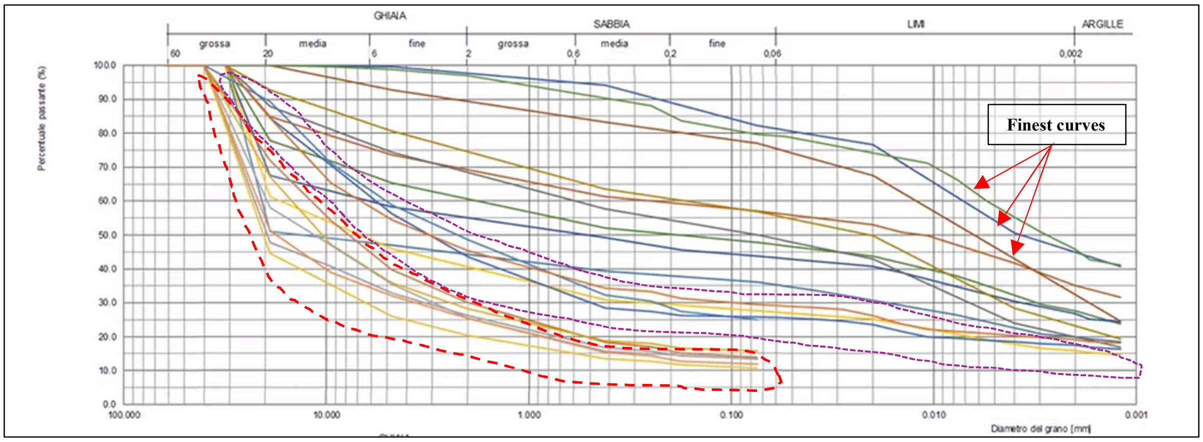

*Figure 5.3 – Granulometric curves of the collected samples for **GU1**.*

The second unit ***GU2*** presents many differences concerning the previous one, indeed the presence of finer grains is dominant with a lower presence of lithoid elements that remains quite random.

The collection of the granulometric curves that have been associated with the **GU2** are shown in Figure 5.4, where is possible to appreciate the difference with the unit **GU1**.

The **GU2** shows a bigger content of finer grains that goes from 20% to 80% as extremes, however, the average concentration remains about 40%, which gives the possibility to consider and treat the soils as silty clay with a coarser component of sand and lithoids.

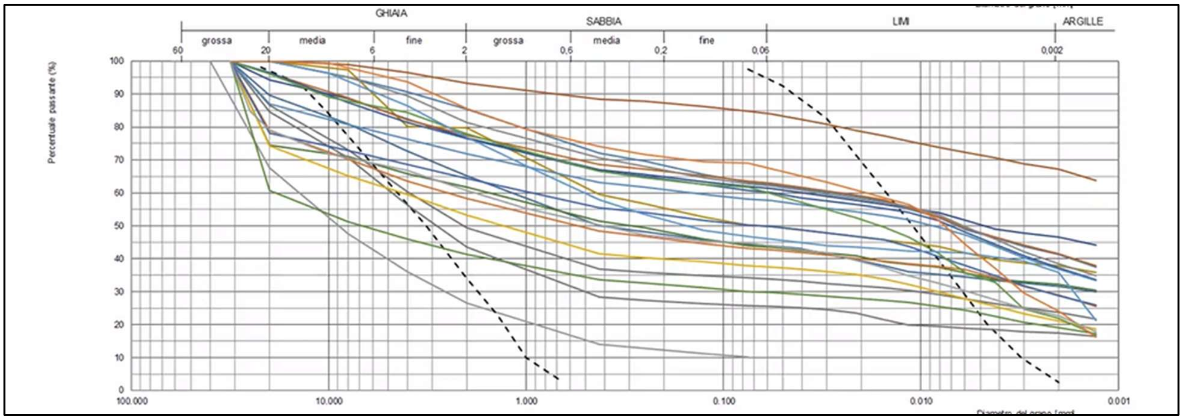

Figure 5.4 – Granulometric curves of the collected samples for ***GU2****.*

5.1.4 Plasticity

The description of the plasticity features discussed in (§ Clay formations) have been explored also in the characterization phases of the project, indeed thanks to standardized tests the PI and the LL for the two geological units have been assessed following the graphical summary in Figure 5.5.

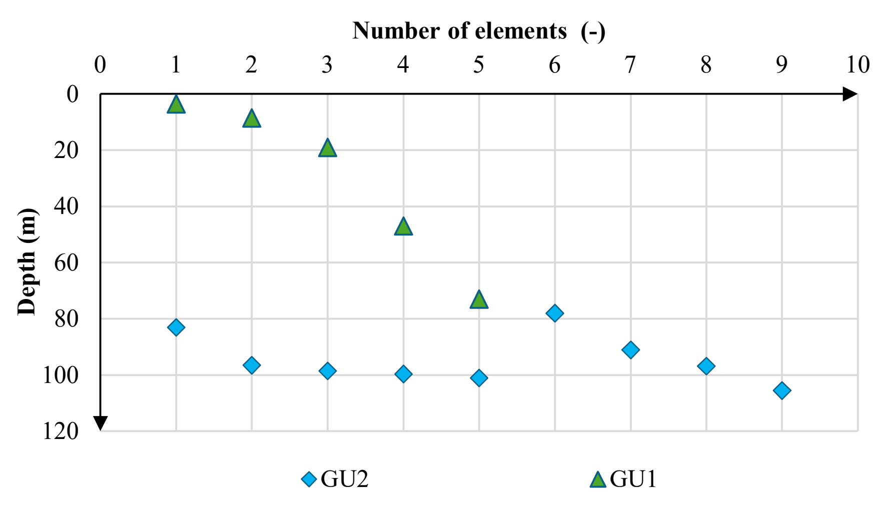

Figure 5.5 - Distribution of samples along depth for plasticity assessment.

Below, in Figure 5.6 the values of **PI** and **LL** have been reported in the plasticity chart where the different classes of soils are identified. Particularly, is possible to observe that the two geological units have an appreciable dispersion. However, by plotting the two variables (PI and LL) against the depth at which the sample has been cored some useful information can be retrieved.

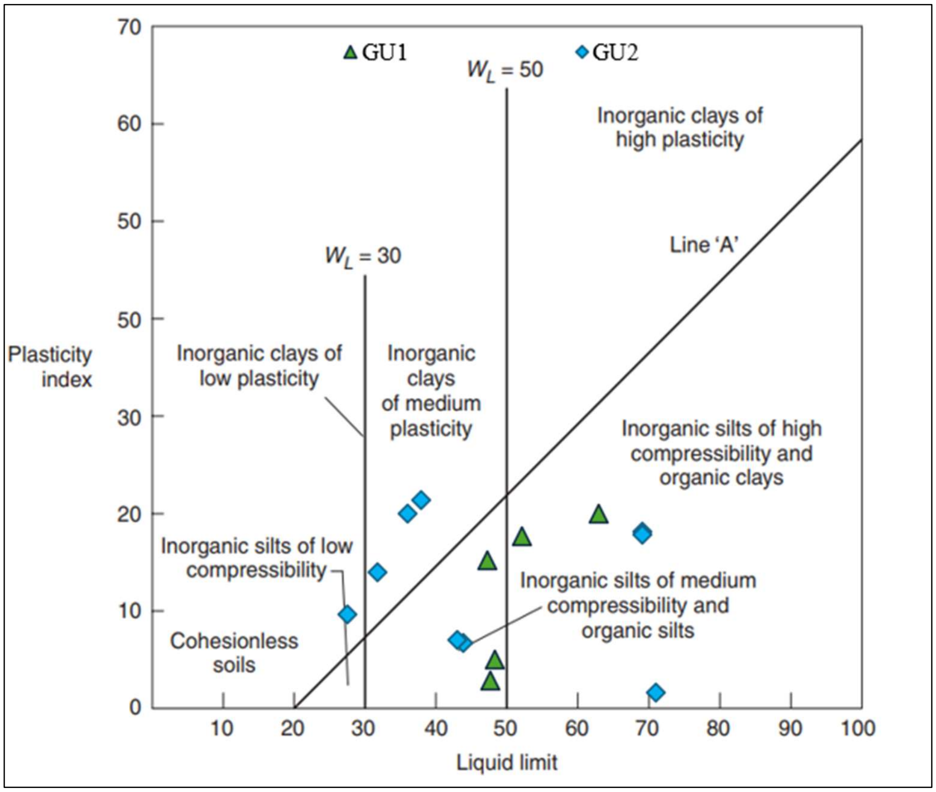

Figure 5.6 – Plasticity chart of GU1 and GU2.

By looking at the plot where **PI** and **Depth** are compared, a clear correlation cannot be assumed between the two variables, mainly since the mineralogic constituent controls the plasticity. However, two main classes of behaviour can be identified for different depths and units.

Considering **GU2**, most samples have a value of PI between 5 and 20 which corresponds to medium plasticity for all ranges of depths, and only one specimen has a low PI. A similar consideration can be made for the **GU1** but paying attention to the fact that fewer specimens have been tested.

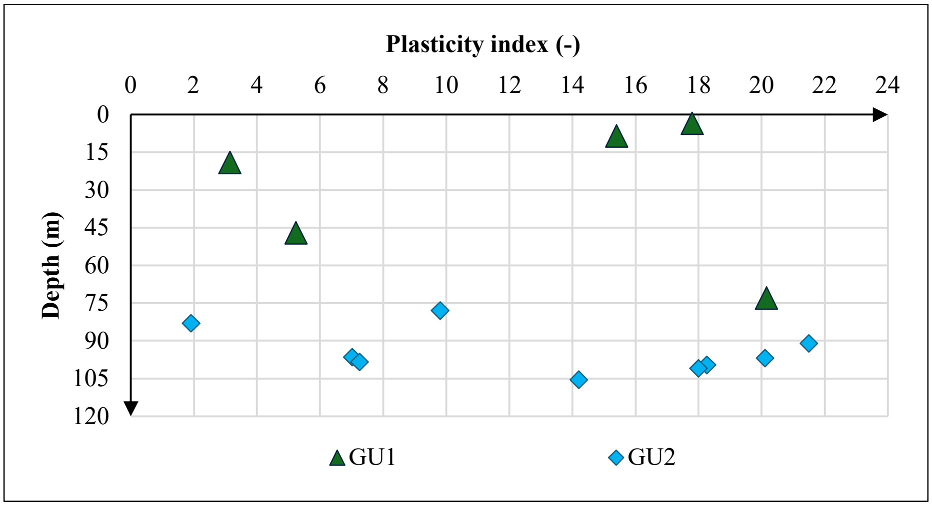

Figure 5.7 - Distribution of PI along depth.

By analysing the plot where **LL** and **Depth** are compared, a clear correlation cannot be assumed between the two variables but is appreciable that the **GU1** has values of **LL** around 50, while the **GU2** between 30 and 40, with a couple of samples that reach **LL** of 70.

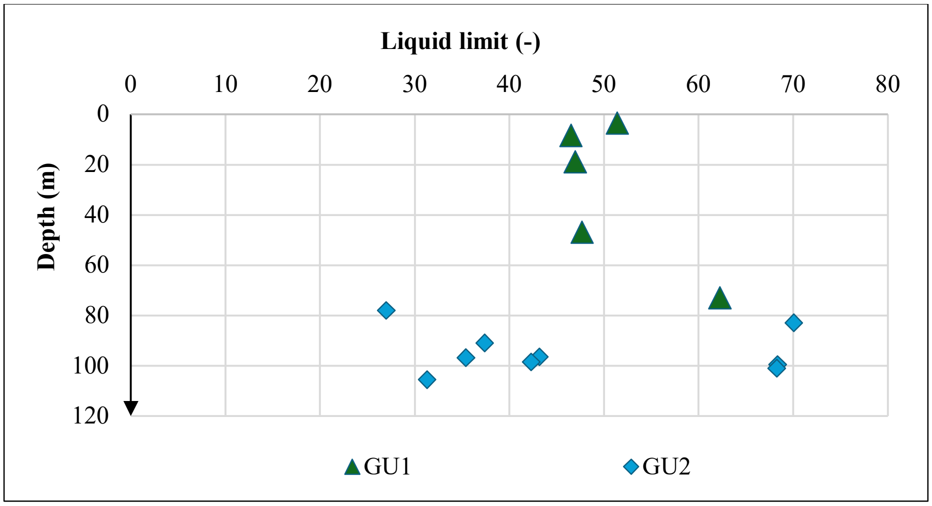

Figure 5.8 - Distribution of LL along depth.

5.1.5 Direct Shear Test

The series of direct shear tests performed for the two geological units led to the determination of two parameters: the friction angle (**φ**) and the cohesion (**c'**) that will be used as a design parameter.

The common practice in geotechnical engineering is to perform a linearization of the shear test results in the plane **τ - σ_n**, defining in this way the linear Mohr-Coulomb failure. However, often this simple mathematical operation disregards the physical phenomena that characterize the soil behaviour, leading to wrong parameter estimation that will affect the design process.

As said in the previous paragraphs the characterization has been performed in different ways for the two geological units due to operational and contractual issues, however, is important to understand the difference in the results related to changes in the operational setup.

The GU1 has been characterized by repeating three direct shear tests at increasing vertical consolidation pressure, specifically, the samples retrieved from a depth of 19.5m, the three vertical stresses applied correspond to 300, 400 and 500 kPa.

The second test for the GU1 has been performed on a sample of 47.5m depth, again with three increasing vertical stress levels higher respect the first test (800, 950, 1100 kPa), presumably to simulate the higher vertical stress that is acting in situ.

To give a complete overview of the geotechnical characterization, the shear stress – horizontal displacement (Figure 5.9 (a)) and vertical- horizontal displacement (Figure 5.9 (b)) plots have been reported below, where is appreciable the contracting behaviour of loose sand that is characterized by shear stress increases with shear displacement reaching a maximum value which then remains constant.

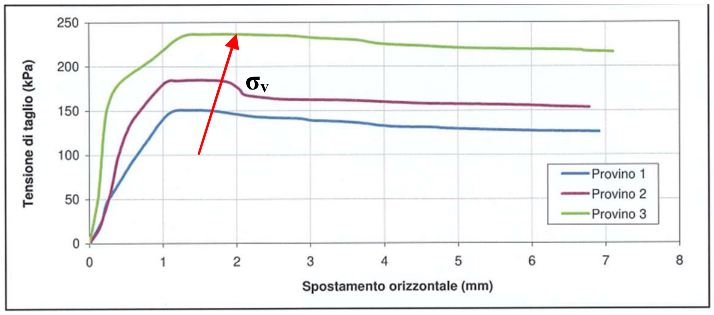

a)

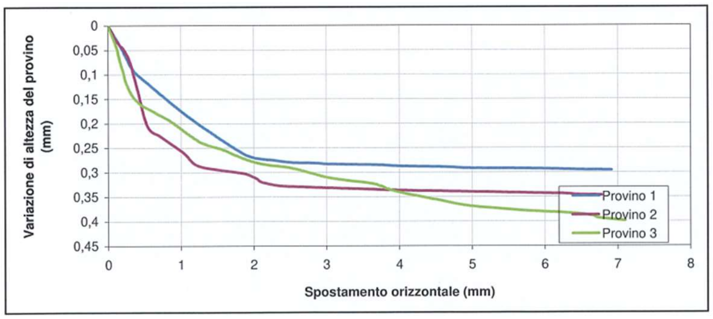

b)

Figure 5.9 – (a) Shear stress- horizontal displacement for three vertical stresses (500,400 and 300kPa.). (b)Vertical–horizontal displacement for three vertical stresses applied.

The linearization process performed has been conducted by operating a critical analysis that focuses on the samples and test results, especially from the coring box (Figure 5.10) is possible to observe the state of aggregation for the material tested (red-dashed lines) which will be considered in the derivation of the parameter.

Figure 5.10 - Samples box of the tested material for GU1.

The GU2 has been characterized by repeating three direct shear tests at increasing vertical consolidation pressure, specifically, the samples retrieved from a depth of 73m to 110m and the three vertical stresses applied correspond to 100, 200 and 300 kPa.

As before, shear stress-displacement (Figure 5.11 (a)) and vertical-horizontal displacement (Figure 5.11 (b)) plots have been reported below, where the contracting behaviour of NC clays is maintained also for higher depth.

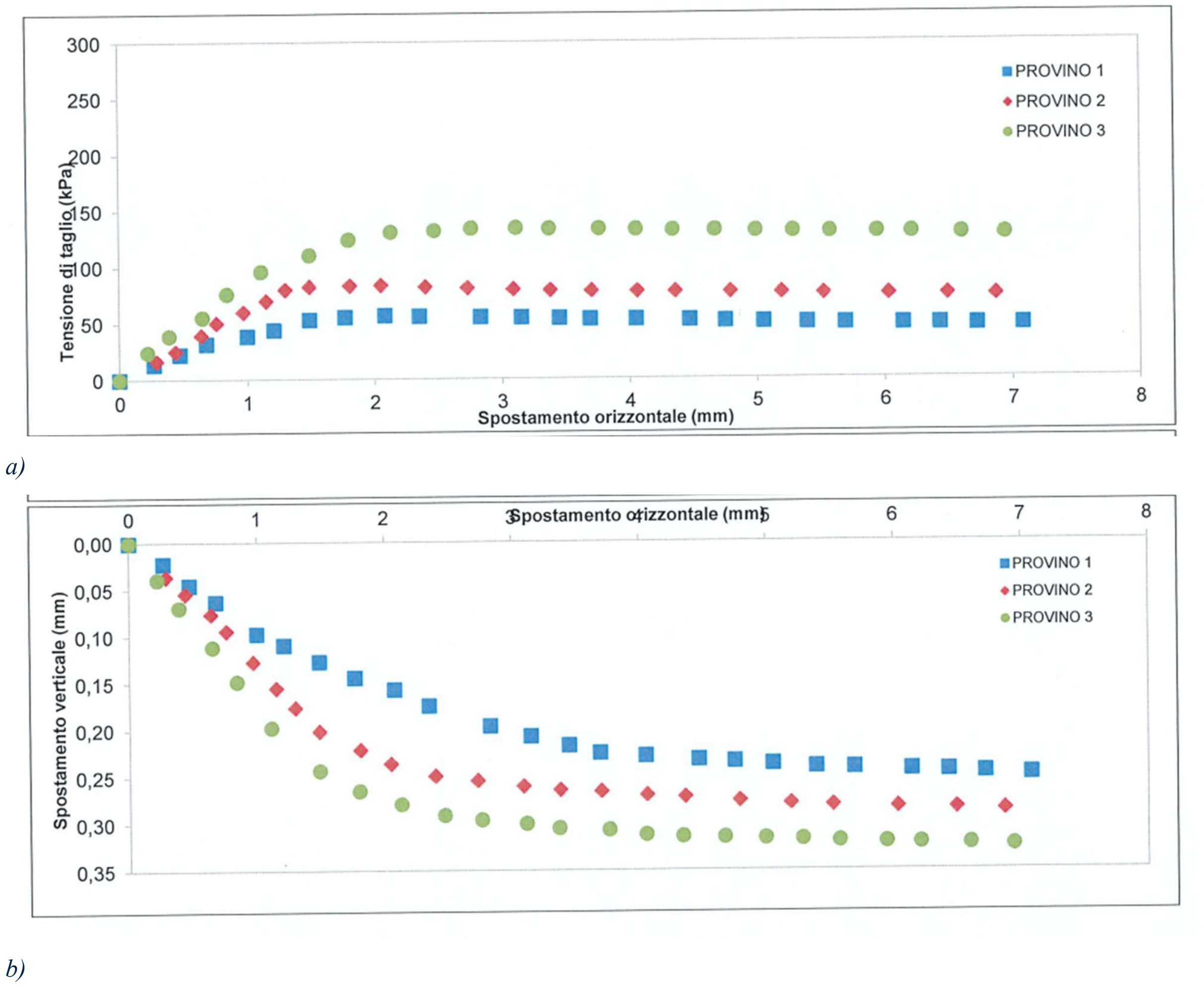

Figure 5.11- (a) Shear stress- horizontal displacement for three vertical stresses (100,200 and 300kPa.). (b) Vertical–horizontal displacement for three vertical stresses applied.

The GU2 presents material with a higher content of clays to the detriment of sand and gravel, additionally is visible that at higher depths (>100m) the material is more compact and able to maintain its own shape which in terms of mechanical properties means higher strength (see §5.1.6).

The coring box related to the tested samples has been reported in Figure 5.12.

Figure 5.12 - Samples box of the tested material for GU2.

5.1.6 Derivation of friction angle and cohesion

In 1900, Mohr presented a theory explaining that failure in material develops along a plane by a critical combination of normal and shear stresses, and not by normal or shear stress alone.

The functional relation between normal and shear stress on the failure plane usually adopted in soil mechanics was developed in 1776 by Coulomb through the following equation (5.1).

$$\tau = c' + \sigma'_n * \tan(\varphi) \qquad (5.1)$$

T = shear stress (kPa)

c'= cohesion (kPa)

σ_n = effective normal stress (kPa)

φ = friction angle (°)

However, the equation (5.1) is valid only in the case of cohesive soils, instead for soils that are cohesionless such as granular ones the equation becomes the following (Eq.6.5.2).

$$\tau = \sigma'_n * \tan(\varphi) \qquad (5.2)$$

An additional consideration is needed concerning the correct couple of τ-σ_n to be chosen for the linear interpolation following the previous relationship (5.1). Depending on the type of application or yielding state (elastic or plastic) the parameter values could vary and have consequences on the design aspects causing over/under dimensioning.

In the following graph (Figure 5.13) two linearization have been performed, the first taking into consideration the peak value of $\boldsymbol{\tau}$ corresponding to the maximum value in Figure 5.9 (a) and also by adopting the relationship for cohesive soils because the tested sample (Figure 5.10) present characteristics coherent with the assumption.

The second is considering the shear stress at a constant volume corresponding to a residual condition, where the cohesive component can be discarded since the soil already reached the plastic state in which cohesion is lost.

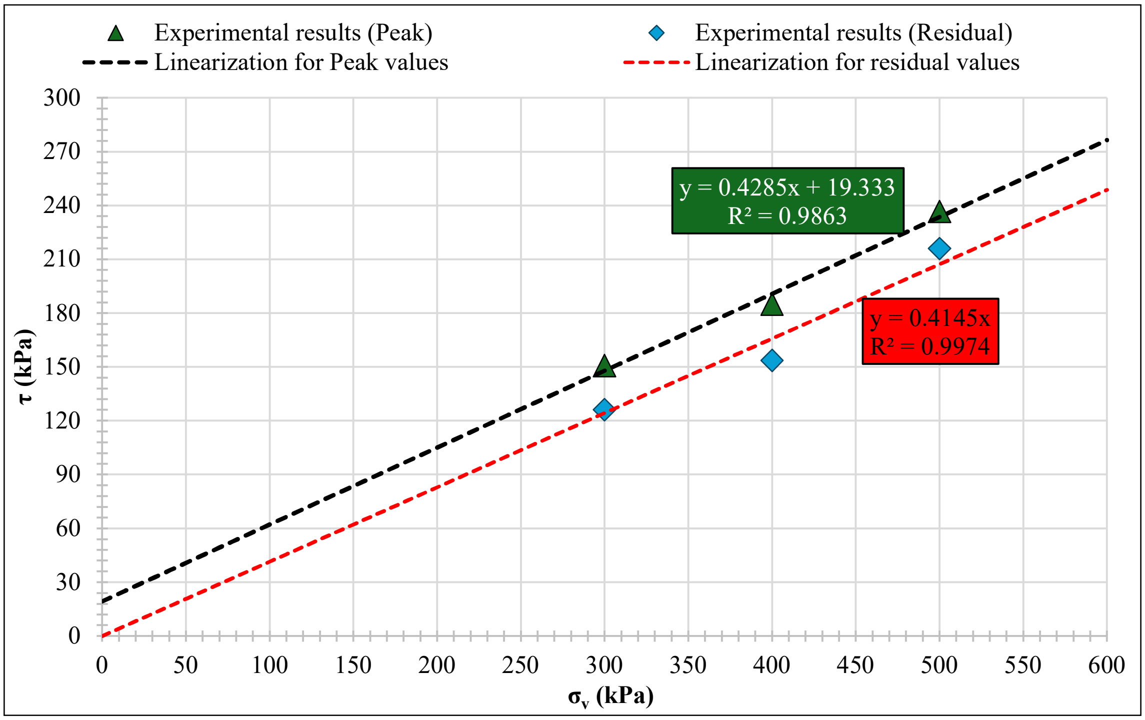

Figure 5.13 – Linear interpolation for the peak and residual conditions results of direct shear tests.

The approach explained above has been adopted on all the shear tests conducted for samples at different depths and summarized in the figures (Figure 5.14), where in both geological units is appreciable the reduction of a few degrees (2-3°) of friction angle from peak and residual condition.

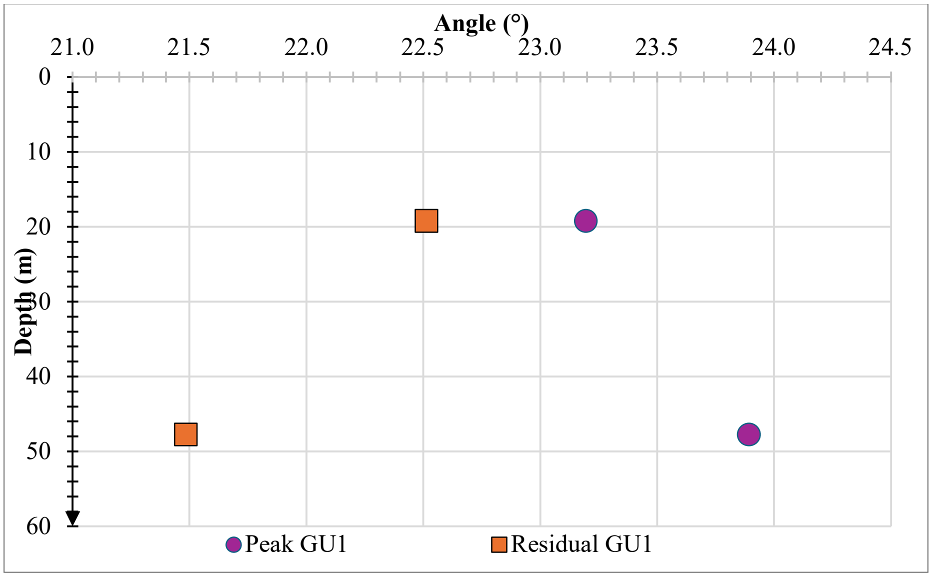

Figure 5.14 – The friction angle of GU1 respects the depth for residual and peak conditions.

As mentioned previously (), from 100m to 110 the soil presents better mechanical characteristics both in terms of friction angle and cohesion concerning the soils laying between 94 and 100m despite the soil having the same grain size and mineralogic origin.

These considerations have been synthesized in the plots Figure 5.15 and Figure 5.16, where a significant increase is recorded from 95 to 101m.

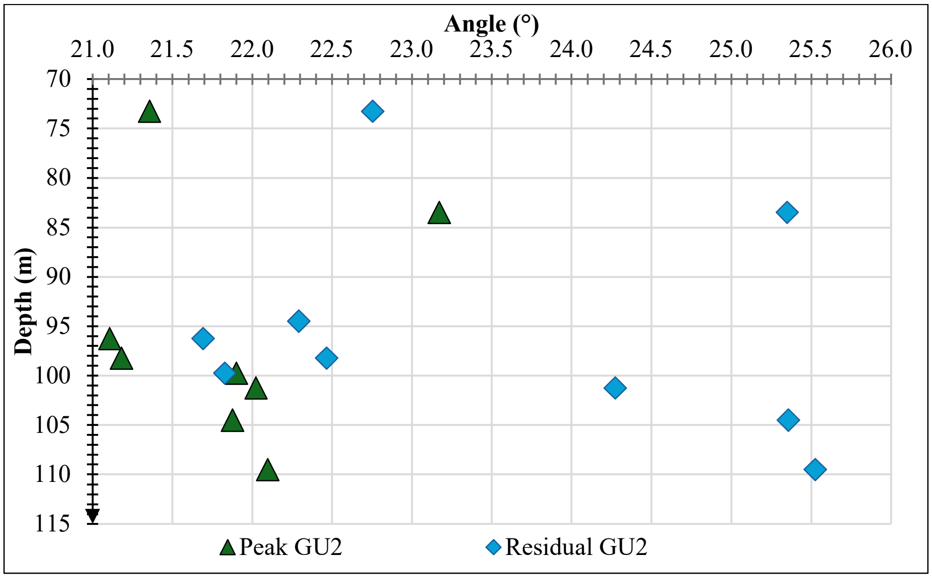

Figure 5.15 – The friction angle of GU2 respects the depth for residual and peak conditions.

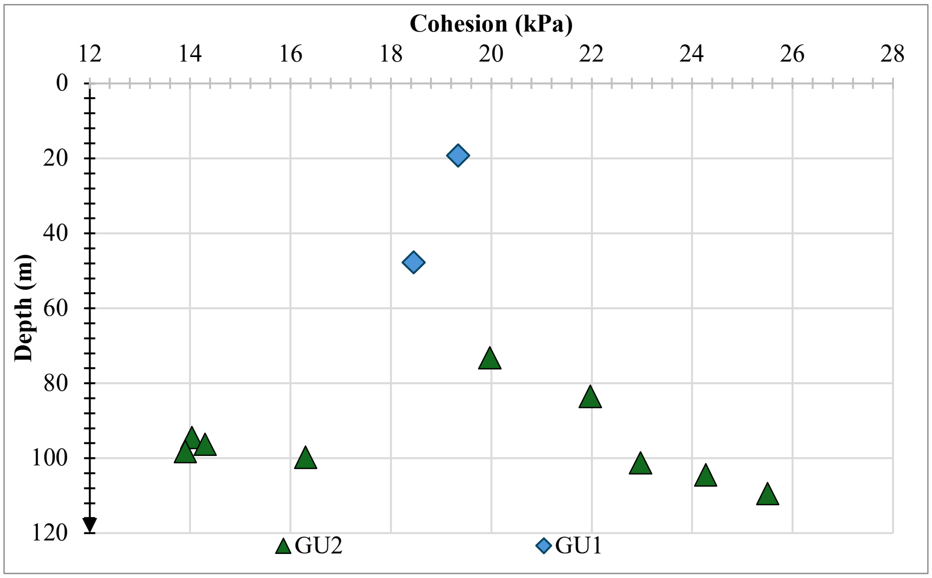

Figure 5.16 – Interpolated cohesion respects the depth for GU1 and GU2.

Table 5.2- Obtained parameters for the geological formations.

Geological Unit	Depth (m)	Cohesion (kPa)	Friction Angle (°)
GU1	19.25	19.3	23.2
	47.75	18.5	23.9
GU2	73.25	20.0	21.4
	83.50	22.0	23.2
	94.50	14.0	21.0
	96.25	14.3	21.1
	98.25	13.9	21.2
	99.75	16.3	21.9
	101.25	23.0	22.0
	104.50	24.3	21.9
	109.50	25.5	22.1

5.1.7 Coefficient of earth pressure at rest K_0

As initial input for any kind of geotechnical design, the coefficient of earth pressure is determinant in the estimation of the undisturbed state of stress. However, some deviation in the determination must be considered due to the geological phenomena that could cause a variation with respect to the hypothesis formulated for the calculation of K_0.

The coefficient of earth pressure "at rest" for normally consolidated clays can be estimated through Eq.5.3 and 5.4 or the similar expression suggested in Brooker & Ireland (1965) and Simpson (1992).

$$K_0 = 0.95 - sen(\varphi) \qquad (5.3) \qquad \text{(Brooker \& Ireland,1965)}$$

$$K_0 = \frac{\sqrt{2} - sen(\varphi)}{\sqrt{2} + sen(\varphi)} \qquad (5.4) \qquad \text{(Simpson,1992)}$$

In Figure 5.17 the variation of K_0 respects the range of values for friction angle obtained from the direct shear test (§5.1.6) have been plotted, showing a quite limited range of variability ($0.54<K_0<0.61$).

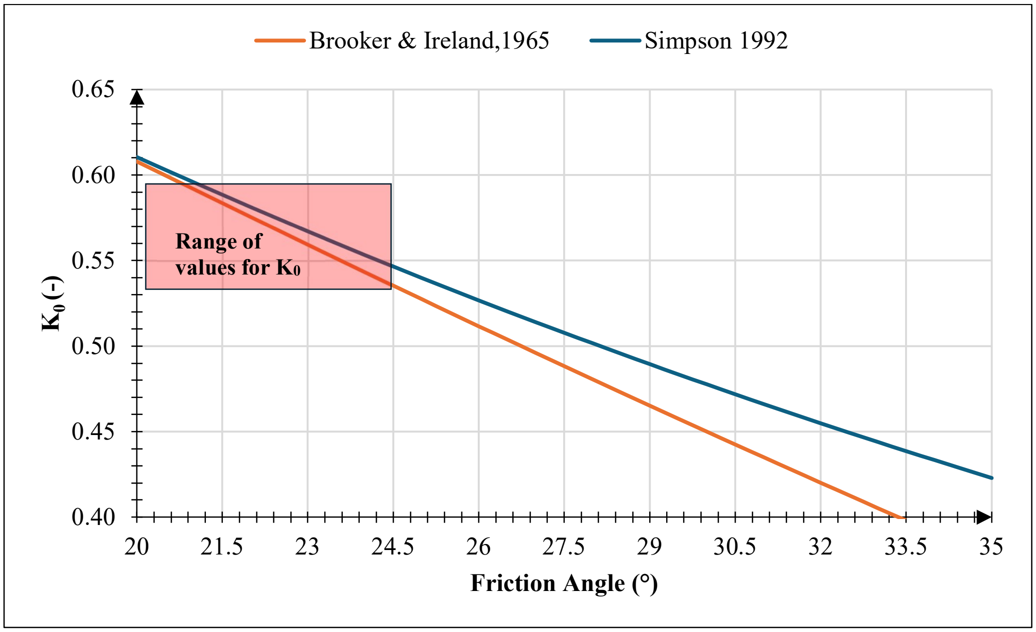

Figure 5.17 – Typical relationships between K_0^{NC} and ϕ' following (Brooker & Ireland,1965) and (Simpson,1992).

The availability of several plasticity tests allows the computation of $\mathbf{K_0}$ by using two empirical correlations valid for normally consolidated cohesive soils that match the characteristics of **GU1** and **GU2**.

For cohesive soils, K_0^{NC} can also be related through empirical correlations with soil plasticity.

$K_0 = 0.19 + 0.233\log(PI)$ (5.5) (Alpan,1967)

$K_0 = 0.44 + 0.0042PI$ (5.6) (Holtz & Kovacs, 1981)

PI = Plasticity index.

Again, the values of $\mathbf{K_0}$ have been plotted at different depths (following the tests performed) in Figure 5.18 and Figure 5.19, showing a range of variability lying between (0.35 and 0.53).

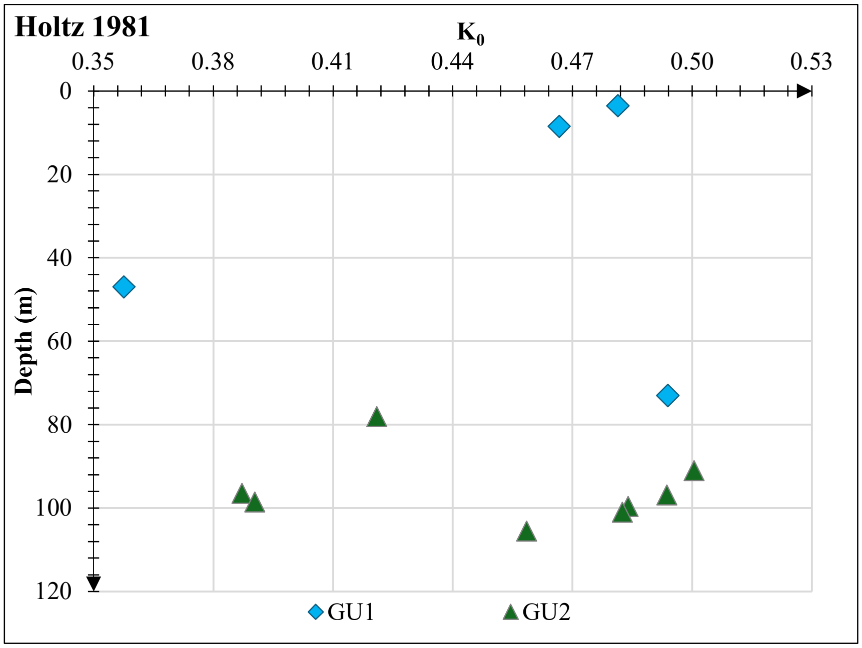

Figure 5.18 – Values of K_0 along the depth obtained with Holtz's formulation (1981).

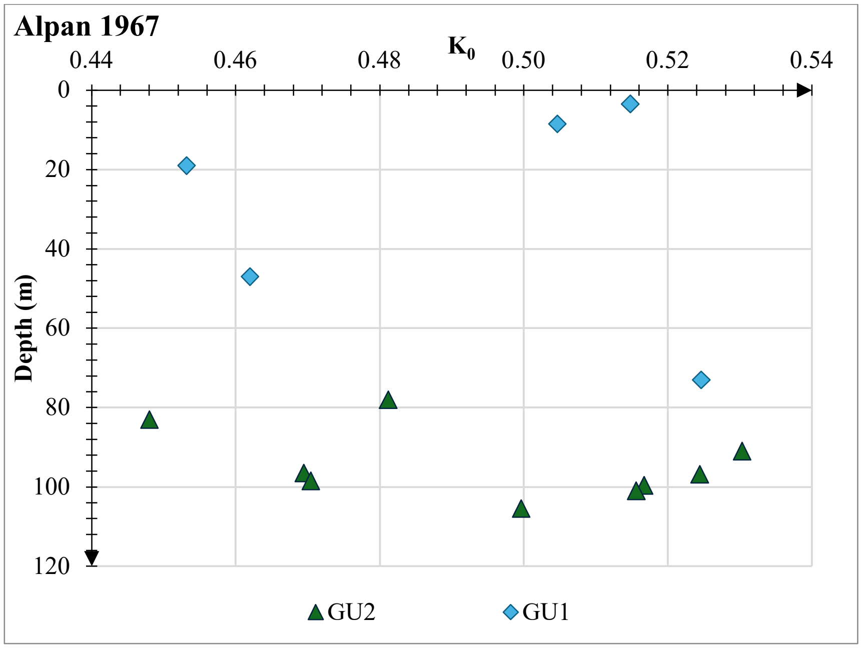

Figure 5.19 - Values of K_0 along the depth obtained with Alpan's formulation (1981).

The main outcome coming from the comparison of different formulations is that a high agreement is obtained allowing a sort of verification between more "theoretical formulation" such as (5.3 and 5.4) and empirical one (5.5 and 5.6) based on a dataset coming from laboratory tests of the survey campaign.

5.1.8 Oedometer test

The process of characterization involves also the execution of oedometer tests in which the soil specimen is placed inside a metal ring with two porous stones, one at the top of the specimen and another at the bottom.

The load on the specimen is applied and kept for 24 hours, to allow the consolidation of the sample. After that, the load has been doubled, which doubles the pressure on the specimen, until the maximum axial load is reached.

The second phase of the test is conducted by operating an unloading phase where the load is reduced by one quarter until the initial condition, additionally, at the beginning and the end of the test, void ratio ($\mathbf{e_0}$) and $\boldsymbol{\gamma_{dry}}$ are determined.

However, the main goal of this kind of test is to obtain information, firstly regarding the deformability parameters in the elastic and elastoplastic state respectively quantified by $\mathbf{C_c}$ (compressibility coefficient) and $\mathbf{C_s}$ (swelling coefficient), secondly, the consolidation state (**OCR**) and finally the consolidation coefficient ($\mathbf{c_v}$) useful to describe the long-term behaviour.

5.1.8.1 Pre-consolidation stress

The first information that is possible to obtain is the tensional history of a soil quantified by the preconsolidation stress $\boldsymbol{\sigma'_p}$ understood as a threshold point beyond which the important plastic straining occurs, which is difficult to establish unambiguously. Among several methods proposed in the literature for determining $\boldsymbol{\sigma'_p}$, the following ones are commonly used owing to their simplicity and robustness:

- Casagrande's method (1936) [27] reported in Figure 5.20, uses an empirical method developed in the following manner: firstly, the point of maximum curvature is identified on the eodometric compression curve where the tangent (**t**) is traced to that point. Then a horizontal line (**h**) is drawn to this point, and the bisector (**b**) to the angle formed by the straight lines (tangent and horizontal). The final stage foresees the extension of the straight portion of the eodometric curves (*virgin compression line*) that will intersect the previous bisector, the x-coordinate of this point identifies the preconsolidation stress.

  The procedure explained is rigorous and returns a unique value of σ'_p, however depending on the inclination of the different portions of the experimental curve is not possible to obtain a unique value and so is better to return a range of values as illustrated in Figure 5.21 (a).

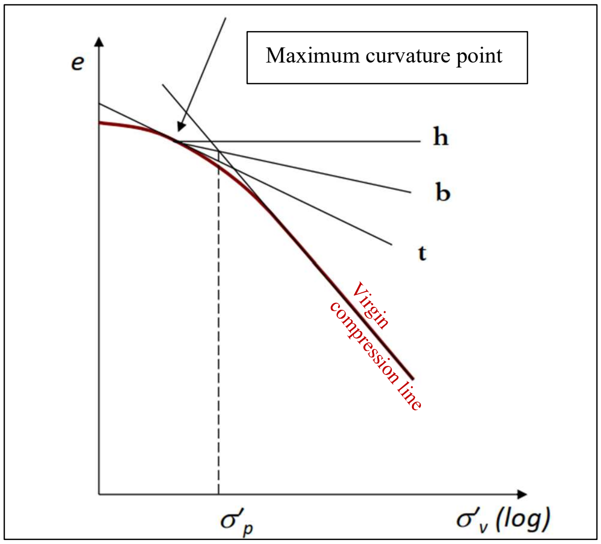

Figure 5.20 - Casagrande's method (1936).

- The Pacheco-Silva method (1970) [28], reported in Figure 5.21 (b) adopts a simple graphical procedure: by drawing the tangent to a rectilinear branch of the oedometer curve (3) is possible to intercept the horizontal line representing the initial void ratio (4). From point (4) with a vertical the eodometric-curve is intersected, then as the final step by continuing with a horizontal line the previous tangent is met (2), and at this point is possible to retrieve the x-coordinate corresponding to the preconsolidation stress.

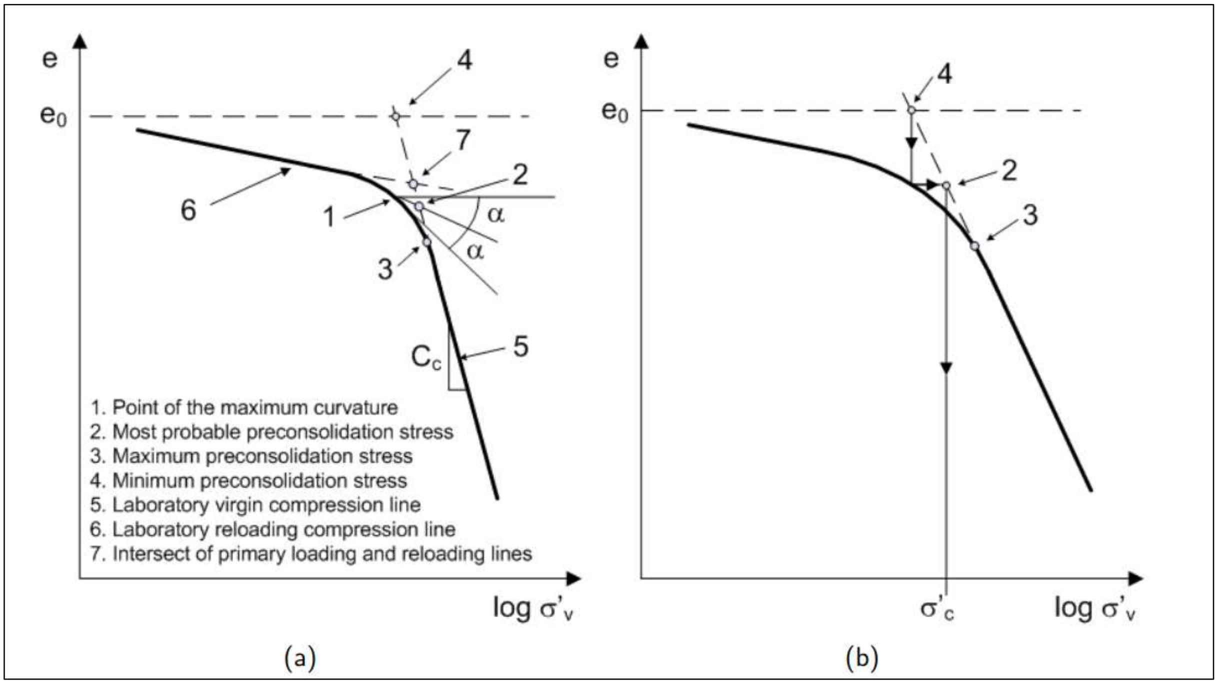

Figure 5.21 - Estimation of preconsolidation pressure (a) Casagrande's method, (b) Pacheco Silva's method. [29]

The procedures just described have been applied to all the available oedometer tests, here for the sake of simplicity the experimental curve related to the sample of GU1 in Figure 5.1 from a depth that goes from 47.5m to 48m. Both methods return the same values of preconsolidation stress σ'_p that correspond to 500kPa.

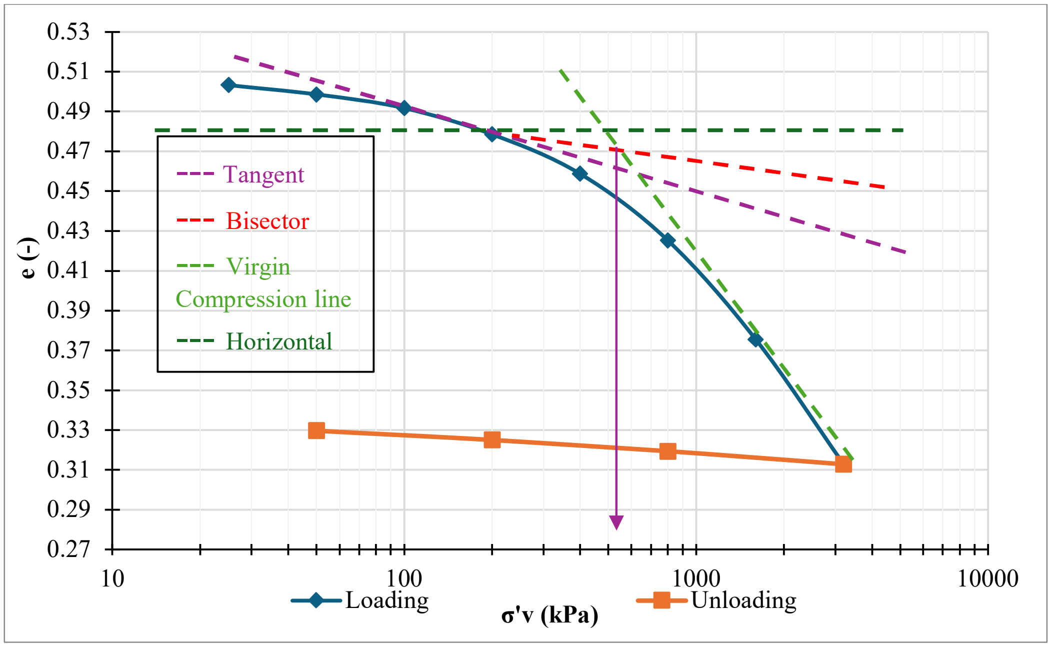

Figure 5.22 - Casagrande's method applied on a sample of 47,5m of GU1.

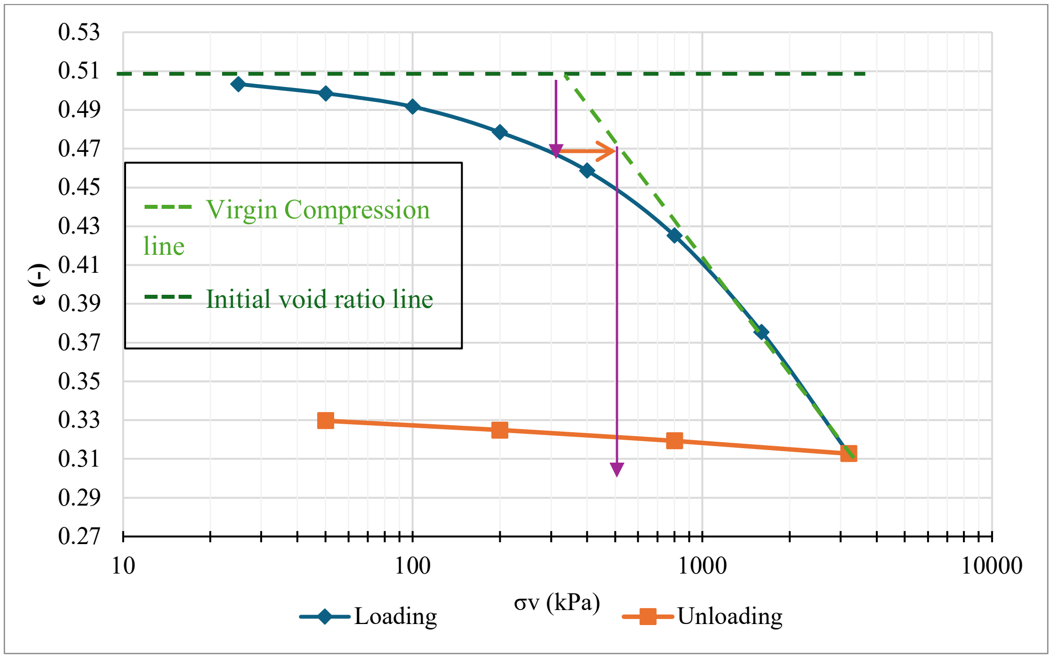

Figure 5.23 Pacheco-Silva method applied on a sample of 47,5m of GU1.

After obtaining the preconsolidation stress is possible to estimate the OCR by calculating the vertical stress acting in correspondence with the specimen depths as follows:

$$\sigma'_v = \sigma_v - u = \gamma_{sat} * z - h_w * \gamma_w$$

Where, σ'_v = to vertical effective stress, γ_{sat} = saturated unit weight of soil, z = depth, h_w = height of the water table and γ_w = unit weight of water

In addition to the $\boldsymbol{\sigma'_p}$ and OCR, from the oedometric curve in the plane σ-ε_{vol} (Figure 5.24) is possible to retrieve the deformability modulus defined as eodometric modulus $\boldsymbol{E_{oed}}$ coherently with the condition which is determined, indeed by computing the slope between two subsequent point of experimental curve.

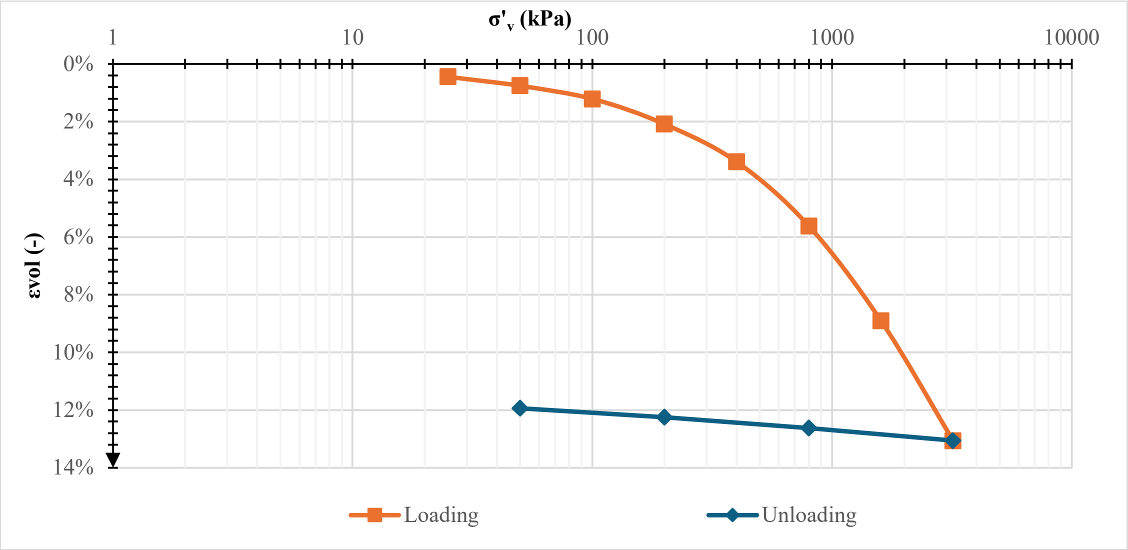

Figure 5.24 – Oedometric curve in the plane σ-ε_{vol}.

$$E_{oed} = \frac{\Delta\sigma_v}{\Delta\varepsilon_{vol}} \tag{5.7}$$

However, the oedometric modulus is a measure of the deformability into the specific range which has been determined, indeed, to be appreciable both visually and numerically in the variation into the slope for each couple of points during the loading phase and consequently in the magnitude of $\boldsymbol{E_{oed}}$.

However, the eodometric modulus has a theoretical limitation due to the one-dimensional deformation condition, but a direct relation with Young's modulus can be obtained by assuming linear isotropic elastic behaviour that links Young's modulus and Poisson's coefficient with $\boldsymbol{E_{oed}}$.

$$E_{oed} = \frac{1-v}{(1+v)(1-2v)*E} \tag{5.8}$$

The values of Young's modulus obtained are reported in Table 5.3, for a fixed value of the Poisson's ratio (**υ**) corresponding to 0,25. In addition, a sensitivity analysis has been performed to study the impact of **υ** on the elastic modulus determination(Figure 5.25).

Table 5.3 – Experimental data of oedometer test and deformability parameters.

σ'$_v$ (kPa)	ε_{vol} (-)	Oedometric Modulus (MPa)	Young's Modulus (MPa)
25	0.45%	7.9	6.6
50	0.76%	11.0	9.2
100	1.22%	11.5	9.6
200	2.09%	15.3	12.7
400	3.40%	18.0	15.0
800	5.62%	24.3	20.3
1600	8.91%	38.5	32.1
3200	13.06%	558.1	465.1
800	12.63%	160.0	133.3
200	12.26%	47.6	39.7
50	11.94%	0.4	0.3

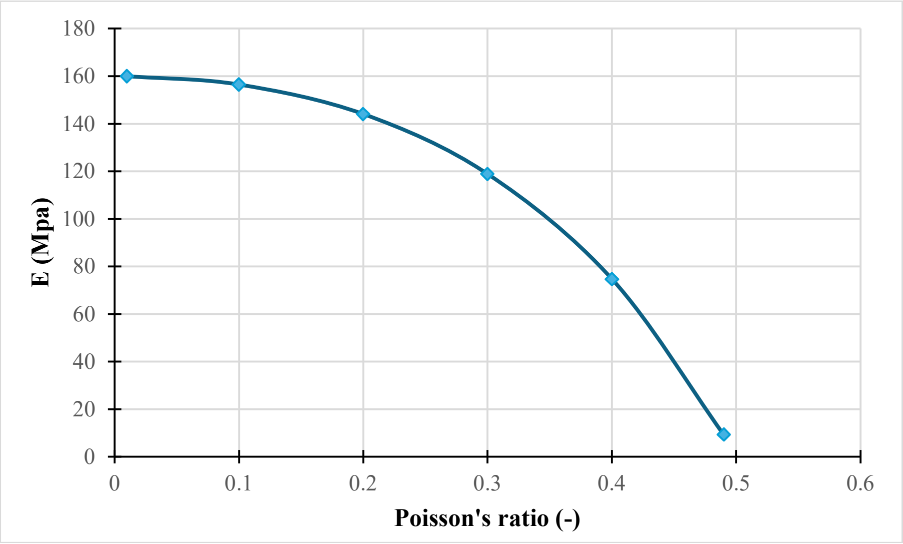

Figure 5.25 - Evolution of Young's modulus for different Poisson's ratios.

5.1.9 In-situ testing

5.1.9.1 Pressuremeter test

The pressuremeter test is an in-situ testing method used to determine the stress-strain response of the tested soil, at a given depth after the realization of the borehole used for the sampling recovery. The pressuremeter test, called also the Ménard Pressuremeter, is reported in Figure 5.26. The probe is constituted by an inflatable sheath at which three displacement transducers are connected at three mutual directions with an angle of 120°.

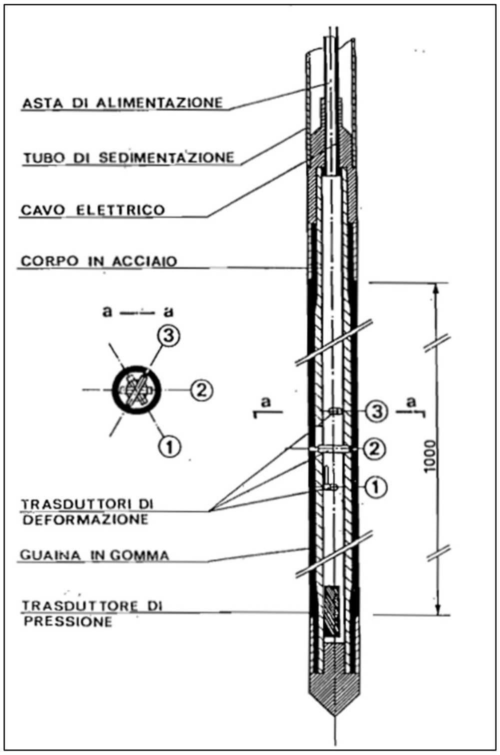

Figure 5.26 – Scheme of 95mm pressuremeter used for the in-situ test campaign

The computation of Young's Modulus has been carried out by making a hypothesis about the surrounding soil: isotropic, linear-elastic behaviour and plane-stress state at the centre of the apparatus thanks to the ratio between the length and the diameter of the probe.

So, it is possible to apply the Lamé elastic solution (Rocha et al. 1966 [30]) expressed by:

$$\Delta D = \frac{(1+\upsilon)D_0\Delta p}{E} \qquad (5.9)$$

Where Δp is the variation of pressure, ΔD is the variation of diameter, and E and υ are respectively the Young's modulus and the Poisson coefficient.

In Figure 5.27, is possible to observe the results of a test carried out in situ for a depth of 85m, particularly the test is characterized by three phases, the first regards the so-called 'mise en contact' where the external membrane of the probe is expanded until touches the surrounding material, in this phase the pressure increase without any displacement (vertical curve), the second phase regards the expansion and the pressurization to reach the in-situ stress **P_0**, the third apply two or more cycle of loading and unloading for increasing levels of pressures going from 2 to 3 times the P_0.

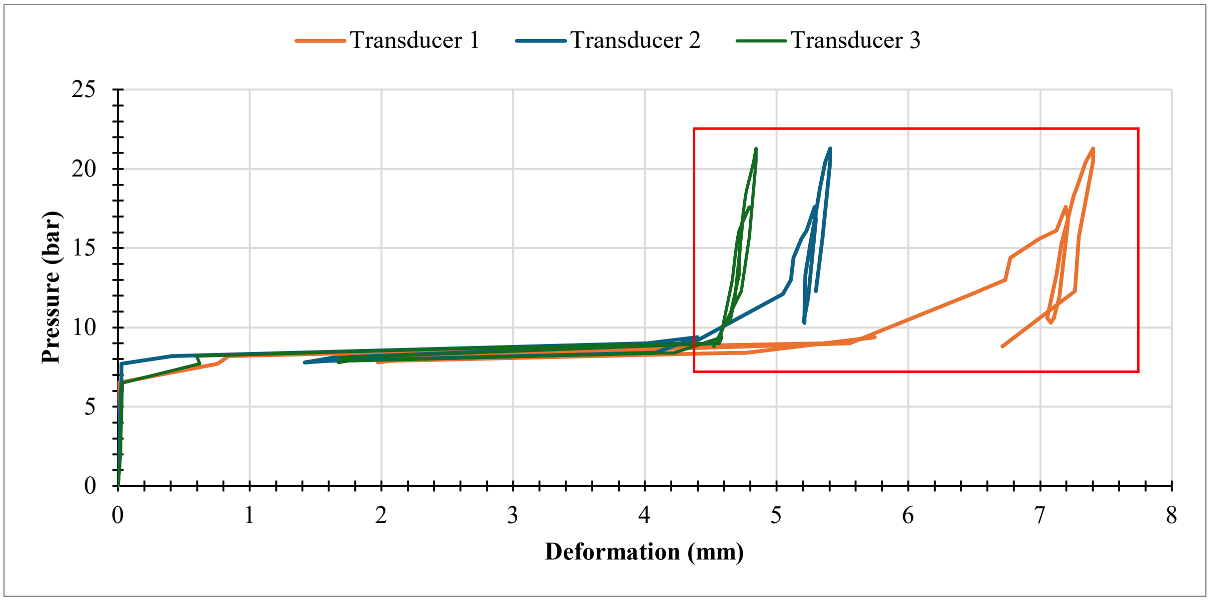

Figure 5.27 - Experimental results of the Pressuremeter test.

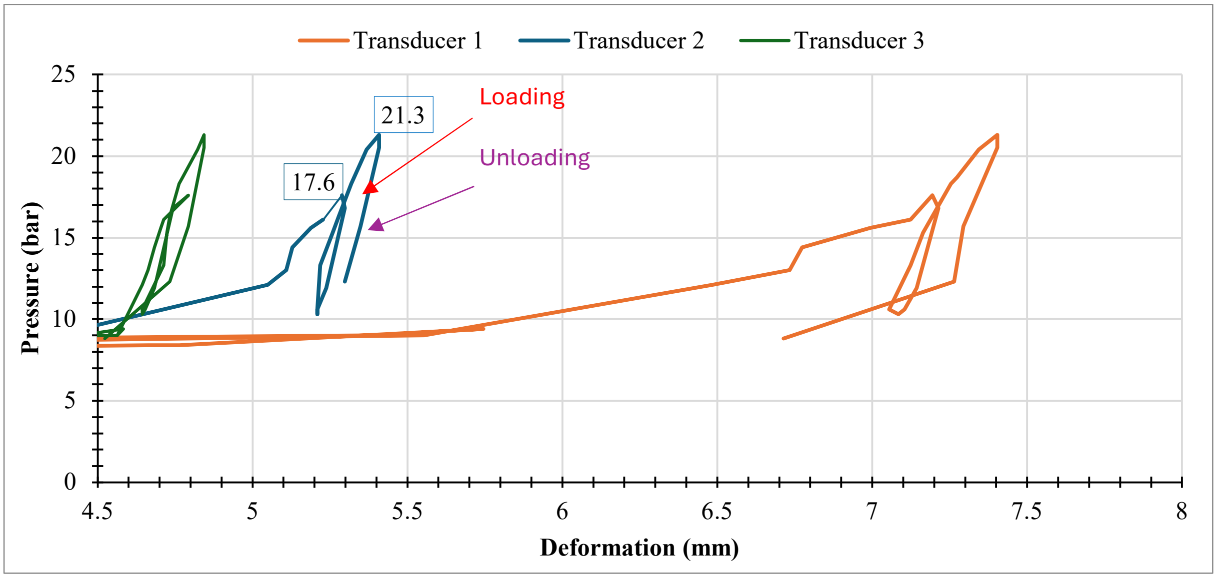

Figure 5.28 - Detail of the pressuremeter tests with the different loading and unloading paths.

The results obtained by applying (Eq. 5.9) are summarized in Table 6.3. An increase in Young's modulus was recorded between the 1st and 2nd cycles, attributed to the higher applied pressure. Another important aspect, which will be discussed in the next paragraph, is the notable difference between the loading and unloading elastic modulus. Specifically, while the loading modulus increases with higher pressure values, the unloading modulus remains consistent across cycles and is greater than the loading modulus.

Table 5.4 – Values of the Elastic Modulus for the loading and unloading phases at different cycles.

Cycle - Pressure	**Phase**	**Transducer-1 E - (MPa)**	**Transducer 2 E - (MPa)**	**Transducer 3 E - (MPa)**	**Mean E - (MPa)**	$\frac{E_{load}}{E_{unloading}}$*
1st - 17.6 bar	Loading	120	246	340	235	2.8
	Unloading	638	877	468	661	
2nd – 21.3 bar	Loading	330	529	529	462	1.58
	Unloading	618	786	786	730	

** The ratio has been computed on the mean value.*

Unfortunately, among the available tests, the reported one is the only one with a correct execution, indeed during the first and second phases some elements like lithoid or some coarser aggregates present in the soil matrix could enter contact before the surrounding soils causing a disturbed measurement (example in Figure 5.29) that will return completely wrong values in the computation phase.

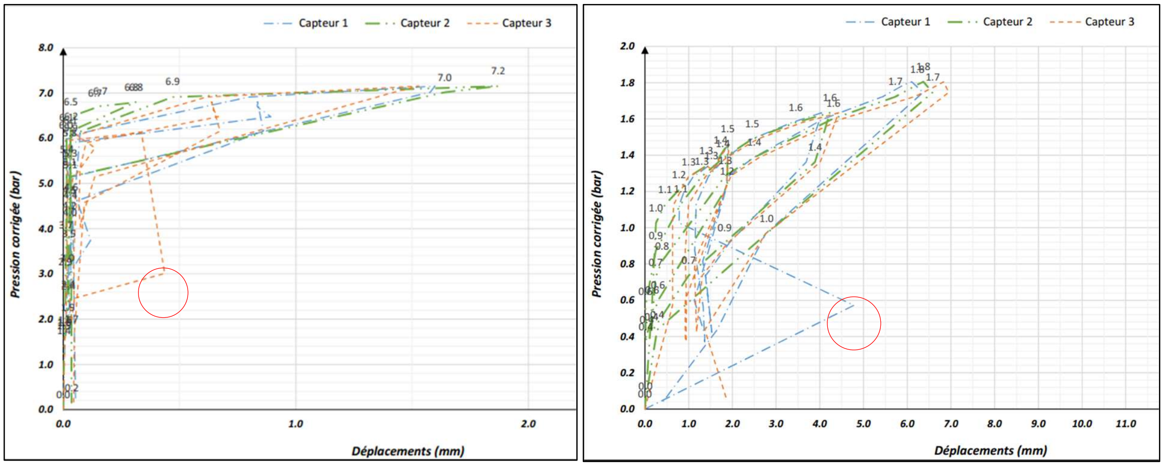

Figure 5.29 – Irregular trends during the test's competition.

5.2 Main characteristics of the project and model setup

The section adopted in the project was a truncated cone with vertical walls of 2.6m respecting the excavation working plane, and an arched roof with a radius of 7.35m (respecting the arch reference level), starting from the midpoint of the sections (Figure 5.30). Then, after the excavation of the face, the bottom portion is excavated with the realization of the invert.

The final project foresees preliminary support (summarized in Table 5.5) during the advancement by applying 30cm of fiber-reinforced shotcrete at the crown and the adoption of steel ribs IPN 240 with a spacing of 1m, while regarding the excavation face the installation of 75 GFRP with valves to be injected with a length of 24m and an overlapping of 8m between one installation and the next one.

However, concerning the original project the intervention at the excavation face was changed and substituted with the improvement on undrained shear strength quantified for the pressurized reinforcement in the previous chapter.

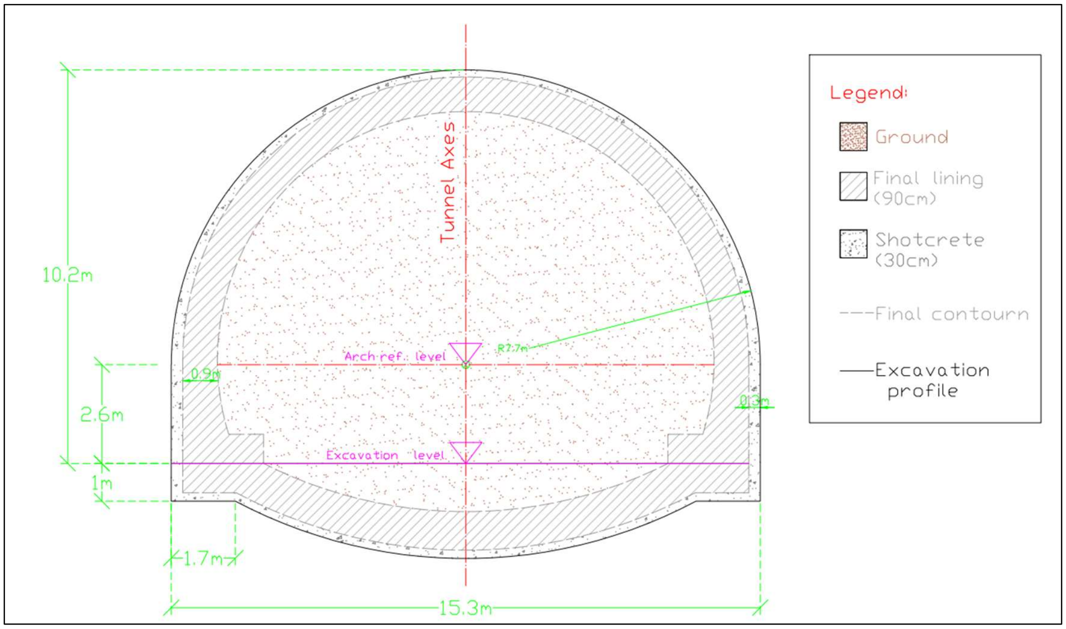

Figure 5.30 - Tunnel cross-section analysed in the numerical model

Table 5.5 – Characteristics of the typical cross section advancement.

CROSS-SECTION CHARATERISTICS		
Excavation area	158.12 m^3/m	
Theoretical Pull	1.00 m	
Intervention ahead of the face	Shotcrete 10 cm for each advancement + 15 cm at the end of pull n. 75 GFPR 40/60mm with valves (2 valves/m) Length= 24.00 m overlapping = 8.00 m	
Consolidation in the contour	n. 55 GFRP 40/60 with valves (2 valves/m) Length= 24.00 m overlapping = 8.00 m	
Temporary support	Crown	Shotchrete 30cm + 2 IPN 240, spacing=1.0m
	Invert	Magrone 10 cm
Impermeabilization	Crown	PVC + TNT
Final lining	Crown	Thickness. Min. = 90 cm
	Invert	Thickness. Min. = 100 cm

In the 3D model, a proper subdivision of the different regions was implemented by the realization of different zones that allow high flexibility to the model for the simulation of different phases of the work. The perfect elastoplastic Mohr-Coulomb constitutive model was adopted in order to use the SR technique.

The model geometry was 65m high, where the upper boundary corresponds to the ground surface, while the width was 200m with a zone characterized by a larger mesh going towards the boundary and a fine mesh in the inner region close to the tunnel (Figure 5.31).

The main excavation steps simulated regard the installation of support elements, the advancement of the tunnel and the simulation of primary support after the excavation, while the final lining installation was discarded in the analysis. In addition to the excavation cycle, the stability of the face was investigated in the case of an unsupported span of 1m (corresponding to the pull) and only use of intervention at the face. All the steps have been summarized in Table 5.6.

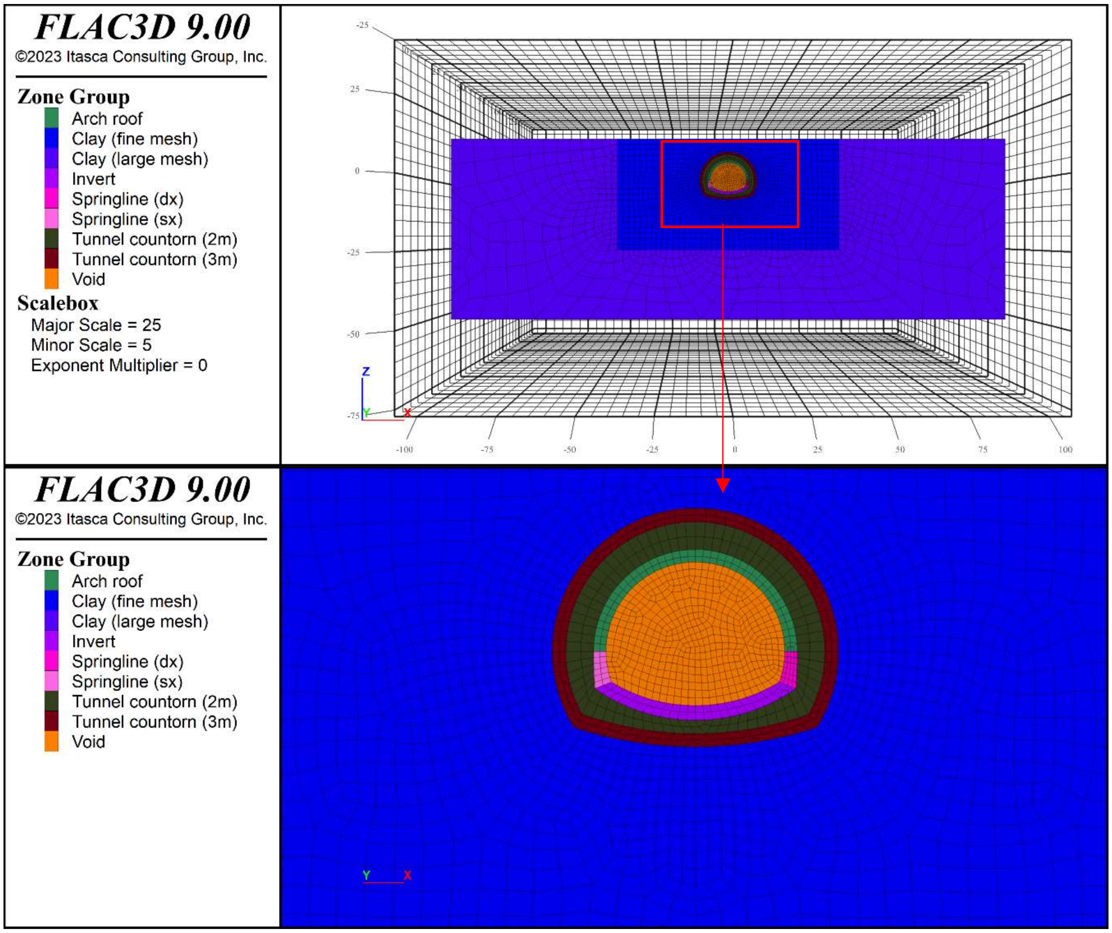

Figure 5.31 – Model geometry and group differentiation.

Table 5.6 – Stages adopted in the numerical model.

Steps	Description
1	Consolidation ahead of the excavation face
2	Excavation with an advancement of 1m
3	Activation of primary support (shotcrete + steel ribs) 1m behind the excavation face
4	Check on the stability at the face (SR technique)

The temporary support structure composed of steel ribs and shotcrete was simulated thanks to the use of shell elements with linear elastic behaviour. Due to the composite nature of the final material, the stiffness was calculated considering a homogenous section with an equivalent stiffness of 26.5 GPa. In the numerical analysis the stiffness modulus of the shotcrete is variable as a function of the advancement rate, especially according to the curing curves of Sezaki et al. ([31]).

The characteristics and properties used to simulate temporary support are reported in Table 5.7, then an example of shell installation after the excavation is given in Figure 5.32.

Table 5.7 - Characteristics of temporary supports.

Element	**Distance from the face [m]**	**Curing**	**Thickness[m]**	**E [MPa]**	**υ [-]**
Temporary lining	1	30%	0.25 – 0.30	7950	0.2
	2	60%	0.25 – 0.30	15900	
	3	70%	0.25 – 0.30	18550	
	≥4	100%	0.25 – 0.30	26500	

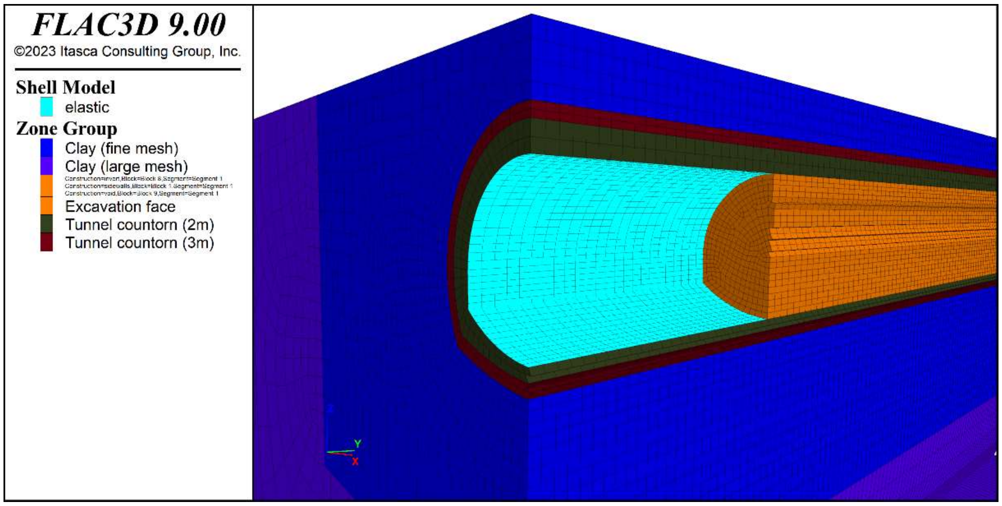

Figure 5.32 - Shell installation after the excavation of the medium.

5.2.1 Strength reduction techinique (SR)

Particularly, a complete 3D model was implemented in FLAC3D to simulate all the phases (Table 5.7) for the realization of a tunnel by adopting a conventional excavation technique.

The main goal of this section is the verification of the **F.S.** (Factor of Safety) of the excavation face, which determines the stability of the tunnel and its possible effect on the ground surface for low overburden conditions.

The effects on the F.S and deformation for different spacing conditions were compared by a procedure implemented in FLAC3D called **SR** (Strength Reduction technique) carried out by the progressive reduction of the shear strength of the material thanks to the decrease of the cohesion **c'** and friction angle **φ** related to the Mohr-Coulomb failure criterion (applications by Zienkiewicz et al. 1975 [32]).

Generally, the safety factor FS is defined according to the equations (Eq.5.10 and 5.11) after a series of simulations where a trial value for FS_{trial} is applied until the limit conditions are found.

$$c'_{trial} = \frac{c'}{FS_{trial}} \qquad (5.10)$$

$$\varphi_{trial} = \arctan\left(\tan\left(\frac{\varphi}{FS_{trial}}\right)\right) \qquad (5.11)$$

However, for the case under study the shear strength parameter is the **C_u** (undrained shear strength) useful for the simulation of process that happens much faster than the time needed for the consolidation of clays, and so the equation for the identification of FS is defined as:

$$C_{u_{trial}} = \frac{C_u}{FS_{trial}} \qquad (5.12)$$

For the simulation of the application of the pressurized reinforcement, a simplified method is applied in order to reduce the computational time needed, because, for a 3D model, the time spent to reach the final limit condition is more than 2 hours if the setup of SR is already optimized (e.g., Set the amplitude between two trial, define the decimal of FS to be found, etc…).

The simplified method consists of changing the properties of the soil medium for the length of the consolidation intervention according to the increment of undrained shear strength computed in previous sections for different spacing (§4.5.5.2)

5.3 Simplified Reinforcement Simulation at Excavation Face

The calculation of the factor of safety was carried out considering the stability at the face just after the realization of the advancement, and so without the installation of the temporary lining able to support the tunnel contour, in addition, the criterion for the failure was assumed considering the undrained shear strength.

Starting from this condition, the characteristics of the zone ahead of the tunnel face were changed according to the results of the previous sections (§4.6) obtained for different spacing. This method highly simplifies the effects of the reinforcement considered at the excavation face, but a complete simulation will lead to a not non-sustainable computational time to obtain the results and study different conditions.

Figure 5.33 shows the model configuration (before starting the SR technique) thanks to a visual command, it is possible to see a portion of the complete model by properly setting the range of visualization, set in the central axes of the 3D model. Particularly, Figure 5.33 highlights the application of the shell until the last excavation advancement and the change in property of the zone ahead of the excavation phase corresponding to 20m, equal to the length of the pressurized reinforcement.

The initial value of undrained shear strength estimated considering the mean effective stress corresponds to 60 kPa, this condition represents practically an unsupported face, with an expected value of **F.S** equal to 1 or less, which means an unstable condition or next to it.

Starting from the initial value of **Cu**, different percentage increments were applied following the results of section §4.6 for the different spacing conditions. Then, as an additional comparison the Young's modulus was increased in the same zone ahead of the tunnel according to the growth estimated in paragraph §4.6.

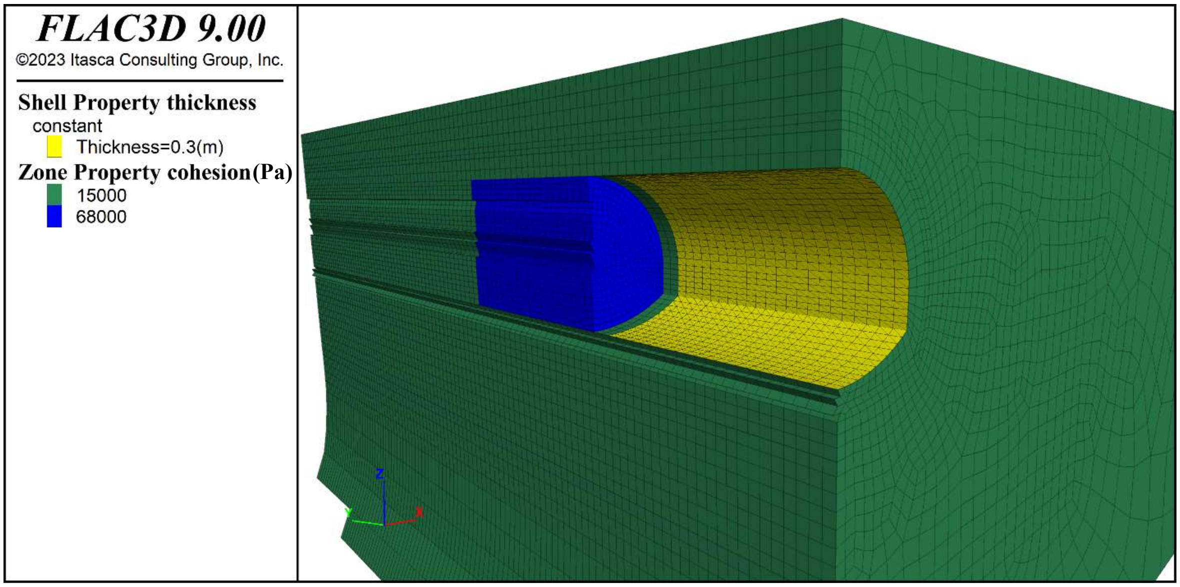

Figure 5.33 – Longitudinal section of the model setup before starting the computation regarding the face stability.

5.3.1 Deformation at the Excavation Face for different conditions

Before starting the computation of the safety factor at the excavation face by using the SR method, the displacements were calculated for six different scenarios, summarized in Table 5.8.

Table 5.8 -Different values of properties ahead of the excavation face for simulation of six different scenario.

ID	Cases	Increment of Young's Modulus	Increment of Cu	Young's Modulus (MPa)	Cu (kPa)
A1	Spacing =0.5m	0%	53%	150	92
A2		27%	53%	190	92
B1	Spacing =0.7m	0%	30%	150	78
B2		20%	30%	180	78
C1	Spacing =1m	0%	13%	150	68
C2		13%	13%	170	68

However, as reference condition the case without any reinforcement at the face is reported in Figure 5.34, where the maximum displacement at excavation face is around 22cm, with the consequent creation of 10cm of settlements at the ground surfaces at a distance of around 10 meters (about 1 times the diameter of the tunnel).

Then, from Figure 5.35 to Figure 5.37 the displacement at the excavation face were plotted, by coupling for the same spacing conditions two different case: the case **a** where the increment regards the undrained shear strength and Young’s modulus, and case **b** with the increase of **C_u** without any stiffening .

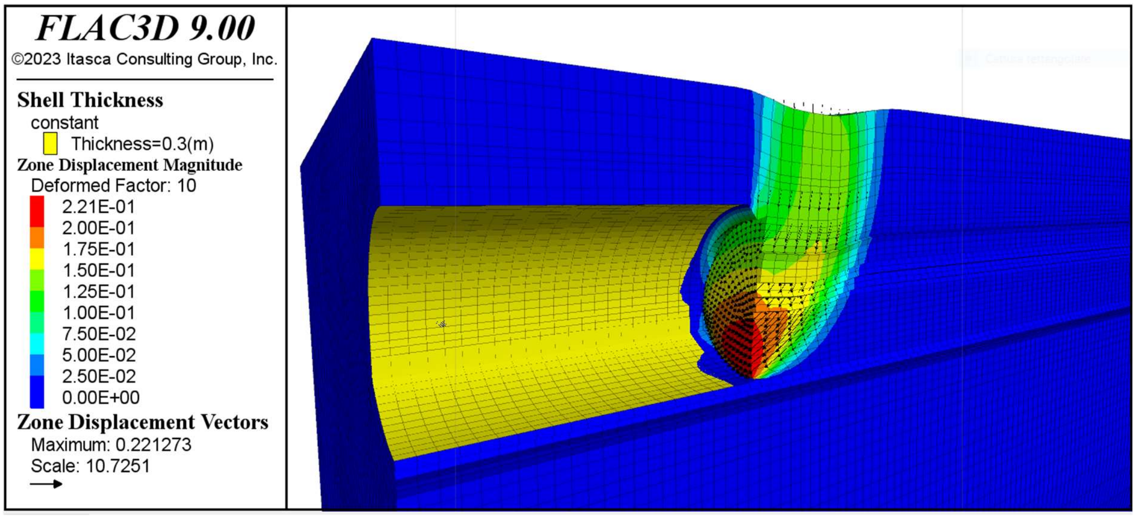

Figure 5.34 – Displacement at the face for the unsupported case.

The most important aspect to be highlighted from the comparison of different conditions was that an increase of 13% of the **C_u** leads to highly reduce the displacement at the excavation face to 15cm, considering instead the stiffening effects, the final maximum displacement was of 14cm.

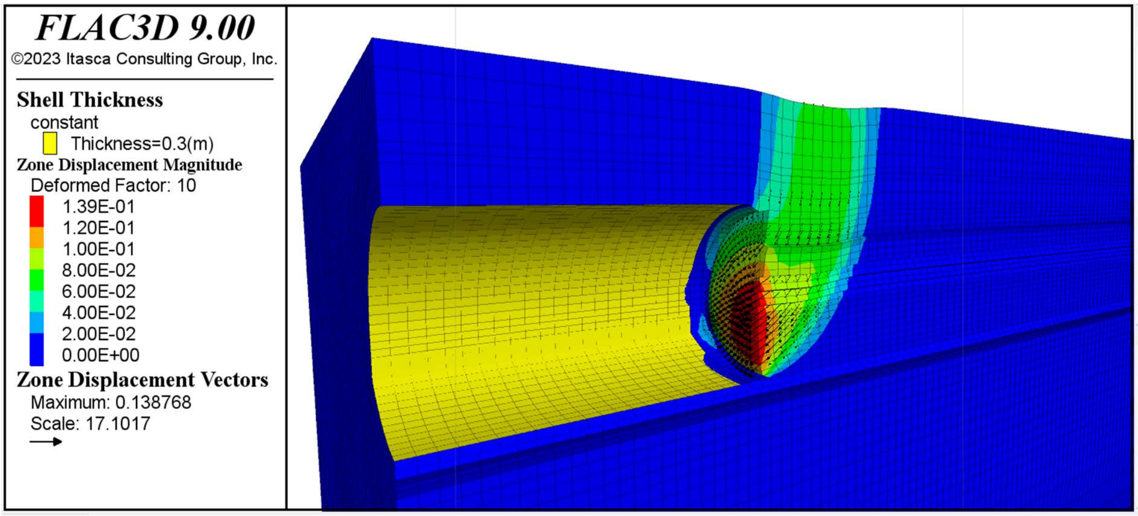

a)

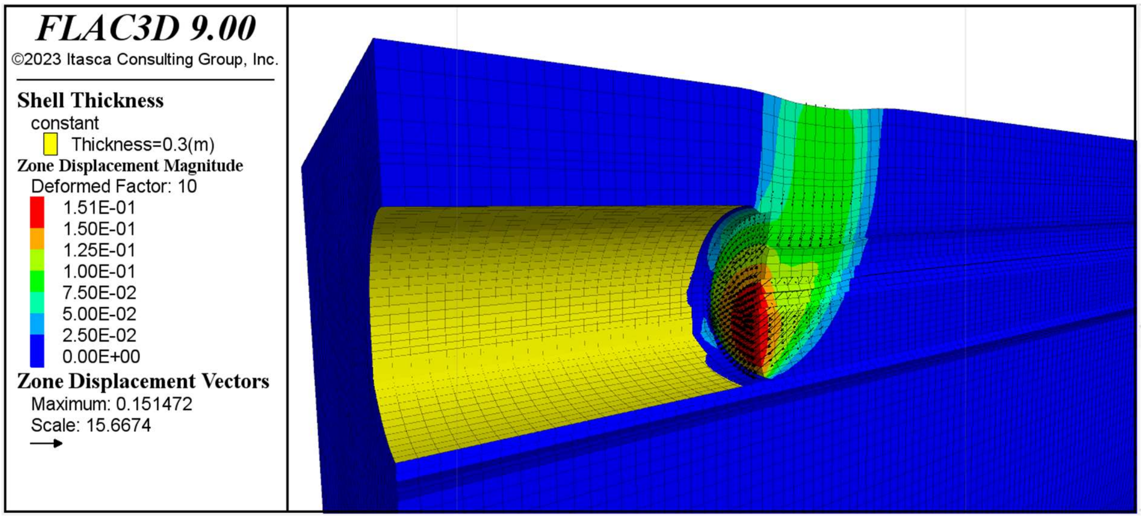

b)

Figure 5.35 – Displacement at excavation face for(a)13% of Cu and Young's modulus increase (b)13% of Cu increase.

The further increase of the **C$_u$** (30%) lead to a further reduction of the displacement at the excavation face with a maximum extrusion of 11,2cm corresponding 4 cm less respects the previous case (**C$_u$** + 13%).

In addition, from the visual comparison of the displacement contour in Figure 5.36, the portion of soil involved in the movement towards the tunnel face is reduced in width (in case of stiffening E +20%) and showed lower settlement at the ground surface, around 3cm.

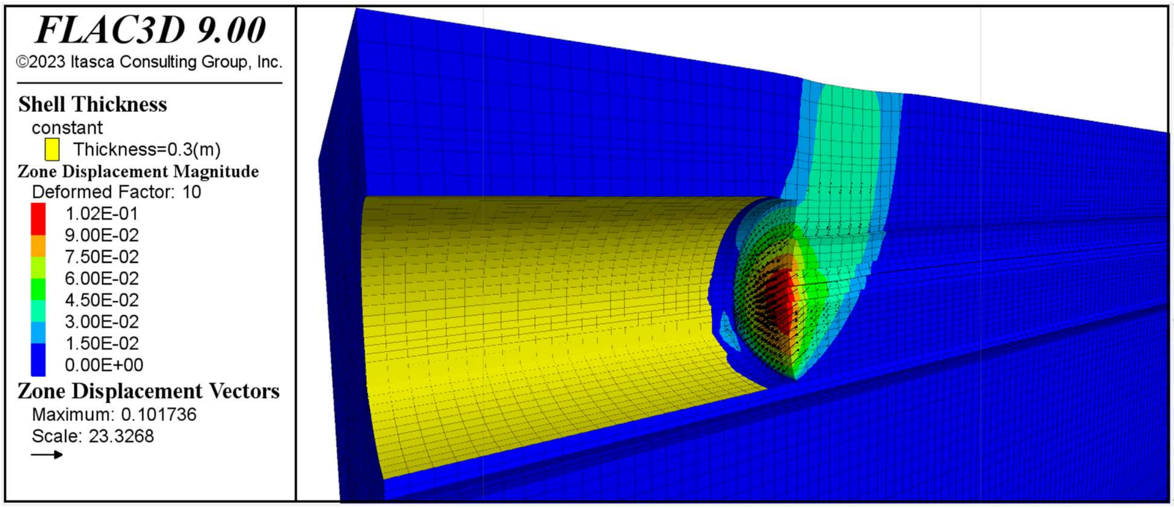

a)

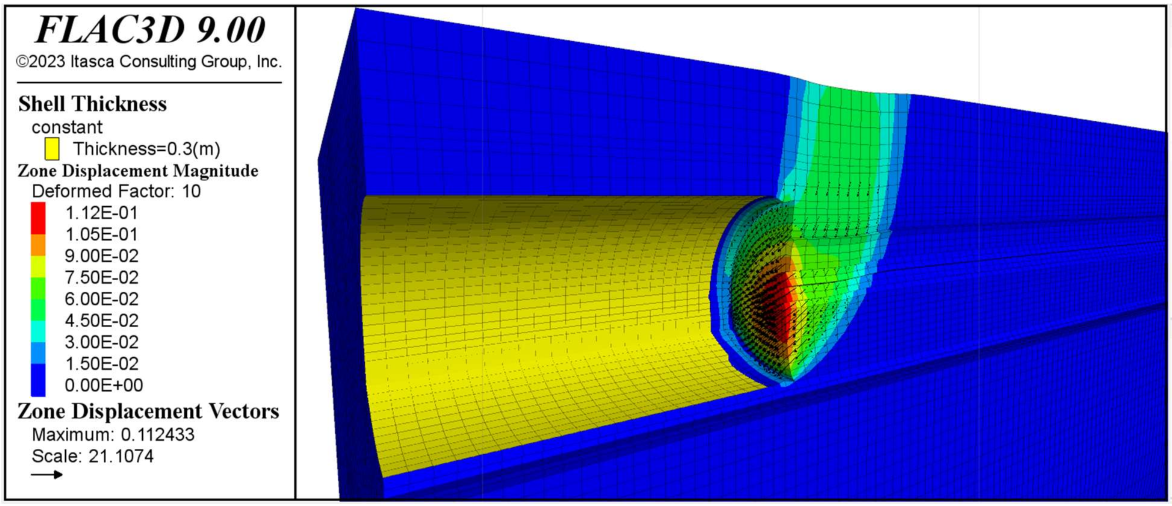

b)

Figure 5.36 - Displacement at excavation face for (a)30% of Cu increase and 20% of Young's modulus growth, (b)30% of Cu increase.

The last case simulated the intervention with lower spacing between element with the consequent highest increase in **C$_u$** (53%) and in **E** (27%), and as expected, the displacement at the face further reduces and reached 8cm without any propagation of the central core displacement, and the settlements at ground surface do not exceed 1,5cm.

If the stiffening effects is not considered, the central zone shows an extrusion that reaches higher values (9.22cm) than in the case just described. However, the most important aspect lies in the propagation of the displacements, which in this case would reach the ground floor with a subsidence of 4.5cm.

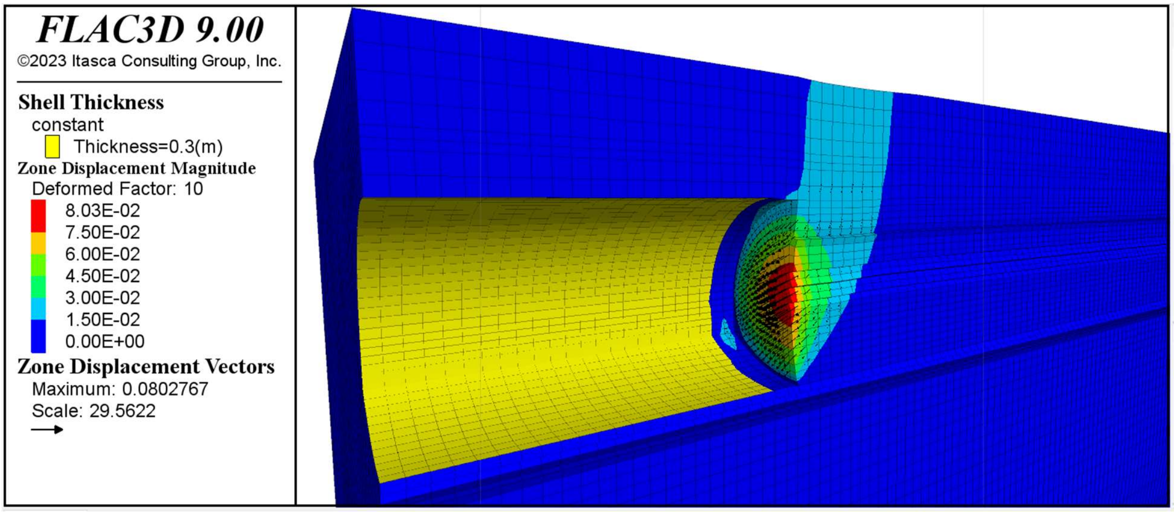

a)

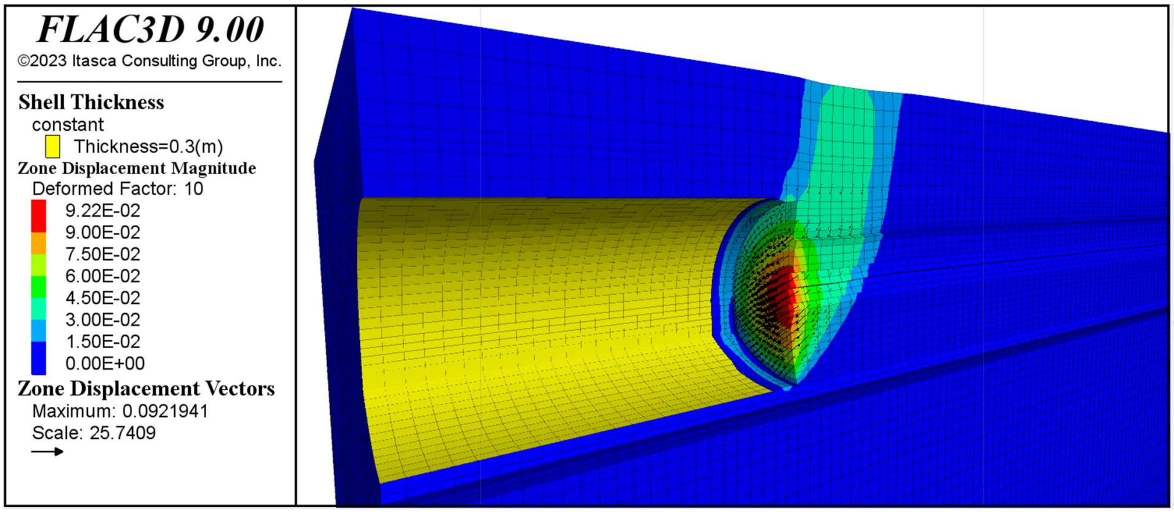

b)

Figure 5.37 - Displacement at excavation face for (a) 53% of Cu increase and 27% of Young's modulus growth, (b)53% of Cu increase.

5.3.2 Factor of Safety at Excavation Face for different conditions

The second step performed in the analysis of the face stability was the computation of the **F.S** for the different scenarios exposed previously in which the displacements were calculated.

The first case studied (considered as reference) was the condition without reinforcement ahead of the face. As predictable by the order of magnitude of the maximum displacements obtained (22cm), the factor of safety assumed a value lower than 1, which practically means an unstable conditions (Figure 5.38).

Then, as done in the previous sections, the **F.S** was analysed for the different cases (summarized in Table 5.8) comparing the effects of the strength increase by rising **Cu** and stiffening by growth of **E**.

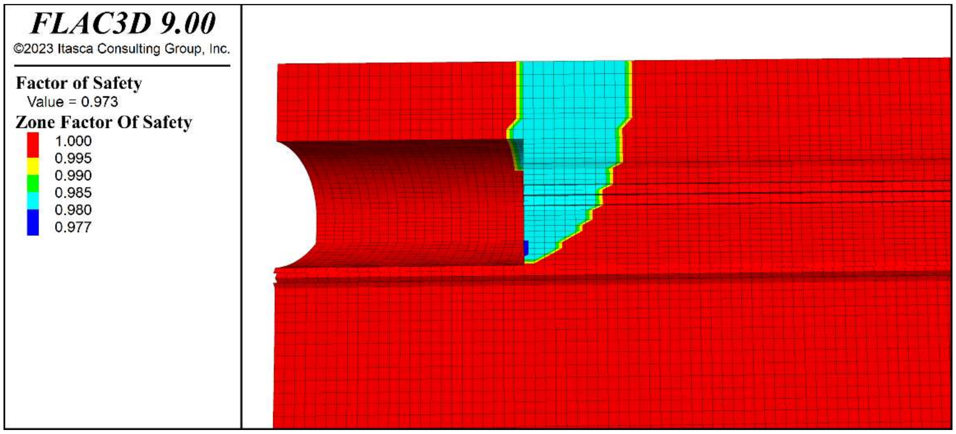

Figure 5.38 – Factor of safety contour in case of no intervention at the excavation face.

The first assessment of the results, for case C1 and C2 (Table 5.8) shows that the factor of safety increase until 1.05 by increasing only the strength, while was noticed that stiffening does not affect the final F.S that was equal to 1.08.

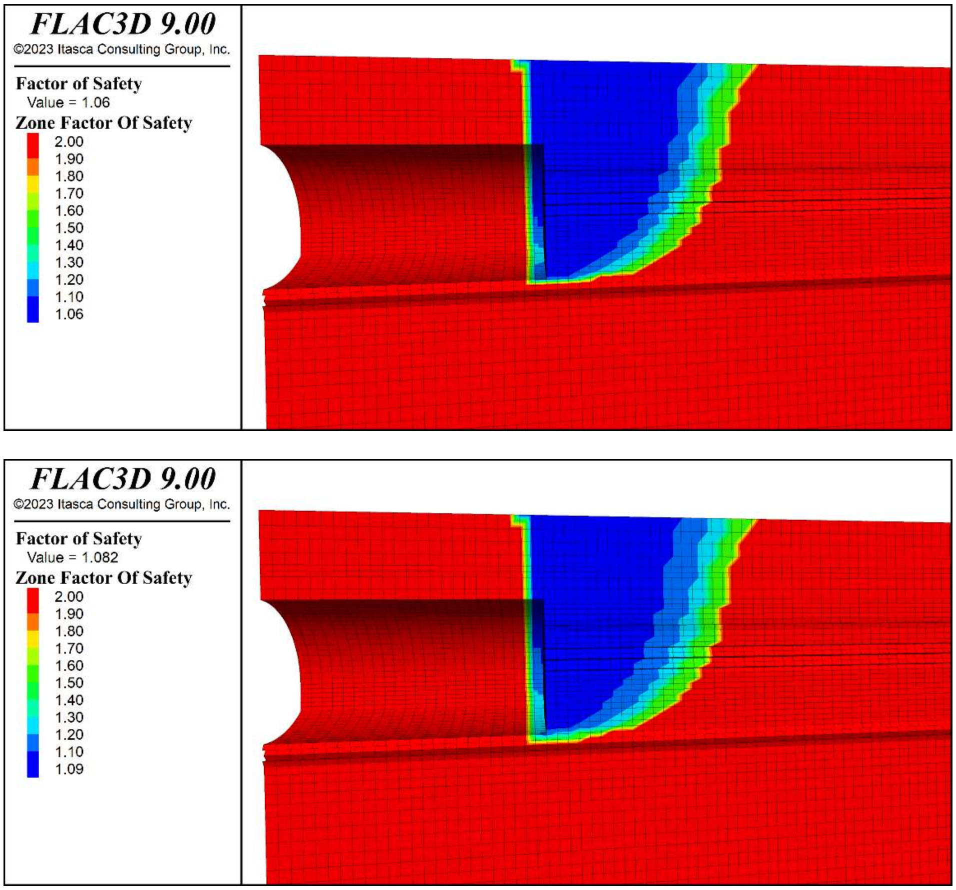

a)

b)

Figure 5.39 - Factor of safety contour in case of: (a)13% of Cu increase, (b)13% of Cu and E increase.

The second assessment of the results regards the cases B1 and B2 (Table 5.8), which show that the factor of safety increase until 1.1 by increasing only the strength, while the stiffening slightly affect the final F.S that was equal to 1.17.

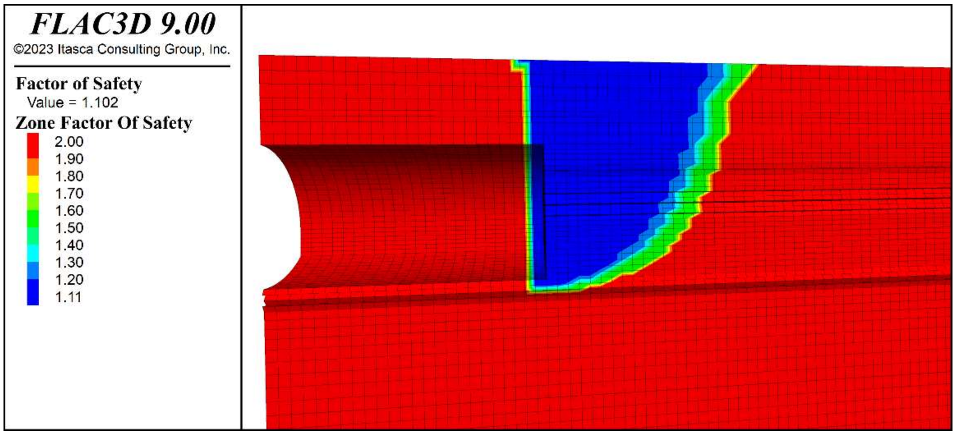

a)

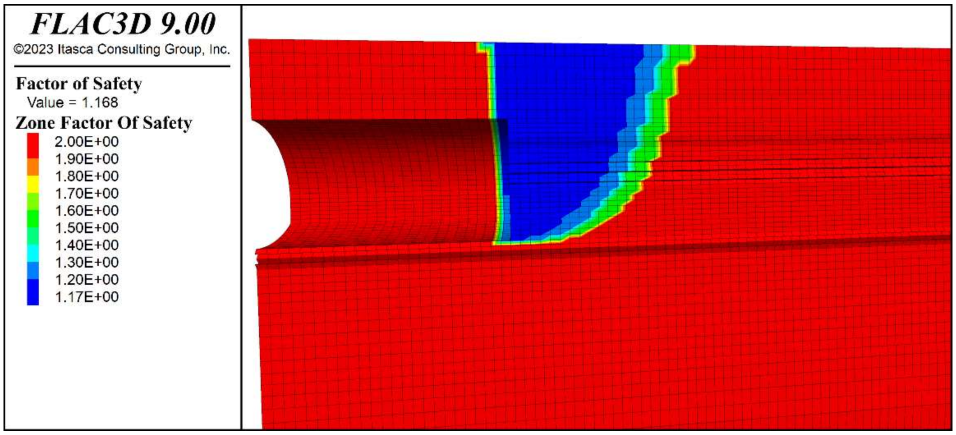

b)

Figure 5.40 – Factor of safety contour in case of: (a)30% of Cu increase, (b)30% of Cu and 20% of E increase.

The last assessment of the results involves the cases A1 and A2 (Table 5.8), which show that the factor of safety raise until 1.2 by increasing only the strength, while the stiffening moderately affect the final F.S that was equal to 1.3.

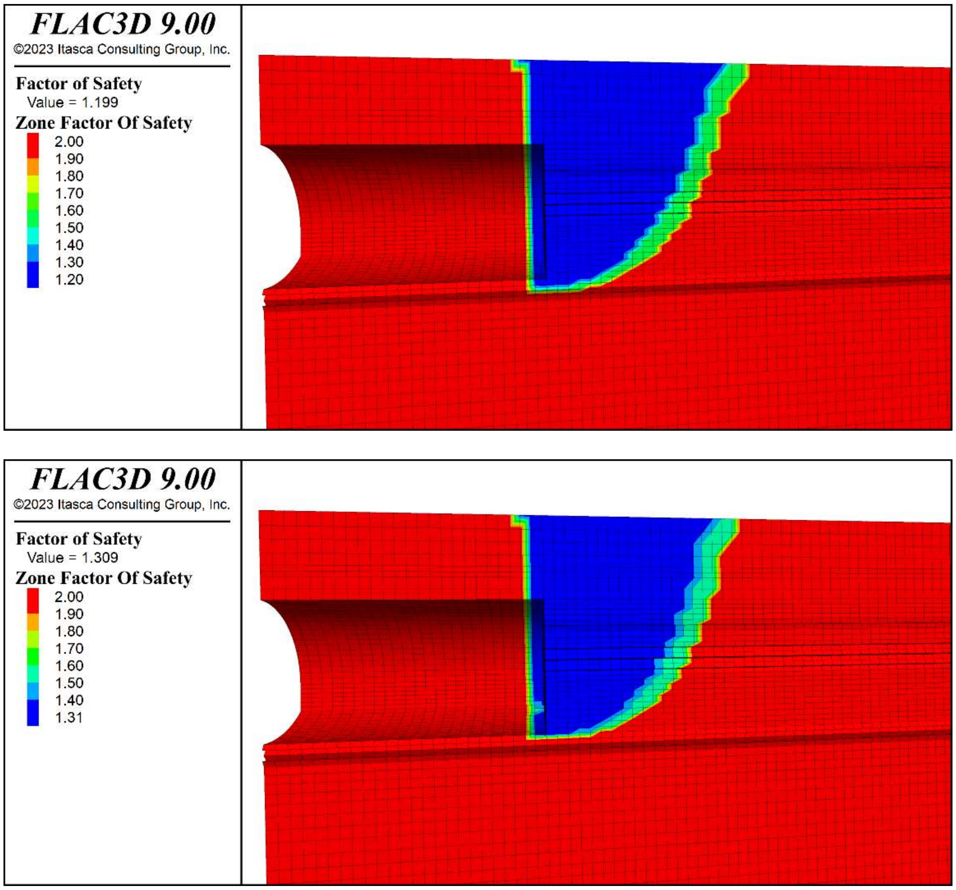

a)

b)

Figure 5.41 - Factor of safety contour in case of: (a)53% of Cu increase, (b)53% of Cu and 27% of E increase.

5.3.3 Summary of the results

The analysis carried out in the previous paragraphs (§5.3.1 and §5.3.2) highlights that the deformation at the excavation face highly depends on the undrained shear strength adopted for the simulation of the consolidation intervention ahead of the excavation face, indeed an increase of 13% in Cu allows to a relevant reduction in the displacement.

Then, to show clearly what is the incidence of an increment in the **Cu** with or without considering the stiffening effects estimated, the trend of **F.S - Cu** was plotted in Figure 5.42, while the trend of maximum displacements at the excavation face (**extrusion**) was plotted as function of **Cu** in Figure 5.43.

In both cases, the increment of Cu leads to better stability and deformations control, that is further enhanced by concerning in the analysis the effects of the Young's modulus increase.

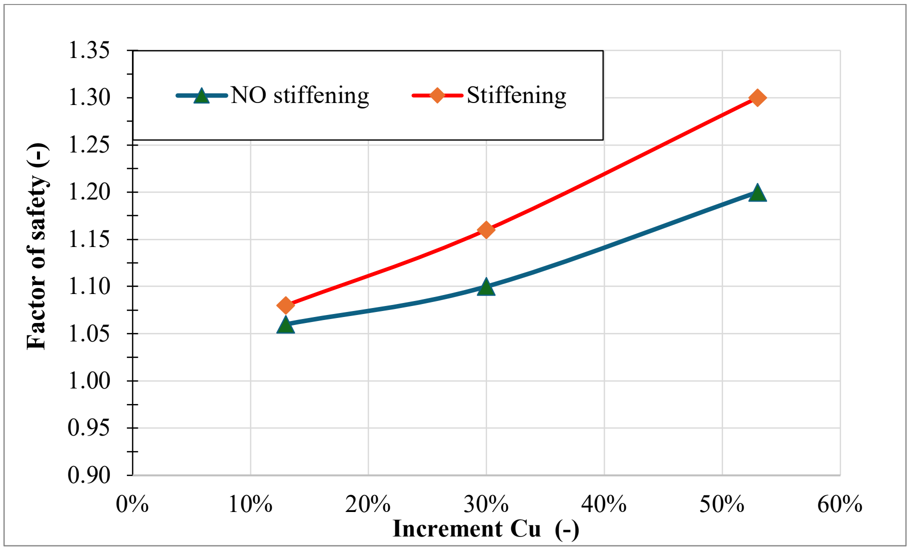

Figure 5.42 - Factor of safety as function of Cu increment.

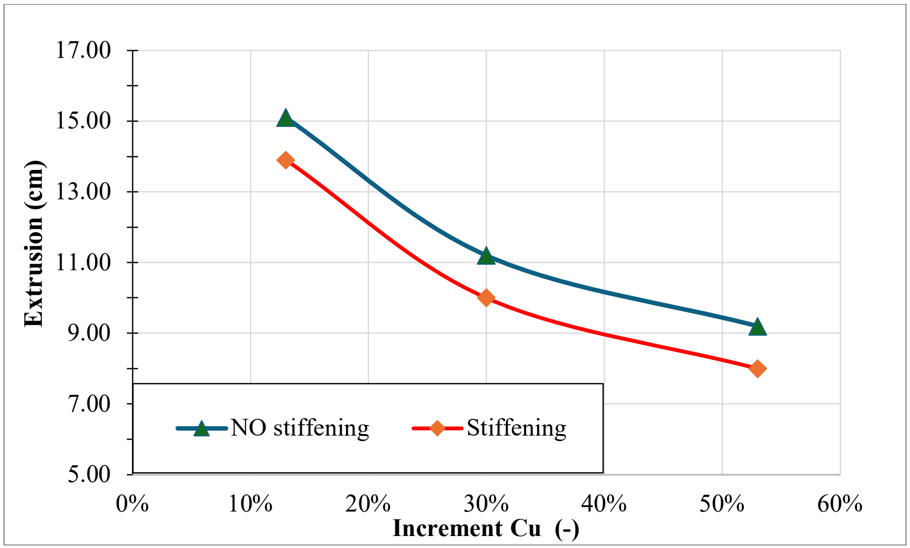

Figure 5.43 – Extrusion as a function of Cu increment.

The summary of all the results of this chapter and the parameters involved in the numerical analysis are reported in Table 5.9.

Table 5.9 – Summary of the results for the analysis carried out.

		Initial values		Value adopted for the simulation					
ID	Cases	Cu (kPa)	E (MPa)	Increment Cu	Increment of Young's modulus	Cu (kPa)	E (MPa)	Extrusion (cm)	Factor of safety
Reference	No intervention	60	150	-	-	-	-	22	0.92
A1	Spacing = 0.5m	60	150	53%	0%	92	150	9.2	1.20
A2				53%	27%	92	191	8.0	1.30
B1	Spacing = 0.7m	60	150	30%	0%	78	150	11.2	1.10
B2				30%	20%	78	180	10.0	1.16
C1	Spacing =1m	60	150	13%	0%	68	150	15.1	1.06
C2				13%	13%	68	170	13.9	1.08

6 CONCLUSION

The current thesis deals with the ground improvement for soft soil in saturated condition using a reinforcement system that combines drainage with a fibreglass element encased in a geotextile sheath. The purpose is the quantification of the combined effects in terms of short-term cohesion and stiffness of the soil.

This intervention is particularly beneficial in soils with low permeability where the cement mixture cannot adequately propagate through the surrounding soil to create a consolidated soil mass. The innovative technology foresees the enclosure of the fiberglass pipes within a geotextile cover, obtaining an enhancement in the adherence between the reinforcement element and the soil. Simultaneously, the compression of the surrounding area takes place with the increase of pressure around the application area. The resulting compression accelerates the consolidation process, reducing the pore pressures, increasing undrained shear strength, and stiffening of the soil.

The analysis focused the attention on these aspects, trying to quantify the improvement effects generated. Particularly, the influence of element spacing was investigated by using a three-dimensional numerical modelling technique. The model was developed at a meter scale, corresponding to the dimensions of the reinforcement elements. The results indicate that the degree of soil improvement strongly depends on the spacing of the elements, and so by varying the spacing, the study provides valuable insights to guide the design of stabilization systems for excavation works.

The most important variable affected by the improvement was the undrained shear strength, due to the recompression coupled with drainage that promotes the increase in mean effective stress and accelerates the pore pressure reduction process. A comparison between the adoption of a simple drainage system and a drainage system coupled with the "pressurized nail" revealed that the latter significantly enhances the undrained shear strength, which is critical for tunnel face stability. Following the analysis of the undrained shear strength increment at various element spacings, a 3D numerical model was developed to evaluate the factor of safety and predict the deformations at the tunnel face for a case study involving a shallow-depth tunnel currently in the executive design phase.

Numerical analyses demonstrated how the factor of safety increase by reducing spacing between the elements. Simultaneously, the impact of improvement on soil stiffness modulus was examined in two scenarios: the first considered the stiffness ahead of the face as unchanged, and the second took into consideration the stiffness increment previously estimated by the small-scale model's numerical analyses.

The analysis of the two scenarios revealed that even modest increases in soil stiffness (on the order of 10–20%, as quantified by the small-scale model) result in reduced deformations at the excavation. These findings highlight the significant contribution of deformation parameters to tunnel face strength and stability. As such, these parameters must be carefully considered in the design and evaluation of stabilization measures.

One of the most significant challenges in the development of the hydro-mechanical models starting from a set of available tests conducted for an Italian project in clay, was the absence of triaxial tests (CD[§§] or CU[***]). These tests would have provided a more reliable estimation for the key geotechnical parameters, such as cohesion and friction angle concerning the strength, and young modulus referring to deformability.

[§§] CD: Consolidated Drained testing procedure

[***] CU: Consolidated Undrained testing procedure

Especially, for the deformability parameters the simulation of different loading conditions in triaxial tests would offer valuable insights for the understanding of deformational behaviour during expansion and drainage. Additionally, accurate modelling requires the use of complex constitutive models capable of simulating hardening and softening processes, which are closely associated with the volumetric deformations occurring in the physical process.

One of the most promising directions for future development is the implementation of a physical model useful for the validation of the numerical models. Therefore, it would be possible to complete two keys objective: verifying the accuracy of the results obtained and enabling the joint calibration of the physical and numerical models.

This development could bring an easier identification of critical parameters influencing the modelling process, leading to a definition of tests (laboratory or in situ) to be suggested during the planning of the geotechnical survey, which would fulfil acquire a precise design purpose.

Moreover, the study highlights the attention on the interpretation and use of the results in the design process. In addition, the scale of the intervention and consequently the improvement effects quantified can vary significantly depending on whether it is considered in a limited box, such as a laboratory test, or directly applied at the excavation face. For these reasons, a comparison between different scales becomes necessary: at least two configurations must be explored. The small-scale study can be implemented to understand the physical process and results while maintaining low the cost of realization. On the other hand, the implementation at a bigger scale is needed as final verification of the results and compatibility with the improvement works

In conclusion, the necessity of developing a physical model to validate the estimated positive results is evident. Additionally, the realization of several in-situ experimental test (already conducted in Italy for the case of “Timpa delle Vigne tunnel”) would provide valuable insights into the know-how of the innovative technology with the ultimate goal of implementation in engineering practice.

BIBLIOGRAPHY

[1] Lancellotta, R. (2009). Geotechnical Engineering (2nd ed.). CRC Press. https://doi.org/10.1201/9781482265934

[2] D.M. Wood (1990) Soil Behaviour and Critical State Soil Mechanics. Cambridge University Press.

[3] Wright, S. G. (Stephen G. & Brandon, T. L. (2014) *Soil strength and slope stability*. 2nd ed. Hoboken, New Jersey: Wiley.

[4] Lambe, W. T. et al. (1997) Meccanica dei terreni. Palermo: Flaccovio.

[5] Ladd C.C., (1964), *Stress-strain behaviour of saturated clay and basic strength principle*, Research in Earth Physics, Research Report R64-17, Soil Mechanics Division, Department of Civil Engineering, Massachusetts Institute of Technology.

[6] ITA Report n°002 - General Report on Conventional Tunnelling Method - N°ISBN : 978-2-9700624-1-7 / APRIL 2009

[7] Bilotta, E. et al. (2022) Handbook on tunnels and underground works: volume 1: Concept - Basic principles of design. Boca Raton: CRC Press.

[8] Lauffer, H. 1958. Gebirgsklassifizierung für den Stollenbau. Geol. Bauwesen 24(1), 46-51.

[9] Anagnostou G., Kovari K. (1996), Face stability conditions with Earth Pressure Balanced Shield, Tunnelling and Underground Space Technology, vol 11, n°2, pp. 165-173.

[10] Vermeer P.A., Ruse N., Marcher T. (2002), Tunnel heading stability in drained ground, Tunnelling, Felsbau, vol. 20, n°6, pp. 8-18.

[11] Manquehual, C.J., Jakobsen, P.D. & Bruland, A. Corrosion Level of Rock Bolts Exposed to Aggressive Environments in Nordic Road Tunnels. *Rock Mech Rock Eng* **54**, 5903–5920 (2021). https://doi.org/10.1007/s00603-021-02547-3

[12] GEO 2008. Guide to Soil Nail Design and Construction (Geoguide 7). Geotechnical Engineering Office, Hong Kong.

[13] Lunardi P. (2000). Design & constructing tunnels – ADECO-RS approach. Tunnels & Tunnelling International, Supplemento Speciale, maggio 2000

[14] P. Perazzelli, G. Anagnostou,Stress analysis of reinforced tunnel faces and comparison with the limit equilibrium method,Tunnelling and Underground Space Technology,Volume 38,2013,Pages 87-98,

[15] Grasso P, Mahtab A, Pelizza S (1989) Riqualificazione della massa rocciosa: un criterio per la stabilizzazione di gallerie. Gallerie e grandi opere sotterraneo 39:35–41

[16] Dias D, Kastner R, Dubois P (1997) Tunnel face reinforcement by bolting: strain approach using 3D analysis. In: Proceedings of the international conference on tunneling under difficult conditions, Basel

[17] Dias D, Kastner R, Dubois P (1998) Effects of pre-lining on the tunnel design, Proceedings of the International Conference on underground in modern infrastructure, Stockholm

[18] Dias D, Kastner R (2005) Mode´lisation nume´rique de l'apport du renforcement par boulonnage du front de taille des tunnels. Can Geotech J 42:1656–1674

[19] Dias D, Kastner R, Jassionnesse C (2002) Sols renforce´s par boulonnage. Etude nume´rique et application au front de taille d'un tunnel profond. Geotechnique GE52:15–27

[20] Littlejohn, G. and Stadler, G. Joint lectures on anchoring and grouting at SAICE, South Africa; and EUROCK 2004 & 53rd Geomechanics Colloquium, Salzburg,Austria.)

[21] Huang, J. et al. (2022) Optimization design and characteristic of retarding and low-early-strength grouting material for capsule grouting technology: laboratory and field evaluation. Journal of materials research and technology.

[22] Mohammad Zahidul I. Bhuiyan, Shanyong Wang, and John P. Carter. 2021. Experimental study of an innovative driven and grouted soil nail (x-Nail). Canadian Geotechnical Journal. 58(8): 1205-1215

[23] Sterpi, D., Rizzo, F., Renda, D., Aguglia, F., & Zenti, C.L. (2013). Soil nailing at the tunnel face in difficult conditions: a case study. *Tunnelling and Underground Space Technology,* Vol. 38, pp. 129–139

[24] Itasca Consulting Group, Inc. (2023) FLAC3D — Fast Lagrangian Analysis of Continua in Three-Dimensions, Ver. 9.0. Minneapolis: Itasca.

[25] Schanz, T., Vermeer, P. A., & Bonnier, P. G. "The hardening soil model: formulation and verification," in ***Beyond 2000 in computational geotechnics***, 281-296 (1999).

[26] Cheng, Z., and A. Lucarelli. Plastic hardening model II: Calibration and validation. In Proc. 4th Itasca Symposium on Applied Numerical Modeling. 2016.

[27] Casagrande, A. (1936). The determination of the pre-consolidation load and its practical significance. In Casagrande, A., editor, *In Proc. 1st Int Soil Mech and Found Engng Conf, 22-26 June 1936*, volume 3, pages 60–64, Cambridge, Mass. Graduate School of Engineering, Harvard University, Cambridge, Mass.

[28] Pacheco-Silva, F. (1970). A new graphical construction for determination of the pre-consolidation stress of a soil sample. In *4th Brazilian Conf on Soil Mech and Found Engng*, volume 1, pages 225–232, Rio de Janeiro.

[29] R. Obrzud A. Truty, the hardening soil model a practical guidebook, Z Soil 100701 report (revised 2.01.2020)

[30] Rocha M., SILVEIRA A., GROSSMAN N.F., OLIVEIRA R. (1966) - Determination of the deformability of rock masses along boreholes. Proc. 1st Congress of the International Society of Rock Mechanics, Lisbona.

[31] M. Sezaki, O. Aydan, T. Kawamoto – Mechanical and numerical modelling of shotcrete (1992).

[32] Zienkiewicz, O. C., C. Humpheson and R. W. Lewis. "Associated and non-associated visco-plasticity and plasticity in soil mechanics," *Géotechnique*, ***25***(4), 671-689 (1975).

[33] W. K. Pun; W. M. Cheung; K. W. Shum."Geoguide 7 – Guide to soil nail design and construction" 17th International Conference on Soil Mechanics and Geotechnical Engineering (Alexandria)